

Tunable single-photon sources for integrated quantum photonics

Citation for published version (APA):

Petruzzella, M. (2017). *Tunable single-photon sources for integrated quantum photonics*. [Phd Thesis 1 (Research TU/e / Graduation TU/e), Applied Physics and Science Education]. Technische Universiteit Eindhoven.

Document status and date:

Published: 07/12/2017

Document Version:

Publisher's PDF, also known as Version of Record (includes final page, issue and volume numbers)

Please check the document version of this publication:

- A submitted manuscript is the version of the article upon submission and before peer-review. There can be important differences between the submitted version and the official published version of record. People interested in the research are advised to contact the author for the final version of the publication, or visit the DOI to the publisher's website.
- The final author version and the galley proof are versions of the publication after peer review.
- The final published version features the final layout of the paper including the volume, issue and page numbers.

[Link to publication](#)

General rights

Copyright and moral rights for the publications made accessible in the public portal are retained by the authors and/or other copyright owners and it is a condition of accessing publications that users recognise and abide by the legal requirements associated with these rights.

- Users may download and print one copy of any publication from the public portal for the purpose of private study or research.
- You may not further distribute the material or use it for any profit-making activity or commercial gain
- You may freely distribute the URL identifying the publication in the public portal.

If the publication is distributed under the terms of Article 25fa of the Dutch Copyright Act, indicated by the "Taverne" license above, please follow below link for the End User Agreement:

www.tue.nl/taverne

Take down policy

If you believe that this document breaches copyright please contact us at:

openaccess@tue.nl

providing details and we will investigate your claim.

Tunable single-photon sources for integrated quantum photonics

PROEFSCHRIFT

ter verkrijging van de graad van doctor aan de
Technische Universiteit Eindhoven, op gezag van de
rector magnificus, prof.dr.ir F.P.T. Baaijens, voor een
commissie aangewezen door het College voor
Promoties in het openbaar te verdedigen
op donderdag 7 december 2017 om 16.00 uur

door

Maurangelo Petruzzella

geboren te Terlizzi, Italië

Dit proefschrift is goedgekeurd door de promotoren:

vorzitter:	prof.dr.ir. G.M.W. Kroesen
1 ^e promotor:	prof.dr. A. Fiore
2 ^e promotor:	prof.dr. J. Gómez Rivas
Leden:	Prof.dr. K.A. Williams
	prof.dr. J. Finley (Technische Universität Munchen)
	prof.dr. A. Rastelli (Johannes Kepler University)

Het onderzoek of ontwerp dat in dit proefschrift wordt beschreven is uitgevoerd in overeenstemming met de TU/e Gedragscode Wetenschapsbeoefening.

A catalogue record is available from the Eindhoven University of Technology
Library
ISBN: 978-90-386-4396-0

Tunable single-photon sources for integrated quantum photonics
By Maurangelo Petruzzella

The work described in this thesis has been carried in the group of Photonics and Semiconductor Nanophysics, at the Department of Applied Physics of the Eindhoven University of Technology, The Netherlands.

This research is supported by the Dutch Technology Foundation STW, applied science division of NWO, the Technology Program of the Ministry of Economic Affairs under project No. 10380

Printed by Gildeprint

SUMMARY

Tunable single-photon sources for integrated quantum photonics

The control over the generation of single photons constitutes the momentous requirement in envisioned quantum photonic integrated circuits (QPICs) to implement advanced experiments such as boson sampling and, ultimately, quantum simulations. As a result of the spectacular progress in epitaxial growth and material science, it is nowadays possible to realize semiconductor nanocrystals (Quantum Dots, (QDs)) showing atomic-like transitions. Among the different approaches to the generation of single and entangled photons, the radiative recombination originated in these nano-islands has the potential to outperform traditional schemes based on down-conversion processes. Moreover, due to their compatibility with planar fabrication technology, several of these emitters can be integrated together in a III-V photonic circuit to create a parallel array of single photons travelling on a single chip. In spite of these achievements, when QDs are positioned in a bulk material, only a modest fraction of their emission can be actually collected. Additionally, the resulting photons have limited coherence time, as the decoherence rate exceeds the spontaneous emission rate. In order to face these challenges, photonic crystal (PhC) cavities - created by point-defects in periodic dielectric patterns - are commonly employed to increase the efficiency of the single-photon generation by exploiting the Purcell effect. However, a major obstacle to the implementation of scalable single-photon sources is represented by the unavoidable energy mismatch between the emitter and the cavity, and among distinct cavity-emitter nodes. This arises from the variations in size and compositions of these nano-islands, and from the fabrication disorder that strongly affects the cavity properties.

Local, electrical and reversible methods to independently control the resonances of both QDs and cavities are therefore crucial in order to make several Purcell-enhanced QDs indistinguishable in energy. This thesis addresses this key challenge by investigating tunable devices working at the single-photon level that meet the above criteria. The physical core underpinning the operation of these systems relies on a mechanically-tunable nano-cavity obtained through the evanescent coupling of two photonic crystal membranes.

The first chapter illustrates the state-of-the-art of quantum photonic integrated circuits with a particular focus on schemes based on gallium arsenide. Quantum dots and photonic crystal cavities are introduced along with the description of their interaction within the Jaynes-Cummings formalism. A variety of tuning strategies to modify the energies of emitters and cavity modes are reviewed along with a comparison of several figures of merit for the different tuning methods such as interdependency, speed and tuning range.

Chapter 2 illustrates the methods adopted to fabricate the devices employed in this project. The process flow is described in detail, illustrating the critical steps for the realization of the free-standing micro-membranes and

the p-i-n diodes. This chapter also describes the stress-releasing structures adopted to mitigate the buckling effects on the structure, induced during the fabrication process.

Chapter 3 describes our approach to tuning the modes of a PhC cavity. This is based on a double-layer cavity obtained by the vertical coupling of two photonic crystal membranes. The interaction of this system with a near-field tip is employed to investigate the dynamics of the system. Besides, an ultra-wide wavelength control of the photonic crystal resonances spanning over 37.5 nm is achieved via the local pressure induced by the near-field tip. On one side, the high-resolution obtained through the read-out of the mechanical and optical properties of the system gives direct access to the structural parameters of the device, necessary to accurately model its opto-mechanical behavior. On the other side, the application of this local force produces a shift of the cavity wavelength which is not limited by the pull-in effect.

A cavity-emitter node composed of an electrically-tuneable quantum dot embedded in a nano-opto-electromechanical system (NOEMS) is experimentally demonstrated in chapter 4. By controlling the Stark voltage applied to the emitters and the distance between two PhC slabs through capacitive forces, the tuning of the on-chip cavity-emitter node is reported for the first time. The interdependency between the nano-electromechanical actuation and the static field applied to the dot region is discussed as well. Time-resolved photoluminescence experiments demonstrate a large Purcell enhancement of a QD transition positioned at two different energies.

The electrical excitation of a single quantum dot exciton in a photonic crystal cavity is proved in chapter 5. Firstly, a tuneable PhC light-emitting diode featuring a large tuning range (≈ 15 nm) is presented. Then, the operation of these devices at the single-emitter level is demonstrated by injecting a relatively low current through the QD p-i-n diode. In this way, electroluminescence from an excitonic transition coupled to PhCC is achieved for the first time. The application of electromechanical forces within the PhC NOEMS makes it possible to bring an electrically-pumped excitonic transition into resonance with a cavity mode, resulting in a ten-fold enhancement in its emission rate. Anti-bunching experiments performed on a single dot line prove the non-classical nature of the emission from this light-emitting diode.

In the sixth chapter, an anti-stiction coating is developed to make the PhC NOEMS reliable against the pull-in-induced stiction of the membranes. By coating the PhC NOEMS with a conformal alumina layer deposited via atomic layer deposition methods, we demonstrated that the device can be actuated from pull-in back to its release status, both in static and in dynamic experiments. Besides significantly improving the reliability of tunable cavities, this also allows for the application of the device as a switch between two mechanical configurations, potentially enabling integrated switches for QPICs. A systematic study shows that the device can be actuated over 0.5 million cycles without a significant deterioration of its optical properties.

Chapter 7 presents the integration of the tunable QD-PhC node with ridge waveguides (RWs), which provide a low-loss channel to redirect the single-photon emission towards other elements of the chip. The light generated by

the optical excitation of the QD-layer is firstly funnelled into a broadband photonic crystal waveguide, and then it is transferred into the modes of a supported waveguide via a tapered mode adapter. We theoretically and experimentally explore different designs over a wide parameter space in order to maximize the coupling efficiency from the PhC cavity into the photonic circuit. By equipping these devices with electrical gates for cavity actuation, the side-collection of a mechanically-compliant and narrow (bandwidth 0.65 nm) waveguide-coupled photonic crystal mode is realized, which is essential to filter a single exciton line on a chip. The additional integration with Stark contacts enables the transfer of energy programmable single photons into the passive circuit, while proving Purcell enhancement in this geometry as well. The RW-coupled architecture has been further integrated with a 50:50 beam splitter realized on the double-membrane platform. Firstly, the design of this element using beam propagation methods is discussed. Then, this component has been characterized both classically and at the single-photon level. An integrated Hanbury-Brown and Twiss experiment, featuring a source and a splitter co-integrated on the same chip, is carried out from the single-exciton emission generated in the PhC waveguide.

Chapter 8 elaborates on the integration of multiple tunable cavity-emitter nodes on a single chip. The tuning methods developed in this work have been employed to suppress the energy mismatch of dots and cavities from different devices, providing a way to produce indistinguishable single-photons from remote emitters. Besides, the coherence properties of the QD-light excited by a non-resonant laser are analysed in view of their application in experiments based on interference between indistinguishable photons.

Finally, in the last chapter the most relevant findings of this dissertation are summarized and many possible future directions of this research line are pointed out.

CONTENTS

1	INTRODUCTION	3
1.1	Materials for QPICs	5
1.2	Gallium Arsenide QPICs	6
1.3	Quantum dots	8
1.4	Cavities	10
1.4.1	Photonic Crystal Cavities	11
1.5	Jaynes-Cummings model	13
1.5.1	Weak and Strong coupling	14
1.6	Review of tuning methods	16
1.6.1	QD tuning	18
1.6.2	Cavity Tuning	28
1.6.3	Comparison	36
1.7	Thesis goals and outline	39
1.A	Tuning range for cavities and quantum dots	41
2	FABRICATION METHODS	43
2.1	Introduction	43
2.2	Process flow based on optical and electron beam lithography	44
2.2.1	Part I: wafer growth	44
2.2.2	Part II: diodes	46
2.2.3	Part III: photonic crystals, waveguides and release	48
2.3	EBL-only process flow	51
2.4	Stress-releasing structures	53
2.5	Conclusions	55
3	NEAR-FIELD ACTUATION	57
3.1	Introduction	57
3.2	Description of the device	57
3.2.1	Optics	57
3.2.2	Mechanics	59
3.3	Methods	60
3.3.1	Fabrication details	60
3.3.2	Experimental Setup	61
3.4	Measuring the contact force	62
3.5	Imaging	63
3.6	Tip-induced tuning	64
3.7	Force reconstruction	67
3.8	Topography reconstruction	68
3.9	Conclusions	69
4	FULLY-TUNEABLE CAVITY-EMITTER	71
4.1	Introduction	71
4.2	Description of the device	71

4.2.1	Electromechanical Actuation	71
4.2.2	Dual-tuning device	73
4.3	Fabrication details	73
4.4	Experimental setup	74
4.5	Cavity tuning	75
4.6	QD tuning	76
4.7	QD-Cavity tuning	77
4.8	Time-resolved experiments	78
4.8.1	Time-resolved setup	78
4.8.2	Decay dynamics	79
4.9	Conclusions	81
5	TUNEABLE SINGLE-PHOTON LED	83
5.1	Introduction	83
5.2	Device Description	84
5.3	Tunable Light Emitting Diode	85
5.4	Single-exciton electroluminescence	88
5.5	Anti-bunching	89
5.6	Conclusions	92
6	ANTI-STICKION COATING	93
6.1	Introduction	93
6.2	Coating	94
6.3	Results and discussion	95
6.3.1	Static Actuation	97
6.3.2	Dynamic Actuation	99
6.4	Conclusions	102
7	WAVEGUIDE COUPLING	103
7.1	Introduction	103
7.2	Experimental setup	104
7.3	Ridge waveguide	106
7.4	Coupling to ridge waveguides	108
7.4.1	Mode adapter	108
7.4.2	Design PhC-PhCWG Coupling	111
7.5	Tuning	119
7.6	Beam splitter	123
7.7	Integrated Hanbury Brown-Twiss experiment	128
7.8	Conclusions	131
8	INTEGRATION OF MULTIPLE SINGLE-PHOTON SOURCES	133
8.1	Introduction	133
8.2	Design	134
8.3	Cross-talk cavity tuning	134
8.4	Bringing two dots on resonance	137
8.5	Spectral dependence on the excitation power	138
8.6	Coherence time	139
8.7	Preliminary experiments	140
8.8	Conclusions	144

9 CONCLUSIONS AND PERSPECTIVES 146

BIBLIOGRAPHY 159

In the late 1970s, the physics community started looking at the intriguing behaviour of quantum mechanical objects - revealed as entanglement and superposition - not just as a pure scientific curiosity, but as a new possible way to manipulate information. The field of quantum communication was born in 1984, after the proposal of the first communication protocol to safely transmit a cryptographic key over an untrusted channel, the famous BB84 quantum key distribution (QKD) [30] algorithm. Later, a class of hard computational problems, such as factorization in prime numbers and searching in a database, were reformulated using quantum resources by Deutsch–Jozsa [87], Shor [394] and Grover [148]. Despite these algorithms forecasted an exponential speed-up compared to their best-known classical counterparts, the community had to wait many years before the first basic experimental implementations [442]. This stems from the fact that quantum information processing (QIP) requires encoding information in a state of matter, namely the qubit, which is normally affected by decoherence due to the interaction with the surrounding environment. Nowadays it is still under debate which physical realization is the most suitable for implementing some of the proposed algorithms. Superconducting circuits, trapped atoms, colour centers, Majorana fermions and photons are some of the possible physical candidates for QIP applications. Photons are exceptionally attractive to build distributed quantum networks, since they combine low decoherence rate and high propagation speed. While the information can be encoded as a quantum bit in one of the degrees of freedom of light such as polarization, spatial or temporal modes, frequency and even angular momentum, protocols that rely on a continuous variable can be implemented as well. While the linear manipulation of most of these variables on a single-photon is straightforward with linear optics, photons interact very weakly with each other because of the small optical non-linearities in materials. Yet, non-linearities are fundamental to construct quantum gates in circuit-based models [222]. To circumvent this issue, Knill, Laflamme and Milburn (KLM) [213] proposed a new paradigm to carry out a probabilistic computation, known as Linear Optics Quantum Computation (LOQC) [216]. This approach makes use of a limited set of linear optical components, composed of beam splitters and phase shifters along with single-photon sources (SPSs) and an active network to feedforward the signals from single-photon detectors (SPDs). The probability of success for each probabilistic quantum gate can be increased by employing additional single-photon sources.

More recently, other schemes based on linear-optics circuits have attracted attention. A notable case is represented by *boson samplers* (BSs) [1] (fig.1.1 (left panel)). These are photonic circuits consisting of a nested network of interferometers that couple m photonic modes fed by a number n of indistinguishable single photons. The probability that n single photons are detected

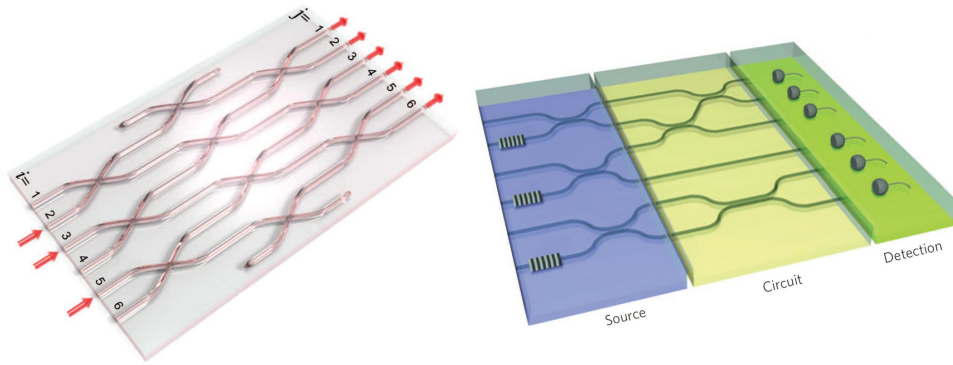


Figure 1.1: (left panel) Sketch of a boson sampling circuit made on silica-on-silicon waveguides with 6 input and output ports. Reprinted from [404]. (right panel) Schematic of a QPIC with SP sources, waveguides and SP detectors on the same platform. Reprinted from [17]

at n output ports of the system can be calculated by evaluating the permanent of the matrix that describes the unitary transformation of the circuit. If the circuit is realized in such a way that the input-output transformation is characterized by a uniformly random matrix, then calculating the transition probability has been shown to belong to a class of computationally hard problems [1]. The direct measurements of the outcome from a physical boson sampler will produce results much faster than any classical machine. From a fundamental perspective, these circuits can provide a way to disprove the extended Church-Turing thesis, which states that the behaviour of any realistic model of computation can be simulated by a probabilistic Turing machine in a polynomial time [370]. The number of single photons and photonic modes that are required to accomplish the so-called *quantum supremacy* (also known as *quantum advantage*) is currently under debate [307]. While previous studies indicated that for $n = 20 - 30$ [1, 34, 346] this limit can be reached, more efficient classical algorithms from one side, and refined versions of BS from the other side, increase or lower this threshold to $n > 50$ [307] and $n = 7$ [228], respectively.

Even the most simple implementations of LOQC and BSs involve interfacing a large number of components without losses. Bulky table-top implementations face some practical issues in this respect, arising from the mechanical stability and the reduced coupling efficiencies of each part. As in the case of electronics, scaling up the number of (qu)bits demands an integrated architecture, a quantum photonic integrated circuit (QPIC) (fig.1.1 (right panel)). But, differently from electronics, where the material of choice is silicon and the building block is the transistor, quantum photonic circuits require a large number of functionalities that are challenging to implement within a single material. For this reason, several devices and small-circuits that address specific tasks have been developed on parallel for different materials, as discussed in a recent review[41]. In next section we briefly introduce some platforms adopted in the realm of quantum photonic integrated circuits. At the end of this section we describe a possible implementation in Gallium Arsenide (GaAs).

1.1 MATERIALS FOR QPICS

The first demonstrations of single LOQC gates relied on silica-on-silicon circuits, mainly composed of few waveguides and phase shifters [341]. Although these circuits are still employed for quantum communication experiments, due to their large mode size compatible with the out-coupling to fibres, they have gradually been replaced by silicon-on-insulator (SOI) platforms, which provide higher components densities. The development of quantum photonic circuits based SOI waveguides has undoubtedly benefited from well-established fabrication processing [329, 395]. In these architectures, waveguides are typically composed of 220-nm thick silicon stripes encapsulated in silica. The high confinement provided by the high contrast in the refractive index of these two materials allows for the reduction of the bend radii of the waveguides below a few microns, and consequently for the increase of the number of devices per unit of area. A clear advantage of silicon compared to other materials stems from the compatibility with the complementary metal-oxide-semiconductor (CMOS) technology. This is particularly convenient for feed-forwarding the detection signal in the LOQC philosophy. Thanks to this mature fabrication technology, boson sampling circuits featuring 15 [53] and, more recently 56 [153] reconfigurable interferometers were reported, along with the demonstration of small simulation problems [376]. While most experiments so far have employed external sources and detectors, integrated SPSs can be obtained on SOI exploiting spontaneous four-wave mixing (SFWM) [102]. This is an elastic process where two photons from a bright pump are converted through a $\chi^{(3)}$ non-linearity into two correlated photons, named *signal* and *idler*, which have a slightly different wavelength. In contrast to the generation in free-space, the use of well-defined modes automatically satisfies phase- and mode-matching conditions. Despite the proof of small-scale quantum circuits, silicon presents several drawbacks. Contrary to the emission from single emitters (discussed in section 1.3), the quantum state produced by these sources is - in general - a state characterized by a poissonian statistics. In other words, there is a finite probability of generating either (i) zero or (ii) more than one photon per pulse. Events belonging to the former category can be rejected employing the detection of one signal photon ("herald") to flag the presence of the idler photon. Besides, if a photon number resolving detector (PNR) is adopted in this heralding process, multi-photon events (ii) can be also discarded. However, due to the lack of commercially available PNR detectors, a common strategy to avoid (ii) consists in attenuating the pump power at the expenses of source brightness. This compromises the scalability of these sources. In fact, it can be proved that the probability for n heralded sources to produce one and only one pair drops exponentially with n [395]. Multiplexing schemes employing a programmable switching network equipped with SPDs have been proposed to mitigate this efficiency problem [287], but no significant improvement has been reported so far. Besides, two-photon absorption introduces additional losses in the propagation along the waveguides, since single photons can be re-absorbed with a photon from the pump, thus creating free-electrons. From the detector side, nanowire superconducting single-photon detectors (nSSPDs) have been also implemented in silicon

[332]. However, it is an open-question whether the operation of these detectors is compatible with non-linear sources and switching. In fact, the use of very high pump powers in the non-linear generation process will require optical filters with high suppression rates, each characterized by a specific loss. Besides, the scattering of the pump power outside the waveguide region cannot be easily suppressed using integrated filters, possibly resulting in spurious detector counts. At the same time, the need of low-temperatures for the operation of the detectors affects the thermo-optic coefficient employed for reconfiguring the interferometers in silicon circuits. For a detailed review on the current status of silicon-based quantum photonics, see [395].

Other materials are currently being investigated. For example, glass-based circuits, which can be patterned via laser writing, offer a versatile way to prototype complex linear circuits made of several directional couplers. These can be controlled in polarization and along three-dimensions. They have been employed in first boson sampling circuits [77, 431] and their subsequent verification protocols [401]. However, these circuits typically show very weak non-linearities and the difficulty to integrate sources. Diamond circuits and, in particular, diamond-on-insulator (DOI) are recently being explored due to the improved fabrication technology over recent years. Here, nitrogen-vacancy centres represent a valid single-photon source also at room temperature [378], despite they are characterized by low coherence time and efficiency due to the presence of the phonon sidebands. Besides, spin-manipulation is possible via single-shot optical spectroscopy. Other materials for QPICs include Lithium niobate, mainly used for quantum communication [317] and Silicon Carbide.

Starting from the next paragraph, we will focus on GaAs QPICs [49, 88, 252].

1.2 GALLIUM ARSENIDE QPICS

Among the many advantages of QPIC based on GaAs, the possibility to embed deterministic sources within a III-V semiconductor chip represents an outstanding benefit compared to approaches based on indirect bandgap materials and glasses. In particular, the use of quantum dots (QDs) as artificial two-level atoms enables the generation of ultra-pure single photons. The brightness of these sources is ultimately limited by their radiative decay rate. Therefore, up to a GHz single-photon rates can be in principle achieved for dots embedded in bulk materials. At the same time, these sources can be activated on-demand by external optical triggers, allowing the generation of trains of SPs with a well defined temporal waveform. In order to further increase their internal and external efficiency, these emitters are typically embedded in nano-resonators, such as photonic crystal cavities (PhCC), to accelerate their generation rate via the Purcell-effect, and to funnel their radiation into a single mode. Single photons are not the only photonic quantum resources that can be produced by the excitation of single QDs. By exploiting for example the radiative decay of multi-excitonic species belonging to a single dot, entangled states can be created as well [26, 31, 139, 409, 435]. Furthermore, the capability to manipulate the spin

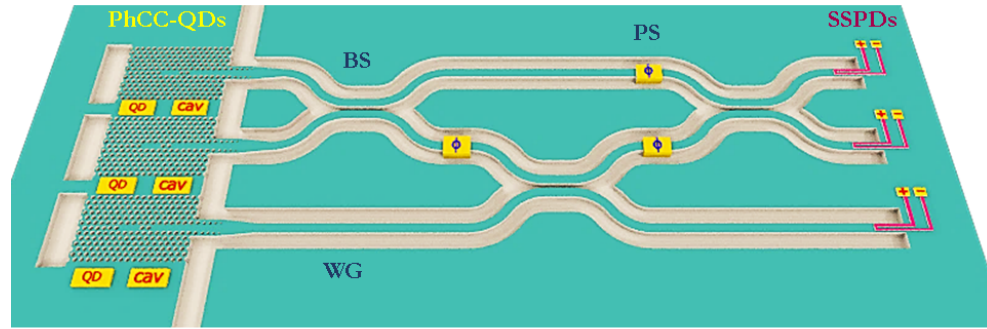


Figure 1.2: Prototype of a GaAs-based quantum photonic circuit. Single photons generated PhC cavities are transferred to waveguides (WGs) via engineered adapters. A reconfigurable network of splitters (BSs) and phase shifters (PSs) allows the linear manipulation of the quantum states of the light and - in the example reported here- the realization of a probabilistic CNOT gate. Alternatively, by increasing the dimensions of the linear waveguide network, boson sampling circuits can be implemented as well. Finally, a set of nanowire superconducting single-photon detectors (nSSPDs) generates electrical signals from the absorption of the single photons. These can be used as a feedback to reconfigure the state of the linear network

of electrons and holes populating the dot levels opens new avenues to spin-dependent propagation directions of single photons, in schemes that deviate from the original LOQC proposals [260, 261, 400, 479]. Equally important is the ability in III-V QPICS to realize single-photon light-emitting diodes (SP-LEDs). These devices, fabricated by integrating the QD layer inside a p-i-n junction, can generate quantum light upon the application of electrical pulses, and will play a crucial role in the generation of multi-dimensional single-photon states from multiple emitters.

Along with the availability of active quantum sources, GaAs is characterized by a non-zero electro-optic (EO) coefficient [455] ($\gamma = 2.5 \times 10^{-11} \text{ m/V}$), due to the lack of inversion symmetry in its crystal structure. The use of EO effects for the realization of phase-shifters is particularly important due to the impossibility to employ thermo-optics effects in circuits operated at low-temperature. EO tuning thus provides a way to reconfigure a set of interferometers that are compatible with the operating conditions of both quantum dots and SSPDs detectors.

Finally, many applications involving superconducting nanowire detectors have been demonstrated in GaAs QPICS [129, 143]. In these detectors, the absorption of a single-photon induces a local disruption of the superconductivity, caused by an increased concentration of quasi-particles (the so called hot-spot mechanism) and the creation of crossing vortices [366]. The resulting increase in the resistance of the wire is read as voltage pulse on the loading resistance and is characterized by a jitter as low as 60 ps for GaAs substrates [403]. Particularly relevant geometries in the context of QPICS are waveguide-coupled nSSPDs [403]. Here, a very thin (4-5 nm) niobium

nitride film is sputtered on top of a GaAs waveguide and patterned as a unidimensional wire. The overlap of the evanescent field of the travelling guided mode with the superconducting film leads to a modal absorption coefficient in the order of several hundreds of cm^{-1} , resulting in a practically perfect absorption for a waveguide length of few tens of μm . In addition, by integrating multiple nanowires on top of a single waveguide, an autocorrelation equipped with integrated detectors that shows negligible cross talk has been implemented [371]. Moreover, by increasing the number of wires it is possible to resolve the photon-number states [93, 179, 492], also in a waveguide geometry [372].

Fig. 1.2 shows a sketch of a prototypical QPIC based on a GaAs platform, where the generation, the manipulation, and the detection of single photons is carried out within a single chip. In order to erase the energy mismatch between multiple resonators and quantum dots, each cavity-emitter node is equipped with a dot-tuning and a cavity-tuning mechanism. As we will widely illustrate in this chapter, these mechanisms are essential to overcome the initial energy detuning between remote sources and to produce indistinguishable single photons. With a suitable choice of the PhC designs, a photonic crystal cavity can be directly coupled to a photonic crystal waveguide. Alternatively, a *filter* can be realized by a configuration waveguide-cavity-waveguide. Filtering is important to select a single dot line among the many produced by the non-resonant excitation. The deterministically generated single photons can be transferred to low-loss waveguides (WGs) via engineered mode couplers. Supported ridge waveguides can be fabricated by preserving the AlGaAs layer underneath the GaAs. Linear optical components such as beam splitters (BSs) and phase shifters (PSs) can be designed to implement probabilistic logic gates for LOQC computation. Additionally, waveguides can transport light off-chip via input/output couplers. These elements are useful to implement quantum state tomography, to introduce long delays difficult to implement within the circuitry, or to distribute the excitation pump among the different sources. Lastly, waveguide-coupled nanowire single-photon detectors can be employed to absorb the quanta of light and to convert them into electrical pulses. An electronic control circuit can be used to update the status of the interferometers based on the outcome of the measurements.

In the following paragraphs, we will introduce the basic ingredients to build deterministic single-photon sources, i.e. quantum dots and photonic crystal cavities, and outline their interaction in the Jaynes-Cumming framework. Then, we will review the state-of-the-art of post-fabrication methods to control their energies.

1.3 QUANTUM DOTS

Quantum dots, often referred to as *artificial atoms* or *quantum boxes*, are aggregates of semiconductor atoms embedded in a hosting material that shows a wider energy gap.

These nano-structures are spontaneously created in a number of ways that include the variations in the thickness of a quantum well, the fluctuations

in the crystal structure in a nanowire, and the self-aggregation of nano-islands in the epitaxial growth of two lattice-mismatched materials. The latter, named Stranski-Krastanov (SK) method, is very popular due to its relative simplicity, and has been adopted in this thesis. This method employs molecular beam epitaxy to deposit a direct semiconductor material (here InAs) on a substrate (here GaAs) characterized by a different lattice constant. In the case of InAs and GaAs, the lattice mismatch is 7 percent, resulting in the accumulation of strain between these two materials. During an initial phase, a quantum well of few monolayers of InAs is created, which is referred to as *wetting layer*. Then, the creation of small InAs islands is energetically favourable due to the increasing strain. This nucleation process is purely random with no control over the spatial position of the dot. Dots grown using this technique have diameters in the range of 10-30 nm and heights varying from 1 to 10 nm. As a final step, the dots are typically capped with GaAs to limit the effects of oxidation and non-radiative channels from the presence of surface states. The final geometry of the dot after capping corresponds to an elongated shape [11] (as shown in fig. 1.3(a)) while the inter-diffusion of gallium into the dot modifies its composition in InGaAs. In this thesis, instead, we employ dots capped with a $\text{In}_{0.2}\text{Ga}_{0.8}\text{As}$ layer, which shifts their energy around 1300 nm at low temperatures [11, 12]. For quantum optics experiments it is crucial to control the dot density in order to isolate single dot lines. This can be achieved by carefully tuning the temperature and the nucleation rate during the growth. In this way it is possible to grow dots with density below 5-10 QDs per μm^2 , as shown in fig.1.3(b). Despite being solid-state mesoscopic objects, made of thousands of atoms, QDs show a discrete energy set associated with atomic-like transitions. The optical properties of quantum-dots are commonly investigated by photo-luminescence experiments at temperatures below 60 K. The need for cryogenic temperature arises from the dephasing channels introduced by the interactions with phonons, which broaden the linewidth of the emitters and decrease their intensity at high temperature. Under the application of an external electrical or optical excitation, electrons are promoted to the conduction band, leaving empty states in the valence band, known as *holes*. These produce free electron-hole pairs that can diffuse in the semiconductor and can relax very quickly - in a ps time-scale - into the QD. Due to the quantum confinement within the dot, they form a bound state known as neutral *exciton* (X, fig. 1.3 (c)) which then decays radiatively emitting a single-photon. In this picture, due to the fast relaxation processes involved in the population of the exciton, the single-photon emission takes place within a $\approx\text{ns}$ time after the excitation trigger, and is referred to as *on-demand*. In strained QDs, light-holes are typically separated in energy from heavy-holes (hh) by tens of meV and are commonly neglected in the description of the ground-state of the exciton transitions, an approximation often referred to as *single-band approximation*. Since the z-projection of total angular momentum for the electron and the heavy-hole is respectively $|S_z = \pm 1/2\rangle$ and $|J_z = \pm 3/2\rangle$, the total angular momentum of the composite particle ($M_z = J_z + S_z$) can be in four different configurations, $M_z = \pm 1$ and $M_z = \pm 2$. As the generation or absorption of a photon can induce a change in the angular momentum of ± 1 in the dipole approximation, the states having $M_z = \pm 1$ are optically

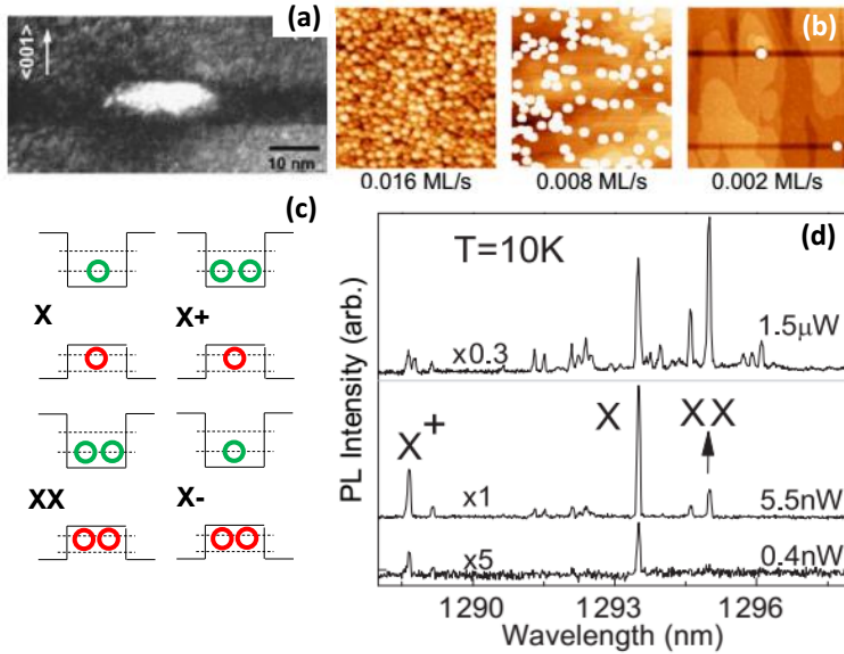


Figure 1.3: (a) Transmission electron microscopy image of a dot capped with InGaAs. From [12] (b) AFM image of the dot density obtaining varying the In flux [12] (c) Excitons in a dot (X neutral; XX bi-exciton, X_{\pm} trions) (d) Photoluminescence spectrum showing several exciton lines at different excitation powers. Adapted from [493]

active and are referred to as *bright* excitons as opposed to the *dark* excitons that have $M_z = \pm 2$. Spin-flip processes can change an exciton from dark to bright and vice versa, and are usually manifested as a second, slower decay in the exciton transition. Besides, a dot can also capture multiple carriers (fig. 1.3) (c)), leading to bi-excitons (BX) composed of two electrons and two holes and trions, i.e. three-particle excitons made of a neutral exciton bounded to an electron (X^-) or a hole (X^+). These quasi-particles are typically non-degenerate in energy due to the Coulomb interaction between the composing particles (fig. 1.3) (d)). A typical strategy to identify the exciton species relies on the use of power-scans or cross-correlation experiments. However, the presence of the cavity and the possible existence of several dots within the excitation area, make this classification challenging. For this reason, in the rest of this thesis we will generally refer to one of the aforementioned species as excitonic line.

1.4 CAVITIES

Cavities are primarily important for two reasons: to increase the collection efficiency from single emitters and to produce indistinguishable single photons. The need of a photonic structure to maximize the number of collected photons arises from the low out-coupling efficiency of quantum dots in bulk due to total internal reflection (TIR). More quantitatively, it can be shown [28, 338] that the fraction of photons emitted by a dipole that reaches the

first collection objective can be written as the product of a transmission coefficient of the air-GaAs interface (T) and a geometrical factor (C_g), accounting for the finite numerical aperture (NA) of the lens

$$C = T \cdot C_g = \left[1 - \left(\frac{n-1}{n+1} \right)^2 \right] \cdot \frac{1}{8} (4 - 3 \cos \theta_{\text{TIR}} - \cos(\theta_{\text{TIR}})^3) \quad (1.1)$$

where $\theta_{\text{TIR}} = \arcsin \left(\frac{\text{NA}}{n_{\text{GaAs}}} \right)^{-1}$. Plugging $n=3.42$, $\text{NA}=0.45$ into this equation, gives $C = 0.45\%$. Therefore, the potential GHz single-photon rate of quantum dots is reduced below the MHz range, without accounting additional losses from the coupling to a fibre, blinking and other non-radiative channels. On the other hand, any scattering event with phonons limits the coherence properties of quantum dots. Moreover, the presence of charges in the vicinity of the dots induces a variation on their energy - the so-called spectral wandering- over a time scale of the order of milliseconds. Two different, yet complementary, solutions have been proposed to circumvent the detrimental effects of decoherence on these emitters. On one side, the exciton can be forced to emit faster before the occurrence of scattering processes. The acceleration of the spontaneous emission can be obtained through the Purcell effect by positioning the emitter inside a resonant cavity (see discussion in section 1.5). On the other side, the dot can be excited using a resonant laser to limit the influence of the fluctuating carriers produced by the non-resonant excitation. In this thesis we focus on the integration of the emitters with cavities, and we leave to the future work their resonant excitation.

Generally speaking, confinement of light in semiconductor materials can be achieved exploiting two different phenomena: total internal reflection and the creation band gaps (BGPs). Due to the high refraction index of semiconductors compared to air, total internal reflection can be used by itself to trap light inside the dielectric. This is the case for a class of cavities known as whispering-gallery resonators, which include micro-disks, micro-toroids and micro-spheres. The TIR angle, which is about 15 degrees for GaAs/Air, limits the minimum volume of these resonators to more than $(2-5) \left(\frac{\lambda}{n} \right)^3$. Surface roughness represents the main experimental limitation to secure narrow resonances in these resonators.

1.4.1 Photonic Crystal Cavities

Another approach for light confinement has been proposed in the seminar papers of Eli Yablonovitch [471] and Sajeev John [183] in 1987, and relies on the creation of a photonic bandgap. In a strong analogy with the electronic potential produced by the regular arrangements of nuclei in a crystalline solid, a periodic modulation of the dielectric constant over a sub-wavelength scale can originate bandgaps for photons. More formally, the dielectric permittivity (ϵ) of a PhC has a discrete translation symmetry with respect to a defined primitive basis ($\mathbf{a}_x, \mathbf{a}_y, \mathbf{a}_z$) and can be written as

$$\epsilon(\mathbf{r} + \mathbf{R}) = \epsilon(\mathbf{r}) \quad (1.2)$$

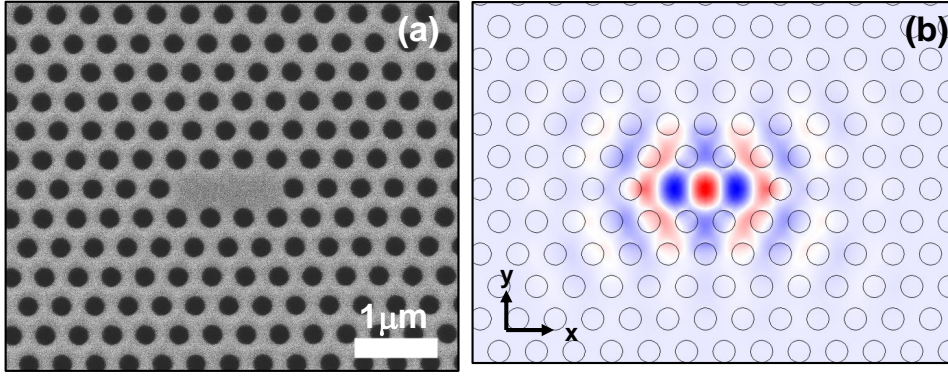


Figure 1.4: (a) SEM images of a photonic crystal cavity realized by omitting three consecutive holes from the lattice. (b) Y-component of the electric field calculated by finite element methods

for every position \mathbf{r} of the space, with $\mathbf{R} = n_x \mathbf{a}_x + n_y \mathbf{a}_y + n_z \mathbf{a}_z$ and n_i integer numbers. The solutions of the Maxwell's equations in this lattice can be expanded in the m -countable basis set formed by the eigenfunctions

$$\mathbf{E}_m(\mathbf{k}) = \mathbf{u}_m(\mathbf{r}, \mathbf{k}) \exp(i\mathbf{k} \cdot \mathbf{r}) \quad (1.3)$$

where \mathbf{k} is known as Bloch wave-vector and spans over the first Brillouin zone of the reciprocal space. The expression of the electric field differs from a plane wave due to the periodic part of the Bloch function $\mathbf{u}_m(\mathbf{k})$, which inherits the symmetry of the crystal, $\mathbf{u}_m(\mathbf{r}) = \mathbf{u}_m(\mathbf{r} + \mathbf{R})$. The set of the corresponding eigenfrequencies $\omega_m(\mathbf{k})$ represents the *bandstructure* of the crystal. Notably, for a given choice of primitive vectors, polarization, and refractive index, a range of frequencies that does not correspond to any Bloch functions can exist. This frequency region is called *bandgap*. Remarkably, if the frequency of a dipole is located inside this region, its spontaneous emission is totally suppressed, because of the absence of available optical states. The physical origin of the bandgap can be also understood in terms of Bragg interference arising from the coherent superposition of light waves partially reflected from the lattice sites. Due to the scale invariance of Maxwell's equations, the homogeneous scaling of the primitive vectors leads to a change in the frequency of the PGB that preserves the band structure. Despite these intriguing properties, after the first experimental demonstrations in the microwave [472] and later in the mid-[39, 243] and near-infrared[309], it became clear that the realization of three-dimensional PhCs was technologically challenging for standard planar fabrication processing, particularly when electrical contacts for carrier injection or field control are needed.

From this perspectives, hybrid approaches that make use of total internal refraction to confine light in one or two dimensions and of photonic bandgaps in the remaining dimensions, are definitely more convenient. Examples of these types of resonators are nano-pillars and PhC slabs. Nano-pillars can be fabricated by etching a dielectric cylinder. Here the lateral confinement is provided by TIR, while Bragg mirrors can confine light in the vertical directions. These resonators have been the workhorse for many single-photon experiments [362, 363] due to the high-extraction efficiency obtained through the mode matching with a top objective. Alternatively,

two-dimensional photonic crystal slabs have been developed (fig.1.4). These resonators typically consist of a thin semiconductor membrane drilled by an array of holes, surrounded by a cladding of lower refractive index. One of the main advantages compared to nano-pillars arises from the fact that these structures can be engineered for in-plane coupling to a circuit, which is essential for the realization of QPICs. Distinctly from 3D-PhC, 2D-PhC do not support complete bandgaps due to the radiation leakage outside the plane of the membrane. It is instructive to decompose the k -vectors of the modes following the structure symmetry $k_0^2 = k_{\parallel}^2 + k_{\perp}^2$. The waveguiding condition, equivalent to the Snell's law, requires that $k_{\parallel} > \frac{n_{\text{clad}}\omega}{c}$, where n_{clad} is the refractive index of the cladding surrounding the slab. Modes with small in-plane k -vectors lying inside the so-called *light-cone* represent a loss channel associated to the so-called leaky modes. In the remainder of this thesis, we employ air as a cladding material and a hexagonal lattice. The latter provides a transverse electric (TE) bandgap aligned with the dipole moment of the e-hh transitions. Besides, cavities (PhCCs) and waveguides (PhCWGs) can be created altering the photonic crystal periodicity, for example omitting n consecutive holes from the regular pattern (fig.1.4). This leads to one or more isolated states located in the photonic bandgap, where light is not allowed to propagate. It is convenient to define the mode volume (V) as

$$V = \frac{\int_V \epsilon(\mathbf{r}) |\mathbf{E}(\mathbf{r})|^2 dV}{\max(\epsilon(\mathbf{r}) |\mathbf{E}(\mathbf{r})|^2)} \quad (1.4)$$

which is of the order $(\lambda/n)^3$ for PhCCs. Given the total energy loss rate of these resonators (κ) which accounts for (1) the aforementioned leaky-modes, (2) fabrication imperfections, it is convenient to define the quality factor as $Q = \frac{\omega}{\kappa}$. As discussed in the next section, these two figures of merit, Q and V , represent the fundamental parameters determining the interaction with QDs.

1.5 JAYNES-CUMMINGS MODEL

The Jaynes-Cummings (JC) formalism describes the interaction of an atom (here a quantum dot) and the quantized electromagnetic field. In this general framework, known as cavity-quantum electrodynamics (c-QED), the atom is treated as a system consisting of two energetic levels, the ground state $|g\rangle$ and the excited state $|e\rangle$ separated in energy by $\hbar\omega_a$. The electromagnetic field, characterized by a single mode having angular frequency ω_c , is instead expanded in the Fock basis $|m\rangle$. Assuming a dipole interaction and neglecting fast oscillating components in the atom-field coupling - an ansatz historically referred to as rotating wave approximation - the Hamiltonian describing the two interacting systems can be written as

$$\hat{H} = \hbar \left[\omega_c \hat{a}^\dagger \hat{a} + \omega_a \hat{\sigma}_+ \hat{\sigma}_- + g(\hat{a}^\dagger \hat{\sigma}_- + \hat{\sigma}_+ \hat{a}) \right] \quad (1.5)$$

where \hat{a} (\hat{a}^\dagger) represents the bosonic annihilation (creation) operator of the electromagnetic field, satisfying $\hat{a}|m\rangle = \sqrt{m}|m-1\rangle$ and $\hat{a}|0\rangle = 0$, while $\hat{\sigma}_+ = \hat{\sigma}_-^\dagger = |e\rangle\langle g|$ is the raising operator of the atom. The first two terms

of \hat{H} correspond to the free Hamiltonian of the cavity and the atom, respectively, while the third term encodes the exchange of a quantum of energy $\hbar\omega$ between these two systems. g is the interaction strength between the atom and a single-photon. This quantity is proportional to the transition matrix $\langle g | \vec{d} \cdot \vec{E}(\mathbf{r}) | e \rangle$, where \vec{d} is the dipole moment of the atomic transition and $\vec{E}(\mathbf{r})$ is the one-photon electric field [255]. If the interaction term is switched off, for small atom-cavity detuning $\delta = \omega_a - \omega_c$, the eigenvectors of the bare-system are arranged in a set of doublets $|g, m\rangle, |e, m-1\rangle$ separated in energy by $\hbar\delta$. For a finite interaction rate g , the eigenvectors and the associated eigenfrequencies of the interacting system are

$$|0\rangle = |g, 0\rangle \quad (1.6)$$

$$E_0 = 0; \quad (1.7)$$

$$|m, -\rangle = -\cos\theta_m |g, m\rangle + \sin\theta_m |e, m-1\rangle \quad (1.8)$$

$$|m, +\rangle = \sin\theta_m |g, m\rangle + \cos\theta_m |e, m-1\rangle \quad (1.9)$$

$$E_m^\pm = \hbar \left(m\omega_a + \delta/2 \pm \sqrt{mg^2 + \delta^2/4} \right) \quad (1.10)$$

where $\theta_m = \frac{1}{2} \arctan \frac{2g\sqrt{m}}{\delta}$ for $m \geq 1$. It is then clear that (i) the states of the systems, referred to as *polaritons*, cannot be factorized in the basis of the original atom and cavity. (ii) The JC Hamiltonian predicts an anharmonic ladder of states. For zero detuning, every uncoupled state in fact splits in two *dressed* states of energy E_m^\pm separated in energy by $\Omega_m = 2\hbar\sqrt{mg}$. (iii) In the time domain, if the initial state is prepared in the basis of the atom, the system experiences a coherent oscillation of frequency Ω_m in the population of the atomic levels, which is referred to as *Rabi-oscillation* (iv) The energy anharmonicity is manifested by a *photon blockade*, which consists in the reflection of the second of two consecutive single photons, resonant with a dressed state. This produces a strong non-linearity useful to build deterministic quantum gates. (v) A typical experimental signature of strong-coupling is the anti-crossing between the atom-cavity states while the detuning δ is varied (as observed for example in fig.1.12(c) and in fig.1.10(b)).

1.5.1 Weak and Strong coupling

So far we have considered the case of a prototypical cavity-emitter node with no losses. In general, all c-QED implementations are subjected to coupling with the environment. A typical approach to describe this non-hermitian interaction that does not preserve the energy of the system consists in writing a master equation for the density matrix $\hat{\rho}$ [255]

$$\frac{\partial \hat{\rho}}{\partial t} = -\frac{i}{\hbar} [\hat{H}, \hat{\rho}] + \kappa L_{\hat{a}}(\hat{\rho}) + \gamma L_{\hat{\sigma}_-}(\hat{\rho}) \quad (1.11)$$

where we defined the decay rate of the atom outside the cavity mode γ and the previously introduced decay rate of the photon number κ . The Lindblad super-operator $L_{\hat{\delta}}$ is

$$L_{\hat{\delta}}(\hat{\rho}) = \hat{\delta}\hat{\rho}\hat{\delta}^\dagger - \frac{1}{2}(\hat{\delta}^\dagger\hat{\delta}\hat{\rho} + \hat{\rho}\hat{\delta}^\dagger\hat{\delta}). \quad (1.12)$$

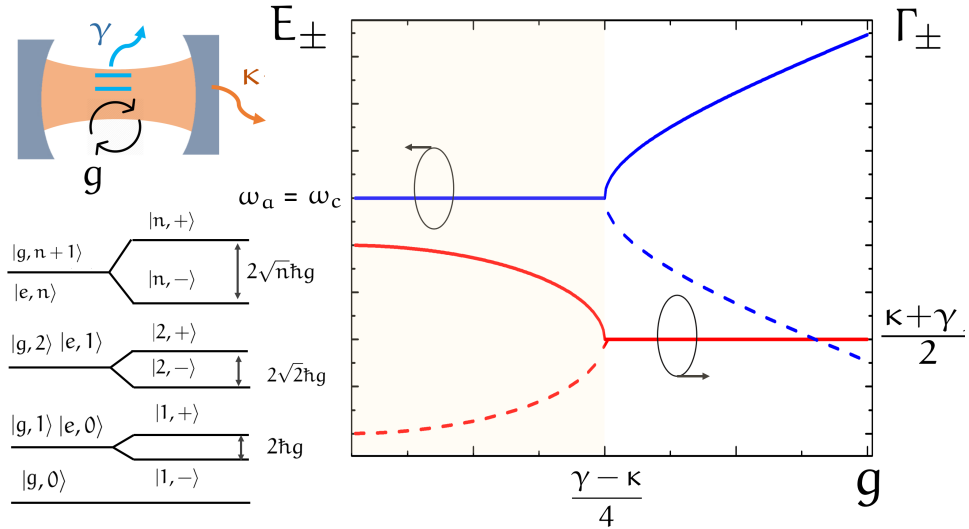


Figure 1.5: (Upper left) Sketch of a lossy c-QED node. (Bottom left) Eigenstates of the Jaynes-Cummings Hamiltonian. (Right) Angular frequencies (E_{\pm}) and losses (Γ_{\pm}) of the states of the open system

Considering only the states $m = 0$ and $m = 1$, the spectrum of the spontaneous emission of the atom can be calculated analytically [52, 71] and, for zero detuning, reads

$$S(\omega) \propto \int_0^{\infty} dt \int_0^{\infty} dt' e^{-i(\omega - \omega_a)(t-t')} \langle \hat{\sigma}_+(t) \hat{\sigma}_-(t') \rangle \propto \quad (1.13)$$

$$\propto \left| \frac{\Omega_+ - \omega_a + i\kappa/2}{\omega - \Omega_+} - \frac{\Omega_- - \omega_a + i\kappa/2}{\omega - \Omega_-} \right|^2 \quad (1.14)$$

This expression has two poles located at the complex frequencies

$$\Omega_{\pm} = E_{\pm} + i\frac{\Gamma_{\pm}}{2} = \omega_a - \frac{i}{4}(\kappa + \gamma) \pm \sqrt{g^2 - \left(\frac{\gamma - \kappa}{4}\right)^2} \quad (1.15)$$

From the evolution of the real and imaginary parts of Ω_{\pm} as function of g , as shown in fig.1.5 we can define two distinct regimes: the *strong-coupling* if $g > \left|\frac{\kappa - \gamma}{4}\right|$ and the *weak-coupling* where $g < \left|\frac{\kappa - \gamma}{4}\right|$ holds.

In the weak-coupling regime, the dissipation prevents the appearance of the Rabi-oscillations. The original states are degenerate in energy while their dissipation rates are strongly modified. To illustrate this point, it is convenient to further distinguish between the *bad cavity* regime, where $\kappa \gg \gamma$ and the *bad emitter* regime where $\kappa \ll \gamma$. For quantum dots the former condition applies since typical values of decay rates are $\frac{\gamma}{2\pi} = 1$ GHz and $\frac{\kappa}{2\pi} = 50 - 100$ GHz. We can then expand the last term in eq. 1.15 obtaining

$$\Omega_a = \omega_a - i\left(\frac{\gamma}{2} + \frac{2g^2}{\kappa}\right) \quad (1.16)$$

$$\Omega_c = \omega_c - i\frac{\kappa}{2} \quad (1.17)$$

This expression suggests that the effective decay rate of the atom-like state Γ_a is modified by the presence of the cavity. To have a direct link with the

experimental evidence, we can compare the cavity-enhanced rate with the emission of an emitter in a homogeneous medium Γ_0 . The Purcell-effect of an emitter positioned in the field maximum, matched in frequency and polarization with the mode, can be then expressed as [255]

$$F_p = \frac{\Gamma_a}{\Gamma_0} = \frac{3}{4\pi^2} \left(\frac{\lambda}{n}\right)^3 \frac{Q}{V} \quad (1.18)$$

The Purcell-enhancement is determined by the ratio of Q/V , defined in section 1.4.1.

In the strong coupling regime, the system resembles c-QED dynamics without losses and is dominated by the presence of two polaritonic states with splitting

$$2\hbar\sqrt{g^2 - \left(\frac{\gamma - \kappa}{4}\right)^2} \quad (1.19)$$

and losses equally-distributed among the polaritons, $(\kappa + \gamma)/2$. The condition to achieve strong coupling can be reformulated in terms of the cavity figures of merit. Since $g \propto V^{-1}$ [255], strong coupling demands high Q/\sqrt{V} ratios.

The spontaneous emission enhancement obtained in the weak-coupling regime has been firstly demonstrated in pillars [135] and later both enhancement and inhibition of the QD emission have been observed in 2D-PhC slabs [107]. The improvement in the fabrication technology enabled the achievements of larger quality factors, essential for the demonstration of strong coupling. The clear anti-crossing signatures from QDs strongly-coupling to a pillar and to PhC membrane [478] were observed in 2004.

In practice, semiconductor c-QEDs studies also have to take into account the effect of dephasing and of non-Markovian processes, which have been neglected in this discussion. For recent reviews, see [252, 265, 352]

1.6 REVIEW OF TUNING METHODS

The quality factor and the resonant wavelength of a photonic crystal cavity are extremely sensitive to the configuration of the periodic hole pattern. A notable example of this strong dependency is provided by the creation of high-Q cavities [6]. A tiny, nanometre-sized displacement of the holes surrounding a cavity defect can in fact suppress the radiation losses by several orders of magnitude. The extreme sensitivity of the confinement in PhCC to the geometric perturbations makes them very sensitive to disorder. In fact, small random variations in the positions and radii of the PhC holes, arising from the unavoidable imperfections in the fabrication process, can drastically alter the optical property of a PhCC. In particular, these can introduce a considerable deviation from the designed wavelength. More quantitatively, the current fabrication process in our cleanroom leads to a variation in the lattice constant and radii within a photonic crystal with standard deviations in the order of $\sigma_a = 3 - 4$ nm and $\sigma_r = 1 - 2$ nm, respectively, estimated from the statistical analysis of SEM images of the final devices [76, 320]. This uncertainty is translated into a dispersion of the resonant wavelengths of ≈ 10

nm for nominally identical cavities, without taking into account the variation over different fabrication runs related to compositional and epi-layer thickness uncertainty. A fluctuation of 10 nm in the GaAs membrane thickness, for example, can lead to a wavelength shift of 15 nm [157]. Designs to mitigate the effect of disorder on the Q-factor have been recently proposed [290]. Another experimental stratagem to hit the desired wavelength, referred to as lithographic tuning [322], consists in making several copies of a cavity with varying lattice constant, and hope that one of them has the desired nominal parameters. Nevertheless, the cavity wavelength can fluctuate during time in low-temperature experiments, due to the gettering of residual molecules in the vacuum chamber (described in par.1.6.2.3), and can be additionally affected in the long term by ageing effects and oxidation.

On the other side, a substantial uncertainty of the energy of the QD excitonic states also exists. In fact, semiconductor QDs have slightly different shapes, sizes and chemical compositions because of the stochastic nature of their nucleation process. Therefore, contrary to real atoms, each quantum dot posses a different spectrum. The energy broadening associated with this physical inhomogeneity can span up to 20 meV, or even more for distant dots, due to a gradient in the growth temperature across the wafer. It is then clear that finding a QD on resonance with a cavity mode is unlikely. Quantitatively, if we assume Fourier-limited emitters having a linewidth of a few μeV , and suppose that the spectral density per unit excitation area of the exciton lines is in the range of $0.1 \text{ dots/meV}/\mu\text{m}^2$, the probability to find an exciton line within the full-width half maximum (FWHM) of a low-Q mode ($Q=1000$) is roughly $P_{(\text{dot,cav})} = 0.1$. This value drops by one order of magnitude for narrower resonances that can lead to strong coupling ($Q = 10000$, $\text{FWHM} = 0.1 \text{ eV}$). Although it might be reasonable to investigate tens of devices for conducting studies at the single dot-cavity level, the success probability of multi-source experiments is very low. For example, the probability to find two dots aligned within their linewidth - a prerequisite for two-photon interference from remote dots- is below $P_{(\text{dot,dot})} = 10^{-4}$. Then, finding two distinct cavity-emitter nodes matched in wavelength is a very rare event, $P_{(\text{dot,cav,dot,cav})} = 10^{-6}$. It is thus expected that the future of QD-based sources in QPIC applications relies on the capability to independently govern the energy of cavities and emitters. To date, the community has developed a set of *tuning knobs* to control their emission *a posteriori*, after their growth and fabrication. In the following sections we present a review of some of these techniques, and we compare their tuning range, modulation speed, sign, locality, and integration with electrical signals. We distinguish between QD and cavity tuning depending on which of the two elements is mostly affected in the tuning process. QD-tuning methods have been mainly inherited from spectroscopy, while cavity-tuning schemes have been developed in the context of classical integrated photonics for applications in filters, modulators, and spectrometers.

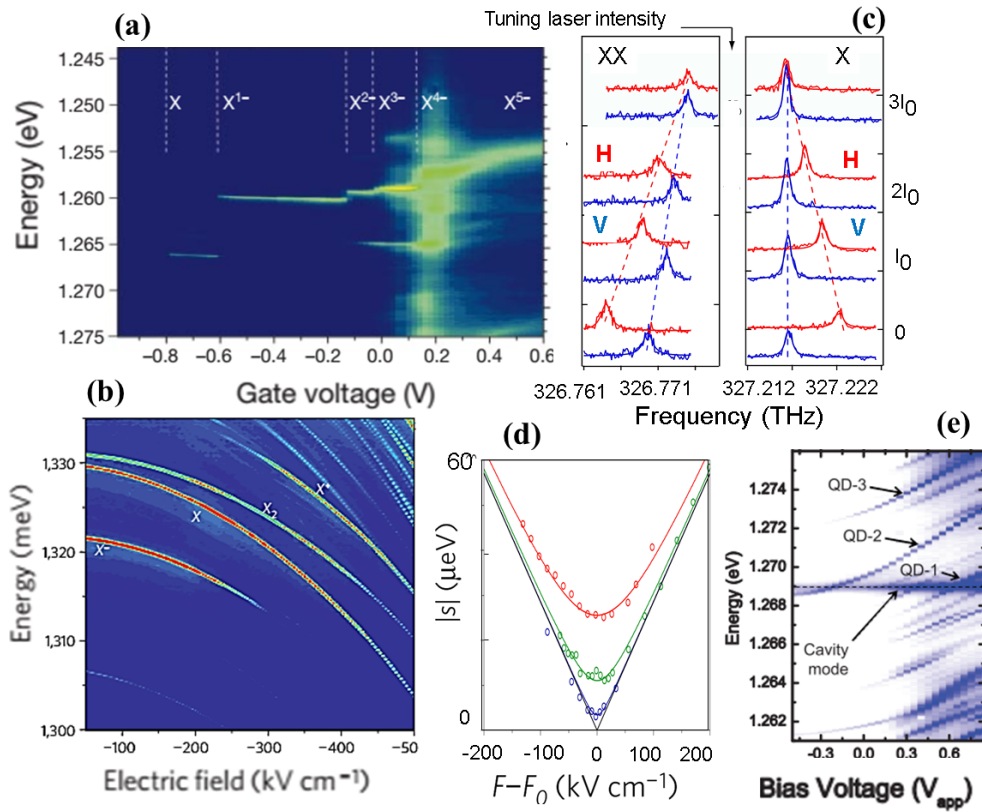


Figure 1.6: (a) Charge control in a QD-diode [456] (b) Stark-Tuning in a QD-diode employing AlGaAs barriers [26] (c) Optical stark tuning to erase the FSS [301] (d) FSS as a function of the vertical Stark-voltage [26] (e) Photoluminescence spectra of a QD-diode integrated with a PhCC as a function of the bias applied to the junction [229]

1.6.1 QD tuning

1.6.1.1 Electric-field tuning

The evolution of QD-based sources has undeniably benefited from the processing of III-V materials, which has been mainly developed to fabricate classical optical components such as lasers, light-emitting diodes, waveguides and photodetectors. In this framework, the opportunity to embed the QD layer inside the intrinsic region of a diode structure has opened up the possibility to govern its properties by an electrical knob. In particular, depending on the type of diode employed (n-i-p or n-i-Schottky), two different tasks can be accomplished: (i) the charge configuration of the exciton can be varied, (ii) a vertical field can be applied to shift the excitons' energy via the quantum-confined Stark effect (QCSE).

CHARGE TUNING The first demonstration of charge control in a Schottky diode dates back to the pioneering paper of Warburton *et al.* [456]. As shown in fig.1.6(a), the authors observed discrete jumps in the dot photoluminescence map while the gate voltage was varied. These discontinuities were attributed to a change in the charge configuration of the dot, due to the transfer of single electrons from the Fermi sea - at the metal-semiconductor

interface - to the dot region. Ediger and colleagues [101] were able to modify the charge configuration of the dot from $-6e$ to $6e$. Moreover, complex many-body phenomena can arise from the strong interaction between the 2D Fermi gas and the localized exciton states, as investigated by Kleemans *et al.* [212]. Charge control has been implemented in resonators, both in micro-pillars [354] and PhC cavities [336]. More recently, graphene has also been proposed as a transparent Schottky electrode [207]. While some spectral tuning is also obtained due to the Stark effect, their tuning range is typically limited (below 0.5 nm).

QUANTUM-CONFINED STARK EFFECT Quantum dots grown via the Stranski-Krastanov method show a gradient in the Indium concentration, and a strain distribution along the growth direction.

This induces a variation in the depth of the potential well along the growth axis. Since electrons have a smaller effective mass compared to holes, they are located in the lower, less confined region of the dot [125]. The resulting vertical separation between electrons and holes gives rise to an effective dipole moment (\vec{p}_0) pointing downwards. This dipole couples with the vertical electric field (\vec{F}) produced by an ohmic p-i-n diode (fig.1.7(a)). The presence of the field can slightly modify the wave-functions of holes and electrons and, consequently, the as-grown dipole moment. Therefore, the actual dipole moment \vec{p} depends on \vec{F} . Considering the wave-function perturbation small, we can write $\vec{p}(\vec{F}) = \vec{p}_0 + \beta\vec{F}$ where β is the scalar polarizability of the exciton. Hence, the energy variation of the excitonic complex (ΔE) due to the quantum-confined stark effect (QCSE) can be written as

$$\Delta E = -\vec{p}(\vec{F}) \cdot \vec{F} = -\vec{p}_0 \cdot \vec{F} - \beta|\vec{F}|^2. \quad (1.20)$$

In the case of a p-i-n diode biased with a voltage V , the field is constant along its intrinsic region, and its amplitude is given by

$$|\vec{F}(V)| = \frac{V_{bi} - V}{t} \quad (1.21)$$

where V_{bi} is the built-in voltage and t is the thickness of the intrinsic region. This quadratic dependence on the field has been firstly observed in photocurrent spectroscopy [125] and, later, in single-dot photoluminescence experiments [119]. A main shortcoming in employing external electric fields is represented by *tunnelling* of the carriers outside the dot. In fact, the electric field tilts the conduction and the valence bands of both GaAs and InAs, giving rise to a triangular barrier. The barrier width is reduced for increased electric field, leading to an increased probability for the carriers to escape and drift towards the contact region [319]. This effect constitutes a non-radiative channel that adds to the radiative decay and compromises the internal efficiency of the source. Thereupon, tunnelling is manifested as a quenching and broadening of the PL emission when the field acting on the dot is sufficiently high. If the membrane is thin enough, this can quench the QD emission also at zero bias. A drastic improvement in the tuning range was reported by Bennett *et al.* [29]. In this work, the authors employed a pair of 72-nm thick AlGaAs barriers, positioned below and above the dot region (fig.1.7(b)), with the aim of suppressing the tunnelling probability. Using this

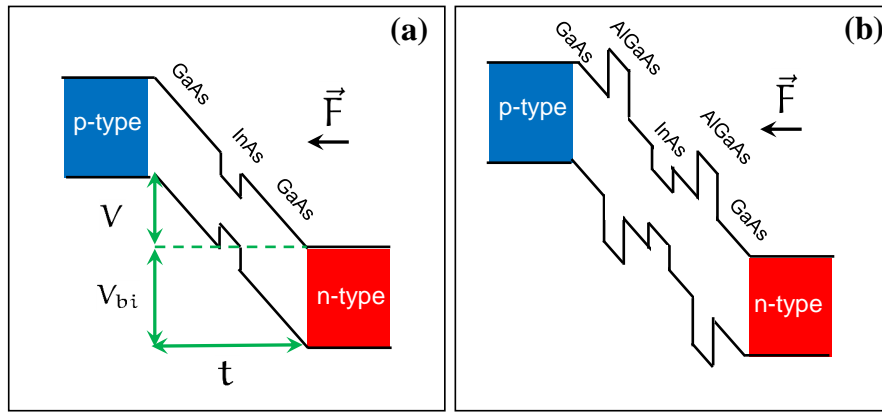


Figure 1.7: Schematic band-diagram of a p-i-n diode under the application of a reverse bias (V) without (a) and with (b) AlGaAs barriers, which suppress the probability of tunnelling

configuration, the exciton lifetimes were not affected up to 500 KV cm^{-1} , obtaining a record tuning range above 25 meV (fig.1.6(b)). The level of control provided by QCSE is sufficient to overcome the inhomogeneous broadening of QDs, and will be extensively used in this thesis.

APPLICATIONS OF STARK DIODES Stark-tuning diodes have been integrated with micro-pillars [211] and PhCC [229] (fig.1.6(e)). Laucht *et al.* [229], reported a detailed study on the lifetime reduction in PhCC-diodes, elaborating on the interplay between the Purcell effect and the tunnelling process. Besides, Stark-tuning has also been used to align the excitons' energies to the Fabry-Perot modes of a short PhC waveguide [160].

The integration with cavities, along with the fast control provided by the QCSE, allows the modification of the QD-cavity dynamics at a frequency close to the decay rate of the emitter. For instance, by controlling the energy of polaritons in a PhCC-dot system, Faraon *et al.* [112] were able to modulate the reflectivity of the system with a frequency of 150 MHz . More recently, Pagliano *et al.* [321] demonstrated the alteration of the QD emission via the QCSE, by adjusting the QD-cavity detuning during the spontaneous decay. The upper limit of the modulation frequency is settled by the RC-constant of the diode, which can be reduced below the radiative decay rate for optimized contact geometries and materials.

Stark-tuning can also be employed to bring multiple excitons into resonance. In fact, quantum dots dissimilar in size and composition can exhibit slightly different tuning profiles due to the diverse p and β . Exploiting the differential tuning rate of two separated dots in a PhCC, Laucht *et al.* [230] were able to bring a pair of excitonic lines in resonance with a cavity mode using a single control voltage, discerning a strong coupling between this tripartite system. Nevertheless, for most of the QPIC applications, an independent control on the energy of two emitters is needed. A solution consists in growing two separate quantum dot layers, one embedded in a diode structure, and the other below any doping layers, as proposed in [200]. An alternative scheme to independently tune two or more dots, which does not require the growth of multiple dot-layers, employs proton implantation to

electrically insulate remote parts of the chip. Using this approach, Thon *et al.* [427] showed a negligible cross-talk among the Stark-tuning of the dots located at the two ends of a photonic crystal waveguide. Fully-integrated and deterministic sources can be made combining Stark-tuning with other functionalities, such as the use of integrated excitation sources, and site-positioning of the emitter. In this direction, Lee *et al.* [234] demonstrated the optical pumping of a Stark-tunable dot by an integrated LED placed in its proximity (fig.1.8(a)). On the same line, Munnelly *et al.* employed a whispering-gallery laser to excite a single dot embedded in a micro-pillar both in continuous wave (CW) [304] and pulsed operation [303]. In order to control the spatial position of the emitter with respect to a pillar, Nowak *et al.* [312] developed an in-situ lithography method to find a self-assembled dot and align it with a micro-cavity, which is equipped with a Stark diode.

MANIPULATION OF FINE STRUCTURE SPLITTING The Stark field, as well as other tuning methods described below, can be also employed to regulate the energy transitions among the multi-excitonic states of a quantum dot [340]. This characteristic is particularly appealing for the generation of entangled photon pairs via a biexciton-exciton cascade, as initially suggested by Benson *et al.* [31]. In general, owing to the in-plane asymmetry of the confinement potential of dots grown on a [001] substrate, the bright exciton state (X) splits into two levels, X_H and X_V , which are in a superposition of states with different projections of the total angular momentum ($J_z = \pm 1$) along the growth axis. The energy difference between these two states, named fine-structure splitting (FSS, s), is caused by the spin-dependent exchange interaction. This splitting is typically in the order of 10-100 μeV . For large s , the excitonic states have dipole moments aligned to the [110] - $[\bar{1}\bar{1}0]$ crystallographic directions. If the FSS is reduced below the values of the excitonic linewidth, a pair of entangled single-photons having circular polarization is generated. The Stark field can be used to reduce the fine-structure splitting as demonstrated in a number of works [26, 138, 139, 259, 271, 344]. In particular, Bennett *et al.* (2010) [26] observed that s depends linearly on the vertical electric field for a large fine structure splitting (fig.1.6(d)). The authors ascribed this behaviour to the different in-plane confinement potentials, which yield to a dissimilar vertical dipole moment for the two bright excitons. This trend was observed also for different types of QDs [138, 259, 271, 344] with ds/dF having values between 0.1 to 0.3 $\mu\text{eV cm kV}^{-1}$ [344]. Then, erasing the fine-structure splitting via Stark-fields permitted the demonstration of entanglement [26, 139].

LATERAL STARK FIELD So far, we have discussed the application of electric fields oriented along the growth directions. Several works also investigated the effect of a lateral in-plane field applied by two laterally-separated gates. A main advantage of using this geometry lays in the possibility of displacing the wavefunction of electrons and holes along one of the in-plane directions [306, 373]. This can reduce or increase the lateral electron-hole overlap and, consequently, the oscillator strength, as observed by Stavarache *et al.* (2006) [407]. In this work the authors proved a 25% reduction of the dot lifetime by the use of lateral n-i-n and p-i-n diodes. The tuning range of this geometry is

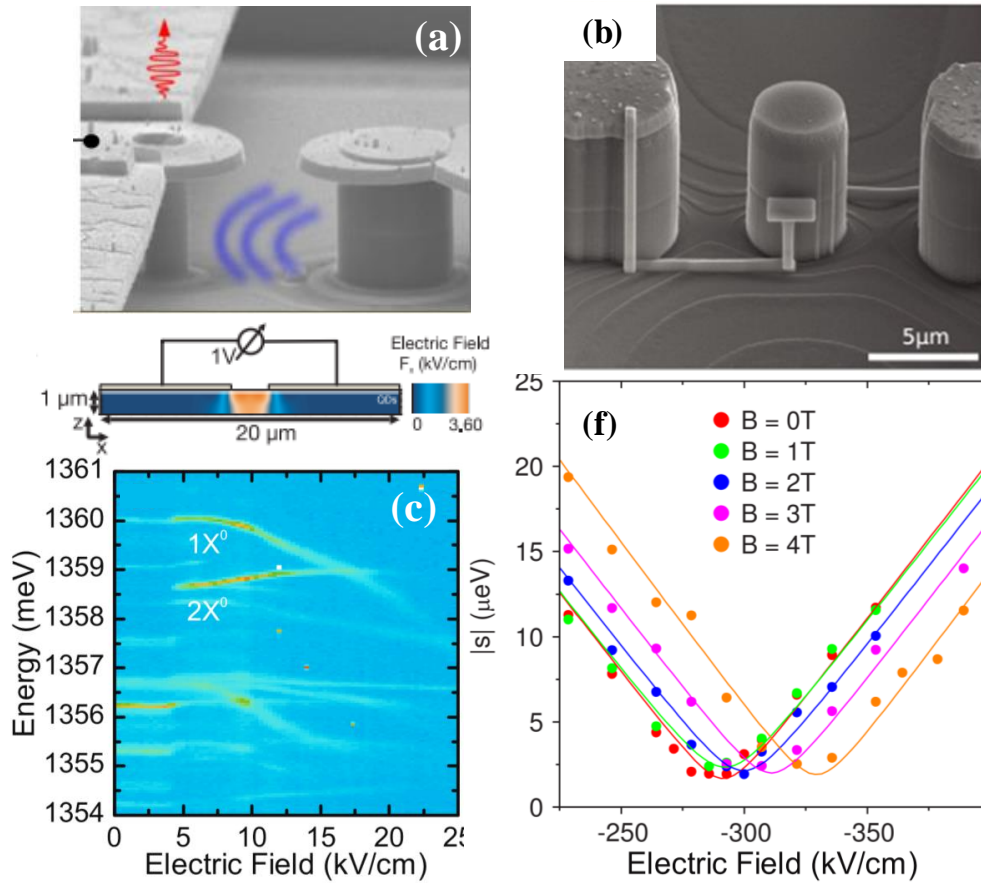


Figure 1.8: (a) Integrated excitation in a Stark-tunable pillar [304] (b) Lateral gates in a pillar [25] (c) Color-coded PL spectra as a function of the lateral E-field in bulk. X and XX can be brought into resonance [195] by the application of lateral Stark-fields. (f) Combined effect of electric and magnetic field in order to reduce the FSS [343]

generally small (below 1 nm) by reason of the absence of a permanent dipole component in the in-plane direction [448]. Applying lateral fields can also be convenient to restore the spatial symmetry of the exciton discussed in the previous paragraph. In that vein, several groups showed the reduction of the fine structure splitting due to the application of lateral fields [136, 219, 270, 448]. Furthermore, the control of the binding energy of the X and XX has been presented in [195, 357] (fig.1.8(c)). Lateral-gates for in-plane field application have been integrated with pillars [25] fig.1.8(b) and with ridge waveguides [297].

1.6.1.2 Magnetic fields

When a magnetic field (B) is applied to a dot, different effects on the exciton lines can be observed according to its orientation. In particular, if the field is orthogonal to the growth axis - a geometry often referred to as Voigt configuration - the dark and bright X states can be coupled together, and the FSS can be altered. This geometry has been employed in the first demonstration of entanglement generation [409]. On the contrary, in the Faraday

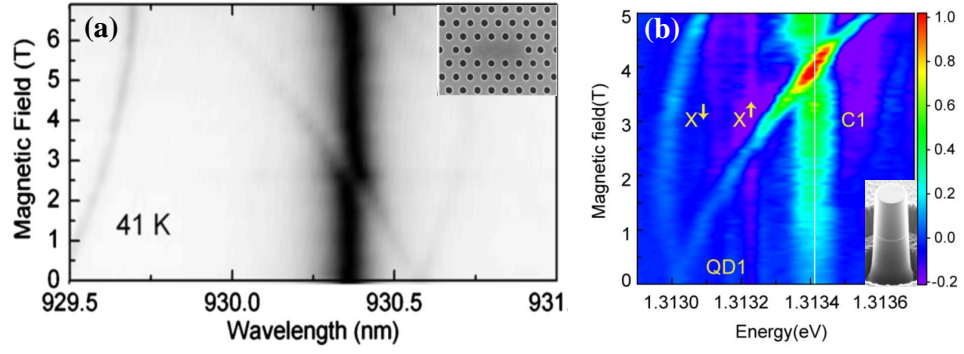


Figure 1.9: Magnetic field tuning in a PhCC (a)[201] and in a pillar (b) [365]

configuration, i.e. when the B-field is parallel to the growth direction, the neutral exciton with opposite angular momentum projections splits in two branches σ^\pm having circular polarization. Here, the energy shift is determined by two contributions: (i) the Zeeman energy, proportional to the field and having opposite sign for these left- and right- circular polarized excitons; (ii) the diamagnetic effect, equal for both states σ^\pm , and proportional to $|B|^2$. Magnetic fields have been employed both in voltage-regulated devices [343, 425] to achieve the reduction of the FSS for multiple dots (fig.1.8(f)), and in cavities, including micropillars [364, 365] (fig.1.9(b)) and PhCs [201, 202] (fig.1.9(a)). Interestingly, by virtue of the angular momentum-dependent sign of the tuning, two exciton lines having opposite angular momenta can be coupled to a resonator [202], and a spin-dependent Purcell-effect can be achieved [365]. Furthermore, this tuning method has been employed to align the dot lines to the transitions of Rubidium atoms [8], in order to store single photons for around 8 ns [7]. Despite these demonstrations, the application of magnetic fields affects the sample globally, and its integration is still challenging.

1.6.1.3 Optical Stark Effect

In the previous discussion, we considered only static electric or magnetic fields. However, the energy of a two-level system can be influenced by an electromagnetic wave, having amplitude \vec{E}_0 and a certain detuning (Δ) from the atomic transition. Also this system can be viewed as a pair of harmonic oscillators (section 1.5), where the atom and the field interacts via the Rabi energy $\Omega \propto \vec{p} \cdot \vec{E}_0$. The field modifies the energy of the dressed atom by an amount (ΔE), which depends on both the detuning and the strength of the field [440]

$$\Delta E = 2\sqrt{\Omega^2 + \Delta^2} \quad (1.22)$$

This effect, named optical Stark-effect (OSE), has been studied on semiconductor QDs by Unold et al [440]. The OSE offers the possibility to either blue- or red- shift the QD frequency very quickly, i.e. within a picosecond time scale. Exploiting this property, OSE has been used to suppress the FSS [301] (fig.1.6 (c)). Notwithstanding, the tuning range is very limited, even though it can be extended by making use of a cavity. In fact, Bose *et al.* [47]

showed a QD-shift of 0.06 nm by resonantly pumping a PhC cavity, slightly detuned from the QD transition. The main difficulty in this configuration arises when the QD is brought on resonance with the cavity mode, since the resonant laser spectrally overlaps with the QD emission, and therefore cannot be easily distinguished from the QD line. A solution to this problem has been advanced later by the same authors [46] and makes use of strongly-coupled PhC cavities. By pumping one of the two photonic modes, the authors were able to match the frequency of a dot line with the other, demonstrating anti-bunching. By shifting the QD resonance faster than the vacuum Rabi period in the same system, Bose *et al.* (2014) [45] reported the coherent energy transfer between a dot and a cavity mode in the strong coupling, dynamically regulating the Rabi oscillations.

1.6.1.4 Strain

As outlined in section 1.3, the chemical composition, the geometry and the strain profile determine the band structure of quantum dots. While the former properties cannot be controlled after the growth, the application of a tensile or compressive stress can affect the optical properties of the emitters (fig.1.10(a)) by a direct modification of their band structure. As originally proposed in Seidl *et al.* [387], in-plane stress can be applied by bonding a GaAs membrane on top of a piezoelectric substrate, such as zirconate titanate (PZT), and lead magnesium niobate-lead titanate (PMN-PT) [225]. Although PZT was employed in the first studies of strain-tuning [387], it has been progressively replaced by PMN-PT, which offers a larger tunability at low-T. The sign of the wavelength shift is related to the gallium composition of the dot. In fact, both blue-shift and red-shift have been recorded on two dots in the same sample under tensile stress [185]. An advantage of this technique is the possibility to control the energy difference between the exciton complexes of the same QD. For example, Ding *et al.* demonstrated that, under isotropic biaxial stress, the difference in the emission energy of XX and X can be reduced below their linewidth [90]. Anisotropic biaxial strain can also modify the fine structure splitting and the polarization of neutral excitons as shown in [339]. More advanced functionalities can be achieved by the effect of strain in QD-diodes as described in a recent review [432]. For instance, controlling the strain and the E-field in a p-i-n junction (fig.1.10(c)) allows shifting the relative energy between the X-XX complexities [434] (fig.1.10(e)), or between the energy of different dots [224], and to obtain a record tuning range spanning more than 30 meV (fig.1.10(d)). On the other hand, when strain is exerted on a QD-LED, the single-photon electro-luminescence can be tuned over a wide range (20 meV) in both CW [436] and pulsed operation [487]. Importantly, by exploiting two independent fields, the control of the FSS is obtained independently from the specific details of the QD, as described by Trotta *et al.* [437]. By exploiting strain tuning, entanglement has been demonstrated both in photo-[433] and electro-[488] luminescence. It is worth noting that there is only one configuration of the two fields that gives the right condition for the suppression of FSS [432]. This implies that the QD-energy cannot be controlled independently of the degree of entanglement. More recently, this problem has been addressed by Trotta *et al.*(2016) [435],

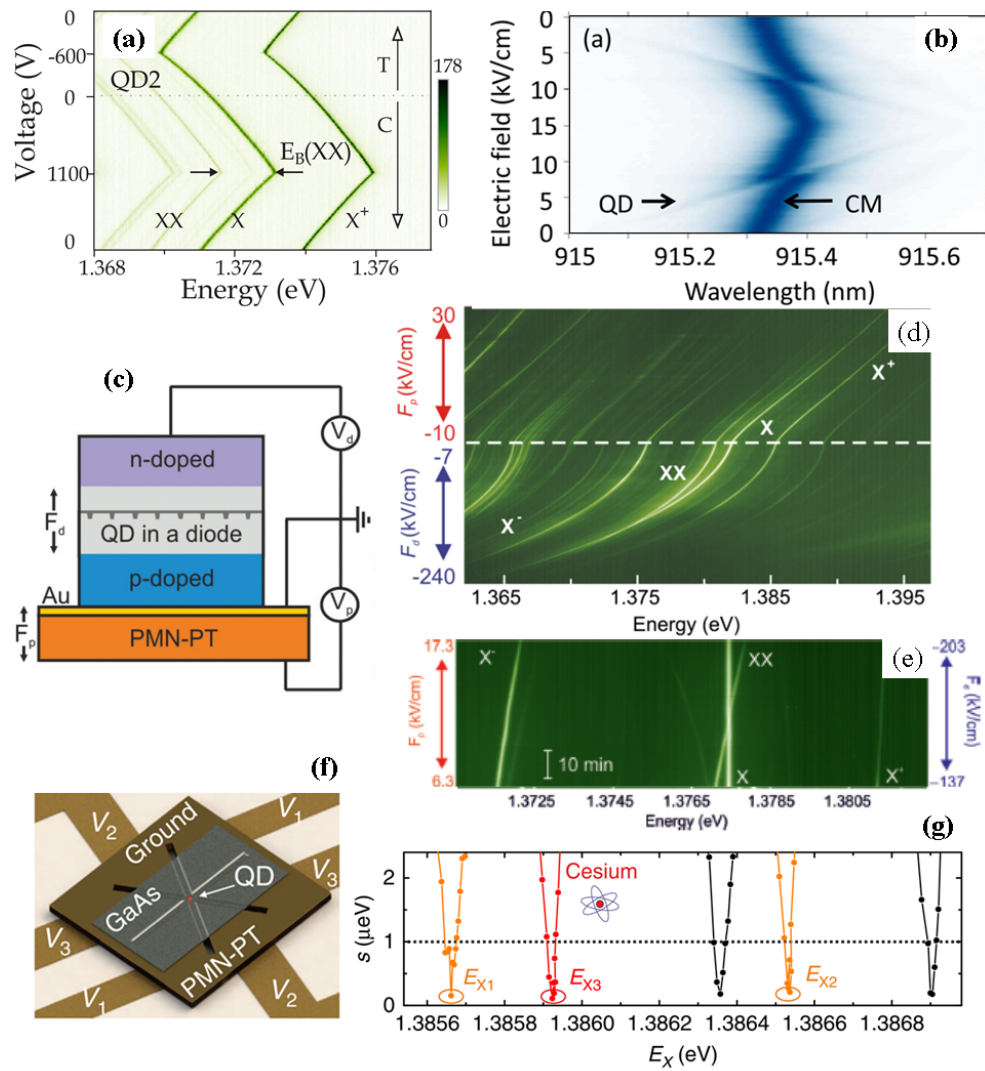


Figure 1.10: QD-Tuning methods based on the application of strain. (a) Effect of the compressive (C) and tensile (T) stress on the PL emission of single exciton [90]. (b) Integration of strain tuning with a PhCC [416]. (c) p-i-n diode for Stark-tuning bonded on a piezoelectric substrate [434]. (d,e) The combined effect of an electric field (F_d) and strain (F_p) leads to a record tuning range (d) [437] and to the possibility to match the energy of X and XX (e) [434]. (f) Sketch of a six-legs device that enables the application of strain in three different in-plane directions. (g) The FFS of a neutral exciton can be erased for several wavelengths. From [435]

who have shown that, by applying three independent stress components along the QD-plane via a *six-legs* device (fig.1.10(f)), entanglement can be obtained at tunable wavelengths (fig.1.10(g)). In the experiments discussed so far, stress is induced on a chip scale using a bulky actuator, typically requiring voltages above hundreds of volts. Bryant *et al.*(2010) [48] have suggested the use of micro-electromechanical systems (MEMS) to locally transfer strain to a dot. This idea has been realized experimentally [490] and, more recently, a four-legs actuator has been integrated on a silicon substrate [63]. Strain tuning of QDs has been implemented in cavities including micro-rings [486], micro-disks [242], and PhCC, both in strong [416] (fig.1.10(b)) and in weak coupling regimes [24]. As shown in these experiments, the strain produces a deformation on the resonators that induces a substantial shift in the cavity wavelength, in the same direction of the QD tuning. According to the studies reported here, the cross-tuning between dots and cavities (see definition in eq.1.24) lies between 0.2 and 0.6. For this reason, it is more convenient to integrate this tuning scheme with broadband waveguides. This has been achieved by embedding the dot into dielectric nanowires, oriented vertically [221] or horizontally [62] with respect to the growth direction. Besides, the mechanical oscillations of a nanowire enables the QD transition to be dynamically modulated via the strain at the mechanical frequency of the wire (0.5 MHz, fig.1.11(b)) [476].

Finally, bonding a membrane on a piezo-substrate is not the only way to obtain strain-tuning. For example, through the use of a diamond anvil cell and piezo actuators, which allow pressure up to 4 GPa, Wu *et al.* demonstrated a ultra-wide tuning range that exceeds 160 nm [464, 465]. Less conventional methods, different from piezoelectric actuation, have also been proposed, and include burning of holes in pillars [42, 43, 151] or locally inducing stress by a scanning-near field microscope (SNOM) tip [419].

SURFACE ACOUSTIC WAVES For applications that require the modulation of the QD properties at high frequencies (GHz), surface-acoustic waves (SAWs) generated by an interdigitated transducer can be used to apply a time-varying stress [134]. For instance, using these devices, Metcalfe *et al.*(2010) were able to resolve the phonon side-bands in the resonant fluorescence of a quantum dot [280]. Besides, SAWs have been employed to regulate the occupancy probability of distinct exciton species [383, 449, 450]. The combination of Stark tuning and the SAW generated in a LiNbO₃ chip [351], allowed for the dynamic alteration of the dot emission over 3 meV (fig.1.11(a)), and for statically shifting its central wavelength via QCSE. Finally, interdigitated transducers have been integrated with PhCCs [459] (fig.1.11(c)) to actively detune the cavity-dot node.

1.6.1.5 Temperature Tuning

An easy strategy to red-shift the wavelength of dots (and cavities) is that of increasing the operating temperature. Broadly speaking, varying the temperature introduces a wavelength perturbation of the dot owing to the modification of the InAs bandgap [61, 137]. Yet, since the refractive index of semiconductors depends also on the temperature via the thermo-optic coefficient,

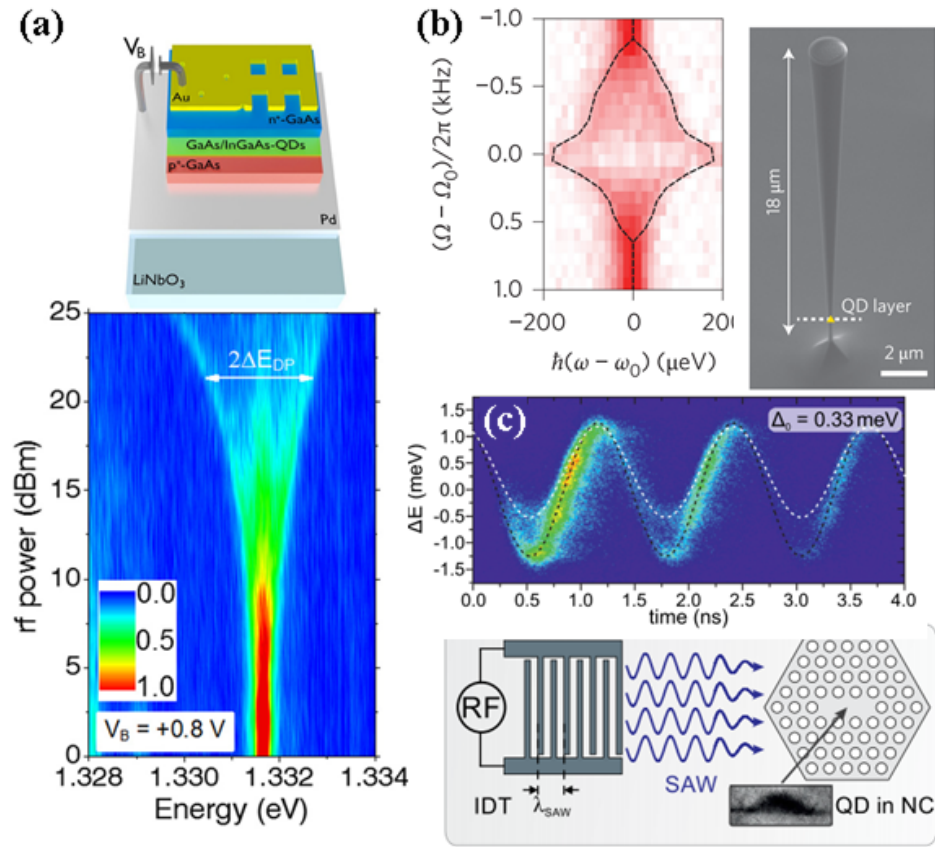


Figure 1.11: (a) Modulation of the PL of an exciton by surface acoustic waves. In this device (top panel) the central energy can be shifted by the Stark effect [351], while the temporal modulation is carried out by the application of a SAW. (b) Stress-induced modulation of the wavelength of a dot embedded in an oscillating nanowire [476]. When the mechanical frequency of the structure is hit (Ω_0), a broadening of the QD emission is observed. (c) SAW-regulated tuning of a PhCC(black line)-dot(white line) node [459]

the cavity wavelength is varied as well. Nevertheless, due to its simplicity, temperature tuning has been employed to control the QD energies in many pioneering c-QED experiments. The temperature can be controlled globally, for example by reducing the flux of Helium reaching the sample, or by a Peltier cell installed on the sample holder.

For cavity control, tuning rates of the order of 0.01 nm/K have been reported for GaAs and InP [460]. In contrast, laser beams [14, 113, 273, 323, 447] or electrical heaters [69, 110, 150, 176] located in the proximity of the device, can produce a local modification of the temperature profile in a PhC cavity. For example, the spatial extent of the laser-assisted perturbation, lying in the microns range, makes it possible to bring two PhC cavities into mutual resonance [323]. This can be further reduced via near-field excitation [447]. The typical switch on/off time of thermal effects is in the microseconds range [273].

In the context of c-QED, methods based on temperature variations show the following drawbacks: (i) limited tuning range. The temperature can be

usually varied from 5 to 55K, since above this temperature the emission of InAs QDs quenches. This temperature range corresponds to a cavity tuning range below 1 nm. (ii) The temperature increase yields to a broadening of QD lines associated with a decrease of their coherence time due to phonon scattering. (iii) Excitons and cavity mode shift in the same direction with a differential tuning of $\sim 35\%$. (iv) Degradation of quality factor [113]. These hindrances restrict the applicability of thermal tuning for multi-node experiments

1.6.2 Cavity Tuning

1.6.2.1 Oxidation

The effect of high-energy laser beams on a PhC cavity can result in the conversion of a thin layer of semiconductor into its native oxide [80]. In the case of GaAs membranes, this yields to a blueshift, since the oxide has a lower refractive index compared to GaAs [233]. Tuning ranges up to 13 nm have been produced by the irradiation of a green laser [171]. The area involved in the laser-assisted oxidation is in the order of the laser spot size. This resolution allowed for a differential energy tuning between two strongly-coupled PhC defects [335] (fig.1.12(b)).

The spatial resolution of the oxidation can be further improved using an atomic force microscope (AFM) [60, 158, 477]. In fact, the so-called *anodic* oxidation is obtained when a negative voltage is set between the conductive AFM-tip and the target. Specifically, by a suitable choice of the oxide pattern, a differential tuning of distinct PhC eigenmodes can be achieved [60]. For example, as shown in fig.1.12(a) [158], it is possible to restore the frequency degeneracy of a pair of cross-polarized PhC modes. This method has also been employed to create a local refractive index perturbation on a pre-existing silicon PhC waveguide, obtaining an *on-demand* high-Q ($Q = 10^6$) cavity [477]. However, the increasing native oxide limits the current injected in the anodic oxidation and, consequently, the obtainable oxide thickness is in the range of few nanometers at most. In this regard, the use of a SNOM tip makes it possible to combine the flexibility of laser-assisted oxidation with the spatial resolution provided by anodic oxidation. In combination with micro-infiltration techniques (par.1.6.2.4), the coupling strength of two diamond-like cavities was controlled using SNOM-oxidation [57], along with the parity of the photonic ground state [56]. Since oxidation methods are not reversible and do not enable a real-time control in a high-vacuum environment, they will not be considered in the rest of this thesis.

1.6.2.2 Near Field Probes

The local density of states (LDOS) of a photonic crystal cavity is strongly altered by the presence of a sub-wavelength dielectric object (fig.1.12(d)). Using a perturbative treatment, Koenderink *et al.* [214] derived the energy shift ($\Delta\omega$) induced when a tip - characterized by a dielectric constant ϵ and effective polarizability α - is brought in the near-field region of a cavity mode.

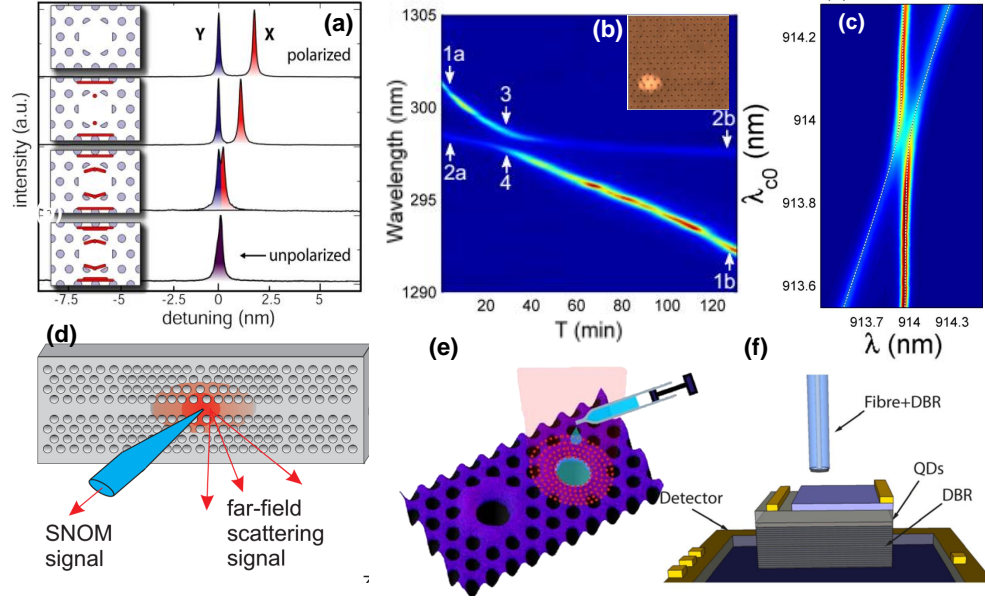


Figure 1.12: (a) Spatially-selective nano-oxidation and differential tuning of two modes (X,Y) in a PhCC [158]. (b) Coupling of a PhC molecule via laser-assisted oxidation [335]. (c) Cavity-tuning via gas deposition [428]. (d) Sketch of SNOM tuning via a dielectric tip in proximity to a PhCWG [300]. (e) Liquid infiltration in the pores of two coupled PhC cavities [446] (f) Open cavity realized by a DBR and a fibre [288].

As a first approximation, and neglecting propagating terms, the energy shift can be written as

$$\frac{\Delta\omega}{\omega} = -\frac{\alpha}{2V} \frac{|\vec{E}(\vec{r}_{\parallel})|^2}{\max[\epsilon(r_{\parallel})]|\vec{E}(\vec{r}_{\parallel})|^2} e^{-\frac{z}{d}} \quad (1.23)$$

where V is the effective cavity volume defined before (eq.1.4), d is the out-of-plane decay constant of the field, and (\vec{r}_{\parallel}, z) is the position of the tip. This equation has been used to map the LDOS of a cavity mode [165, 173, 232, 300]. Employing a curved nano-fibre as a perturber, offers the additional advantage of high coupling efficiency [147] and the possibility to create a cavity starting from a PhC waveguide [205]. This method is characterized by a speed in the sub-MHz range [72, 294]. Although this scheme allows the precise tuning and probing of the cavity eigenmodes with a spatial resolution around 100 nm, it is not easily implemented in a cryogenic environment.

1.6.2.3 Thin films

DEPOSITION OF DIELECTRIC LAYERS An alternative way to change the effective refractive index of the PhC slab is based on the alteration of its physical thickness. This can be done either via a controlled etching step [9, 157], or via the deposition of a conformal dielectric layer at the end of the fabrication process. In this respect, atomic layer deposition methods (ALD) are particularly attractive due to their high conformality and monolayer thickness control, characteristic of their self-limiting chemical process.

ALD has been used to change the bandgap properties of PhC lattices [130, 144] and defects [59, 208, 475], attaining small redshift (0.14 nm) per ALD cycle [59]. Commonly-employed oxide layers are aluminium oxide Al_2O_3 [208] and hafnium oxide [59, 475]. Equivalently, nitrides grown in plasma-enhanced chemical vapor deposition (PECVD) or polymeric films can also be used [347, 380, 491].

GAS ADSORPTION The methods described in the previous paragraph cannot be implemented in real-time during low-temperature experiments. Nonetheless, an alternative solution for thin-film deposition at these temperatures exists, and consists of the adsorption of gasses.

This effect, known as cryo-gettering, was initially considered detrimental for long c-QED experiments, since it appeared as a constant redshift of the cavity mode. This redshift was attributed to the deposition of residual gas molecules in the chamber, thus creating a gradient in the chamber pressure, and attracting additional molecules to the cold finger. In order to curtail this problem, self-assembled mono-layers of polypeptide molecules have been employed [413]. Vice versa, the adsorption process can be actively controlled by inputting a certain amount of Xe or Ne through an external tank [299]. After the first demonstration [299], this technique has been employed as a workhorse for cavity-tuning in a number of experiments operating both in the strong-coupling [316, 318, 359, 428, 463] and Purcell-regime [20, 79, 105]. While this method globally affects all the cavities on the chip, the heating induced by a laser can restore the energy of a selected cavity to the value prior to the deposition [203]. A clear advantage is represented by the fact that quantum dot-energy remains unchanged during the deposition process. However, it is questionable whether the gas-based methods can offer a reproducible and continuous control for wavelength tuning, required for multi-source experiments.

PHOTOCROMIC An alternative way to gain a real-time control on the mode resonance is provided by the use of thin-film materials that are sensitive to the laser irradiation. In this context, photochromic layers [51, 405, 406] and chalcogenide glasses [114, 235] are particularly appealing materials, since their refractive index can be altered semi-permanently by the irradiation of a green or UV light. The wavelength-tuning resulting from change in the refractive index [406] lies in the nanometre range. This is usually related either to the re-bonding at surfaces of the film, or to the transition between two meta-stable states of the glass. Faraon *et al.* [114] implemented this cavity-tuning at low-T, and observed a drastic perturbation of the QD energy attributed to the induced stress in the phase-transition of the glass. The spatial resolution of this method, as in the case of oxidation and thermal effects, is in the micron-range, and has enabled multiple PhC cavities to be brought into resonance [51].

1.6.2.4 Nanofluidics

The infiltration of fluids [349] in the cladding of a PhC slab is one of the first approaches developed to obtain a high refractive index modulation

($dn/n=0.1$) [289]. This method has been adopted to tune PhC lasers [4, 35, 199], to displace the slow-light edge in PhCWGs [54] (fig.1.12(e)), and to create a *heterostructure* cavity by selectively filling a restricted region of a PhCWG [40, 397, 398]. Employing sub-micron pipets, a *pixel-by-pixel* control at level of single holes has been investigated as well [172], and has been used for the spatial and spectral control of coupled PhC modes [174, 402, 445, 446] (fig.1.12(e)). A fully-integrated optofluidic circuit, comprising a delivery architecture and fluid-control engine, has also been studied [108].

INFILTRATION OF LIQUID CRYSTALS Infiltration typically involves a wavelength tuning in a single or multiple discrete steps. A continuous tuning can be achieved by infiltrating the PhC slab with polymers sensitive to the exposure of UV light [188], with elastomeric materials [218] or liquid crystals (LCs) [384]. The latter option offers the possibility to adjust the orientation of the liquid crystal either via electric fields [276, 278, 467], or by a writing laser beams [277]. The high thermo-optic coefficient of LCs has been employed in temperature tuning [98, 99, 118]. In this way, an opposite energy-shift from the modes having different orientation can be obtained [99, 453]. While liquid-infiltrated PhC slabs show interesting properties for sensing and lab-on-chip applications, they cannot be tuned at cryogenic temperatures.

1.6.2.5 "Open-access" Cavities

An interesting approach that allows the spatial and the spectral control on the dot-cavity coupling is based on the so-called open-access cavities [21, 97, 146]. These are highly-miniaturized Fabry-Pérot mirrors, created by a semiconductor distributed Bragg reflector (DBR), located below the dot layer and a top dielectric DBR, usually integrated with the collection fibre (fig.1.12(f)). The top mirror is movable, and has a concave shape to provide a sufficient lateral confinement. Mode tuning is obtained by controlling the sample-fibre distance as in a standard Fabry-Pérot cavity, while the lateral movement of the fibre allows for changing the dot under investigation. Recently, this cavity actuation scheme has been employed in combination with a charge-tunable sample [288]. This class of cavities is well suited for free-space single-photon applications, since their emission is already coupled with a collection fibre, but not for integrated quantum photonics.

1.6.2.6 Optical Nonlinear Effects

In semiconductors, three main contributions characterize the non-linear response to strong laser excitations: the thermo-optic effect discussed above (par.1.6.1.5), the free-carrier injection, and the Kerr effect. In particular, the use of nanocavities in combination with non-linearities has found applications in fast and low-power switches [311], while its implementation at single-photon level is still missing.

CARRIER INJECTION The excitation of free carriers (FC) induces a change in the refractive index. This can be decomposed in three main contributions: free-carrier dispersion, band-filling, and band-shrinkage [295]. The latter is usually negligible in III-V semiconductors at telecom wavelength. As a

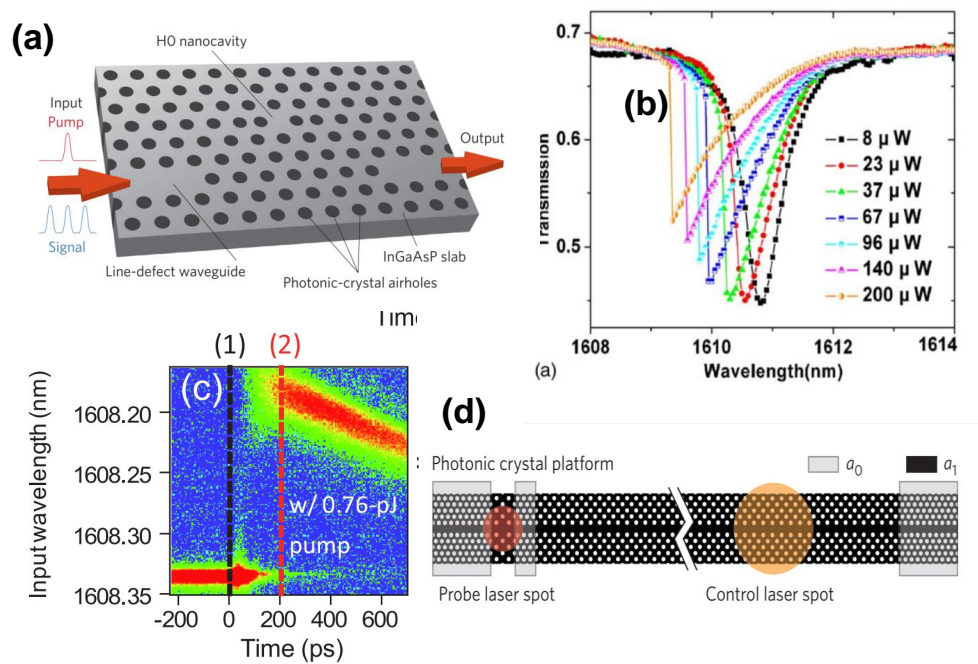


Figure 1.13: (a) Typical PhC configuration to study non-linearities induced by strong optical fields. From [314]. (b) Bistability observed in transmission experiments when the intensity of the laser is increased. From [204]. (c) Effect of the fast excitation of free carrier in a PhC. From [421]. (d) Target-Control configuration for remote injection of FC. From [181]

result of the combination of these effects, the PhC modes move to shorter wavelength when short laser pulses are absorbed, as originally reported in Ranieri *et al.* (2005) [353]. Moreover, the effect of this non-linearity is manifested as bi-stability, as reported in CW transmission experiments [22, 204](fig.1.13 (b)). Many studies have investigated the effect of free-carrier injection in transmission experiments featuring a nanocavity coupled to an input and an output PhCWG waveguide (fig.1.13 (a)) [169, 314, 420, 421, 481, 482]. In this scheme, two short laser pulses are commonly employed, i.e. a pump that creates the carriers, followed by a low-intensity probe that senses the time-energy response of the system. Carriers can be excited using either an above bandgap pump [421] or via two-photon absorption processes [169]. Both the probe-cavity detuning and the energy of the pump laser play an important role in the time response of the system [169, 481, 482]. While the first transient of the mode tuning is fast (below 40 ps), and is associated with the photo-generation of free-carriers (fig.1.13(c)), the recovery time is predominantly governed by their recombination time, and is much longer (>100 ps). In turn, the latter is dependent on the dimensions of the cavity (faster for small cavities) and on the non-radiative effects involved with the trapping of the carriers [74, 106]. Furthermore, this dynamics can be controlled by extracting (or injecting) the carriers via a lateral p-i-n diode [422, 423]

Importantly, the possibility to spatially localize the carrier injection in a limited area allows the control of the dynamics of coupled PhC resonators.

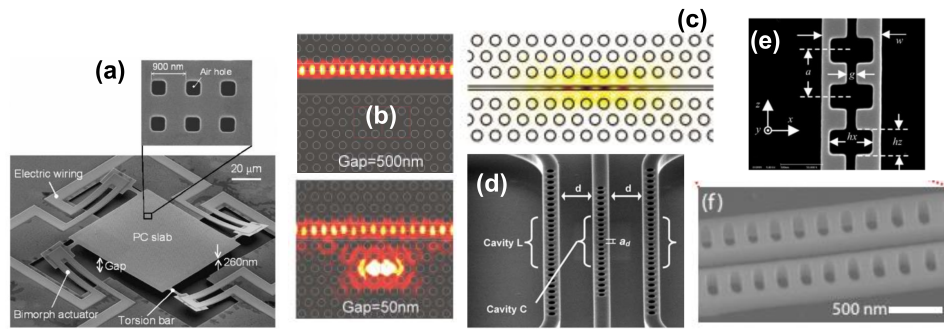


Figure 1.14: Example of PhC NOEMS (a) [192], (b) [193], (c) [461], (d) [67], (e) [429], (f) [330]

In this regard, Sato *et al.* [379] were able to resolve the Rabi oscillations between two coupled PhC cavities connected via a PhC bus. In addition, Tanaka *et al.* showed that the losses of a PhC cavity could be modulated by one order of magnitude, by adjusting the interference between a PhC mirror and a cavity via FC effects [424]

The presence of free carriers can be detrimental to QDs [127], since it can introduce unwanted pumping and charging. In order to avoid the presence of charges in the dot region, Jin *et al.* [181] have proposed the use of two directly-coupled cavities, named target and control cavity (fig.1.13(d)). The spontaneous emission of a dot ensemble located in a target cavity was controlled remotely by detuning the control cavity via carrier injection.

KERR EFFECT The ultimately fast method to switch the wavelength of a cavity is the instantaneous third-order Kerr effect. To avoid the injection of free-carriers via virtual states, both the pump and the probe energies must be below half of the bandgap of the semiconductor [296]. In this way, Ctistis *et al.* demonstrated a fast red-shift of a planar cavity [78], limited only by the storage time of the photons in the cavity (≈ 300 fs). The Kerr effect, although very small, should be taken into account also when modelling the carrier injection from ps-long pulses [74, 295, 485].

1.6.2.7 NOEMS

Nano-opto-electro-mechanical systems (NOEMSs) have been employed in a number of ways to reconfigure the wavelength and the mode profile of a cavity, as recently reviewed in [94]. For instance, the evanescent perturbation described in par.1.6.2.2 can be integrated on a chip by controlling the relative positions between a PhCC and a dielectric tip via electromechanical actuation. Iwamoto *et al.* [177] and Abdulla *et al.* [3] achieved a high modulation in the transmission of a SOI PhCWG, by the mechanical displacement of a cantilever placed above the crystal region. Kanamori *et al.* (2007) [192] employed the vertical movement of a PhC slab towards the substrate to adjust the reflectivity of a guided resonance (fig.1.14(a)). One [64] or multiple [66] nano-tips have been employed to perturb the local dielectric environment of a PhC nanobeam. Although these methods allow a controllable red-shift lying in the nanometer range, the Q-factor can be strongly affected by the additional losses introduced by the perturbation [315].

Electromechanical systems have been also adopted to re-configure discrete parts of a photonic crystal cavity. For example, Kanamori *et al.* (2009) [193] developed a comb-drive actuator to modify the in-plane coupling between a PhCWG and a L₃ cavity (fig.1.14(b)), achieving a drop efficiency of 12.5 dB. More recently, Lin *et al.* [245] demonstrated the ability to electromechanically control a Fano resonance originated by the in-plane coupling of a lossy and high-Q cavity. The so-called air-slot cavities, introduced theoretically in [368], have been also employed in this context. The tight confinement in these resonators is based on the dielectric discontinuity at the gap of two adjacent slabs (fig.1.14(c)). Despite their limited tuning range, these devices have shown large non-linearities arising by the strong coupling between the electrical, the optical and the mechanical degree of freedom [324, 337, 461], plus the possibility to dynamically tune the cavity wavelength with a frequency in the MHz range [461]. A similar confinement can be achieved in split-ladder nanobeams [429] (fig.1.14(e)), along with a large (16 nm) tuning range. 1D nanobeams offer a vast parameter space thanks to the possibility to displace the resonators along several directions. For example, a 1D PhC nanobeam can be separated in two parts along the axial direction. Tuning the gap between these two parts makes it possible to change the quality factor without significantly perturbing the wavelength of the mode [392]. Conversely, the gap can be kept fixed while varying the out-of-plane [248] or the in-plane [244] positions of the beams.

In general, since the field maximum is located in the air region, these cavities cannot be employed to enhance the emission of quantum dots located in the semiconductor region. A more convenient approach, which ensures both a high tunability and high field intensity at the dot location, is based on coupled photonic crystal cavities; this process will be described further in Chapter 3. Pairs of PhC nanobeams have been coupled laterally [65, 95, 96, 124, 247, 331] (fig.1.14(f)) and vertically [285]. Furthermore, the extension to three nanobeams has been presented by Chew *et al.* [67]. In this thesis, we will focus instead on the coupling between a pair of 2D photonic crystal membranes [284]. This structure has shown the important capability to be operated at low temperature to achieve dot-coupling [286], and represents the starting point of this work. It is worth mentioning that the mechanical re-configuration of resonators can also be obtained all-optically via the use of radiation pressure. A class of devices and phenomena arising from the interaction between mechanical resonators and photons - forming the field of cavity optomechanics - has been reviewed elsewhere [15].

1.6.2.8 Acousto-optics and flexible resonators

Another strategy to adjust the optical property of a PhCC makes use of the continuous deformation of the material due to strain and photoelastic effects. For example, Luxmoore *et al.* [262] restored the mode degeneracy of an H₁ cavity through the application of an in-plane uniaxial strain. Moreover, the integration of a surface acoustic wave generation close to the cavity allows the dynamic modulation of the cavity properties at GHz frequencies. Using the acoustic waves generated by an interdigital transducer electrode, Fuhrmann *et al.* [126] reported the compression and expansion of a

PhC on a time scale comparable to the radiative emission of QDs. Later, Kapfinger *et al.* [196] extended this technique to modulate the coupling strength of coupled-cavities. Stress-mediated tuning methods have been recently adopted in hybrid materials, realized by embedding photonic crystal resonators in polymeric substrates [68, 131, 258, 470, 480]. By integrating a PhC array of silicon nanowire with polydimethylsiloxane, Yu *et al.* [480] reported a tuning range of 60 nm, due to the application of tensile strain along two orthogonal directions. Moreover, the use of active InGaAsP organized in a PhCC array, enables the demonstration of a widely-tunable (26nm) laser [68]. The main disadvantage of using strain in the context of integrated c-QED consists in the high interdependency between cavity and QD tuning, as will be discussed in the next section.

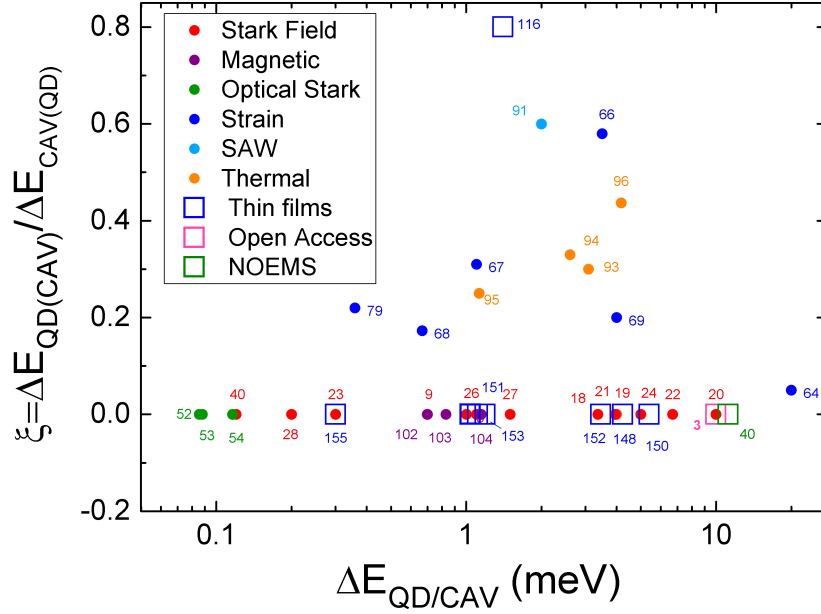


Figure 1.15: Cross-tuning coefficient extracted from the data reported in the literature versus maximum tuning range of the QD (cavity) tuning. The zero value corresponds to the resolution of the set-up employed for the specific experiment. QD tuning. Stark field: 40 [25], 28 [288], 23 [112], 9 [354], 26[304], 27[312], 18 [427], 21 [229], 19[200], 24[321], 22[160], 20[211]. Magnetic Field: 102 [364], 103[201], 104[202]. Optical Stark: 52[47], 53[46], 54[45]. Strain: 79[42], 68[416], 67[242], 66[486], 69[24], 64[436]. SAW: 91[459]. Thermal: 95[110], 94[113], 93[137], 96[61]. Cavity tuning. Thin Films: 116 [114], 155[318], 151[105], 153[316], 152[215], 148[299], 150[79]. Open access: 3[21] NOEMS: 40[286]

1.6.3 Comparison

In order to facilitate the alignment of multiple c-QED nodes, the effect produced on the energy of quantum dots (cavity modes) when the energy of cavity modes (quantum dots) is tuned, should be preferably small. We define the cross-tuning coefficient as

$$\xi = \frac{\Delta E_{CAV}}{\Delta E_{QD}} \quad \text{or} \quad \xi = \frac{\Delta E_{QD}}{\Delta E_{CAV}}, \quad (1.24)$$

depending on whether the QD or the cavity is tuned, respectively.

Fig.1.15 reports the values of the cross-tuning coefficient for the experiments reviewed in this section. This figure shows that the application of magnetic or electric fields, the use of NOEMS and gas adsorption, feature cross-tuning comparable with the resolution of the measurements (below 0.01 nm in most of these experiments). Differently, temperature and strain-tuning produce a non-negligible energy shift in both the cavities and dot emission. Another key figure of merit for advanced QPIC applications is the time scale involved in the tuning mechanism. This time-scale can in fact limit the rate of reconfigurability of the circuit. Additionally, dynamic tuning (i.e. on time-scales faster than the natural dynamics) can open new opportunities. In the strong coupling regime, for example, if the detuning between a dot and a cavity is regulated with a rate comparable to their interaction

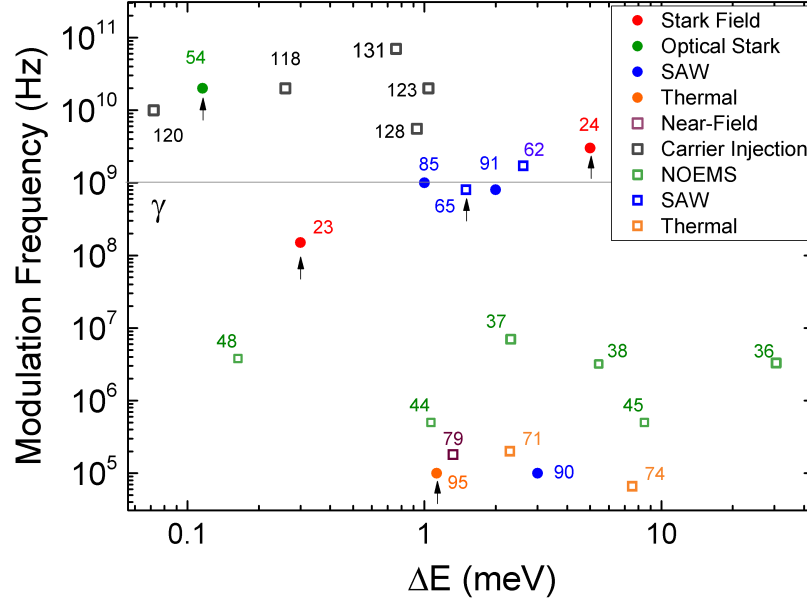


Figure 1.16: Modulation frequency as a function of the tuning range for the QD- (circles) and cavity- (squares) tuning methods. The arrows indicate experiments conducted on a dot-cavity system. Cavity tuning: [36] [167], [37] [331], [38] [284], [44] [64],[45] [64], [48] [461], [62] [126], [65] [196], [74] [116], [79] [272], [118] [420], [120] [421],[123] [128], [128] [181],[131] [379]. QD tuning:[23] [112], [24] [321], [54] [45], [85] [134], [90] [351], [91] [459], [95] [110]

rate, the Rabi oscillations can be initialized and stopped upon the application of an external trigger. The realization of such ultra-fast control, which requires a modulation time faster than ≈ 10 ps, can enable the preparation of entangled states between matter qubits and photons with high fidelity. Fast control methods are also important to re-shape the temporal profile of single photons travelling between two c-QED nodes. Generally speaking, the time-profile of photons emitted during the spontaneous decay of quantum dots is typically asymmetric, with a fast rise time followed by a ns-long exponential decay. However, the maximum absorption of a single-photon from a target two-level system is obtained when the incoming SP temporal profile matches the time-reversed photon state originated by the target emitter [411]. In this context, a fast energy modulation represents an effective way to produce temporally symmetric SPs, allowing the coherent energy exchange from two dots via a photonic channel [117]. Besides, for applications that require the transfer of the SP emission into an optical circuit, a Gaussian shape with large bandwidth is also desirable to increase the tolerance against modal mismatch [369]. Fig.1.16 compares the modulation frequency achieved in the experiments reported in this section as a function of the tuning range. In this figure, the arrows highlight the experiments realized on a c-QED node. Stark-field -obtained by electrical or optical gates-, FC effects, and the use of SAWs provide sufficiently fast modulation frequency, above the typical decay time of semiconductor dots ($\frac{\gamma}{2\pi}$).

Finally, in the following table, we present a summary of semiconductor c-QED experiments carried out on architectures tunable on real-time. The

type of the cavity adopted for the demonstration of strong (SC) and weak (WC) coupling is indicated as well.

Tuning method	Paper	SC/WC (F_p)	Cavity Type
Stark field	Pinotsi <i>et al.</i> [336]	WC(7)	PhCC
	Kistner <i>et al.</i> [211]	SC	Pillar
	Kim <i>et al.</i> [200]	WC	PhCC
	Laucht <i>et al.</i> [229]	SC, WC(7)	PhCC
	Hoang <i>et al.</i> [160]	WC(2)	PhCWG
	Faraon <i>et al.</i> [112]	SC	PhCC
	Rakher <i>et al.</i> [354]	WC(7)	Pillar
	Laucht <i>et al.</i> [229]	WC(7)	PhCC
	Munnely <i>et al.</i> [304]	WC(2.2)	Pillar
	Nowak <i>et al.</i> [312]	WC(0.8)	Pillar
	Pagliano <i>et al.</i> [321]	WC(3)	PhCC
	Miguel <i>et al.</i> [288]	SC, WC	Open access
Beetz <i>et al.</i> [25]	WC	Pillar	
Magnetic field	Reitzenstein <i>et al.</i> [364]	SC	Pillar
	Kim <i>et al.</i> [201, 202]	SC	PhCC
	Ren <i>et al.</i> [365]	WC	Pillar
Optical Stark	Bose <i>et al.</i> [47]	SC	PhCC
	Bose <i>et al.</i> [45, 46]	SC	Coupled PhCC
Strain	Bonato <i>et al.</i> [42]	WC	Pillar
	Trotta <i>et al.</i> [436]	SC	DBR
	Zhang <i>et al.</i> [487]	SC	DBR
	Lin <i>et al.</i> [242]	SC, WC	Microdisk
	Sun <i>et al.</i> [416]	SC	PhCC
	Beetz <i>et al.</i> [24]	WC	PhCC
	Gudat <i>et al.</i> [151]	WC	Pillar
Weiss <i>et al.</i> [459]	WC	PhCC	
MEMS	Midolo <i>et al.</i> [286]	WC(4.5)	PhCC
Thin film	Faraon <i>et al.</i> [114]	WC	PhCC
	Cai <i>et al.</i> [51]	SC	Coupled PhCC
Open Cavities	Barbour <i>et al.</i> [21]	WC(2.1)	DBR

Notice that the reported experimental values for the Purcell-enhancement (F_p) are obtained by the ratio of the dot decay when it is on resonance with the cavity mode, and the typical excitonic decay in the bulk. A discrepancy between the acceleration of the spontaneous emission obtained experimentally and the values predicted theoretically from equation 1.18 is evident from these values. Indeed, while a maximum enhancement of 12 is obtained experimentally - with most of the experiments showing Purcell enhancement below 10 - theory predicts Purcell factors higher than 30 for the experimental quality factors. This disagreement is often attributed to the spatial mismatch and polarization misalignment between the maximum of the field and the dot. We must also highlight that the best resolution of the time-resolved measurement, mainly dictated by the detector jitter, does not allow record-

ing Purcell enhancements higher than 20 (for radiative lifetime of 1 ns). Recently, Liu *et al.* [251] have demonstrated a Purcell factor of ≈ 42 by using a double-pi resonant fluorescence technique, which is not limited by the detector response time and by the carrier relaxation from higher energy states of the QD. For completeness, in figures fig.1.17 and fig.1.18 in appendix A we present a summary of the tuning ranges (ΔE) reported in this chapter for dots and cavities, respectively.

1.7 THESIS GOALS AND OUTLINE

As discussed in paragraph 1.2, gallium arsenide represents a promising material platform to realize many QPIC elements, spanning from SP sources that manifest excellent figure of merits (purity, indistinguishability, brightness) to advanced single-photon detector schemes that embed additional integrated functionalities (autocorrelation, filters, photon number detection). However, despite the impressive progress made in the development of these components at the single unit level, and in the improvement of their individual performances, GaAs-based QPIC faces some challenges to the realization of large-scale circuits. Some of these are represented by the scalability, reconfigurability and interconnection of multiple single-photon sources. These characteristics are compulsory requirements to build LOQC logic and boson sampling computation employing SPs generated from remote emitters.

One of the most striking problems in this context was represented by the energy control of both elements constituting a semiconductor c-QED node.

While a variety of tuning methods have been developed to reconfigure either the cavity's or the emitter's energy, as examined in sec. 1.6, a device able to simultaneously regulate both degrees of freedom was not demonstrated before this thesis.

As will be discussed in the following chapters, the motion of a membrane with a nanometre control provides an elegant way to reconfigure the modes of a PhC cavity. Although this system has been previously demonstrated by our group [284, 286], its operation was limited by the pull-in effect and the corresponding irreversible device failure: after a certain voltage, the system undergoes an instability that leads to the permanent stiction of the moving parts of the device. During this thesis project, we have developed a pull-in free method that avoids the use of electromechanical forces to obtain a three-fold improvement in the tuning range of the device. More importantly in the context of QPIC applications, a coating layer has been implemented to prevent the collapse during its electromechanical actuation, hence guaranteeing the operation of the device for hundreds of thousands of cycles from the pull-in to the release status. This cavity tuning mechanism has been combined with the tuning of QD lines via a static Stark field to demonstrate the energy tuning of an integrated c-QED for the first time. While integrated quantum photonic experiments make use of an external laser to produce single photons, the implementation of electrical pumping schemes offers clear advantages for the use SP sources both for practical off-chip applications and for on-chip integration with detectors. While electrical injection has been previously demonstrated in photonic crystal cavities in order to real-

ize fast nano-LEDs [104] and lasers [103], the excitation of single excitonic transitions - which is compulsory for the demonstration of SP emission- was not demonstrated. In this thesis, we show that the current injected in a vertical p-i-n junction into the dot region can be exploited to produce single-dot electro-luminescence. Importantly, we make use of the cavity actuation to couple electrically-driven dot lines to a cavity mode. This enables the demonstration of the first single-photon PhC LED, which has the supplementary advantage, compared to other demonstrations, of being integrated with an electrically-tunable cavity.

Though the aforementioned results rely on the use of a free-space top collection, from the discussion presented in Sec.1.2 it is clear that an in-plane coupling to a waveguide architecture is imperative for QPIC applications. Coupling a NOEMS to a waveguide channel is a central topic in reconfigurable classical photonics. During this thesis project, we integrated a mechanically-compliant structure with supported ridge waveguides. This monolithic integration strategy makes it possible to funnel the emission of an electro-mechanically tunable cavity into a ridge waveguide. Besides operating the devices at the single-QD level and making use of Stark-tuning, the injection of a Purcell enhanced exciton line into a waveguide channel is demonstrated as well. The possibility offered by the integration with waveguides enables the demonstration of both an antibunching experiment with a PhC source and a splitter integrated on the same chip, and the integration of multiple sources on the same circuit.

These results are described in the following chapters. **Chapter 2** illustrates the methods adopted to fabricate the devices of this thesis. **Chapter 3** describes our approach to tuning the modes of a PhC. This is based on a double-membrane cavity, obtained by vertically coupling a pair of photonic crystal membranes. The interaction of this system with a near-field tip is employed to investigate the dynamics of the system, and to apply a local force that produces a pull-in free wavelength change. **Chapter 4** elaborates on the simultaneous integration of cavity and dot tuning mechanisms within a single device. This is achieved by the combined application of an electrostatic force between a pair of PhC membranes and the Stark-field acting on the dots. In this way, a Purcell effect from a single dot tuned at two wavelengths is observed. **Chapter 5** discusses the electrical pumping of this tunable node. Electroluminescence is observed when the dot-diode is operated in forward bias. Anti-bunching proves the single-photon nature of these quantum light emitting diodes. **Chapter 6** presents a method based on the atomic layer deposition of alumina that prevents stiction failure, and allows for the electrical switching of the cavity emission over 50 nm in wavelength. **Chapter 7** focuses on the integration of the tunable cavity-emitter node with ridge waveguides and the feasibility study of an on-chip Hanbury Brown-Twiss experiment. Finally, **Chapter 8** discusses the integration of multiple interconnected cavity-emitter systems on the same chip.

1.A TUNING RANGE FOR CAVITIES AND QUANTUM DOTS

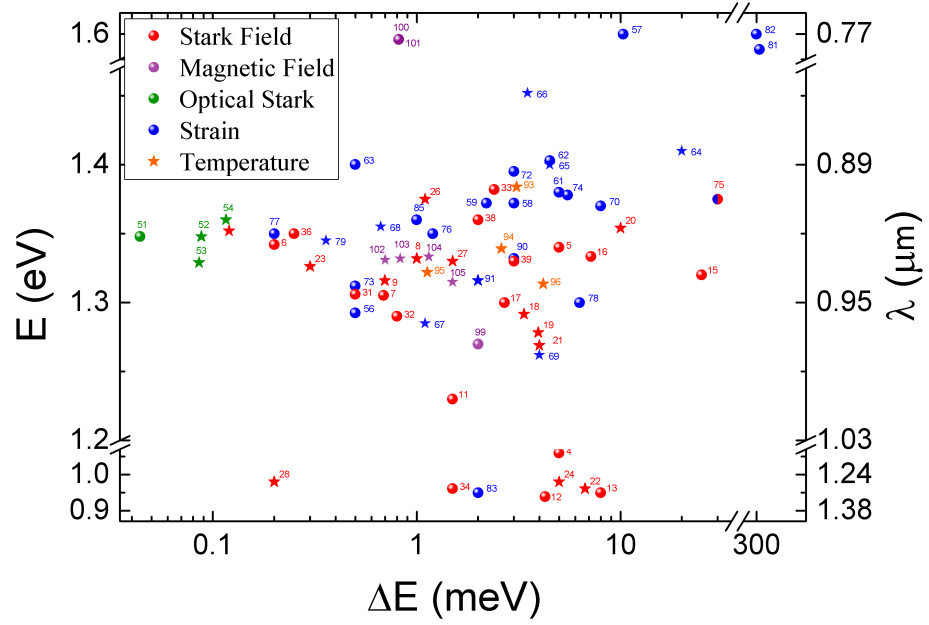


Figure 1.17: Summary of the tuning range for the methods to control the QD energy. A star indicates the integration with a cavity. (4) [101] (5) [212] (6) [269] (7) [207] (8) [336] (9) [354] (10) [125] (11) [119] (12) [291] (13) [292] (14) [293] (15)[26] (16)[234] (17) ([473]) (18)[427] (19) [200] (20) [211] (21) [229] (22) [160] (23)[112] (24)[321] (25)[303] (26)[304] (27)[312] (28) [288] (31) [407] (32) [219] (33)[448] (34) [136] (35) [271] (36) [306] (37) [373] (38) [195] (39)[357] (40)[25] (41)[297] (42)[29] (43) [259] (44) [344] (45)[139] (46)[343] (47)[271] (48) [138] (50)[440] (51)[301] (52)[47] (53) [46] (54)[45] (56)[387] (57)[225] (58)[90] (59)[185] (60)[339] (61)[435] (62)[63] (63)[490] (64)[436] (65)[487] (66) [486] (67)[242] (68)[416] (69)[24] (70)[434] (71)[433] (72) [488] (73)[224] (74) [161] (75) [437] (76)[221] (77)[476] (78)[62] (79)[42] (80)[151] (81)[466] (82)[464] (83)[419] (85)[134] (86)[280] (87)[449] (88)[450] (89) [383] (90)[351] (91)[459] (93)[137] (94) [113] (95)[110] (96)[61] (98)[409] (99)[425] (100)[8] (101)[7] (102)[364] (103)[201] (104)[202] (105)[365]

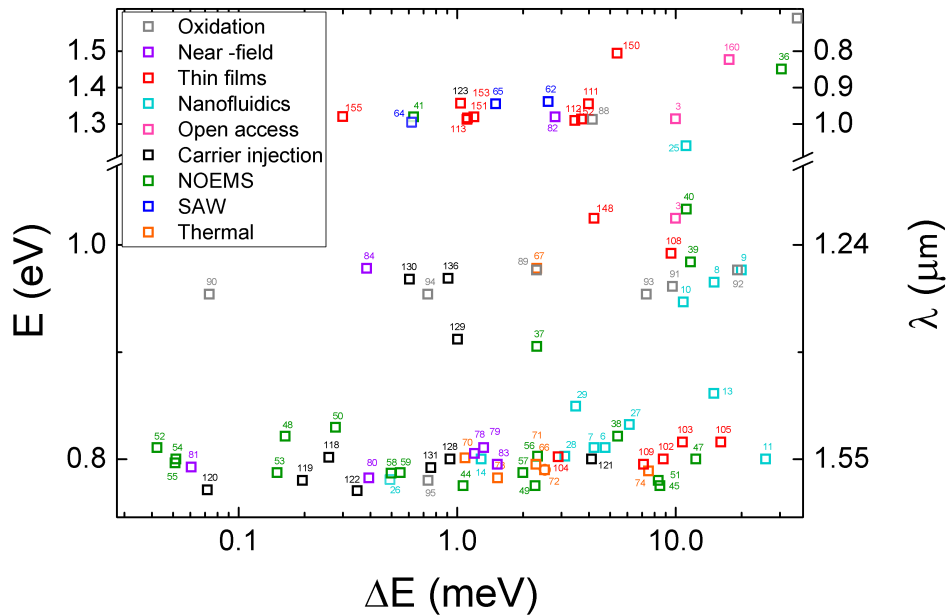


Figure 1.18: Summary of the energy range (ΔE) of the cavity-tuning methods discussed in this chapter as a function of their central energy (E). (3)[21] (5)[289] (6)[4] (7) [188] (8)[174] (9)[446] (10)[445] (11)[402] (12)[35] (13)[54](14)[218] (15)[274] (16)[397] (17)[108] (18)[189] (19)[40] (20)[199] (21) [398],(24) [278] (25)[384] (26)[276] (27)[118] (28)[98] (29)[99] (30)[277] (31)[453] (33)[177] (34)[439] (35)[192] (36)[167] (37) [331](38)[284] (39)[285] (40)[286] (41) [315] (42)[193] (43)[124] (44)[64] (45)[64] (46)[65] (47)[65] (48)[461] (49)[66] (50)[3] (51)[429] (52)[337] (53)[392] (54)[244] (55)[246] (56)[324] (57)[96] (58)[247] (59)[95] (60)[249] (62)[126] (63)[480] (64)[262] (65)[196] (67)[460] (68)[447] (69)[69] (70)[14] (71)[273] (72)[323] (73)[149] (74)[116] (75)[176] (77)[214] (78)[165] (79)[272] (80)[72] (81)[300] (82)[232] (83)[147] (84)[173] (85)[205] (87)[80] (88)[158] (89)[233] (90)[60] (91)[171] (92)[57] (93)[335] (94)[56] (95)[477] (97)[157] (98)[10] (100)[144] (101)[413] (102)[474] (103)[59] (104) [347] (105)[491] (106)[130] (107)[380] (108)[208] (109)[389] (111)[406] (112)[405] (113)[51] (115)[235] (116)[114] (118) [420] (119)[22] (120)[421] (121)[353] (122)[204] (123)[128] (124)[169] (125)[314] (126)[482] (127)[481] (128)[181] (129)[296] (130)[485] (131)[295] (132)[424] (133)[379] (135)[166] (136)[78] (137)[74] (139)[467] (140)[422] (141)[423] (143) [322] (151)[299] (152)[203] (153)[79] (154)[105] (155)[215] (156)[316] (157)[305] (158) [318] (159)[428] (160)[359] (161)[463] (163)[97]

2 | FABRICATION METHODS

This chapter describes the fabrication process developed to obtain the nano-opto-electrical-mechanical systems (NOEMS) based on a double-membrane architecture presented in this thesis. In particular, we focus on the critical steps of the fabrication. Besides, a process flow entirely based on electron-beam-lithography (EBL) is illustrated.

2.1 INTRODUCTION

Micro-electro-mechanical systems (MEMS) are widely adopted for actuators and sensors in various fields, spanning from automotive to optical communications. As an example, today's smartphones embed an increasing number of MEMS, including accelerometers, gyroscopes, pressure sensors, microphones, bulk acoustic resonators, and optical image stabilization systems. Broadly speaking, the fabrication techniques employed for the realization of these devices are very similar to the ones used in silicon integrated circuits. In fact, these devices are fabricated using a standard top-down approach, where a pattern is transferred from a digital or physical mask to a multi-layer stack via lithography and etching. The technology behind the fabrication of the first MEMS was *bulk micromachining* [5, 388]. This scheme exploited the selective removal of materials from a substrate via isotropic and anisotropic chemical etching, in order to create free-standing structures. Nowadays, this scheme has been superseded by *surface micromachining*, which provides higher spatial resolution and allows for a relatively vast material selection. This technique - developed at Berkeley in the early 1980s - employs two different types of layers, namely *structural* and *sacrificial* layers. The former represent the architectural frame of the final device, while the latter are employed as temporary supports that are etched away to create suspended parts. Alternative methods have been proposed and make use of wafer-bonding, electro-discharge micromachining, laser and focused ion beam micromachining [264]. The main drawback of silicon-based MEMS is represented by the impossibility to generate light due to the lack of suitable emitters. In this context MEMS based III-V materials represent an excellent choice for reconfigurable QPICs, since they combine large tunability with direct semiconductor bandgaps. Devices in which the active optical control is conjoined with mechanical tunability are referred to as micro- and nano-opto-electro-mechanical systems (MOEMS and NOEMS), depending on whether they employ a micro- or nano-photonic structure. NOEMS based on III-V compounds show two main technological differences compared to standard silicon-based MOEMS or NOEMS, which differentiate their fabrication processes: (i) the regrowth of active semiconductor layers on top of a structured surface typically produces defects, and therefore is not feasible;

(ii) doping variations are defined more easily in the vertical (growth) direction. As a consequence, while the electrostatic actuation in silicon-based MEMS is realized with metal electrodes and produces a lateral movement, in III-V materials the actuation involves vertical electromechanical forces and vertical displacements. In order to fabricate vertical p-(i)-n diodes in III-Vs, the doped layer must be *opened* before metal deposition. In this thesis we employ an hybrid fabrication approach where sacrificial and structural layers are used (similar to surface micromachining), but are defined during the initial growth (thus corresponding to the *bulk* of the wafer). Gallium Arsenide and Aluminium Gallium Arsenide (AlGaAs) are employed as the structural and sacrificial layers, respectively. Besides, silicon nitride (Si_3N_4 ¹) plays an important role in the fabrication. It is widely used as hard mask for dry and wet etching, and provides an additional support for the release of the NOEMS. The choice of this material is dictated by its excellent mechanical properties and low etching rates [19].

2.2 PROCESS FLOW BASED ON OPTICAL AND ELECTRON BEAM LITHOGRAPHY

The fabrication of the devices presented in this thesis consists of three main parts. In part I, the sample is grown by molecular beam epitaxy (MBE). Part II comprises three sequential lithographic steps (fig.2.1(a-c)) for the realization of the diodes and the bridge employed in the mechanical actuation. Then, in part III, the photonic crystal layout is patterned and deeply etched through the entire structure (fig.2.1(d)). Finally, the AlGaAs sacrificial layers are selectively removed via wet-etching, obtaining the release of two membranes (fig.2.1(e)). In the following, we describe the details of each fabrication stage.

2.2.1 Part I: wafer growth

The fabrication process starts with the epitaxial growth of a GaAs/AlGaAs heterostructure shown in fig.2.2. This layer stack is grown by molecular beam epitaxy with a nm-thickness control. A 2" semi-insulating GaAs wafer, oriented along the [100] direction, is used as a substrate for the growth. Firstly, a 1.5- μm -thick $\text{Al}_{0.7}\text{Ga}_{0.3}\text{As}$ layer is deposited on top of the substrate. This layer serves as a sacrificial spacer to decouple the substrate and the active region. Then, two GaAs membranes are grown, separated by a 240-nm thick AlGaAs layer. Since the processing produces an undesirable reduction of the thickness of the top membrane (ranging from 10 to 20 nm), the top GaAs-membrane is slightly thicker (180 nm) compared to the bottom membrane (170 nm), in order to compensate for the thickness asymmetry induced by the non-perfect selectivity of the etching process. The thickness of the membranes is designed to support a single optical mode for each slab. The value of the inter-membrane distance is selected in order to obtain sufficient electromechanical tuning before pull-in. Although a smaller

¹ for brevity we will refer to silicon nitride as SiN

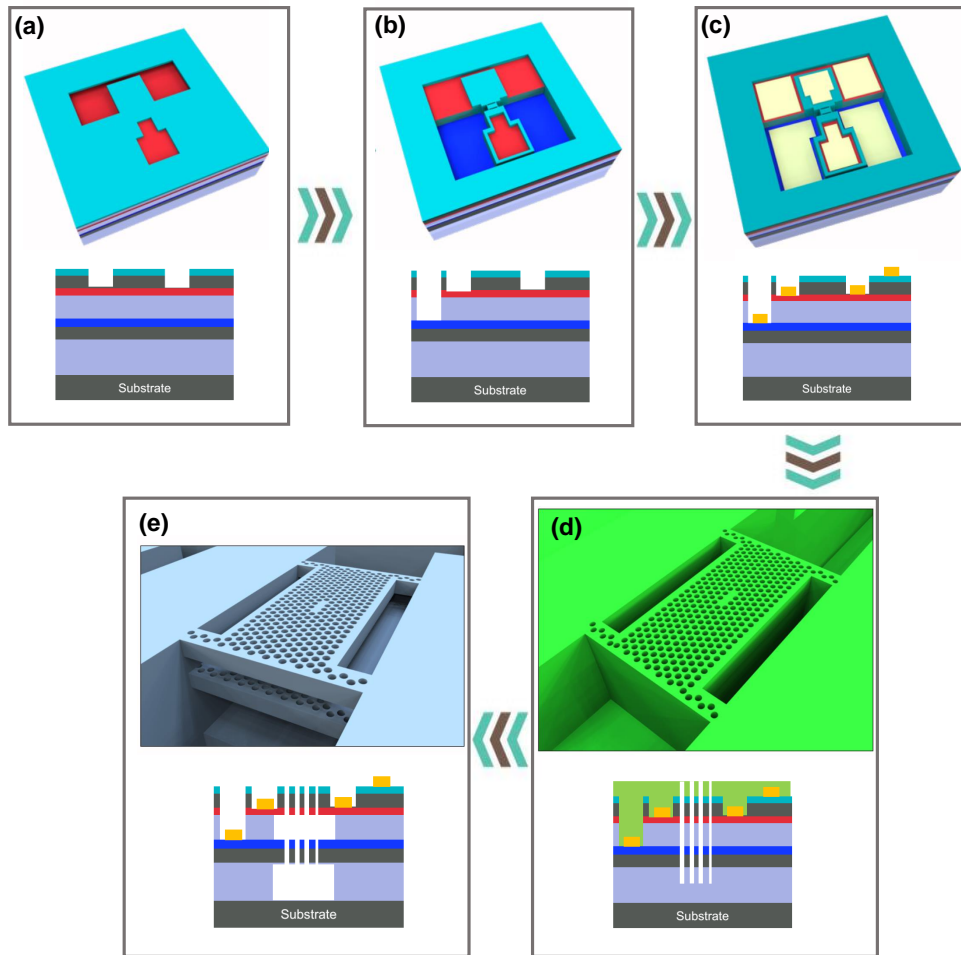


Figure 2.1: Sketch of the main stages involved in the fabrication process (a–c). Realization of the double diode. (d–e) Patterning, deep etching and release of the PhC membranes. The in-plane and cross-section views of the devices are sketched in the top and bottom parts of each panel

initial gap provides a higher tuning range, this is also associated with an increased probability of collapse during the process [281]. With the aim of realizing two p-i-n diodes, for cavity actuation and QD-control (Stark-tuning or electrical injection), the top 55-nm-thick part of the two membranes is p-doped, while the bottom 55-nm thick part of the top membrane is n-doped ($p_{\text{QD}} = 1.5 \times 10^{18} \text{ cm}^{-3}$, $n = p_{\text{CAV}} = 2 \times 10^{18} \text{ cm}^{-3}$).

A layer of low-density self-assembled dots is grown in the middle of the top membrane to obtain the maximum overlap with the optical modes of the structure. In order to obtain the ground-state emission centred around 1300 nm at low temperature, the dots are capped with a $\text{In}_{0.2}\text{Ga}_{0.8}\text{As}$ layer [11, 12]. Two different designs for the top membrane have been adopted (A and B). Design A embodies two 17-nm thick $\text{Al}_{0.3}\text{Ga}_{0.7}\text{As}$ barriers to suppress the tunnelling probability of the dots, as proposed in [29], and has been used for the experiments presented in chapter 4. These barriers are located 8-nm above and 8-nm below the dot region, respectively; design B does not incorporate barriers and is employed in chapters 3, 5, 6, 7. These

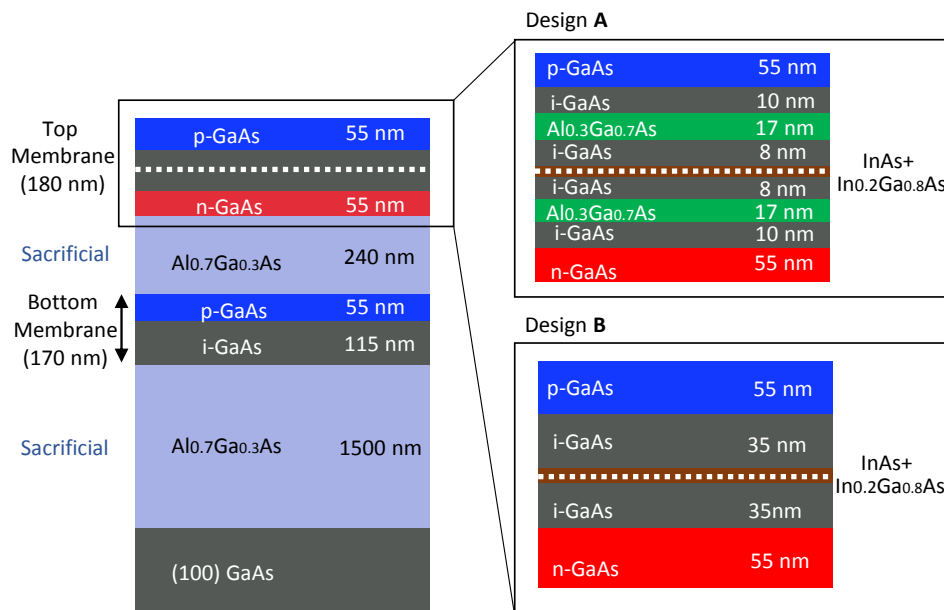


Figure 2.2: Layer stack of the fabricated devices. Two different designs have been employed: design A and B, with and without AlGaAs barriers, respectively

samples have been grown at the TU/e cleanroom by F.W.M van Otten and at the University of Leeds by dr. L.H. Li. Before any further processing, a part of the wafer is typically pre-characterized at low temperature in order to identify single dot lines and evaluate their density.

2.2.2 Part II: diodes

2.2.2.1 *N-via*

The fabrication process starts with the cleaning of the wafer by oxygen plasma (300 W, 10 min) followed by a de-oxidation (NH₄OH:H₂O, (1:10)²). The n-mesas of both diodes are defined in the same optical lithographic step. Firstly, a 50-nm thick SiN mask is deposited by PECVD operating at 300° C and oxidized via plasma stripping (300 W, 10 min). The sample is then immersed in ultra pure water for 5 min, and Hexamethyldisilazane (HMDS) is deposited to favour adhesion of the photoresist (PR). A positive photoresist (HPR-504, Micro Resist Technology) is spun in a closed spinner. A PR thickness of ≈ 700 nm is obtained at 3000 rpm (acceleration 50 rpm/s, time 30 s). Then, the sample is baked on a hot plate for 150 s at 100° C to improve the resist's homogeneity. At this point, the sample is exposed with UV-light using a mask aligner (MA6, Suss Microtec). This optical lithography step is carried out in contact mode, i.e. the sample is brought in direct contact with the chromium mask in vacuum. After a 3.3 s-long exposure, the sample is baked at 115° C for 150 s to reduce the roughness of the resist. The development - realized by immersion in an OCG:H₂O (1:2) solution for ≈ 70 s,

² the solution is expressed in volume ratio of commercial diluted solution

followed by water rinsing - dissolves the exposed parts of the resist³. After the development, low-power stripping (50 W, 5 min) removes possible resist residuals.

The pattern of the n-mesa is transferred from the resist to the SiN mask via reactive-ion etching (RIE) based on a $\text{CHF}_3:\text{O}_2$ mixture. A high-power stripping (30 min, 300 W) is employed to remove the resist after the dry etching of the SiN mask. At this stage, the opened GaAs surfaces are firstly de-oxidized in $\text{NH}_4\text{OH}:\text{H}_2\text{O}$, (1:10) solution, and then immersed in 1% hydrofluoric acid (HF) to remove any residual surface oxide.

Subsequently, the pattern is transferred from the SiN mask to the n-doped layer via a citric acid solution ($\text{C}_6\text{H}_5\text{O}_7:\text{H}_2\text{O}_2$, (40:1)). Because of the absence of selectivity between the intrinsic and doped region of the GaAs, the time of this wet-etching process is carefully calibrated in order to reach the n-doped layer. A longer or shorter etching time results in the degradation of the electrical properties of the diodes. Since the etching rate of this solution might vary over time and slightly depends on the preparation conditions, this etching is separated in two sequential steps. The first step provides the etching speed for the second step. A typical GaAs etching rate of $\approx 1.5 \text{ nm/s}$ is obtained. The final etching profile is verified with a profilometer. Finally, after a cleaning and de-oxidation step, the SiN is removed using HF 5% for 1 min.

2.2.2.2 P-via and bridge definition

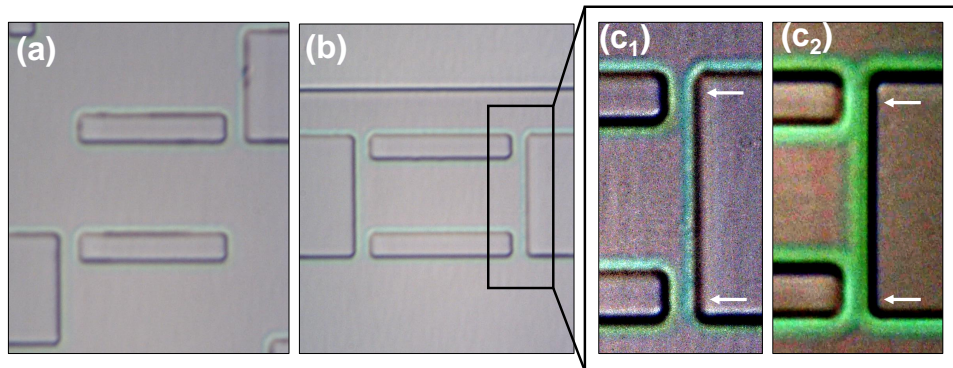


Figure 2.3: Optical microscope images of the top membrane patterned in the form of a micro-bridge, during the p-via etching. (a) Device coupled to waveguides. (b) Device having a stand-alone bridge geometry. (c1) and (c2) show high-contrast pictures of the micro-arms, after etching with a HF-solution (5%) for 20 s and 40 s, respectively

The definition of the p-mesa - which opens the p-layer of the cavity diode - follows the same lithographic steps described in the previous paragraph, with the following exceptions: (i) the SiN mask is not employed, since the top GaAs membrane is exploited as hard mask for the wet-etching process.

³ The exposure and development times might vary depending on the conditions of the UV-lamp

(ii) By using alignment marks, the pattern of the p-mesa is aligned to the n-mesa with a resolution better than $0.5\ \mu\text{m}$. (iii) After the exposure and development of the photoresist, a combination of dry etching and wet etching is employed to reach the bottom p_{CAV} -layer. Specifically, the time of a RIE based on SiCl_4 recipe is calibrated to reach the interlayer AlGaAs. Then, a wet etching in a hydrofluoric acid solution (5%) is employed to selectively remove the inter-membrane AlGaAs, and to open the p_{CAV} layer. Importantly, during this lithographic step, the micro-bridge for cavity actuation is also defined, as shown in fig.2.3 (a,b). In the case of stand-alone⁴ devices, a rectangular bridge connected to a surrounding frame by four ($2 \times 2\ \mu\text{m}^2$) micro-arms is entirely defined in this step (fig.2.3(b)), while wg-coupled geometries present one or multiple lateral accesses (fig.2.3(a)). It is worth mentioning that the time of the wet etching is regulated in order to prevent a critical undercut below the micro-arms, which can lead to a premature release of these parts. As an example, fig.2.3(c1) and fig.2.3(c2) show high-contrast optical images of the micro-arms for an optimized and a long etching time, respectively. The green area represents the region where the interlayer AlGaAs is removed.

2.2.2.3 Contact deposition

The contact layers are deposited on all the three doped surfaces in a single lithography step, followed by contact deposition. Firstly, the sample undergoes a cleaning routine composed of O_2 stripping, followed by de-oxidation in ammonia. Then, a negative resist ($\approx 800\ \text{nm}$, MaN 440) is spun at 2000 rpm (acceleration 50 rpm/s) in a closed spinner. After pre-baking (90°C , 5 min) the sample is exposed with UV-light in three 100s-long consecutive cycles. The not-exposed parts of the photoresist are developed in a Ma-D 332S (Micro Resist Technology) for 90 s. This optical lithography step has been optimized by Tjibbe de Vries (TU/e) in order to obtain a re-entrant shape of the photoresist that facilitates the following lift-off procedure. A Ti/Au alloy (50/200 nm) is then deposited in a electron-beam evaporator (Temescal, FC2000). Finally, a lift-off procedure is carried out, maintaining the sample in vapour bath of acetone for 60 minutes, followed by rinsing in isopropanol (10 min).

2.2.3 Part III: photonic crystals, waveguides and release

2.2.3.1 Photonic crystal definition

In the final part of the process, a $\approx 400\ \text{nm}$ -thick silicon nitride layer is deposited via PECVD. This film acts both as a hard mask for the deep etching of the photonic crystal holes and as a coating for the support of the pre-fabricated bridge. In fact, the presence of this mask increases the stiffness of the micro-bridge, reducing the probability of collapse during the release process. A positive electron-beam resist ($\approx 390\text{nm}$ -thick ZEP-520A, Zeon Corp.) is spun on top of the SiN mask (speed 2500 rpm, 60 s). In order to make the resist harder, the sample is baked on a hot plate for 4 minutes

⁴ i.e. devices not connected to ridge waveguides

with a temperature linearly increasing with time, from $T=100\text{ }^{\circ}\text{C}$ to $T=150\text{ }^{\circ}\text{C}$, followed by 2 minutes at $200\text{ }^{\circ}\text{C}$.

Then, the actual exposure of the pattern comprising PhCs and waveguides is carried out in a 30-KV Raith-II-150 system. Since this system is a SEM-based EBL, it requires a manual adjustment of the aperture alignment, astigmatism, focus, origin and angle correction with respect to the sample. The digital design is divided in writing fields (WFs) of $100\times 100\text{ }\mu\text{m}^2$ and the electron beam is automatically deflected to pattern structures inside the WF. Long waveguides are patterned employing the fixed-beam-moving-stage (FBMS) method, where the sample is scanned instead of the beam gun, in order to avoid misalignment error and *field stitching* along consecutive WF. The photonic crystal layout is aligned to the centre of the

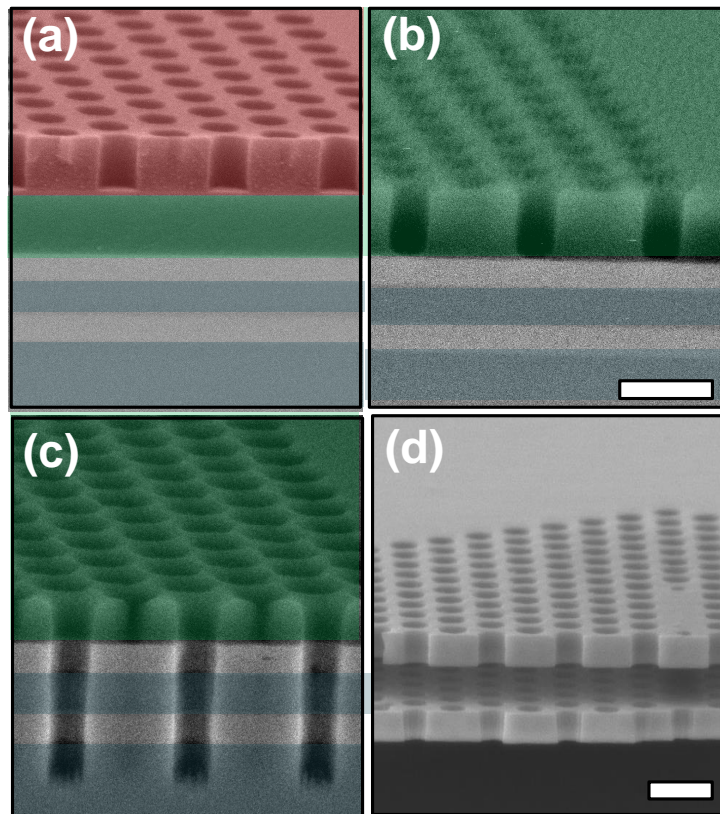


Figure 2.4: False-colour SEM cross sections of the cleaved PhC region after (a) e-beam resist development, (b) SiN dry etching, (c) ICP etching, (d) wet etching and release. The red, green, grey and blue colours represent the e-beam resist, the SiN mask, the GaAs and the AlGaAs layers, respectively. The bars correspond to 500 nm

pre-fabricated bridge geometry with a resolution better than 100 nm. With the aim of obtaining a homogeneous array of holes, a *proximity-effect correction* (PEC) algorithm is applied to the design, accounting for the back and forward scattering of the electrons [320]. Without PEC corrections, the inner holes of the crystal are characterized by larger radii compared with the holes located at the boundary of the PhC, because of the larger effective dose originated from the patterning of the surrounding holes.

Structures with different dimensions generally require a different electron dose to be fully opened in the development of the resist. In the case of PhCs, a clearing dose of $D = 350 \frac{\mu\text{C}}{\text{cm}^2}$ ⁵ is found to produce optimal results, while a higher dose is employed for the patterning of ridge waveguides $D = 450 \frac{\mu\text{C}}{\text{cm}^2}$. The development of the e-beam resists consists in the immersion in n-amyl acetate (65 s), followed by rinsing in methyl isobutyl ketone (MIBK)-IPA (55 s). The resulting pattern (fig.2.4(a)) is transferred to the underlying SiN mask, employing a RIE method based on pure CHF₃ with an etching rate of ≈ 18 nm/min for features smaller than 200 nm. This etching rate is calibrated in such a way that the process stops at the SiN/GaAs interface (fig. 2.4 (b)). A longer etching time enlarges the PhC holes, while if the etching is stopped before this layer, the pattern might be not transferred to the bottom layers in the following steps. Then, the e-beam resist is removed by stripping in oxygen plasma (power= 300 W, 15 min). Next, the PhC pattern is deeply-etched through both membranes all the way to the bottom sacrificial layer (fig.2.4(c)). Due to the high aspect-ratio required in this step, the dry etching is carried out in an inductively-coupled plasma (ICP) RIE system exploiting a high-temperature (200°C) Cl₂/N₂ recipe. The stoichiometry of the Cl₂/N₂ mixture along with the radio-frequency and inductive coil powers have been previously optimized by dr.F.M. Pagliano during his PhD thesis [320] in order to obtain high etching rates, while maintaining high verticality. The side-wall angle of the PhC pattern is estimated below $\approx 0.5^\circ$ by cross-sectional SEM picture analysis. During the ICP-RIE, the thickness of the SiN mask is reduced to approximately half of its original thickness, as shown in fig.2.4(c), which is still sufficient to support the upper membrane during the release. We observed that the etching rate of the ICP-RIE strongly depends on the tool history and, in particular, by the number of other processes realized after the physical cleaning of the machine. A test fabrication process is typically carried out in order to re-optimize this etching time, based on the condition of the machine.

2.2.3.2 *Releasing of the suspended membranes*

Finally, the two AlGaAs layers are removed by selective wet etching. To this aim, the sample is immersed in cold hydrochloric acid for 6 minutes, and carefully rinsed in pure water. An in-plane anisotropic profile is obtained by employing a cold (1°C) solution. This etching process produces a well-defined undercut below the cavity and - at the same time - the etching stops laterally in wide ($> 1.6\mu\text{m}$) structures, providing a way to realize supported ridge waveguides in the same etching step (see chapter 7). Since the etching solution provides an self-limiting V-groove shape (see fig. 7.2) of the AlGaAs layer, the time required for the wet etching does not require a precise calibration routine. The release of the suspended structure is undoubtedly one of the most critical steps in this fabrication process. In this rinsing stage, the acid located in between and below the membranes is replaced by water. During the subsequent drying, a strong capillary force is created by the surface tension of water droplets, which can lead to adhesion of the membranes or other parts of the NOEMS, as shown in fig.2.5 (a, b).

⁵ before PEC correction

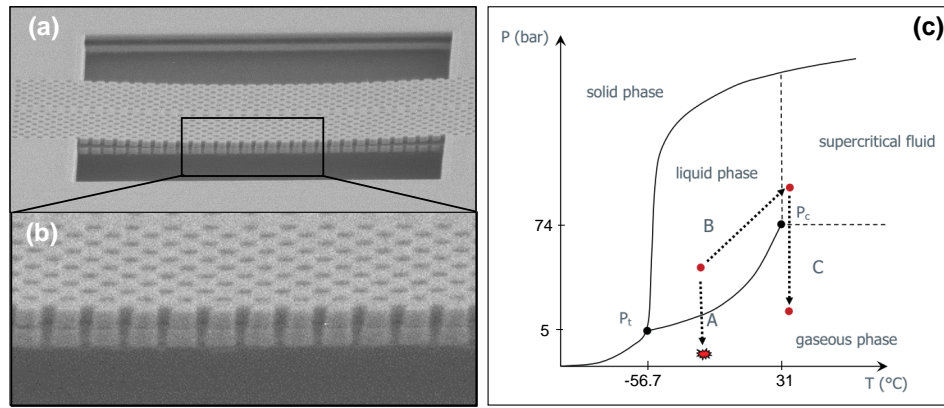


Figure 2.5: (a,b) Example of a fabricated device subjected to stiction after the release process. (c) Phase diagram of carbon dioxide and transitions (B,C) exploited by the super-critical drying method. ((c) reproduced from [240])

This detrimental effect, known as *stiction*, is typically irreversible due to the strong short-distance forces involved. A strategy to limit this effect - demonstrated by dr. L. Midolo (TU/e) - exploits the high-conformality of the SiN nitride mask to clamp the top membrane from all its sides, thus increasing the stiffness of the upper membrane. The probability of collapse is further reduced by drying the sample in hot isopropanol, which is characterized by a lower surface tension than water. Alternatively, super-critical drying methods have been used in order to avoid the direct transition of the interstitial fluid from liquid to gaseous phase (transition A, fig.2.5(c)). In this case, the sample is cautiously transferred in isopropanol, and a super-critical drying system is employed (Leica, EM CPD 300). Here the IPA is substituted by liquid carbon dioxide (CO_2) through a series of dilution steps. The pressure of the chamber is increased by incrementing its temperature (transition B, fig.2.5(c)). When the temperature and the pressure of the liquid CO_2 are larger than its supercritical point ($T_c = 31^\circ\text{C}$, $P_c \approx 74$ bar), the liquid is brought in supercritical status, where the density of the liquid phase and that of the vapor phase are equal. Then, the temperature is maintained constant while the pressure is decreased (Transition C, fig.2.5(c)), hence avoiding a phase transition. Finally, at the end of the process, the SiN mask is removed isotropically employing a dry etching based on CF_4 . The sample is then cleaved orthogonally to the direction of the ridge waveguides (if any).

2.3 EBL-ONLY PROCESS FLOW

In the previous paragraph we presented the process of the double membrane system used in the first three years of this thesis, which comprises three main steps of optical lithography (OL) for the realization of the diodes. In the course of the third year, the 30-kV EBL system in the Nanolab@TU/e cleanroom has been replaced with a new 100-kV EBL (EBPG 5150, Raith GmbH/Vistec), and the process has been updated and optimized accord-

ingly. Specifically, thanks to the fast exposure time of this machine, the n-via, the p-via, and the contact region are patterned using only EBL exposures. This gave us the opportunity to investigate a number of designs for the contact geometry without requiring a new OL-mask. This feature has been particularly crucial to obtain an optimal electrical insulation for devices coupled to waveguides (chapter 7). Besides, the use of EBL patterning allows for the reduction of the dimensions of the mesas, which potentially enables an increased actuation speed. Importantly, due to the enhanced-resolution that can be obtained by EBL (tens of nm), this process can be used to pattern a bridge with an arbitrary shape, featuring sub-microns parts. The etching schemes illustrated before are left unchanged. In this section we present the main features of the process for the EBL-based flow.

ALIGNEMENT MARKS, N-VIA AND P-VIA Differently from the Raith-II-150 system, the new system is characterized by fully-automatized alignment procedure that provides high throughput ⁶. For this reason, the system requires well-defined markers that have a standard geometry (squares of 20x20 μm^2). Therefore, a set of markers is created at the corners of the sample as a first step in the process. These are deeply etched ($\approx 600\text{ nm}$) through both membranes via RIE. This layout is patterned employing the same chemistry described before for the realization of the PhC. High current (80 nA) and large pixel size (80 nm) are employed with a dose of $180 \frac{\mu\text{C}}{\text{cm}^2}$ to obtain high speed patterning. The fabrication of n-via and p-via employs the same resist, developer and EBL configuration.

CONTACT DEPOSITION For the contact deposition a positive 600 nm-thick e-beam resist is used (PMMA A11 960). This is deposited at 6500 rpm for 60 s, and is baked for 3 minutes. The dose employed in the e-beam exposure is $1100 \frac{\mu\text{C}}{\text{cm}^2}$, which gives a suitable profile for the lift-off. After exposure this resist is exposed in IPA/MIBK (80 s) and rinsed in IPA (80 s)

PHOTONIC CRYSTAL DEFINITION The recipe for the photonic crystal is the same as the one described in par. 2.2.3.1. The writing field employed is $500 \times 500 \mu\text{m}^2$, which reduces the errors due to stitching. A beam step size of 4 nm and a current of 1 nA are employed to obtain high spatial resolution. It is worth mentioning that the magnitude of proximity effects represents one of the main differences between the 30 kV and 100 kV systems. These effects are characterized phenomenologically by the point spread function (PSF(r)), which defines the relative energy deposited at a distance r from a point exposure. The correction parameters can be estimated simulating the trajectories of the electrons via Monte Carlo simulations, and fitting the data with a Gaussian PSF:

$$\text{PSF}(r) = \frac{1}{\pi(1 + \eta + \nu)} \left(\frac{1}{\alpha^2} e^{-r^2/\alpha^2} + \frac{\eta}{\beta^2} e^{-r^2/\beta^2} + \frac{\nu}{2\gamma^2} e^{-r/\gamma} \right) \quad (2.1)$$

where α accounts for the forward (short range) scattering range of the electrons due to initial collision of the e-beam with the resists, β specifies the backward (long range) scattering range due to the reflection of electrons at

⁶ Only an initial pre-alignment procedure using an optical microscope is needed

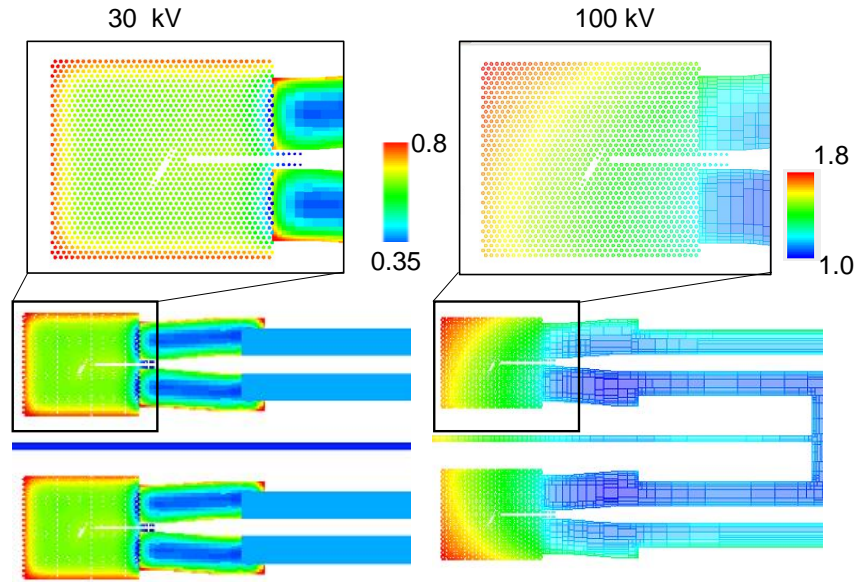


Figure 2.6: Proximity effect correction of a PhC obtained for a 30 kV and a 100 kV system. The color scale represents the dose multiplier

the semiconductors interfaces, and ν has been introduced to account for the collisions with the large atoms of the semiconductor. The weights of the different contributions are η and ν . The simulated parameters for the two systems are compared in the following table, while an example of PEC correction is shown in fig.2.6

PEC Parameter	30 kV	100 kV
α [nm]	28	2
β [nm]	1903	12000
γ [nm]	950	113
η	0.55	1.12
ν	0.28	0.1

In the case of the 100 kV system, due to the higher kinetic energy of the electrons, the back scattering range is larger than in the case of 30 kV by an order of magnitude, while the forward scattering is practically negligible. This means that the effective dose of a structure is influenced by the presence of other e-beam patterns in a 12 μm range, as observed in the PEC corrections of fig.2.6 (right).

2.4 STRESS-RELEASING STRUCTURES

The deformation induced by the residual stress in free-standing mechanical parts is one of the most critical problems in MEMS technology [109, 145]. The origin of the internal stress (σ_0) is often ascribed to the difference in the thermal expansion coefficients of adjacent layers employed in surface micromachining. In particular, for structures characterized by a high length-/thickness ratio, the presence of internal stress can result in a downward or

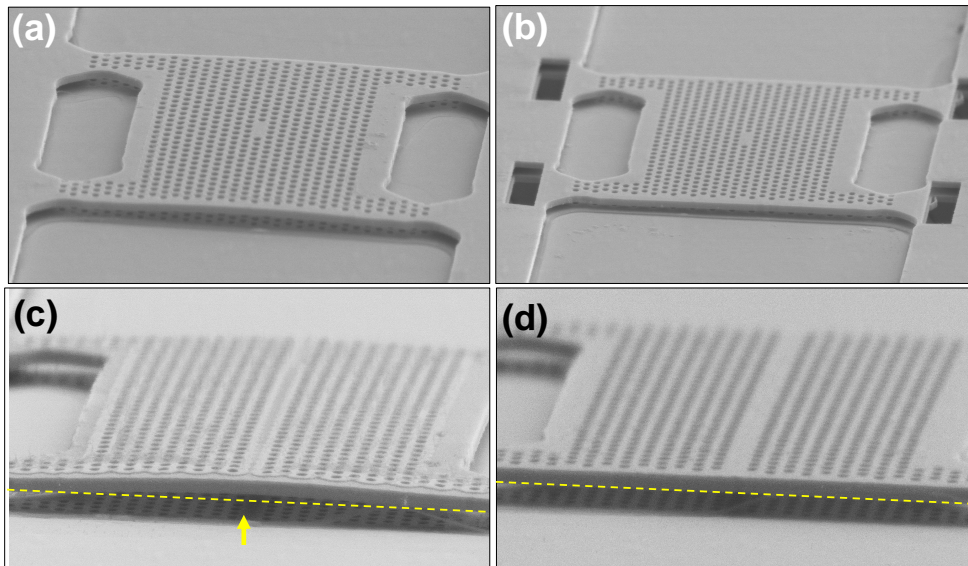


Figure 2.7: SEM pictures of the fabricated bridge geometry without (a, c) and with (b,d) stress-releasing supports. A clear upward bending that deviates from the planar geometry (yellow dashed line) is observed in (c)

upward buckling of the structure. Although in some cases this behaviour can be exploited as a source of non-linearity [469], for most applications the presence of buckling compromises the actual performance of the devices.

This effect has been previously observed in vertically-coupled nanobeams [285, 468], manifested as an unpredictable bending profile of the structure. In the case of suspended 2D-membranes, an upward buckling is commonly observed, as shown in fig.2.7(a,c). This deformation leads to an increased initial inter-membrane distance, which in turn results in a substantial decrease of the tuning range of the NOEMS. A strategy to limit the effect of buckling has been proposed by Iwase *et al.* [178] and makes use of engineered supporting structures for stress releasing. The main idea consists in these supports having an in-plane stiffness smaller than the principal structure, so that only the supporting structures will be affected by the deformation induced by the buckling. In a certain sense, buckling is *guided* towards structures with lower stiffness. This concept has been demonstrated for double 1D nanobeams by dr. T. Xia [468]. In this work, we apply the proposed stress-releasing supports to 2D membranes. To this end, $1 \times 4 \mu\text{m}$ rectangular trenches are etched at a $0.5 \mu\text{m}$ distance from the end of the micro-arms fig.2.7(d). A negligible bending of the upper membrane is obtained experimentally, as shown in fig.2.7(d)

We can derive a theoretical estimation of the buckling probability by making use of the linearised buckling analysis (LBA) [23, 75, 438]. The LBA assumes that the total stiffness matrix of the system can be written as a sum of a linear contribution \mathbf{K}_L , independent on the applied load (\mathbf{f}_0), and a non-linear part (\mathbf{K}_{NL}) that - in the first order approximation- is proportional to the load, \mathbf{f}_0 . An instability is obtained when the total stiffness matrix is

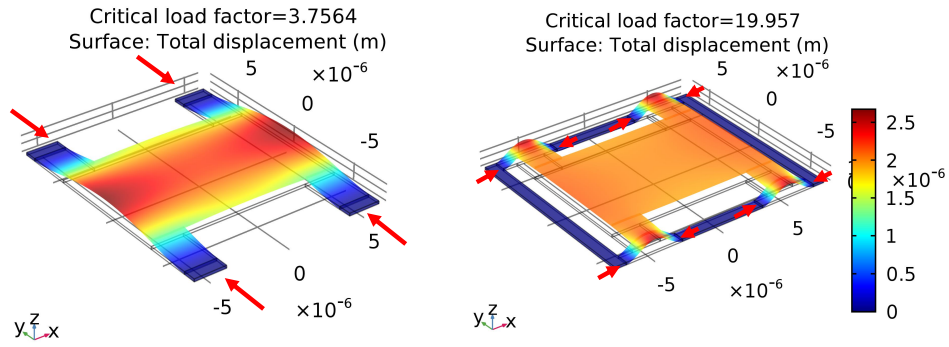


Figure 2.8: Simulated buckling profile and critical load factor for structure without (left) and with (right) stress-released arms. The internal load is applied as indicated by the red arrows. The color scale is not relevant, since the LBA does not provide the absolute displacement

singular, and thus the displacement vector (\mathbf{u}) is indeterminate. The critical load $\mathbf{f}_c = \lambda \mathbf{f}_0$ is therefore found solving the eigenvalue problem

$$\mathbf{K}\mathbf{u} = (\mathbf{K}_L + \lambda \mathbf{K}_{NL}(\mathbf{f}_0))\mathbf{u} = 0 \quad (2.2)$$

and assuming a certain stress configuration \mathbf{f}_0 . The lowest eigenvalue λ is defined as the *critical load factor*, while the eigenvector \mathbf{u} displays the shape of the structure after buckling. If the expected load is applied to the structure, λ can be interpreted as a factor of safety. We simulated the effect of internal stress on the geometry, applying the critical stress $\sigma_0 = 140$ MPa measured experimentally [468]. The results of the LBA are shown in fig.2.8 for the case without (left) and with (right) stress-releasing supports. The latter case shows a critical factor ≈ 4 times larger, indicating a lower probability of collapse. Besides, buckling is observed on the external arms of the structure, while the central core of the device remains planar.

2.5 CONCLUSIONS

In this chapter we described the steps involved in the fabrication of the double-membrane NOEMS employed in this thesis. This process provides a relatively high degree of independence in designing the optical and the mechanical parts of the system. With an optimized recipe, a yield of free-standing device higher than 90% has been obtained in the last fabrication runs. However, the yield may vary from process to process, due to different conditions of the machines. Despite the use of supercritical drying, the final release of the structure remains the most critical step of the process. The active PhC region of the current devices has a footprint in the order of $100 \mu\text{m}^2$, and is equipped with a mesa structure of $(0.3 \times 0.3) \text{mm}^2$. For a 2" wafer, this translates into 1000 devices per fabrication batch. Although this value is reasonable for the academic use of the device, further optimization of the contact geometry is needed to decrease the cost per fabricated unit. Finally,

the packaging of the structure is not discussed here. An important step for real-world applications of the current technology, not limited to the domain of QPICs, is provided by the anti-stiction method presented in chapter 6.

3 | NEAR-FIELD ACTUATION

In this chapter, we employ the contact forces induced by a near-field tip to tune and probe the optical resonances of a mechanically-compliant photonic crystal molecule. Here, the pressure induced by the near-field tip is exploited to control the spectral properties of the coupled cavities in a wide spectral range, demonstrating a reversible mode shift of 37.5 nm. In addition, by monitoring the coupling strength variation due to the vertical nano-deformation of the dielectric structure, distinct tip-sample interaction regimes have been unambiguously reconstructed with a nano-Newton sensitivity. These results demonstrate an optical method for mapping mechanical forces at the nanoscale with a lateral spatial resolution below 100 nm. The results presented in this chapter have been obtained in collaboration with the Nanostructures and nanophotonics group, in Florence (group led by Prof. Gurioli). They have been partially published in Phys. Rev. B vol. 94, 115413 (2016) [334].

3.1 INTRODUCTION

The inherent coupling between motion and light is at the core of a wide research area ranging from gravitational waves detection[2] to cavity optomechanics[16]. From a fundamental perspective, the interaction of mechanical oscillators with photons promises to bring quantum phenomena, such as superposition and entanglement, into the macroscopic realm [268]. On the application side, engineering such coupling may boost the sensitivity of displacement measurements, enabling novel integrated accelerometers[220] and high-precision mass sensors[250]. An approach to force sensing, which relies on a dual-layer PhC membranes, was theoretically presented in Ref.[414] and further elaborated in Ref. [310] and Ref.[257]. In the next paragraph we discuss the underlying theory following Midolo *et al.* [282]. This system, also known as *photonic molecule*, will be extensively used in the next chapters.

3.2 DESCRIPTION OF THE DEVICE

3.2.1 Optics

As discussed in chapter 1, the confinement in a photonic crystal slab is governed by the total internal reflection at the semiconductor-cladding boundaries, while the Bragg-scattering in the periodic 2D array of holes determines the in-plane profile. A PhC slab can be approximately described by first calculating the effective index and the vertical field profile ($\phi(z)$) in

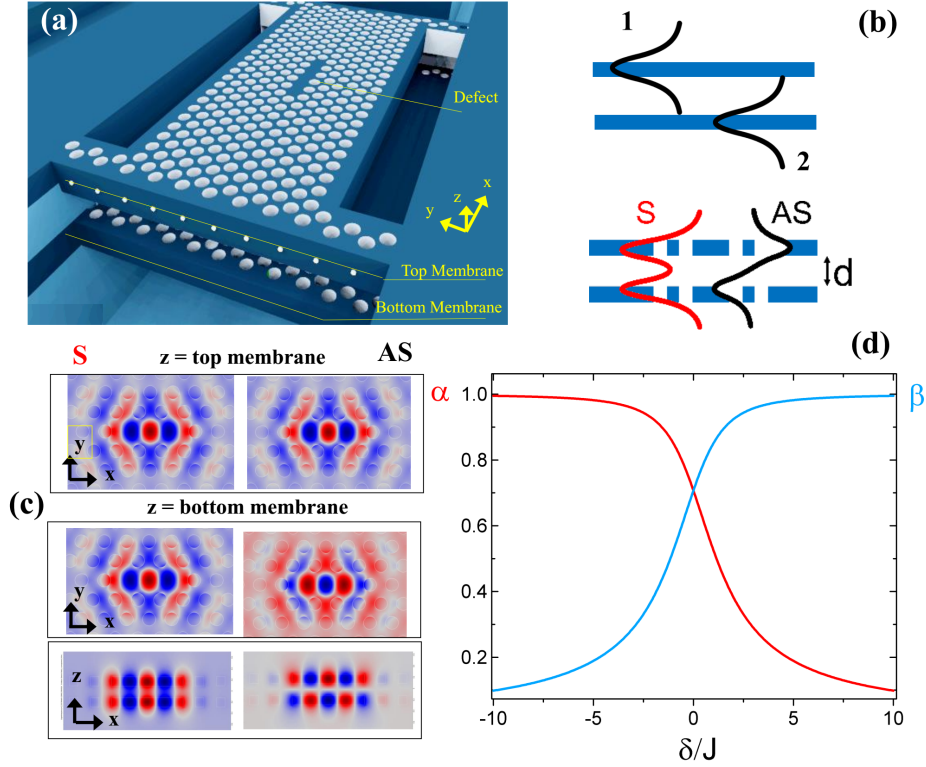


Figure 3.1: (a) Sketch of the double membrane system (b) Supermodes formation (c) Electric field profile (E_y) of the fundamental mode of the double-membrane L3 cavity, recorded at centre and across the two membranes (d) Field coefficients defined in eq.3.2 as a function of the detuning between the uncoupled modes

an unpatterned slab, then solving the electromagnetic problem in the plane to determine the lateral component $E_{\parallel}(x, y)$.

A way to program the frequencies of the PhC mode consists in modifying $\phi(z)$, for example by introducing a dielectric perturbation ($\delta\epsilon$) in the proximity of the system. If we bring two identical PhC slabs at a small distance d with respect to each other, so that their out-of-plane evanescent fields overlap, $\phi(z)$ will tend to delocalize over the two slabs (fig. 3.1 (a,b)), producing a frequency shift dependent on d . In the remainder of this thesis we will refer to this system as double-membrane (DM) PhC. The physical concept underpinning the operation of the DM cavity can be illustrated in the light of the temporal coupled mode theory (TCMT) [154]. The field amplitude of the modes of the PhC slabs can be written as $\mathbf{a}_i = \mathbf{E}_i(x, y, x) \exp(i\omega_i t)$, with $i = 1, 2$ indicating either the top or the bottom membrane, and ω_i their angular frequency. If we neglect the effect of the losses, we can write the time evolution of the fields as [154]

$$\begin{aligned} \dot{a}_1 &= i\omega_1 a_1 - iJ_{12} a_2 \\ \dot{a}_2 &= i\omega_2 a_2 - iJ_{21} a_1. \end{aligned} \quad (3.1)$$

In these equations, J_{ij} represents the rate of coupling from mode i into mode j . The assumption of a loss-free system leads to $J_{12} = J_{21}^* = J$ [182]. Eq.

3.1 represents the evolution of a pair of coupled harmonic oscillators. The stationary solutions of this coupled system that diagonalize eq.3.1 can be expressed as $\alpha_{S,AS} = \mathbf{E}_{S,AS} \exp(i\omega_{S,AS}t)$, where \mathbf{E}_S and \mathbf{E}_{AS} are the symmetric (S) and antisymmetric (AS) superposition of the uncoupled modes

$$\begin{aligned} \mathbf{E}_S &= \alpha\mathbf{E}_1 + \beta\mathbf{E}_2 \\ \mathbf{E}_{AS} &= \alpha\mathbf{E}_1 - \beta\mathbf{E}_2 \end{aligned} \quad (3.2)$$

with $(\alpha, \beta) \in \mathbb{C}^2$ and $|\alpha|^2 + |\beta|^2 = 1$. Inserting eq.3.2 in eq.3.1 allows obtaining the eigenfrequencies of the coupled system

$$\omega_{S,AS} = \frac{\omega_1 + \omega_2}{2} \mp \frac{1}{2} \sqrt{(\omega_1 - \omega_2)^2 + 4J^2}. \quad (3.3)$$

The energy separation between the coupled modes is $\Omega = \omega_{AS} - \omega_S = \sqrt{\delta^2 + 4J^2}$, where $\delta = \omega_2 - \omega_1$ accounts for a possible energy mismatch between the original modes. Notably, this expression is very similar to the energy of the polaritons derived in the JC model. Besides, the coefficients of the eigenvectors can be written as

$$\alpha = \frac{J}{\sqrt{(\omega_{AS} - \omega_1)^2 + J^2}} \quad \beta = \frac{\omega_{AS} - \omega_1}{\sqrt{(\omega_{AS} - \omega_1)^2 + J^2}} \quad (3.4)$$

In case of zero detuning, obtained for example by coupling two identical membranes, the two supermodes are equally distributed over the two membranes and $\alpha = \beta = 1/\sqrt{2}$ (fig. 3.1 (d)). On the contrary, introducing an energy detuning between the uncoupled modes yields to the localization of the field in one of the two slabs. In particular, the S mode will tend to localize on the cavity located at lower energy. Fig. 3.1 (c) shows the principal component E_y of the fundamental mode of a double L3 cavity, calculated by 3D Finite-Element simulations. It is evident that the in-plane profiles of the AS and S mode are identical in the top membrane, while they have opposite sign in the bottom membranes.

3.2.2 Mechanics

The coupling of the optical spectrum to the mechanical degree of freedom is realized by fabricating the upper crystal on a suspended micro-bridge (Fig.3.2a). In this way, a perturbation (δd) of the membrane position due to an external vertical force (δF) is directly transduced into the optical domain as a change in the splitting energy ($\delta\Omega$) of the coupled modes via the change in the coupling constant (δJ). Specifically, the selected bridge geometry is composed of a rectangular photonic crystal area connected to a supporting frame by four external micro-arms ($2 \times 2 \mu\text{m}^2$)¹. The area of the bridge ($14 \times 8 \mu\text{m}^2$) ensures a sufficient in-plane confinement around the cavity defect. Additional external trenches are patterned close to the supporting arms to release any internal stress accumulated during the fabrication process and to avoid buckling of the structure [178]. In order to relate the effect of a vertical local force to the deformation of the bridge we solve the static elasticity

¹ Additional bridge geometries along with the analysis of their mechanical properties can be found in [281] pag. 47

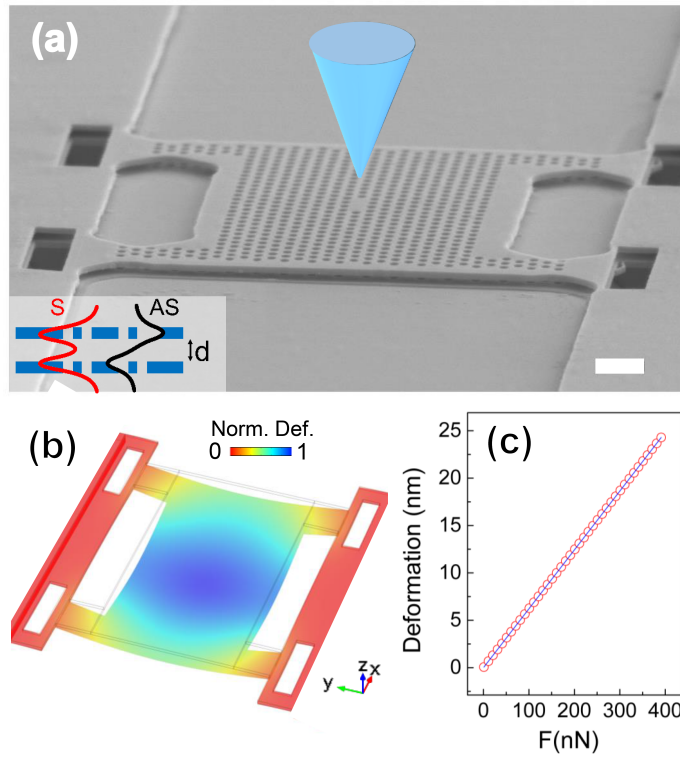


Figure 3.2: (a) Scanning electron micrograph showing the upper free-standing PhC micro-bridge. The scalebar corresponds to $1\ \mu\text{m}$. (b) FEM simulation of the vertical deformation of the structure caused by a localized force applied at the center of the bridge. (c) Calculated linear dependence of the maximum displacement on the applied force

equation employing a Finite Element Method (FEM) algorithm (Fig.3.2b). In particular, we model the local force exerted by the near-field probe as a load (F) uniformly distributed over a circle of radius $R = 100\ \text{nm}$ located at the center of the membrane. The deformation along the vertical direction, here encoded in a color-scale, manifests a parabolic dependence on the x coordinate due to the boundary conditions of this geometry. The maximum deformation is obtained at the center of the membrane where the cavity is located. This displacement is linearly dependent on the applied force (Fig.3.2c) through an effective spring constant $k = 16\ \text{N/m}$.

3.3 METHODS

3.3.1 Fabrication details

The fabrication of the device has been reported in chapter 2 and comprises several steps of optical and electron beam lithography followed by dry and selective wet etching processes, for the release of the membranes [282]. The sample consists of two free-standing Gallium Arsenide membranes which are both nominally $170\ \text{nm}$ -thick. The photonic crystal pattern, composed of a triangular array of holes (lattice constant $a = 380\ \text{nm}$, filling ratio $f =$

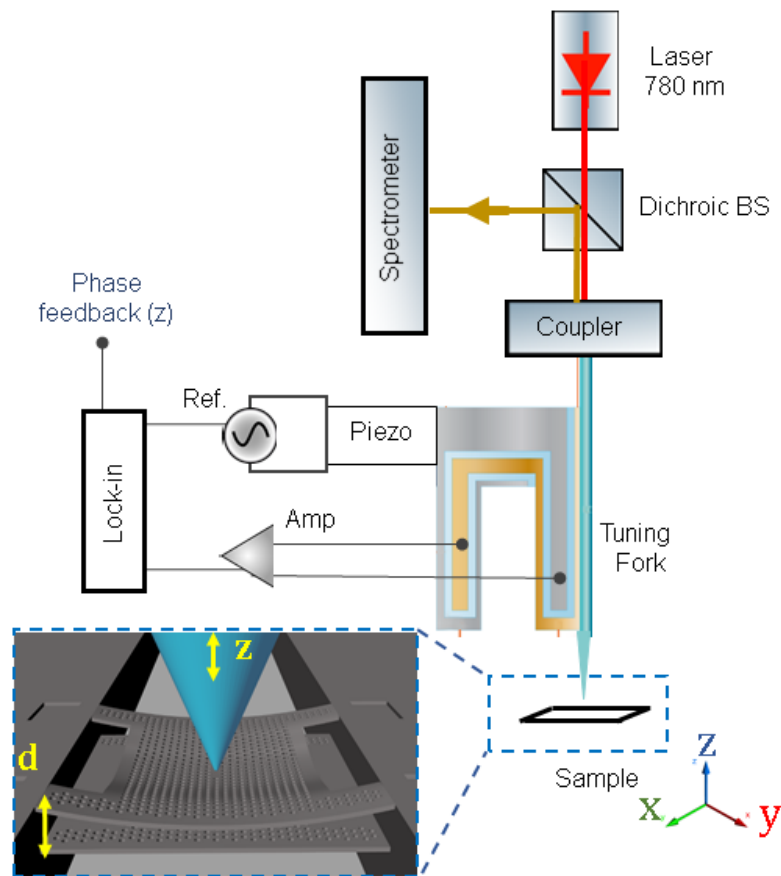


Figure 3.3: Scheme of the experimental setup. A dielectric tip locally excites the cavity and the fluorescence signal is analysed in a spectrometer. The fiber, attached to a tuning fork, oscillates laterally, while the tip-sample distance is maintained constant by the shear-force loop

0.32, holes radius $r = 113$ nm) is etched through both membranes (Fig.3.2a inset). A point-defect cavity is realized by removing three inline holes from the lattice (L_3). In the middle of the top slab a layer of high-density self-assembled InAs quantum dots is grown. The ground state emission of these internal sources is centered around 1305 nm at room temperature and the QD photoluminescence spans over more than 100 nm, including the excited states and the overall inhomogeneous broadening.

3.3.2 Experimental Setup

A commercial scanning near-field microscope (Twinnom, OMICRON) is operated in the illumination/collection geometry (fig.3.3). In the following experiments a dielectric tip, which is a glass tapered optical fiber obtained by chemical etching [412], is exploited both as a near-field probe to collect the photoluminescence spectrum and, simultaneously, to apply a controlled local nN-force. To this end, a 780 nm diode laser is coupled to an optical fiber that terminates in the near-field tip in order to excite the QD photoluminescence. Then, the emitted light is collected from the same fiber and separated from the excitation radiation by a dichroic beam splitter, finally dispersed

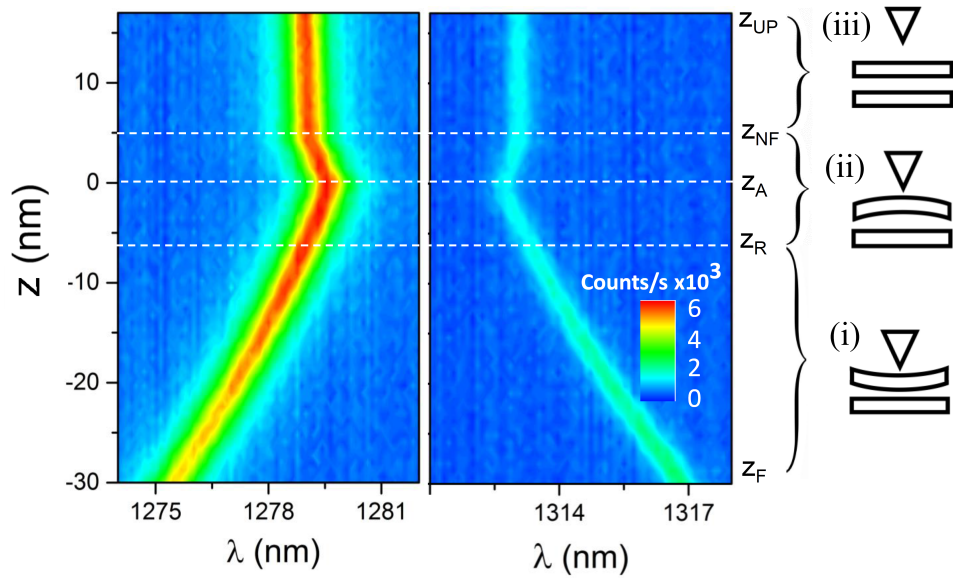


Figure 3.4: Color-encoded photo-luminescence spectra of the anti-symmetric (left panel) and symmetric (right panel) mode acquired while varying the z position of the tip from $z = z_F$ to above the sample ($z > z_{NF}$), where no significant external force is applied and the membranes are at the unperturbed distance. The tip vertical position is measured with 0.7 nm resolution, while the $z = 0$ origin is set at the minimum splitting

by a spectrometer and detected by a liquid nitrogen cooled InGaAs array. The control of the tip-surface separation is realized through the shear-force technique. The probe is attached to a bimorph piezo set to oscillate laterally with a constant amplitude of few Å and the oscillation phase shift, which occurs in presence of contact forces when the tip-sample distance is below 10 nm, is maintained constant by a piezoelectric feedback loop. The sample is mounted on a XYZ piezoelectric scan stage, which enables the control of the sample-tip position with nm (X-Y) and a sub-nm (Z) precision.

3.4 MEASURING THE CONTACT FORCE

Fig.3.4 shows the spectral evolution of the anti-symmetric (left panel) and symmetric (right panel) modes when the z -position of fiber apex is varied.

In this experiment, the tip is positioned above the cavity and then moved downwards until it reaches the position z_F , where the spring force of the upper membrane is large enough that the tip-membrane spacing reaches the value fixed by the phase setpoint of the feedback loop. Then, the tip is moved upwards, from the minimum $z_F = -30$ nm to the maximum $z_{UP} = 17$ nm with a constant speed of 7 nm/s (with the feedback loop turned off), while the spectra are continuously acquired at a frequency of 10 Hz. The origin of the z -axis is defined as the point where splitting between the coupled modes is minimum. From a comparison with Finite-Element Method simulations, these modes have been identified as the fundamental symmetric (Y_S^1

right panel) and anti-symmetric (Y_{AS}^1 , left panel) mode of the investigated photonic molecule, which exhibit the principal polarization perpendicular to the defect line. Based on the energy splitting of the coupled modes, we can identify three interaction regimes accordingly to the different vertical positions z of the tip: (i) $z < z_R$: tip pushing membrane; (ii) $z_R < z < z_{NF}$: tip pulling membrane; (iii) $z > z_{NF}$: no force.

From $z_{NF} = 5$ nm to $z_{UP} = 17$ nm (region (iii)), the splitting energy remains practically unperturbed ($\Omega_{NF} = 25.0$ meV). Therefore, the contact force exerted by the tip is negligible for z larger than z_{NF} and the value of Ω_{NF} corresponds to the splitting of the modes when the two membranes are parallel at their initial distance.

In region (i), which extends from $z_F = -30$ nm to $z_R = -7$ nm, the two modes shift along opposite directions while the splitting decreases. This feature corresponds to an upward displacement of the (top) membrane due to the release of the tip pressure. In this region, the value of the inter-membrane distance is $d(z) = \bar{d} - |z_R - z|$, where \bar{d} is the initial inter-membrane distance. Notably, from $z_R = -7$ nm to $z_A = 0$ (region (ii)), the splitting further decreases to $\Omega_A = 24.5$ meV, below the value of Ω_{NF} , indicating that the inter-membrane gap is larger compared to the case where no force is applied. This effect arises from an attractive force between the tip and the membrane, characterized by a very short range (few nm), possibly originated by the Van der Waals interaction between the tip and the membrane and/or by the surface tension due to the presence of a water meniscus on the surface of the wafer [50].

Finally, in region (ii) from $z_A = 0$ to $z_{NF} = 5$ nm, the splitting energy increases to Ω_{NF} , corresponding to a decrease of the inter-membrane gap to its equilibrium value, caused by the removal of the attractive force applied by the tip.

Noteworthy, the ability of discriminating the sign of the contact force at such small distances with high spatial resolution (see below), represents a key advantage of this system.

3.5 IMAGING

The local excitation and collection via the near-field probe can be additionally exploited to map the intensity of the mode. Fig. 3.5 shows the simulated intensity of the fundamental AS mode, above (20 nm) the top PhC membrane, and the experimental PL intensity map obtained by raster-scanning the area located at the center of the cavity defect. Both maps are characterized by an 'X' shape surrounded by two lobes, which is a distinctive feature of this mode. A qualitative agreement between the two maps is visible.

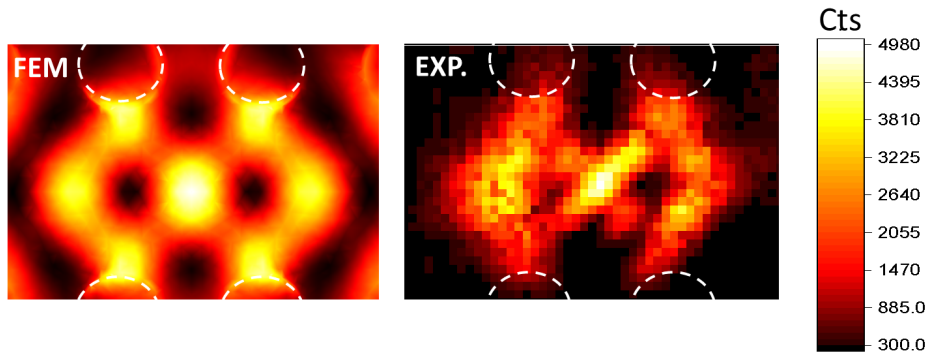


Figure 3.5: (Left) simulated $|E|^2$ and (right) experimental PL intensity map of the fundamental AS mode. The dashed circles represent the PhC holes. The experimental map is $3 \mu\text{m} \times 2 \mu\text{m}$ (60×40 pixels). Courtesy of D. Balestri and N. Granchi

3.6 TIP-INDUCED TUNING

In order to give a quantitative estimation of the forces and the physical variables that come into play, in what follows, we focus on the actuation regime ($z \leq 0$).

Fig.3.6a reports a record tuning acquired when the fiber tip is operated in the repulsive mode and exerts a compressive force on the device. An offset between the different spectra is introduced for clarity. During this experiment, differently from the one in Fig.3.4, the sample is moved in steps and its movement triggers the acquisition of the photo-luminescence spectrum. The total wavelength tuning of Y_S^1 for the z -range investigated in this experiment is 37.5 nm, which is more than three times larger than the record tuning achieved by using the electro-mechanical forces on similar devices [286]. Indeed a clear advantage of this technique compared to the electrostatic tuning [124, 331] rests with the absence of a pull-in limit ($1/3$ of the initial gap), which is exploited in the following to validate the theoretical predictions for a wide range of coupling values. Additional modes enter the experimental spectral window for $z = -70$ nm and correspond to high-order symmetric modes. A crossing with the Y_{AS}^1 is observed, denoting a negligible coupling between these modes.

A monotonic decrease in the quality factor (Q) of both Y_S^1 and Y_{AS}^1 is observed during the tuning experiment (Fig.3.6b, upper panel). This trend is consistent with the behavior predicted by three-dimensional FEM simulations (Fig.3.6b, bottom panel), assuming the nominal initial distance of $\bar{d} = 250$ nm and neglecting the presence of the tip. The increase in losses when reducing the slab distance is attributed to the complex interplay between interference effects [175] and the change in fraction of the k -vector components lying inside the light cone for the two modes [282]. Still the experimental values of Q are smaller than the theoretical ones. This discrepancy is attributed to fabrication deviations which introduce a degree of randomness in the position and radii of the pores, and lower the experimental Q .

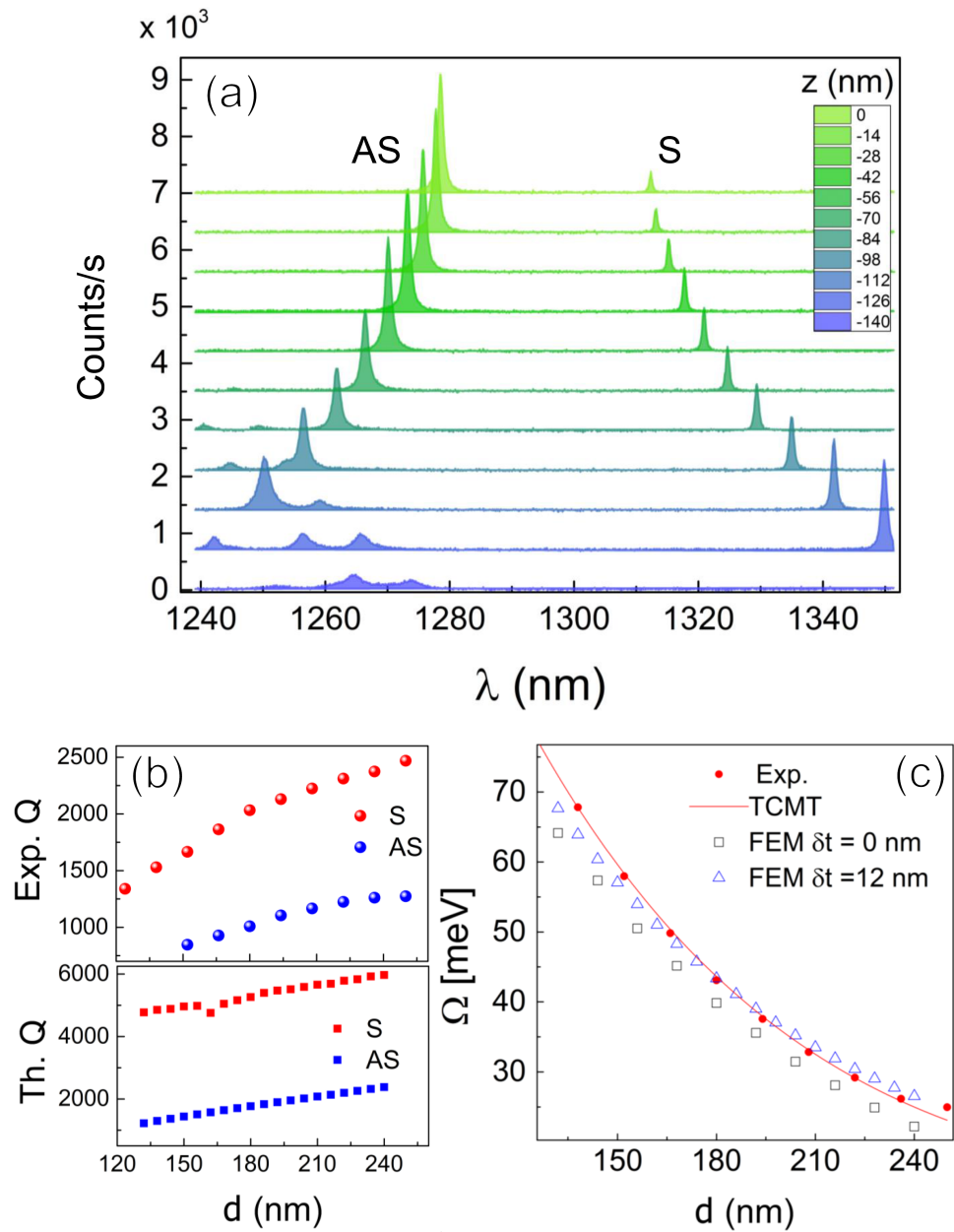


Figure 3.6: Actuation of the photonic crystal molecule due to the mechanical contact force induced by the tip. (a) The wavelength of the symmetric (anti-symmetric) fundamental mode decreases (increases) when the tip is moved upwards. Experimental (b, top panel) and simulated (b, bottom panel) quality factors as a function of the gap d . (c) Experimental (red dots) and analytical fit (solid line) of the splitting energy (Ω) of the photonic crystal molecule. The simulated splitting with zero (black squared) and 12 nm (blue triangles) thickness asymmetry (δt) is shown for comparison.

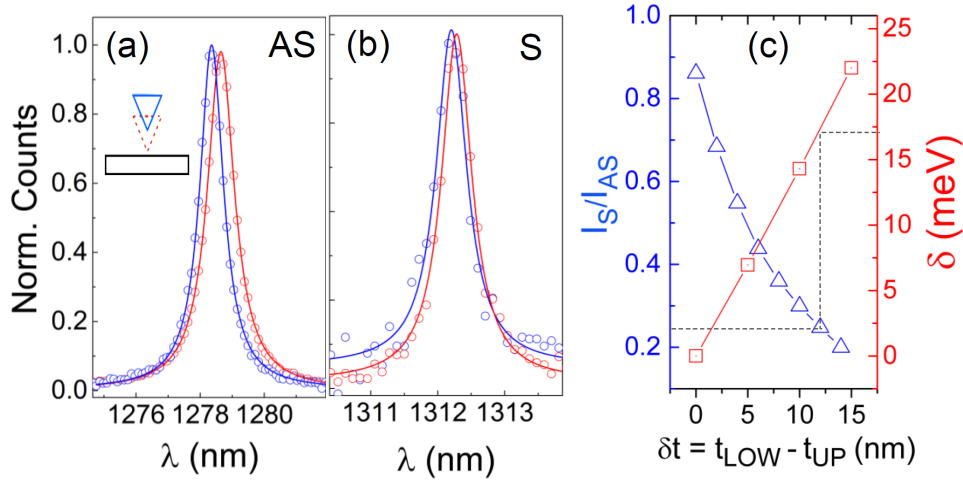


Figure 3.7: Red-shift induced by the dielectric perturbation on the AS (a) and S (b) mode when the tip is brought from $z > 100$ nm to contact. (c) Simulated ratio between the field squared of the S and AS mode at $z = 0$ (c, blue triangles) and detuning δ (c, red squares) as a function of the thickness difference between the lower and upper membrane ($t_{\text{LOW}} = 170$ nm)

Since we have direct access to the value of the inter-membrane distance, we can quantitatively compare the experimental splitting with the one predicted by FEM simulations. Fig.3.6c shows that the measured splitting energy (red circles) is significantly larger than the simulated values (black squares). This discrepancy can be related to an asymmetry in the membrane thickness (δt), arising from the imperfect selectivity of the etching processes, which can reduce the final thickness of the upper membrane by few tens of nanometers [282]. As a consequence, the original uncoupled modes are characterized by a non-negligible energy mismatch δ , which increases the actual splitting energy.

In order to validate this hypothesis, we examine other possible signatures of the thickness difference between the membranes in our spectral data. In particular, we can extrapolate δ from the different frequency perturbations induced by the presence of the dielectric tip in the near-field of the S and AS mode [173, 214]. Indeed, when the tip is brought from well above the cavity ($z = 112$ nm), where the tip perturbation can be considered negligible [72], to the contact z_{NF} both modes experience a red-shift, but with a magnitude proportional to their electric field intensity I_N ($N = S, AS$) at the tip position (i.e. on the upper membrane). Fig.3.7 shows that the tip-induced shift is larger for the AS mode (0.08 nm and 0.28 nm obtained from the lorentzian fit for the S and AS mode respectively). In addition, the tip introduces an additional loss channel, which results in a small decrease (13%) of the Q of the AS mode, while this reduction is below the fitting error for the S mode. By averaging over an area of 200×250 nm² (20 z -scans), centered around the first lobe of the in-plane mode distribution, we derive an experimental energy shift of $\delta E_S = (50 \pm 10)$ μeV and $\delta E_{AS} = (210 \pm 30)$ μeV . Here the error is calculated from the standard deviation of the shift among the differ-

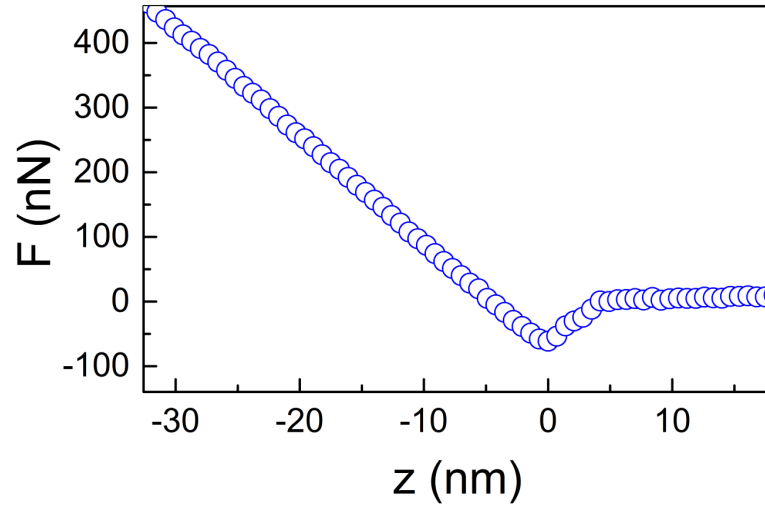


Figure 3.8: Force applied by the tip, derived assuming a spring constant $k = 16$ N/m. The positive (negative) values corresponds to a repulsive (attractive) regime

ent scans. The ratio of the mode intensity just above the top membrane can therefore be calculated as $\frac{I_S}{I_{AS}} = \frac{\delta E_S}{\delta E_{AS}} = 0.24 \pm 0.08$. The relative intensities of the S and AS modes on the top membrane sensitively depend on the membrane thickness asymmetry, since the S (AS) mode tends to localize in the thicker (thinner) membrane. Fig.3.7c reports the FEM simulated intensity ratio between the two modes and the calculated detuning as a function of the thickness difference between the lower and upper membrane ($t_{LOW} - t_{UP}$). From this data, we can estimate a thickness asymmetry of $\delta t \sim 12$ nm, which produces an energy detuning $\delta \sim 17$ meV. A further confirmation of this asymmetry can be found in the opposite behavior of the integrated intensity of the S and AS modes as a function of the inter-membrane distance (Fig.3.6a). Indeed, when d is reduced the collected PL intensity of Y_S^1 (Y_{AS}^1) significantly increases (decreases). This effect is not caused by the change in Q-factor through the Purcell-enhanced spontaneous emission, since the latter shows the same trend for the two modes. Rather, as mentioned above, the field tends to localize in the thicker membrane, when the energy difference between the uncoupled modes is significant with respect to the coupling g . As the QDs are positioned in the top membrane, this produces a stronger PL intensity in the AS mode at large membrane distance, as observed in Fig.3.6a. The difference in PL intensities is reduced for smaller distances as the coupling increases, leading to a more equal distribution of the modes over the two membrane. By introducing the thickness asymmetry $\delta t = 12$ nm derived from the near-field shifts of Fig.3.7, a better overlap of the experimental and simulated tuning curve is obtained (Fig. 3.6c, triangles).

3.7 FORCE RECONSTRUCTION

Intriguingly, from this data we can extrapolate the value of the coupling constant as a function of the gap expected from the TCMT. This can be

expressed analytically [284] as $J = J_0 e^{-d/d_0}$, where J_0 represents the spatial integral of the in-plane profiles weighted on the dielectric constant of the material, and d_0 provides the spatial decay constant of the evanescent field. From the least square fit to the experimental data (continuous line in Fig.3.6c), we obtain $J_0 = (172 \pm 5)$ meV and $d_0 = (83 \pm 2)$ nm. The values of δ , J_0 and d_0 allow calculating the intermediate distance d for each tip position z , through the relation $\Omega = \sqrt{\delta^2 + 4(g_0 e^{-d/d_0})^2}$. This, together with the calculated spring constant, is used to derive the value of the force applied by the tip in the different regimes described in Fig.3.4. The resulting plot (Fig.3.8b) in the region around $z = 0$ is similar to the typical force-distance curve obtained in a SNOM as measured by standard atomic force microscopy (AFM) [227]. The high sensitivity of the system enables to identify the adhesion part of the interaction ($F < 0$), and the maximum value of the attractive force is obtained as $F \sim -60$ nN at $z = 0$. The force resolution of the present measurement is limited by the signal to noise ratio of the SNOM PL. Employing a laser scattering configuration [55] will allow to investigate the tip-sample mechanical interaction with a resolution possibly in the sub-pN range.

3.8 TOPOGRAPHY RECONSTRUCTION

Finally, we compare the topography derived by the bimorph piezo feedback signal (Fig.3.9a) and the topography reconstructed optically from the wavelength shift of the fundamental AS mode at the feedback loop set-point (z_F) acquired at several (x,y) positions (Fig.3.9b). Here the scan consists of 40×20 pixels ($2 \mu\text{m} \times 1 \mu\text{m}$) centered around the cavity defect. The two topography maps show an excellent agreement, confirming our interpretation of the experiment. Large variations of the tip and membrane vertical positions are observed along the scan, showing that the actuation range depends on the in-plane position of the tip. In particular, if the tip is located above a pore (white areas) the actuation is less effective as compared to the configuration where the tip is positioned on the semiconductor region. This results in *inverted* topography maps. The cause of this effect can be ascribed to the presence of lateral forces arising inside the pore volume, which increases the damping in the lateral oscillations of the tip compared to the bulk regions. Since the feedback loop controls the vertical position of the tip by maintaining its oscillation phase constant while scanning along the lateral direction, the effective force applied by the tip is larger in the bulk area resulting in a larger vertical displacement of the membrane and in a dip in the topography. This feature illustrates the peculiar local character of this actuation experiment. Fig.3.9 shows a line scan extracted from the 2D-topographies. The gray dashed curve corresponds to the best fit obtained through the convolution of a step function with a gaussian point function, characterized by a full-width at half maximum FWHM= 70 nm. The latter represents an estimate of the spatial resolution of this tuning scheme.

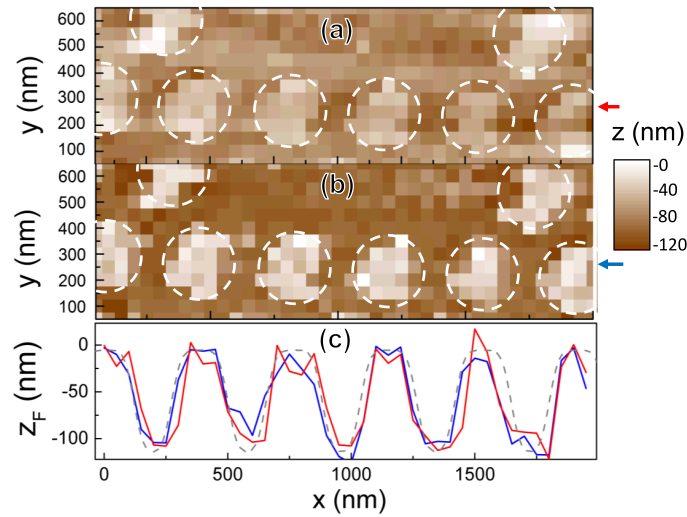


Figure 3.9: Topography map read-out from the feedback loop (a) and optical topography reconstructed from the wavelength shift of the fundamental AS mode (b). (c) Two line scans taken at the arrow positions (red for the topography obtained from the optical shift, blue for topography derived from the feedback loop) compared with the nominal topography (dashed line) convoluted with a Gaussian point spread function with FWHM=70 nm. The radius of the tip is comparable with radius of the pores

3.9 CONCLUSIONS

In conclusion, we studied the coupling of a near-field probe and a nanomechanical resonator composed of a re-configurable photonic crystal molecule. We demonstrated that this interaction can be used to implement a local reversible actuation scheme, achieving record energy tuning on PhC cavity modes. The accurate modelling of the optical properties of the device, combined with the near-field read-out of the field, evidences the role of the detuning in the emitted luminescence signal. Additionally, the splitting of the coupled mode provides a real-time monitor parameter on the dynamics of the contact forces. The device investigated in this work can represent a fundamental building block for integrated sensing applications, and open the way to integrated nanoscale force microscopy.

4

FULLY-TUNEABLE CAVITY-EMITTER

In this chapter we discuss the full energy control over a semiconductor cavity-emitter system, consisting of single Stark-tunable quantum dots embedded in mechanically reconfigurable photonic crystal membranes. A reversible wavelength tuning of the emitter over 7.5 nm as well as a 8.5 nm mode shift are realized on the same device. Harnessing these two electrical tuning mechanisms, a single exciton transition is brought on resonance with the cavity mode at two wavelengths, demonstrating a ten-fold enhancement of its spontaneous emission. The results presented in this chapter have been partially published in *Appl. Phys. Lett.* Vol. 107, 14 141109 (2015) [333].

4.1 INTRODUCTION

Coupling to photonic crystal cavities (PhCCs) is notably attractive due to their engineerable electromagnetic environment which provides record quality factors (Q) in a wavelength-scale volume [6]. One of the leading experimental challenges in this context resides in the spectral matching of multiple cavity-emitter systems, which requires the deterministic control over the energy of both emitters and cavities. To this end, post-processing tuning strategies are imperative because of the QD inhomogeneous broadening and the intrinsic fabrication imperfections which spread the actual cavity resonance over several nanometers. Although a number of techniques have been demonstrated to tune the dot or the cavity energy (see paragraph 1.6), the crucial goal of integrating a simultaneous energy control of an emitter and its cavity has not been attained yet.

4.2 DESCRIPTION OF THE DEVICE

4.2.1 Electromechanical Actuation

In the previous chapter we have shown that the modulation of the intermembrane distance of a pair of photonic crystal slabs can be exploited to induce a large wavelength shift on the coupled modes. For on-chip applications and in particular for QPICs, it is convenient to control the membrane position via electromechanical actuation. In micro-electromechanical systems (MEMS), an electromechanical force is generated by the accumulation of charges at the surfaces of a capacitor. In the case of the double-membrane system, a capacitor could be in principle fabricated by inserting two metal stripes in-between the two membranes. However, the deposition of conformal metal layers is technologically challenging and introduces unwanted losses [281]. A more convenient solution for MEMS in III-V materials

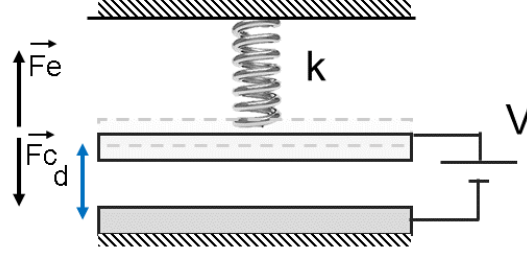


Figure 4.1: Simple capacitive model describing the interaction of the electrostatic force F_c and the elastic force F_e acting on a suspended membrane

employs capacitive forces originated in a p-i-n diode, which is operated below its built-in voltage. In fact, in this condition, the depletion regions of the diode effectively behave as the electrodes of a capacitor. In the case of a double membrane system, a p-i-n diode can be fabricated across the two membranes by doping the bottom (top) part of the top (bottom) membrane. A simple one-dimensional description that illustrates the electrostatic actuation is the so-called *lumped model* (fig. 4.1). For the sake of simplicity, we assume that only one membrane is free to move in the double-membrane system. In the experiments presented here, this is a valid assumption, since the bottom membrane is clamped to the wafer from all sides. Besides, we assume that the top membrane has a mass m , an area A and is connected to an elastic spring having stiffness k . Given d_0 , the inter-membrane distance at equilibrium, and V , the voltage difference between the membranes, we can write the equation of motion for the movable membrane, neglecting the effect of air-damping and gravity, and the built-in charge in the p-i-n capacitor

$$m\ddot{d} = F(d) = -k(d - d_0) - \frac{\epsilon_0 AV^2}{2d^2}. \quad (4.1)$$

Here, the force acting on the system is given by the sum of the elastic force and the attractive electrostatic force. At equilibrium, i.e. when $\ddot{d} = 0$, we have

$$d^3 - d^2 d_0 = -\frac{\epsilon_0 AV^2}{2k} \quad (4.2)$$

This equation provides the tuning curve $d(V)$ once numerically solved. It is important to notice that both the right- and left-hand sides (lhs) of this equation are always negative. However, the lhs possesses a minimum at $d = 2/3d_0$, below which eq. 4.2 might not allow any solutions for a high value of V . This is referred to as *pull-in distance*, and is associated with the instability caused by electrostatic force overcoming the restoring elastic force at small distances. When d is reduced below this value, the two membranes stick together. Nevertheless, if the device is operated above such threshold, the tuning is reversible. Before this study, the electromechanical tuning has been used to allign a cavity mode with a dot by Midolo *et al.* [286]. Here we integrate a second p-i-n in the device to separately control the QD-emission.

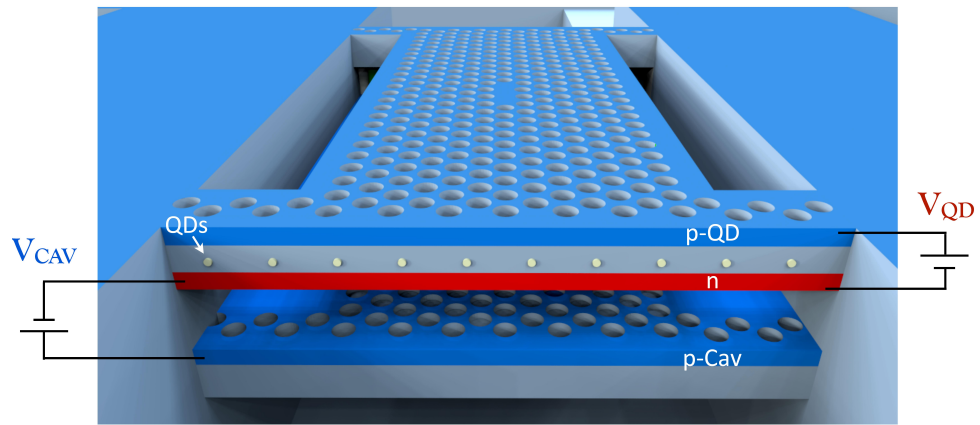


Figure 4.2: (a) Sketch of the device illustrating the photonic crystal cavity patterned through two vertically-coupled membranes. A top p-i-n diode realized across the top slab governs the QD energy via the quantum-confined Stark effect, while a second n-i-p diode controls the cavity resonance through capacitive forces

4.2.2 Dual-tuning device

Our device is sketched in Figure 4.2 and incorporates two parallel photonic crystal membranes which can be vertically displaced by capacitive forces [284]. To this end, a n-i-p diode realized across the membranes provides the electrostatic actuation when it is operated in reverse bias. The resulting nano-mechanical displacement modifies the effective index of the coupled modes of the double-membrane waveguide, leading to a blue(red)-shift of the vertically anti-symmetric (symmetric) modes [310]. The QD region is grown in the middle of the top slab to remove any interaction with the electrostatic field [286]. A second p-i-n diode, sharing the n-layer with the cavity-tuning diode, is fabricated on the top membrane to apply a vertical electric field across the QD layer. In such a way, the emitter's energy is tuned by the quantum-confined Stark effect [125].

4.3 FABRICATION DETAILS

The sample is grown by molecular beam epitaxy and includes two GaAs slabs of equal thickness (170 nm) isolated by a 240-nm-thick sacrificial $\text{Al}_{0.7}\text{Ga}_{0.3}\text{As}$ spacer.

A 1.5 μm -thick $\text{Al}_{0.7}\text{Ga}_{0.3}\text{As}$ layer separates the double membranes from the undoped (001) GaAs substrate. Low-density InAs QDs are grown in the middle of the upper membrane in the Stranski-Krastanov mode at very low growth rate [11]. Additionally, two 17-nm-thick $\text{Al}_{0.3}\text{Ga}_{0.7}\text{As}$ barriers are introduced 8 nm above and below the QDs in order to suppress the tunnelling probability of electron-hole pairs out of the dot and consequently increase the exciton tuning range [29]. The upper 50-nm thick region of both

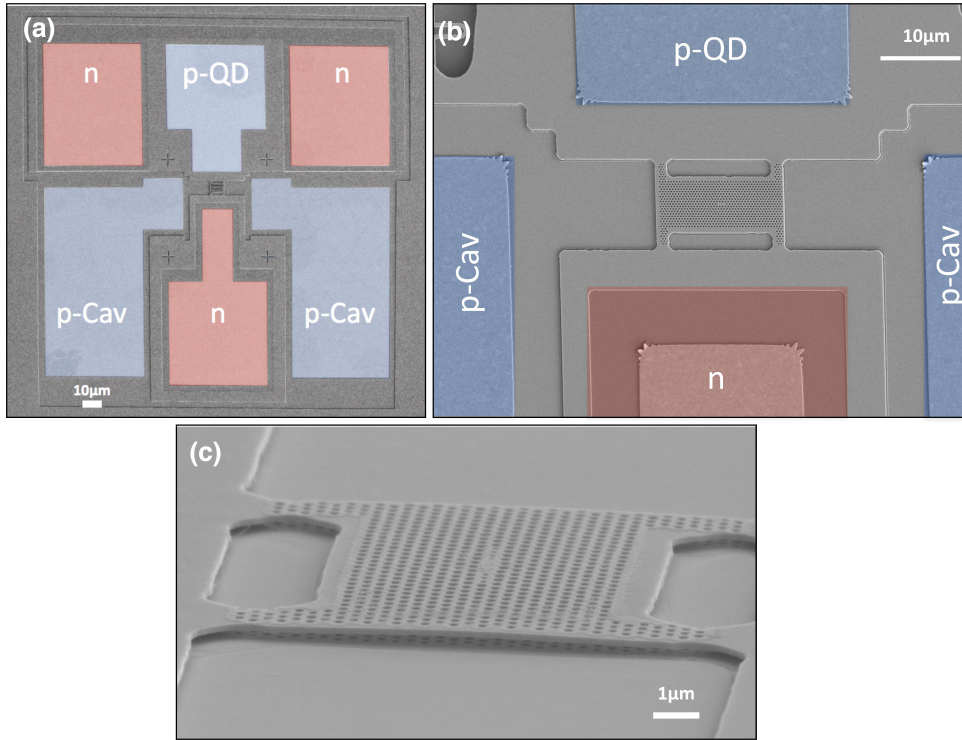


Figure 4.3: Scanning electron micrographs (SEM) of the device showing the contact mesa structure of the double diodes (a) and a zoom (b) into a typical PhCC realized on a four-arms 12- μm long bridge. (c) Tilted SEM image of the device used in the experiments. The cavity is realized by removing three holes from the lattice and modifying the radii and relative positions of the six in-line and four vertical holes surrounding the cavity-defect

membranes is p-doped whereas the bottom 50-nm-thick part of the top slab is n-doped ($p_{\text{QD}} = 1.5 \cdot 10^{18}$, $n = p_{\text{cav}} = 2 \cdot 10^{18} \text{ cm}^{-3}$). The fabrication of the device follows the recipe reported in chapter 2. A PhCC created by three missing holes (lattice constant $a=395 \text{ nm}$, radius $r = 0.31a$) is defined by lithography and a etching steps. The radii and positions of the ten holes surrounding the defect region are modified to provide a theoretical quality factor $Q = 34000$, as calculated by 3D finite-element modelling. Figure 4.3 shows the scanning electron micrographs of the full device.

4.4 EXPERIMENTAL SETUP

Low-temperature ($T=9 \text{ K}$) micro-photoluminescence (μPL see fig.4.4) experiments were performed in a continuous-flow helium cryostat equipped with two electrical probes sharing a common ground and approaching the sample from opposite directions. QDs were excited with an above-bandgap diode laser ($\lambda = 785 \text{ nm}$) and their emission was collected through the same objective (numerical aperture $\text{NA} = 0.4$) and analysed by a fiber-coupled spectrometer, after being spectrally isolated from the pump laser via a dichroic beam-splitter (DBS, fig.4.4, configuration (a)). This setup has

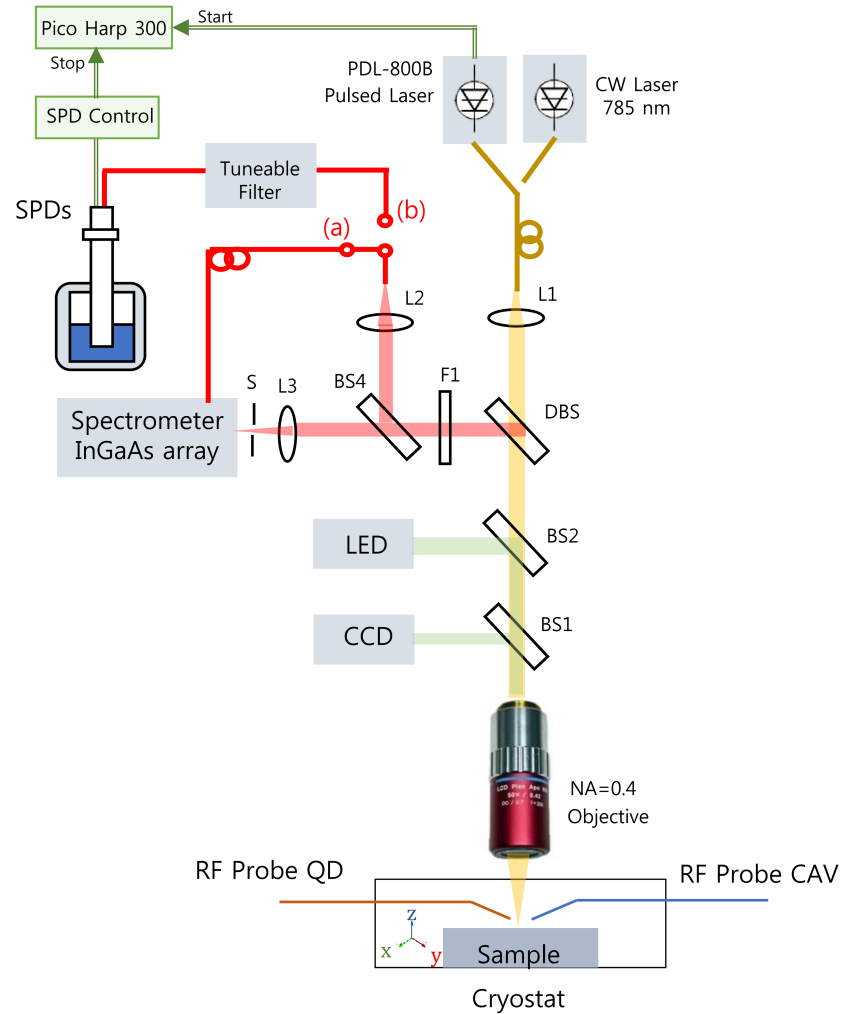


Figure 4.4: Low-Temperature μ PL setup employed for voltage-regulated spectroscopy. BS1, BS2 beam splitters; M flip mirror, DBS dichroic beam splitter. L1, L2 lenses for fiber coupling, L3 lens free-space coupling to the spectrometer; F1 additional long-pass filter with cut-off wavelength at 1050 nm; SPDs nanowire Superconducting Single-Photon Detectors. S Slit. (a) and (b), configurations employed for coupling to the spectrometer or for time-resolved experiments, respectively

been realized by dr. F.M. Pagliano and further details can be found in his thesis [320].

4.5 CAVITY TUNING

Figure 4.5a shows the color-coded μ PL measurements acquired in the strong pumping regime ($50 \mu W$ measured before the objective) in order to probe the cavity modes while sweeping the voltage across the membranes. The spectrum is dominated by four eigenmodes of the PhC cavity. By increasing the reverse bias across the membranes (V_{CAV}) the two pairs of modes

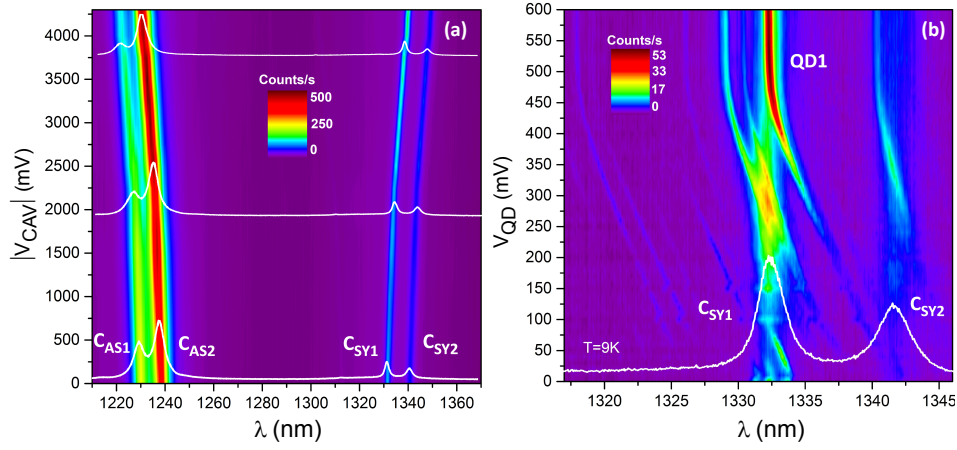


Figure 4.5: Colour-scale μ -PL spectra of cavity modes (a) and QD tuning (b) acquired on the same device at 9 K with a laser power of 50 μW and 90 nW, respectively. (a) By increasing the reverse voltage across the membranes the symmetric (antisymmetric) modes red(blue)-shift up to 8.5 nm at 4.5 V. (b) Blue-shifting of single exciton lines when the Stark-voltage is increased. The high-power cavity profile is shown at bottom (white) for reference

shift in wavelengths along opposite directions. This effect represents the unambiguous signature of the mechanical origin of the mode-tuning and rules out any possible thermal origin. Thermal effects are indeed expected to be negligible during the electromechanical actuation, due to the small $\approx\text{nA}$ current originated in the cavity-diode, when operated under reverse bias.

Here, a maximum and reproducible cavity shift of 8.5 nm is achieved at -4.5 V, without reaching the irreversible pull-in condition that brings the structure to collapse. In addition, from the tuning direction we classify the high-energy modes as anti-symmetric (C_{AS1} , C_{AS2}) and two modes situated around 1330 nm as symmetric (C_{SY1} , C_{SY2}). From a comparison with the spectrum calculated using a finite-element method, we attributed the anti-symmetric modes to lowest-order modes mainly polarized perpendicular to the cavity axis, while the symmetric lines have been identified as higher order-modes with dominant polarization along the cavity axis. The quality factor of these modes is around 1000, while quality factors up to 5000 have been measured on other devices on the same chip, showing that Q factors adequate for the enhancement of spontaneous emission are possible in the double-membrane structure.

4.6 QD TUNING

In the following tuning experiments we focus on the symmetric mode C_{SY1} , which is located around the ground state of the QDs. When this mode is shifted in frequency, a modulation of its quality factor is observed ranging from 620 to 900. The oscillation in the cavity losses can be related to the change in the amount of wave-vector components of the cavity field lying inside the light cone when the two slabs are brought closer[282].

After reducing the laser power to the nW-level (80 nW), just below the saturation level of QDs, single QD lines appear in the spectrum. Figure 4.5b presents the QD tuning experiments carried out on the same device. Here, the color-coded image is built up from several μ -PL spectra acquired while the Stark diode is operated in forward bias. When the voltage applied to the QD-diode is increased (in forward bias) from 0 to 0.6 V, the exciton transitions shift to the blue achieving a maximum tuning range of 7.5 nm. A clear enhancement of the spontaneous emission of single dot lines is observed when their energy crosses the cavity mode position. Remarkably, cavity modes are still visible in the configuration where there is no QD matching their energy due to the pumping from multi-excitons transitions [58, 462] and phonon-assisted feeding mechanisms [162]. At negative bias the QD emission is suppressed suggesting that the built-in junction field ($F_{bi} = -200$ KV/cm) is sufficient to sweep the carriers away from the active region. In addition, we observe the inhibition of the tuning close to the turn-on voltage of the diode (0.6 V) due to the increasing current. Consistently with previous reports on the quantum-confined Stark effect in InAs QDs [125], the blue shifting of single dot lines indicates that the electron wave function is located below the hole wave function with respect to the growth axis, giving rise to an inverted hole-electron alignment. From the fitting of the tuning curves, we estimated for the excitonic line QD₁ a permanent dipole moment $p = -0.15 \pm 0.04e$ nm and a polarizability $\beta = -4.9 \pm 0.1 \cdot 10^{-3}e$ nm kV⁻¹ cm, comparable with previous works [321]. The tuning rate is particularly high ($14.4 \frac{meV}{V}$) due to the thin intrinsic region (70 nm) of the Stark-diode.

4.7 QD-CAVITY TUNING

The simultaneous control over the full emitter-cavity system, is reported in Figure 4.6. Here, a quantum dot line (QD₁) is first spectrally positioned at $\lambda_1 = 1332.2$ nm by applying a Stark voltage of $V_{QD} = 590$ mV. In this situation, resonance with the cavity mode is obtained at $V_{CAV} = 0$ V (Figure 4.6a). By changing the Stark field ($V_{QD} = 320$ mV) the QD is red-shifted at a second wavelength $\lambda_2 = 1334.5$ nm (Figure 4.6b). The cavity can be brought again into resonance at a voltage $V_{CAV} = -1.4$ V (Figure 4.6b). As shown in Figure 4.6c the electrical control on the exciton line does not significantly affect the cavity mode position (Figure 4.6c), despite the presence of an electro-optic effect in GaAs (the calculated electro-optic wavelength shift over the voltage range of Figure 4.6c is below 0.01 nm). However, when the cavity-diode is tuned from 0 to 1.6 V a crosstalk is observed on the QD-diode which results in a small blue-shift of the excitonic line QD₁ by 0.4 nm ($V_{QD} = 320$ mV) as reported in Figure 4.6d, whose origin is not understood. Additionally for $|V_{CAV}| \cong 2.0$ V, the mode tuning rate decreases and the QD lines start red-shifting. We attribute this behaviour to the increasing current flowing across the diodes. For a reverse cavity bias voltage $|V_{CAV}| > 2.0$ V the current in the cavity diode was observed to strongly increase in the presence of a forward QD bias, which is indicative of the expected transistor behaviour in this p-i-n-i-p junction. The corresponding temperature increase produces

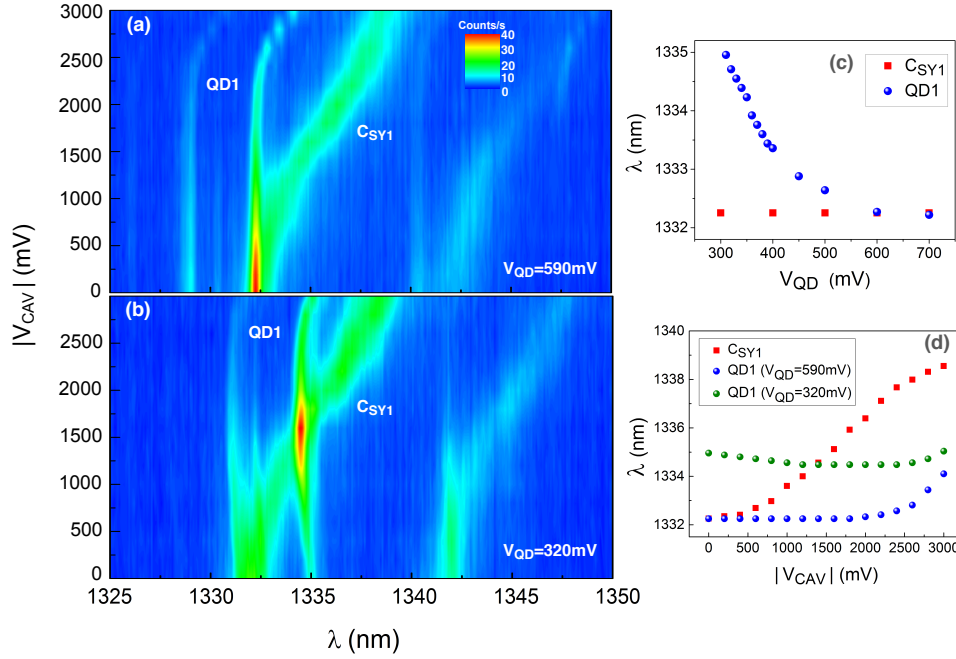


Figure 4.6: Electromechanical tuning of the cavity mode performed when two different voltages $V_{QD} = 590$ mV (a) and $V_{QD} = 320$ mV (b) are applied to the QD diode. Resonant coupling between the mode C_{SY1} and QD1 is achieved at $\lambda_1 = 1332.2$ nm ($V_{QD} = 590$ mV, $V_{CAV} = 0$ mV) and $\lambda_2 = 1334.5$ nm ($V_{QD} = 320$ mV, $V_{CAV} = -1400$ mV). (c) and (d) show the tuning curves for QD1 (red squares) and C_{SY1} (blue dots) as a function of V_{QD} and V_{CAV} , respectively

the red-shift of the QD lines observed in Figure 4.6d. Notwithstanding, for a range of energies spanning over 2.6 meV the wavelength-shift of QD lines is one order of magnitude less than the cavity tuning. This greatly facilitates the tuning of the entire quantum node from λ_1 to λ_2 .

4.8 TIME-RESOLVED EXPERIMENTS

4.8.1 Time-resolved setup

To further explore the QD-cavity coupling we investigated the temporal dynamics of the excitonic line QD1 in the weak pumping regime [298]. As shown in fig.4.4 (configuration (b)), time-resolved experiments are performed employing a 80 MHz pulsed diode laser ($\lambda = 757$ nm, average power $P = 30$ nW, nominal pulse width = 70 ps) as excitation source, sending the PL emission through a tunable fiber-coupled band-pass filter (Kioshin-Kogaku bandwidth = 0.5 nm) and making use of a superconducting single photon detector (SSPD, Scontel) and a correlation card (PicoHarp 300) to measure the photon arrival time.

This method is based on the Time-Correlated Single-Photon Counting scheme (TCSPC, [451]). The trigger provided by the laser controller is used as the start signal to record the time arrival of the detector pulses. The events

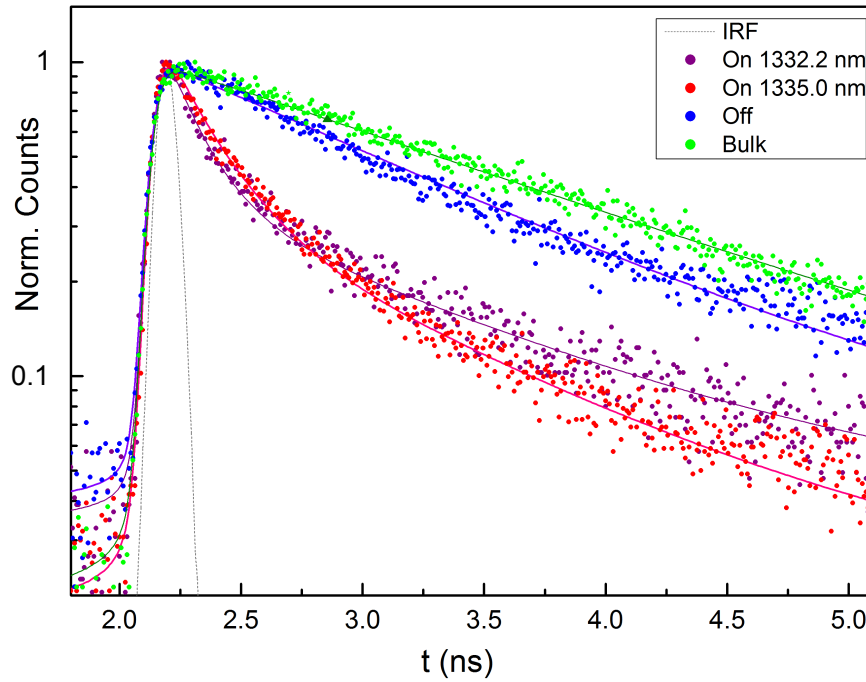


Figure 4.7: Time-resolved normalized photoluminescence dynamics of the excitonic transition QD1 on resonance with the cavity mode at two distinct wavelengths, $\lambda_1 = 1332.2\text{nm}$ (purple dots) and $\lambda'_2 = 1335\text{nm}$ (red dots). The off-resonance decay histogram of the dot positioned at λ_1 , while the cavity wavelength is set at λ'_2 , is shown in blue. The QD ensemble evolution is reported in green as reference. Single and double exponential fits are shown with a continuous line and include the convolution with the IRF of the system (grey dashed line)

registered by iterating this excitation-detection procedure over several cycles are collected in a histogram, which represents the average waveform of the fluorescence photons. The resolution of the technique is mainly determined by the detector and the temporal duration of the laser pulse. Additional reflections at the fiber couplings or in free-space can produce unwanted dot-excitation and deteriorate the temporal resolution. The latter can be quantified by sending the attenuated laser beam through the setup, and measuring its time-resolved signal, known as instrument response function (IRF). In our experiment, the full width at half maximum (FWHM) of the IRF gives a temporal resolution of 90 ps, as shown in fig.4.7 (dashed line). In the following experiments we set the current of the SSPD to $\approx 18\mu\text{A}$, which provides dark count rates below 20 Hz and a detector efficiency $\approx 25\%$.

4.8.2 Decay dynamics

The decay curves of the excitonic transition QD1 are reported in Figure 4.7. When the quantum dot line is spectrally aligned with the cavity resonance at $\lambda_1 = 1332.2\text{ nm}$ (purple dots, $V_{\text{QD}} = 590\text{ mV}$, $V_{\text{CAV}} = 0\text{ mV}$) and at $\lambda'_2 = 1335.0\text{ nm}$ (red dots, $V_{\text{QD}} = 300\text{ mV}$, $V_{\text{CAV}} = -1600\text{ mV}$), a decrease of

its radiative lifetime is visible compared to the case in which the dot is set at λ_1 , off-resonance from the cavity-mode at λ'_2 (blue dots).

From a bi-exponential fit convoluted with the IRE, we derive the on-resonance time constants of the fast decay components related to cavity-enhanced single-QD emission $\tau_{\text{ON}}(\lambda_1) = 140$ ps, $\tau_{\text{ON}}(\lambda'_2) = 190$ ps.

The slow decay component $\tau_{\text{ON,slow}}(\lambda_1) = 960$ ps is attributed to the residual contribution of the background-pumped cavity mode emission, which has a measured time constant $\tau_{\text{Mode}} = 830$ ps. The experimental error bar is estimated as ≈ 20 ps from the standard deviation of values fitted from different measurements. In the off-resonance configuration the dot is characterized by a single exponential dynamics with time constant $\tau_{\text{OFF}} = 1.02 \pm 0.02$ ns. The QD ensemble data set is shown for comparison (green dots) and has a single decay constant $\tau_{\text{Bulk}} = 1.55 \pm 0.02$ ns, similar to previous reports from similar QDs[20].

In general, the actual decay rate Γ of a QD exciton in a PhC environment in the presence of an electric field can be written as [229] $\Gamma = \Gamma_{\text{CAV}} + \Gamma_{\text{Leaky}} + \Gamma_{\text{nr}}(F)$, where Γ_{CAV} represents the Purcell-enhanced emission in the cavity mode, Γ_{Leaky} encodes the decay rate into the leaky modes of the PhC, while Γ_{nr} accounts for the non-radiative processes including tunneling of the electron out of the dot and depends on the applied electric field. However, within the low-field values used in this experiment ($F(\lambda_1) = -135$ kV/cm and $F(\lambda'_2) = -167$ kV/cm), both Γ_{nr} and the possible modification of the oscillator strength are small[29]. Therefore, neglecting the decay channels not related to the presence of the cavity ($\Gamma_{\text{Leaky}} + \Gamma_{\text{nr}}$), estimated in the $(5 - 6 \text{ ns})^{-1}$ range from literature data of similar QD heterostructure[160], we attribute the shortening of the on-resonance decay rate to the Purcell effect [135, 350], quantifying a Purcell enhancement of

$$F_{\text{P}}(\lambda'_2) = \frac{\tau_{\text{ON}}(\lambda'_2)}{\tau_{\text{Bulk}}} = 8 \pm 1 \quad (4.3)$$

$$F_{\text{P}}(\lambda_1) = \frac{\tau_{\text{ON}}(\lambda_1)}{\tau_{\text{Bulk}}} = 11 \pm 2 \quad (4.4)$$

for the two wavelengths. The difference in the spontaneous emission enhancement at different wavelengths can be attributed to the modification of the quality factor when the cavity is tuned. Indeed, considering negligible the variation of the effective mode volume of the cavity (below 2% from simulations) the ratio between $Q(\lambda_1) = 820 \pm 30$ and $Q(\lambda'_2) = 650 \pm 30$ is comparable to the ratio of the on-resonance decay times $\frac{\tau_{\text{ON}}(\lambda_1)}{\tau_{\text{ON}}(\lambda'_2)} = 1.35 \pm 0.34$. We also note that the observed decrease in decay time when tuning the QD-cavity system from λ'_2 to λ_1 cannot be explained by an increase in the tunnelling rate, since the electric field applied for λ_1 is lower than the one for λ'_2 . The suppression of the spontaneous emission off-resonance ($\tau_{\text{OFF}}/\tau_{\text{ON}}(\lambda_1) = 7 \pm 1$) is hampered by the limited tuning range in this experiment, as confirmed by the expected ratio $\frac{\Gamma(\lambda_{\text{CAV}}=\lambda_{\text{QD}}=\lambda_1)}{\Gamma(\lambda_{\text{CAV}}=\lambda'_2, \lambda_{\text{QD}}=\lambda_1)} = 10 \pm 3$, estimated from the spectral mismatch $\lambda_1 - \lambda'_2 = 2.8$ nm, using the expression in Ref. [107] and taking into account the emission into leaky modes and non-radiative recombination processes.

4.9 CONCLUSIONS

In conclusion, we have experimentally demonstrated a solid-state cavity-emitter system where both the energy of the emitter and the cavity resonance are independently and electrically controlled. By combining the Stark tuning of quantum dots with the nano-electromechanical actuation of the cavity the deterministic, reversible and real-time spectral alignment of the entire quantum node has been demonstrated. We studied the regime where the spontaneous emission of single excitons can be modulated by one order of magnitude at several energies. These results open the way to bringing several cavity-enhanced emitters mutually into resonance and therefore represent a key step towards scalable quantum photonic circuits featuring multiple sources of indistinguishable single photons.

5

TUNEABLE SINGLE-PHOTON LED

In this chapter, we report two major steps towards the development of electrically-injected on-chip single-photon sources: 1) we demonstrate electroluminescence from single QDs coupled to a PhC cavity and the antibunched nature of the emitted light and 2) we integrate electromechanical tunability within this PhC LED structure. By combining the nano-electromechanical actuation of a double-layer PhC membrane with the electrical excitation of QDs, a single exciton is brought on resonance with a tuneable cavity mode, and its emission is enhanced.

5.1 INTRODUCTION

So far, optical pumping has been adopted as the only excitation method to study cavity quantum electrodynamics (cQED) phenomena originating from the coupling of quantum emitters to photonic crystal structures. However, in the context of QPIC, this poses severe practical limitations in realizing photonic circuits comprising multiple sources. Firstly, the stability of the external pump laser and of its free-space optical path limits the maximum integration time employed in correlation experiments. Secondly, the excitation area that can be addressed optically is limited by the field of view of the objective (usually in the order of tens of square microns), which restrains the number of sources that can be independently excited. Lastly and most importantly, the scattering of the pump photons into integrated single-photon detectors [403] produces stray counts that affect the visibility of experiments with sources and detectors integrated on the same chip [89, 360, 361].

Electrical injection represents a handy solution to overcome these drawbacks. By sandwiching the QD-layer in a p-i-n junction, single-photon emitting diodes (SPEDs) have been successfully demonstrated [484] and adopted in a number of free-space quantum protocols which include two-photon interference [326, 327], entanglement [70, 374, 488], teleportation [308, 410], quantum key distribution [100, 156] and quantum relays [443]. Electrical injection methods have been implemented also within vertical cavities, such as planar Bragg micro-cavities [27] and nanopillars [104] in order to improve the out-of-plane single-photon efficiency. However, these structures are not suited for funneling single-photons to on-chip waveguides, contrary to PhCs modes that can be engineered to efficiently couple to an in-plane integrated circuitry. Despite several demonstrations of electrical injection in PhC cavities [103, 121, 325, 391], single-photon emission from single excitons in electroluminescence has not been demonstrated so far [44].

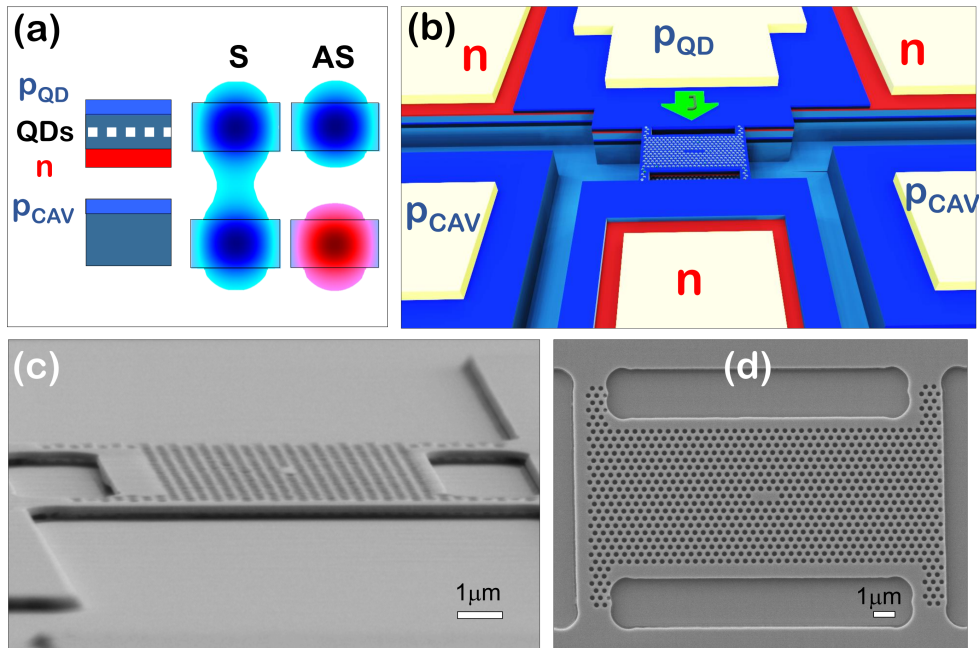


Figure 5.1: Sketch and SEM images of fabricated devices (a) Sketch of the symmetric (S) and anti-symmetric (AS) modes originating by the vertical coupling between the two slabs along with the vertical layers of the device. (b) Sketch of the in-plane contact layout of the device, showing the two diodes surrounding the cavity-bridge region for current injection and cavity actuation. (c) Tilted scanning electron micrograph of the device where the top free-standing membrane is visible and is connected to a supporting frame via four micro-arms. (d) Top-view of the PhC micro-bridge embodying an L3 cavity at its center

5.2 DEVICE DESCRIPTION

The device discussed here has been already described in Chapter 4 and is based on the double-membrane system (Fig.5.1a). However, differently from the previous experiments, here the top QD-diode is employed to inject current across the QD-layer. An electrostatic force, originated by the voltage applied between the membranes, controls the physical separation between the slabs, inducing a reversible change in the mode coupling, which results in an opposite wavelength shift of the S and AS mode. The sample is grown by molecular beam epitaxy and includes two 170 nm-thick GaAs slabs separated by a 220 nm-thick $\text{Al}_{0.7}\text{Ga}_{0.3}\text{As}$ sacrificial layer. At the center of the top slab a layer of self-assembled InAs quantum dots is grown. Their ground state emission is centered at 1225 nm at low temperature (9 K). Differently from the sample used in chapter 4, here we avoid using AlGaAs barriers. In the following experiments the employed in-plane PhC design is composed of a triangular lattice of air holes, where a point-defect cavity is realized rearranging the positions of four holes around a central point (H_0) or removing three holes (L3) (Fig.5.1d). The lattice constant is designed to match the

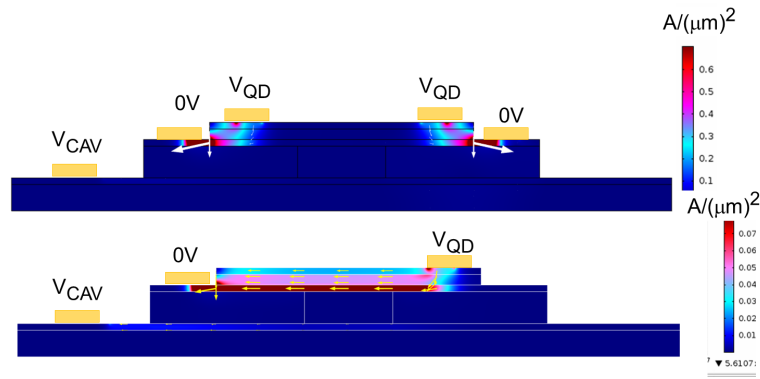


Figure 5.2: Simulation of the current density for two contact geometries. (Top) symmetric contacts (bottom) asymmetric contacts. We used the nominal parameters of the structure, setting $V_{\text{QD}} = 2 \text{ V}$ and $V_{\text{CAV}} = 0 \text{ V}$. The arrows are proportional to the current density

fundamental PhC mode with the QD ground state emission. The fabrication process was carried out by Z. Zobenica in the Nanolab@TU/e cleanroom.

CURRENT INJECTION A key challenge for the electrical pumping of PhC cavities is the injection of both electrons and holes in the cavity region, while keeping the optical loss low. This is achieved in this work by placing the p and n contacts of the QD diode on the opposite sites of the cavity which forces the current to flow laterally along the micro-bridge. Fig.5.1b shows a sketch of the device. The two distinct series of contacts for carrier injection and cavity tuning are realized using the configuration $[\text{n}, \text{p}_{\text{QD}}, \text{n}]$ and $[\text{p}_{\text{CAV}}, \text{n}, \text{p}_{\text{CAV}}]$. The importance of the contact geometry can be further illustrated by making use of 2D-FEM simulations (Comsol, Semiconductor module). Figure 5.2 shows the current distributions obtained in two different contact configurations. When the p and n contacts of the QD-diode are close to each other (top part), and the QD-diode is operated in forward bias, the current prefers to flow vertically. Vice versa, when the metal contacts are located at the opposite sides with respect to the central region (bottom part fig.5.2) the current passes through the central bridge.

5.3 TUNABLE LIGHT EMITTING DIODE

Low-temperature ($T=9 \text{ K}$) micro-electroluminescence (μEL) measurements are carried out in a continuous-flow He cryostat fitted with two electrical probes set at a common ground, employing the same setup described in 4.8. The emitted μEL is collected through an objective (numerical aperture $\text{NA}=0.4$) and analysed in a fiber-coupled spectrometer.

In a first set of experiments we study the possibility to electrically pump the photonic crystal modes. Fig.5.3 (a) shows the images collected by an infrared camera, while sweeping the QD-voltage on a device featuring a modified L_3 cavity. Two bright spots at the bottom of the bridge can be associated to the recombination close to the p-contact (current-crowding). The spot at the centre of the bridge - indicated by the arrows - is instead

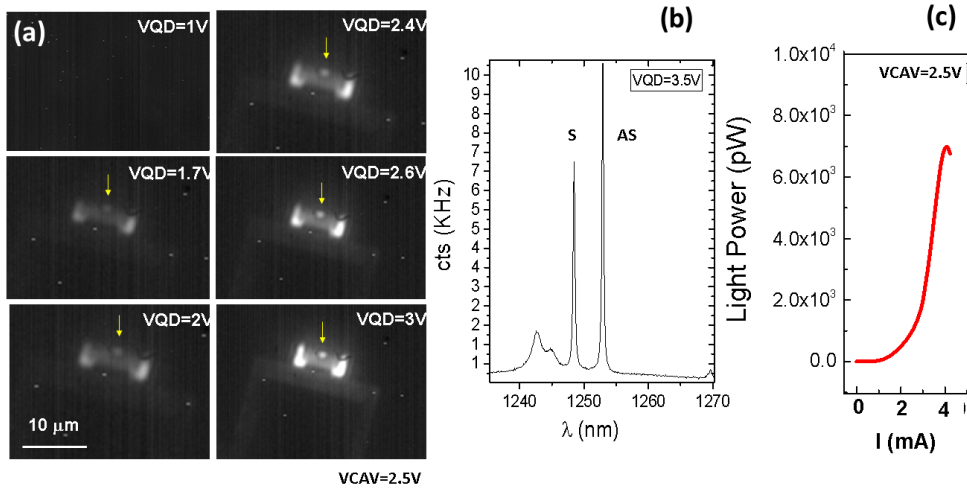


Figure 5.3: (a) Images from IR camera recorded as a function of V_{QD} . The yellow arrows indicate the position of the cavity (b) Electro-luminescence spectrum of the cavity modes of this device when operated at $V_{QD}=3.5$ V. The S and AS modes corresponds to two modes having different in-plane symmetries. (c) Light-current characteristic at $V_{CAV} = 2.5$ V when V_{QD} is varied from 0 V to 4 V

originated by the emission in the cavity modes, as shown in the μ EL spectra reported in Fig.5.3(b). In these experiments, the radiation from the gallium arsenide and the wetting layer is filtered (cut-off wavelength = 1100 nm) in order to collect only the PhC modes. Furthermore, Fig.5.3(c) shows the light-current characteristics of this device, measured with a power-meter after the objective and the filter. The high current necessary to excite the PhC modes (\sim mA) is attributed to current-crowding, which effectively reduces the current reaching the cavity. A kink in this curve provides an additional evidence of this effect [122].

In a second set of experiments we investigated the tunability of these PhC LEDs. To this aim, the QD ensemble in a second device (featuring an unmodified L3 cavity) is electrically excited with a current of (\sim mA), while the cavity wavelength is varied by changing the vertical position of the top membrane by an electrostatic voltage (V_{CAV}). Figure 5.4 shows the μ EL signal of the cavity emission collected when the QD-diode is operated in forward bias ($V_{QD} = 3.5$ V) and the voltage across the cavity-diode is swept from -1.0 V to 2.3 V. The spectra are characterized by several peaks that can be associated with the resonances of an L3 cavity by comparison with the local density of states calculated using 3D Finite-Element-Method (FEM) simulations. We can discriminate the vertical symmetry of the modes from the sign of the frequency tuning, since the S (AS) mode moves towards higher (lower) wavelengths if the cavity actuation voltage is decreased. Indeed, the built-in charge on the actuation junction is increased when the applied voltage is decreased from positive to negative, corresponding to an increased attractive force and decreased membrane spacing. In this tuning experiment, all the modes manifest an AS character except the mode labelled as Y1s, identified as fundamental S mode, which shifts from 1242.3 to 1257.7 nm. The

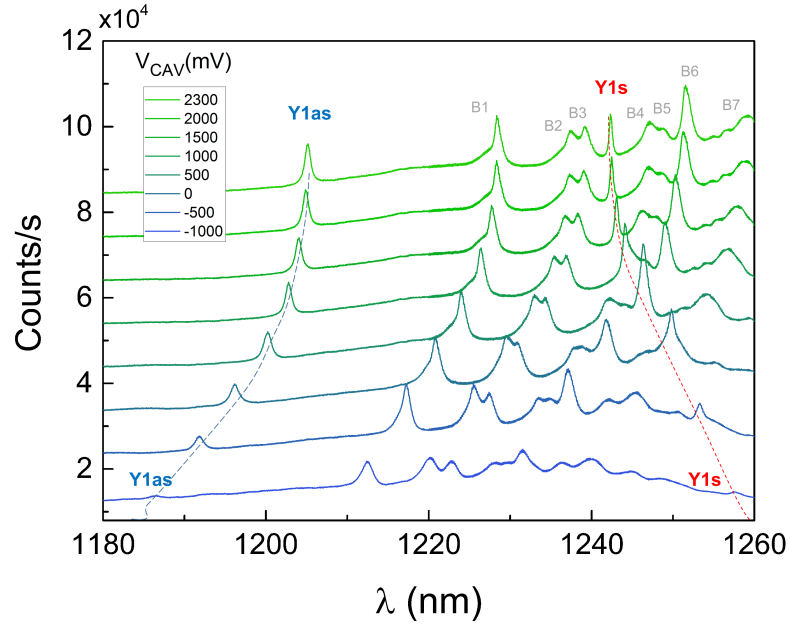


Figure 5.4: Tunable nano-LED. Electro-luminescence spectra of the photonic crystal device acquired at several cavity voltages (V_{CAV}) with a voltage applied to the QD diode $V_{\text{QD}} = 3.5$ V. The fundamental S (AS) mode shifts towards the blue (red) when the cavity voltage is increased. Several AS band edge modes (B1, ... B7) also appear in the spectrum. A maximum electromechanical tuning of more than 15.4 nm is here demonstrated. A constant offset (10kHz) between several measurements is introduced for clarity. The red and blue dashed lines are guides for the eye

mode at the lowest wavelength is identified as fundamental antisymmetric mode, Y_{1as} . Its wavelength can be reversibly varied over almost 20 nm from $\lambda_{-1V} = 1186.5$ nm to $\lambda_{2.3V} = 1205.1$ nm. Due to the high initial wavelength splitting of these two modes (37.2 nm), Y_{1s} falls in the antisymmetric dielectric band where a series of antisymmetric band-edge modes is ascertained (B_1, \dots, B_7). Notice that the intensity of the μEL signal decreases for negative values of V_{CAV} due to the presence of a crosstalk between the two diodes, which effectively reduces the measured injection current from 2.3 mA to 1.7 mA at $V_{\text{CAV}} = -1V$.

The high current necessary to excite the device induces heating that results in a redshift of both the antisymmetric and symmetric modes. As a consequence, the total tuning range of the AS mode is slightly larger compared to the S mode, and from their semi-difference we can extrapolate a thermal tuning range of 1.6 nm. Further optimization of the bridge geometry along with the use of lateral doping profiles [103] may bring this device into the lasing regime. Combining FEM simulations and the experimental S-AS splitting corrected with the thermal shift, we estimate a reduction of the inter-membrane distance from 200 nm to 145 nm in the actuation range investigated in these experiments.

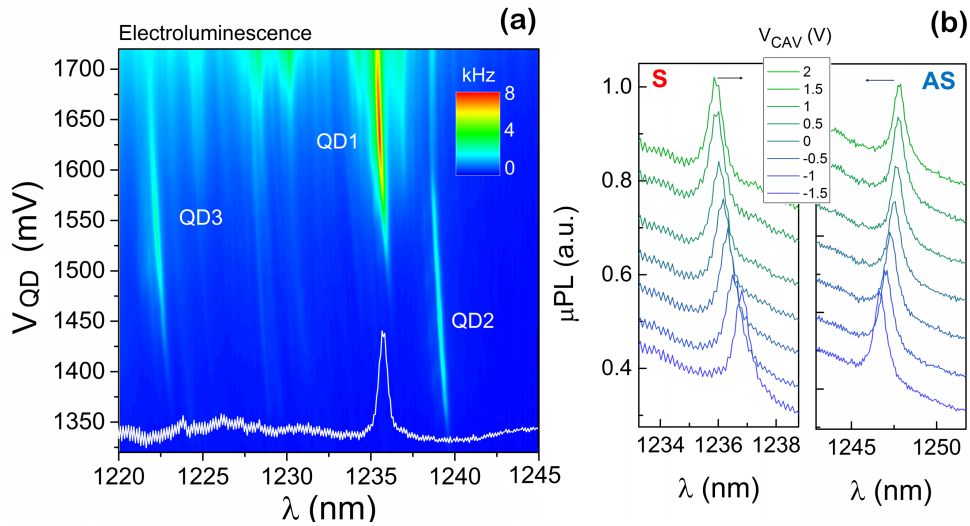


Figure 5.5: Single-exciton electroluminescence (a) Color-coded micro-electroluminescence spectra collected while varying the voltage across the QD (V_{QD}). The bottom white line represents the μ PL spectrum of the cavity mode (b) μ PL spectra of the resonant modes when the cavity is actuated

5.4 SINGLE-EXCITON ELECTROLUMINESCENCE

In order to improve the vertical out-coupling efficiency, which is crucial for single-photon experiments, in the following we employed a device featuring a modified H_0 cavity, whose far-field pattern better matches the NA of the objective. When the injection current is set into the μ A range by operating the QD-diode just above its threshold ($V_{th}=1.2V$), single dots lines emerge in the spectrum. Figure 5.5(a) shows color-coded μ EL spectra acquired varying the voltage across the QD-diode, while setting $V_{CAV} = 2.2V$. The variation in the applied QD-voltage introduces a blue-shift of the excitonic lines, attributed to the quantum-confined Stark Effect. This effect appears also in forward bias, since the increase of the QD-voltage corresponds to a decrease in the modulus of the vertical field acting on the emitters. For the cavity actuation voltage chosen for this experiment, the excitonic line QD1 comes in resonance with the cavity mode (identified from a μ PL spectrum (white line)) at a QD bias $V_{QD}=1630$ mV. A ten-fold enhancement of its electroluminescence signal is observed in this situation, compared to the case when it is detuned by 0.65 nm. Besides the single exciton line, emission within the cavity linewidth is also visible in the off-resonant μ EL spectra, which is attributed to phonon-mediated feeding mechanisms[162]. Other excitonic lines (QD2, QD3) experience a similar Stark-shift, but do not cross the cavity resonance. We tentatively attribute these lines to other excitons, in the same or different dot, spectrally decoupled from the cavity mode. The cavity mode employed here, originating from the second-order mode of the H_0 design, shows a quality factor $Q = 2270$ and is characterized by a symmetric character as shown in the μ PL cavity tuning spectra reported in Fig.5.5(b) left panel.

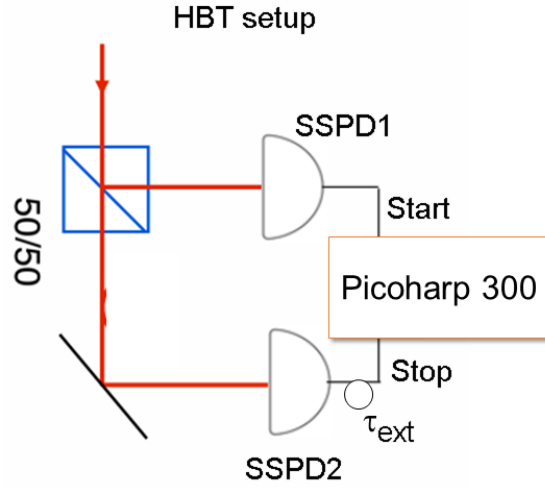


Figure 5.6: HBT setup comprising two single-photon detectors (SSPD1, SSPD2), a 50/50 beam splitter and a correlation card

5.5 ANTI-BUNCHING

Lastly, we investigate the non-classical nature of photons emitted by the cavity-enhanced QD1 line at $V_{\text{QD}}=1630$ mV by performing auto-correlation experiments.

HANBURY BROWN–TWISS EXPERIMENT An important technique to prove the single-photon emission and to appraise its quality is based on the measurement of the second order correlation function, defined as

$$g^{(2)}(t, \tau) = \frac{\langle \hat{a}^\dagger(t) \hat{a}^\dagger(t + \tau) \hat{a}(t + \tau) \hat{a}(t) \rangle}{\langle \hat{a}^\dagger(t) \hat{a}(t) \rangle^2} \quad (5.1)$$

where \hat{a}^\dagger and \hat{a} are the creation and annihilation operators, evaluated at the times t and $t + \tau$ [255], $\langle \rangle$ refers to the expectation value, and τ is the delay introduced by two consecutive measurements. The dependence on t drops for stationary fields. The value of this function at zero time delay is particularly interesting, since it can be interpreted as the probability to detect two photons at the same time and, therefore, gives access to the photon statistics of the light. Specifically, it can be proved [255] that classical systems are always characterized by $g^{(2)}(0) \geq 1$. For example, photons emitted by a thermal source, such as classical LEDs or thermal radiation, show $g^{(2)}(0) = 2$, associated with the so-called super-poissonian statistics. On the other side, lasers have $g^{(2)}(0) = 1$, due to their Poissonian statistics. For a Fock state $g^{(2)}(0) = 1 - 1/n$, where n is the photon number. Although a pure single photon source is characterized by $g^{(2)}(0) = 0$, the practical threshold to affirm single-photon emission is 0.5.

Experimentally, the value of $g^{(2)}(\tau)$ can be measured by splitting the investigated light beam into two paths having equal intensity, ending in two single-photon detectors (fig. 5.6). The normalized coincidences reconstructed by varying the internal electronic delay (τ) between the detection events, corresponds to $g^{(2)}(\tau)$. Similarly to the time-resolved experiment,

one of the two detection path is employed as a start in a time-correlated measurement¹. This relatively simple configuration is known as Hanbury Brown–Twiss (HBT) setup.

In our experiment, we employed a fiber-based Hanbury Brown and Twiss interferometer composed of a 50/50 beam splitter and two superconducting single-photon detectors (Efficiency $\sim 45\%$, Dark Counts $\sim 30\text{Hz}$) interfaced to a correlation card (PicoHarp 300). Additionally, a fiber-coupled band-pass tunable filter (FWHM=0.5 nm) is used to isolate the QD1 single line emission among the others (Fig. 5.7b).

ANTI-BUNCHING MEASUREMENT Figure 5.7a shows the normalized auto-correlation histogram built from the raw coincidences of the two detectors as a function of time delay between the detection events (τ). A clear dip, well below 0.5, is observed in the coincidences at zero-time delay, which is the clear signature of anti-bunching in the emission from a single quantum emitter. The raw value at zero-time delay is $g_{\text{raw}}^{(2)}(0) = 0.11$. By fitting the anti-bunching curve with the function $g^{(2)}(\tau) = 1 - Ae^{\frac{|\tau|}{\tau_t}}$ (red curve) we can extract the zero-delay second order coherence function $g^{(2)}(0) = 1 - A = 0.13 \pm 0.09$ and the decay time associated with this transition $\tau_t = (420 \pm 20)\text{ps}$, assuming that the QD is in the low-excitation regime [355] (the error bars are derived from the standard deviations of the fit). The non-zero value of $g^{(2)}(0)$ is attributed to the residual background from the cavity mode emission, which contributes by 16% to the total μEL signal integrated in the filter range. The low detector jitter (~ 50 ps) provides enough resolution to temporally resolve the dip without need for deconvolution with the instrument response function.

The fact that the time constant associated to the antibunching dip is shorter than the QD lifetime in the bulk (see discussion below) is indicative of spontaneous emission enhancement in the cavity mode. While the assumption of low excitation cannot be proved in this particular device, as the injection rate and the QD-cavity detuning cannot be controlled separately, the strong increase in count rate as the QD line crosses the mode 5.5a provides an additional indication of the cavity-induced enhancement of the emission rate. In general, the decay dynamics of an emitter coupled to a cavity in the presence of a static electric field can be decomposed in several decay channels $\tau^{-1} = \tau_{\text{phC}}^{-1} + \tau_{\text{leaky}}^{-1} + \tau_{\text{tun}}^{-1}$, where τ_{phC}^{-1} is the resonant decay into the mode, τ_{leaky}^{-1} represents the decay channel in the leaky modes and is negligible ($\tau_{\text{leaky}} = 3 - 6$ ns [160]), while τ_{tun}^{-1} is associated with the tunneling rate out of the QD, which strongly depends on the applied electric field. In order to measure τ_{tun}^{-1} we performed μPL time-resolved measurements by exciting the dot ensemble in a bulk region with a 750 nm-pulsed laser (instrument response function = 90 ps) while varying the voltage applied to the dots V_{QD} .

Figure 5.7c shows the fast decay component of the dot emission as a function of V_{QD} . It is evident that for $V_{\text{QD}} < 1.2$ V the decay time decreases when the field (V_{QD}) is increased (decreased). This represents a clear evi-

¹ Experimentally, it is convenient to introduce a known electronic delay (τ_{ext}) in the start path in order to measure also negative delays

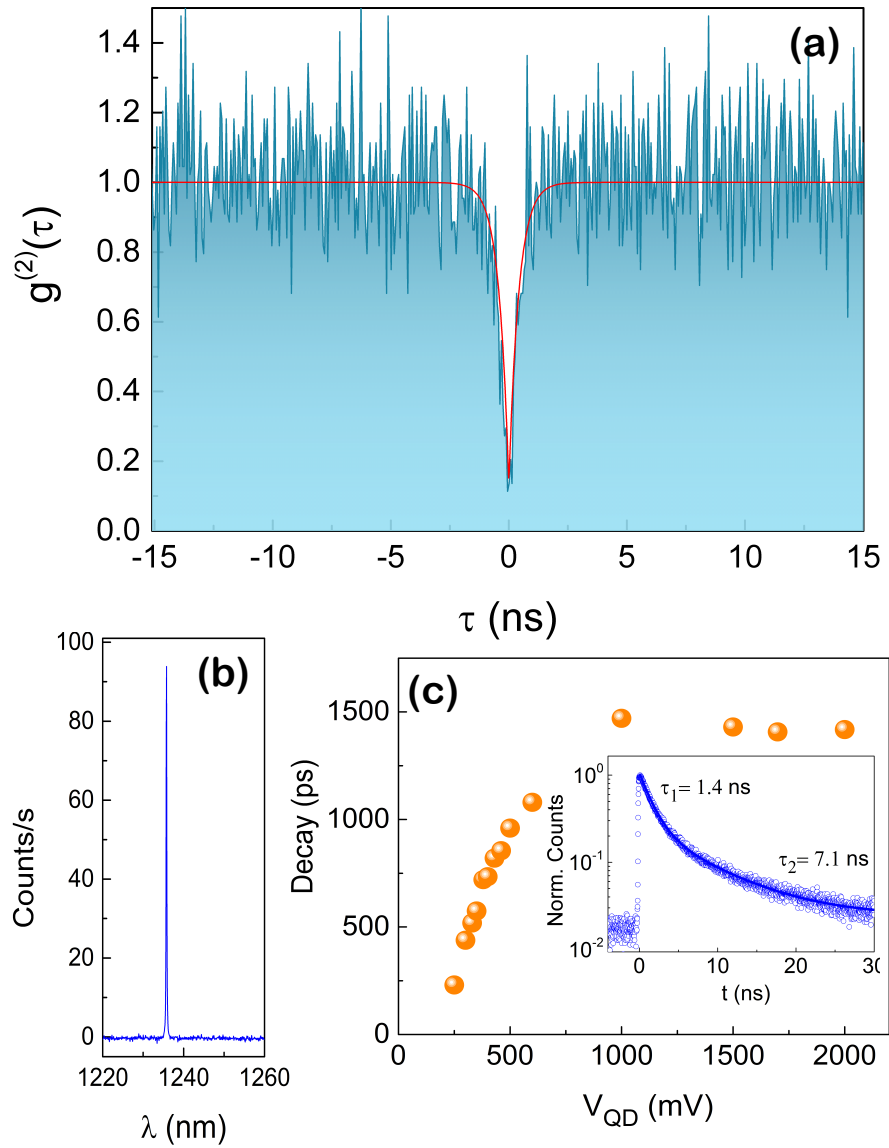


Figure 5.7: Anti-bunching (a) Auto-correlation histogram of the dot QD1 at $V_{\text{QD}}=1630$ mV (total SSPD count rates = 20 KHz), fulfilling the resonance condition with the cavity mode. (b) Bright single line emission after filtering. (c) Decay constants extracted from time-resolved (TR) μPL experiments of the QD ensemble as a function of the voltage applied to the dot layer. The inset show the TR μPL decay for $V_{\text{QD}}=1.5$ V

dence that in this voltage range the decay is dominated by a non-radiative process associated with the tunnelling mechanism. Instead, when the QD-diode is operated at $V_{\text{QD}} > 1.2\text{V}$, the decay time does not depend on the applied voltage. This value corresponds to the radiative time at zero field $\tau_{\text{bulk}} = 1.45\text{ ns}$ [160, 333]. A slower decay component is also visible in the time-resolved data (5.7c inset) and is attributed to the presence of a dark exciton repopulating the bright transition. This second decay constant shows a similar dependence on the applied voltage.

These experiments prove that τ_{tun}^{-1} is negligible for the injection experiments shown in Figure 5.5a and, consequently, that the decay dynamics is dominated by radiative emission in these conditions. The further optimization of the contact resistance along with the suppression of parasitic capacitance will enable the operation of current device in the pulsed regime, allowing the direct measurement of the lifetime and the operation as on-demand single-photon source.

5.6 CONCLUSIONS

In summary, we reported the non-classical light emission from electrically-injected quantum dots in a photonic crystal cavity. The full electrical control of the energy position of cavities and quantum dots, needed to build scalable Purcell-enhanced sources, has been achieved by the combination of electrostatic actuation and Stark tuning. The results presented here can be easily extended to more complex photonic crystal environments, such as slow-light waveguides or chiral structures [253]. While the tuning range of QD lines in this configuration is limited due to the coupling between tuning voltage and injection current in the QD junction, it could be extended by implementing additional strain tuning structures [416]. Importantly, the integration with linear components such as ridge waveguides and phase modulators can pave the way to electrically-triggered QPICs.

6

ANTI-STICTION COATING

In this chapter, we present a method to avoid the stiction failure in nano-electro-opto-mechanical systems based on double-membranes two dimensional photonic crystals. We show that if an alumina coating is applied to the devices described in the previous chapters, these can be reversibly operated from the pull-in back to their release status. This enables to electrically switch the wavelength of a mode over ≈ 50 nm with a potential modulation frequency above 2 MHz. The reliability of the switching mechanism is tested for more than 0.5 million cycles, with no degradation observed in the mechanical and optical properties. These results pave the way to reproducible nano-mechanical tuning experiments of c-QED nodes, fault-tolerant against actuation failures.

6.1 INTRODUCTION

In the previous chapter we have developed an architecture based on a double-membrane photonic crystal cavity to enhance the emission of Stark-tunable or electrically-driven exciton lines. The possibility to electro-mechanically move of one PhC resonator with respect to the other is at the core of these systems.

However, despite their potential, the reliability and performance of these devices is often compromised by the combination of the pull-in instability [489] and surface forces, which can lead to a permanent stiction between two movable mechanical elements. The pull-in instability represents a common problem in MEMS technology. This occurs when the distance between two movable parts is reduced below $2/3$ of its original value upon the action of a constant voltage. Over this threshold, the electrostatic force overcomes the restoring elastic force of the system, resulting in an abrupt transition that brings the movable elements into contact. The latter can adhere permanently due to short-range interactions that include van der Waals and capillary forces. For these reasons, pull-in and stiction failure has represented one of the major drawbacks in the use of MEMS and NEMS for real-life applications. Several solutions to this problem have been proposed for micro-actuators that include the use of self-assembled monolayers [263] and deposition of dielectric layers [85, 163], but they have not been explored so far in the context of NOEMS. Importantly, due to the very short distance (100 – 200 nm) between the moving parts of this class of devices, the application of anti-stiction layers can be very challenging, and may additionally produce a degradation of their mechanical and optical properties.

In this work, we present a method to avoid the permanent adhesion of two active photonic crystal nano-membranes. This method is based on the conformal deposition of a thin layer of alumina via atomic layer deposition

(ALD), which prevents the direct contact between the doped regions of the membranes composing the NOEMS. We present the effect of this dielectric layer on the optical and mechanical properties of this tunable PhC cavity when it is operated statically and dynamically. Besides allowing the reliable recovering from pull-in, this enables the use of the device as a switch between two widely different optical/mechanical states.

6.2 COATING

The device under study has been widely described in chapter 4 and 5. Here we employ membrane thicknesses of $t=170$ nm and intermembrane gaps of $d_0 = 200$ nm. The samples are characterized by a single p-i-n junction for cavity actuation. In addition, a layer of high-density quantum dots is grown in the middle of the top membrane, and is employed as an internal source to excite the photonic modes of the structure. The cavity design is a standard L3 cavity, i.e. three consecutive holes are removed from a hexagonal hole lattice (lattice constant $a = 385$ nm, radii=115 nm). The fabrication of the devices presented in this chapter has been carried out by M. Cotrufo, following the recipe described in chapter 2.

The system can be described by the coupled-mode theory framework. In particular, the field distribution can be approximately factorized in two independent functions: an in-plane component that depends on the actual photonic crystal layout, and a vertical field distribution associated with the effective refractive index (n_{eff}) of the structure. Due to the small distance between the membranes, the single-membrane PhC modes split in a symmetric (s) and anti-symmetric (as) vertical super-modes having higher and lower effective refractive indexes, respectively. The membrane movement modulates the evanescent coupling between the two slabs and, consequently, the effective refractive index of the super-modes and the PhC resonances (Fig. 6.1 (c)). The mode wavelengths therefore represent a unique fingerprint of the mechanical status of the NOEMS, and can be exploited to derive the properties of the NOEMS during the static and dynamic actuation experiments.

In the following experiments, a 15-nm aluminum oxide (Al_2O_3) layer has been deposited in a standard oxygen-based ALD reactor employing trimethylaluminum (TMA) as a precursor [92]. Alumina is expected to avoid short-cuts between the doped layers of the device and has been used before as anti-stiction layer in polysilicon MEMS [163]. The deposition has been carried out in collaboration with V. Zardetto (PMP, TU/e) and A. Mameli (PMP, TU/e). The flux of O_2 is maintained constant for the entire duration of the process at a pressure $P=7.5 \times 10^{-3}$ mbar. The deposition is conducted close to room-temperature ($T=60^\circ C$) and consists of 100 cycles. Each cycle is composed of the following steps: (i) dosing precursor TMA (30 ms); (ii) purging for 3 s; (iii) O_2 plasma for 3 s at a Power=100 W; (iv) purging for 3 s.

Due to the high conformity of the ALD, this dielectric layer is deposited on all the open surfaces of the NOEMS, including the bottom and the top part of both membranes, as illustrated in Fig. 6.1(b)). Fig. 6.1(c) shows the effect of the coating on the effective refractive index of the structure as a function of

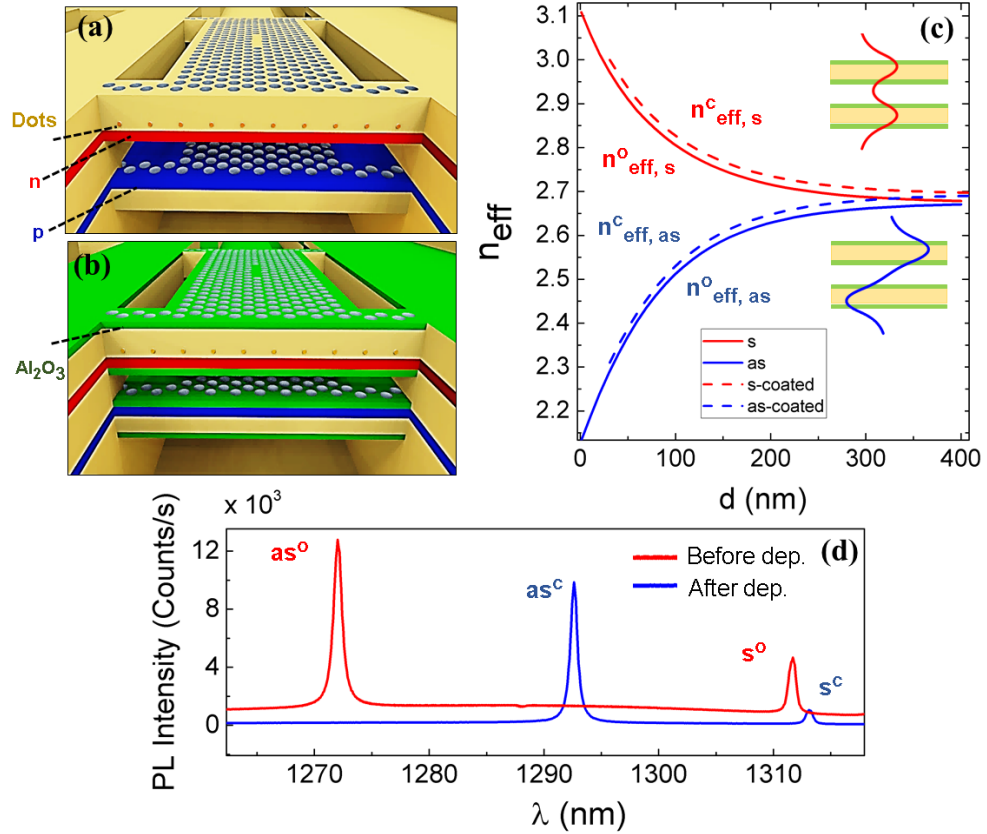


Figure 6.1: Artistic sketch of the uncoated (a) and coated (b) NOEMS composed of two vertically-coupled PhC membranes. (c) Calculated effective refractive index of the symmetric (s) and anti-symmetric (as) modes, with ('o' superscript) and without ('c' superscript) coating. (d) Measured effect of the alumina coating on the optical properties of the photonic crystal cavity. A red-shift with a different magnitude is observed for the fundamental s- and as- modes

the inter-membrane distance (d), calculated assuming the refractive index of the alumina $n_{\text{a}}=1.615$, as measured by spectroscopic ellipsometry. A small increase of the effective index, and therefore a red-shift is expected for both the s- and the as- modes.

6.3 RESULTS AND DISCUSSION

Room temperature micro-photoluminescence (μ -PL) experiments have been carried out to study the influence of the anti-stiction coating on the static and dynamic properties of the device. In these experiments, the quantum dot layer is excited with a diode laser emitting at 650 nm with a power of 0.9 mW before the objective, above the bandgap of GaAs. The emission of the QDs, which is modulated by the local density of states of the PhC, is then collected through an objective (numerical aperture = 0.45) and analysed by a spectrometer. A Ground-Signal-Ground probe is used to apply either a constant or a time-dependent bias to the cavity diode.

As a first set of experiments, we explore the effect of the dielectric coating on the optical properties of the NOEMS. Figure 6.1(c) shows the μ -PL spectrum of a PhC cavity (device A), collected before (red line, as^o and s^o) and after (blue line, as^c and s^c) the deposition of the alumina layer.

The in-plane symmetry of the resonances shown in Fig.6.1 (d) has been identified with the fundamental mode of the L3 cavity (labelled Y1), by a comparison with the eigenmodes obtained from FEM simulations [282], while the vertical profile is attributed to the symmetric (s) and anti-symmetric (as) modes, and further confirmed by the directions of the wavelength shift in electromechanical tuning experiments.

In general, the introduction of the alumina induces a red-shift of the spectrum for both modes as expected by the effect of a dielectric perturbation on the original resonances [208].

Since these two eigenmodes have the same in-plane symmetry - and therefore identical overlap with the alumina coating deposited inside the holes [208] -it is expected that they experience a red-shift having similar magnitude. However, the s-mode shows a smaller wavelength shift compared to the as-resonances. This can be explained by the fact that the deposition process induces a stress on the membranes [417] that increases the inter-membrane distance and thus blue-shifts (red-shifts) the s-(as-)mode, thereby decreasing (increasing) the net red-shift produced. The average wavelength shift induced by the deposition of alumina, measured in three different devices having nominally identical mechanical properties, is $\Delta\lambda(as) = (22 \pm 3)$ nm and $\Delta\lambda(s) = (1.3 \pm 0.3)$ nm, where the error bar is the standard deviation.

In light of these observations, we write the wavelength change due to the alumina deposition as the sum of two contributions, $\Delta\lambda_{total} = \Delta\lambda_d + \Delta\lambda_m$, where $\Delta\lambda_m$ is due to the stress-induced mechanical deformation and $\Delta\lambda_d$ is related to the pure dielectric perturbation. These two contributions can be considered independent, since the change in the effective refractive index due to dielectric perturbation (Δn_{eff}) is practically constant for the inter-membrane distances investigated here (Fig 6.1(c)).

In order to quantify these two wavelength shifts, we simulated the full-3D system using a commercial Finite-Element Method (FEM) (Comsol). We assumed the nominal parameters of the structure, supposing that a layer of alumina of thickness $t_d = 15$ nm is conformally deposited on all the opened surfaces of the devices (above and below both membranes and inside the PhC pores). In this way, dielectric shifts of $\Delta\lambda_d^{FEM}(s) = 15$ nm and $\Delta\lambda_d^{FEM}(as) = 12.5$ nm are obtained for the s- and as- modes, respectively. The fact that $\Delta\lambda_d^{FEM}(s) > \Delta\lambda_d^{FEM}(as)$ is due to the slightly larger field of the s-mode in the inter-membrane gap, which results in a larger overlap between the alumina layers and this mode.

The remaining wavelength shift is attributed to the mechanical deformation of the structures ($|\Delta\lambda_m| = 10 - 14$ nm). From FEM-simulations, we can estimate a $\Delta d \approx 100$ nm increase in the inter-membrane distance due to the induced mechanical stress. Notice that this analysis does not take into account a possible thickness difference between the membranes, which has been excluded from the inspection of cross-sectional scanning electron microscope images.

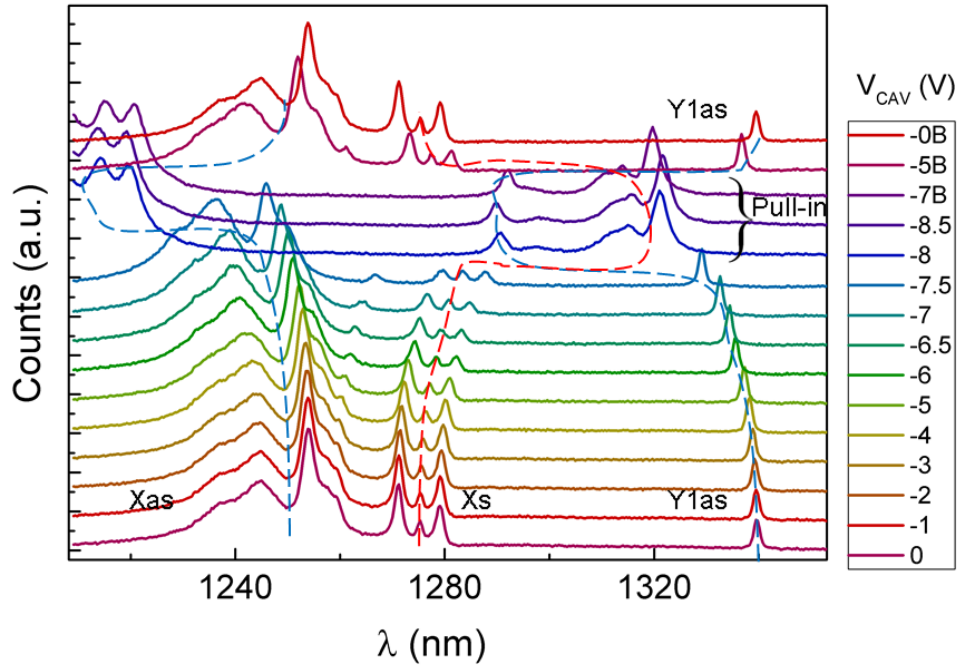


Figure 6.2: Electromechanical tuning of the dual-membrane PhC cavity. The cavity voltage is varied from 0 V to -8.5 V and then back (label 'B') to 0 V. The pull-in instability appears as a jump in the photoluminescence spectra at $V_{CAV} = -7.5$ V. The device can be operated back to the normal actuation when $V_{CAV} = -5$ V. The dashed lines are guides for the eye

Interestingly, no degradation of the optical quality factors is observed. The average experimental quality factors of the fundamental as- and s- modes before the deposition are $Q_{exp}^{as,o} = 1450 \pm 60$ and $Q_{exp}^{s,o} = 1900 \pm 170$, respectively. These values are smaller compared to the Q-factors predicted by FEM simulations ($Q_{FEM}^{as,o} = 1900$ and $Q_{FEM}^{s,o} = 5700$), due to the presence of fabrication disorder. After the deposition, the Q-factors increase to $Q_{exp}^{as,c} = 1810 \pm 50$ and $Q_{exp}^{s,c} = 2300 \pm 300$. Notably, the calculated quality factors for the coated devices vary monotonically from $Q_{FEM}^{as,c}(d = 200\text{nm}) = 1700$ to $Q_{FEM}^{as,c}(d = 300\text{nm}) = 2480$ for the as-mode, and from $Q_{FEM}^{s,c}(d = 200\text{nm}) = 5740$ to $Q_{FEM}^{s,c}(d = 300\text{nm}) = 7160$ for the s-mode, due to the redistribution of the k-vector components inside the light cone [282]. Therefore, the increase in the quality factor observed experimentally can be associated to the stress-induced mechanical reconfiguration of the devices described before.

6.3.1 Static Actuation

In the following, we investigate the behavior of the NOEMS when a static electric potential is set between the two membranes. The wavelength of the anti-symmetric fundamental mode (Y1as) is used to track the mechanical status of the device (device B). These measurements have been carried out in collaboration with Z. Zobenica (PSN, TU/e).

Figure 6.2 shows the tuning spectrum of the PhC modes as a function of the cavity voltage (V_{CAV}). Along with the fundamental as-mode ($Y1as$), other two sets of resonances appear in the spectra (labelled Xas and Xs), identified with higher order modes of the double-membrane L3 cavity [282].

The device is firstly actuated from $V_{CAV} = 0$ V beyond the pull-in voltage ($V_{Pull-in} \approx -8$ V) and then back ('B') to 0V. Three different regimes of operations (I, II, III) can be identified. During an initial phase (regime I) the PhC resonances red-shift or blue-shift depending on their vertical symmetry. This is caused by the continuous reduction of the inter-membrane distance under the application of the electrostatic force. The fundamental as-mode blue-shifts from $\lambda_{Y1as}(0V) = 1339.5$ nm to $\lambda_{Y1as}(7.5V) = 1328.9$ nm (-10.6 nm). The value of the experimental tuning range is in good agreement with the observation that the initial inter-membrane distance is increased due to the stress induced by the coating. In fact, from FEM simulations, when the gap between the membranes is reduced from $d_i = d_0 + \Delta d = 300$ nm to $d_f = 2/3d_i$, the expected tuning range for the $Y1as$ -mode is $\Delta\lambda_{tun}^{th} = -11.6$ nm.

At pull-in, the PhC spectra change drastically (regime II). Here the modes experience an abrupt wavelength jump. In particular - after pull-in - the fundamental mode is located at $\lambda_{Y1AS}(8V) = 1290.32$ nm, resulting in a discrete blue-shift of $\Delta\lambda_{Pull-in} = 38.6$ nm. From simulations, this corresponds to $d_{Pull-in} \approx 115$ nm. The spectrum slightly changes for higher voltages, $|V_{CAV}| > |V_{Pull-in}|$, with a rate of ≈ 1.0 nm/V. We repeated this tuning experiment on the same device in vacuum ($P \approx 10^{-3}$ mbar). Here we obtained $\lambda_{Y1AS}(8V) = 1268.7$ nm corresponding to $\Delta\lambda_{Pull-in}^{VAC} = 60.2$ nm and $d_{Pull-in}^{VAC} \approx 75$ nm, which corresponds to a residual spacing of ≈ 45 nm between the alumina layers. The difference in the maximum tuning range at pull-in is not yet understood. As further discussed below, we attribute the non-zero value $d_{Pull-in}$ to the upward bending of the top membrane. When the electro-mechanical voltage is decreased below $V_{CAV} < V_{Pull-out} \approx -5$ V (regime III), the modes return to their initial wavelengths of $\lambda_{Y1AS}(0V) = \lambda_{Y1AS}^B(0V)$. We ascribe the difference in the pull-in and pull-out voltages ($V_{Pull-in} > V_{Pull-out}$) to the presence of a residual attractive force at contact.

We tested the tuning capabilities of 11 devices having a different bridge area ranging from $8 \times 8 \mu m^2$ to $8 \times 12 \mu m^2$. No permanent stiction was observed in either of the devices. We found an average value of $V_{Pull-in} = 7.4 \pm 0.7$ V and $V_{Pull-out} = 4.4 \pm 1.3$ V.

To further examine the electromechanical tuning at pull-in (regime II), we employed a focused ion beam (FIB) setup equipped with two electrical needles (Fig. 6.3(a)), in order to visualize the cross-section of the device during the electromechanical actuation. Each needle is mounted on a movable stage that enables the positioning of the probe in vacuum with sub-micron control. Ion bombardment directly focused on the needles is employed to remove possible contaminations before contacting the device. These measurements have been carried out in collaboration with S. Kölling (PSN, TU/e) and Z. Zobenica (PSN, TU/e). Ion bombardment has been employed to etch a series of rectangular cuts at the centre of the bridge through both membranes, as shown in figure Fig. 3(d), in order to open a view at the centre of the

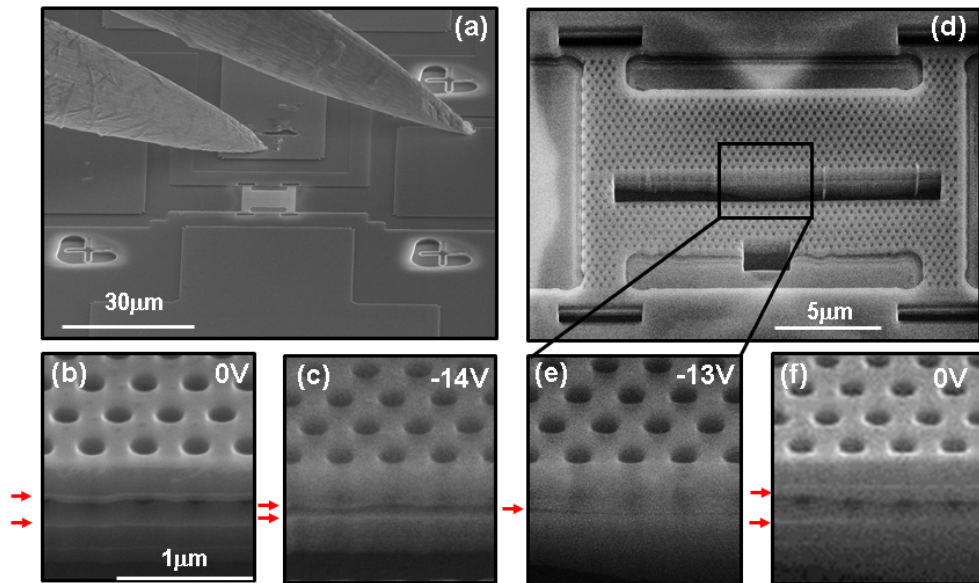


Figure 6.3: Investigation of the static pull-in via cross-section scanning electron images analysis. (a) Tilted SEM view of the device along with a pair of needles employed for the cavity actuation. (b) and (c) SEM cross sections, when V_{CAV} is set to 0 V and -14 V, respectively. (e) and (f) cross-sectional SEM images, after opening a large cut at the center of bridge (d) when the device is operated from -13 V to 0 V, respectively. The red arrows indicate the positions of the membranes. Notice that the layer of alumina is visible and thicker than the one measured by ellipsometry due the re-deposition of this material during the FIB cut.

bridge. We experimentally observed that for a small cut area $A_1 = 3.4 \mu\text{m} \times 1.2 \mu\text{m}$ the distance between the GaAs membranes varies from ≈ 260 nm to $\approx 40 - 60$ nm, when a device (device C) is operated from 0 V to above pull-in (Fig. 6.3(b,c)). The non-zero inter-membrane distance is in agreement with the value derived from the optical measurements. The same experiment is repeated after increasing the area of the cut to $A_2 = 12.0 \mu\text{m} \times 1.2 \mu\text{m}$.

In this configuration, when the membranes are brought to pull-in, a full contact between the two slabs is achieved, as shown in Fig. 6.3(d,e). When the voltage is set back to 0 V, the membranes return back to their original position (Fig. 6.3(f)). These experiments indicate that the presence of internal-stress produced during the coating of the chip bends the central region of the bridge upwards with respect to the peripheral parts of the structure. By opening a large area at the centre of the bridge, the internal stress is released and full contact can be achieved in this region.

6.3.2 Dynamic Actuation

In order to investigate the reliability of the tuning for applications that require digital switching between the rest and the pull-in state [152], device A has been actuated for more than $n = 1000$ cycles from 0 to -10 V, with a square wave signal having a period $T=1$ s. No degradation of the PhC

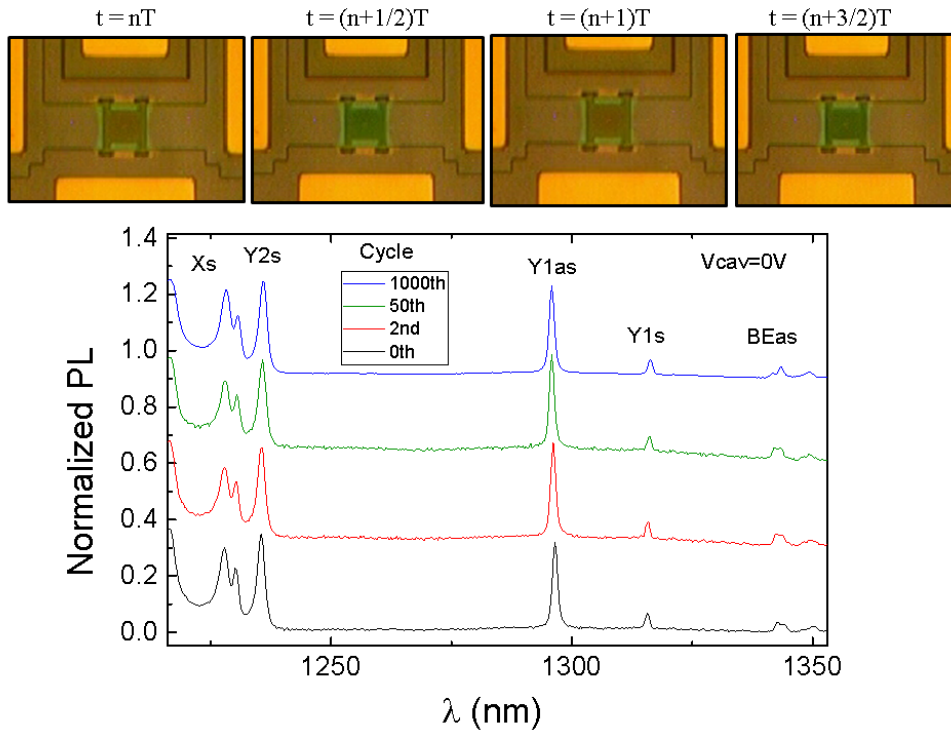


Figure 6.4: (Top) Optical microscope images of a device when it is actuated from 0 V (release) to -10 V (pull-in) with a period $T=1$ s. (Bottom) PL spectra of the L3 cavity after 0, 2, 50 and 1000 cycles

quality factors has been observed as shown in Fig. 6.4 (bottom). A small wavelength shift, comparable with the resolution of the spectrometer (0.32 nm), is observed after 1000 cycles when the cavity voltage is set to 0V. Fig. 6.4 (top) shows the optical microscope images recorded while the device was actuated between the pull-in and release configuration. Here, the colour of the bridge (red/green) arises from the thin-film interference of the vertical layers composing the device when it is either in the pull-in or in the release state.

In order to investigate the optical properties of the device during an even larger number of actuation cycles, we measured the PL spectra of the NOEMS integrated over the modulation experiment (device B). To this end, device B was actuated in vacuum (pressure = 10^{-3} mbar) from $V_{CAV} = V_i = -5V$ to $V_{CAV} = V_f = -10$ V with a square-wave voltage of frequency $f=100$ kHz and 50% duty-cycle. In what follows, we present the results for the higher order cavity mode, labelled Y3s, that - differently from the fundamental Y1as (see Fig. 6.2)-does not overlap with any modes in the spectra range spanned for $|V_{CAV}| > |V_{Pull-in}|$ and $|V_{CAV}| < |V_{Pull-in}|$. Fig. 6.5 (right panel) shows the PL spectrum integrated over 0.5 million modulation cycles. Here, the set of modes labelled Xas and Y3s can be recognized by comparison with the spectra collected in the static configurations at the two voltage values (V_i , V_f) (Fig. 6.5 (left panel)). The range of the wavelength modulation for the mode Y3s is 41.2 nm. The fact the PL spectra can be decomposed as a sum of the spectra obtained during the static actuation experiments indicates that the initial and the final mechanical positions of

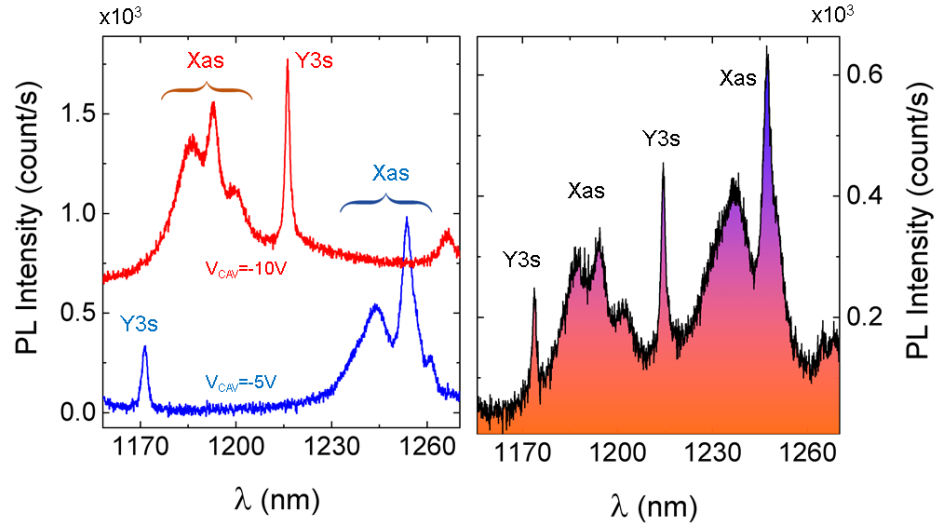


Figure 6.5: Operation of the PhC NOEMS as a digital switch between two opto-mechanical states. (left) PhC modes during the static actuation. (right) PL spectra from pull-in to the release status integrated over 500000 cycles with a modulation frequency of 100 kHz.

the membranes are identical for different modulation cycles. Importantly, no degradation is observed in both the quality factor ($Q(Y3) \approx 1000$) and the PL intensity of the modes.

Finally, we investigated the dynamical modulation of the NOEMS when it is operated under a strong AC signal with a varying frequency, in order to study the effect of the coating on the pull-in dynamics. A DC bias $u_{DC} = -6V$ together with an AC sinusoidal component of amplitude $u_{AC} = 1V$ were used to excite the cavity diode.

Figure 6.6 shows the colour-coded experimental μ -PL data of the mode Y_{1as} collected while varying the frequency (f) of the AC sinusoidal modulation from 0.1 MHz to 2.8 MHz. At low frequencies, the spectrum is characterized by a broad peak centred at $\hat{\lambda} = 1334.7$ nm, featuring a full width half-maximum (FWHM) of 5.5 nm. The minimum and maximum wavelengths of this peak correspond to the static wavelength positions at $\lambda(V_{CAV} = -7V) = 1331.7$ nm and $\lambda(V_{CAV} = -5V) = 1337.2$ nm reported in fig. 6.2. Besides, the maximum of the PL intensity is red-shifted compared to $\hat{\lambda}$ as expected by the non-linearity of the tuning. When the modulation frequency equals the mechanical frequency of the structure, a broadening of the spectrum is expected due to the amplification of the membrane oscillations. At $f_0 = 2.3$ MHz, a drastic broadening of more than 30 nm in the PL peak is observed and assigned to the fundamental mechanical mode of the structure, which has a calculated mechanical frequency of $f_{th} = 2.2$ MHz. Since the electrostatic force has a quadratic dependence on the actuation voltage, a broadening at $f_0/2$ is also visible. We speculate that the broadening of the experimental PL below 1 MHz - where mechanical modes are not expected from FEM simulations and have been not observed in experiments employing small modulation amplitudes [284]- can be due to non-linear high-order terms in the elastic force in this strong modulation regime. It is worth to mention that in the same experimental conditions, the collapse of the structures

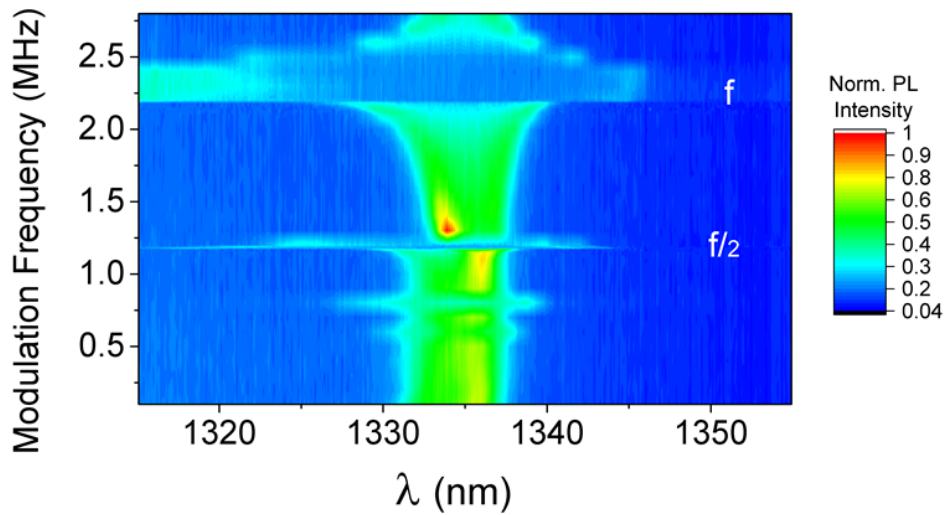


Figure 6.6: Photo-luminescence color-coded map obtained under the application of an AC bias. Broadening at 2.3 Mhz and 1.2 MHz arises from the motion amplification at f and $f/2$, where f is the mechanical frequency of the resonator

is observed for uncoated devices produced in the same fabrication run. This clearly indicates that the coating prevents the structure from the permanent collapse also when the device is modulated with a frequency comparable to its natural frequency.

6.4 CONCLUSIONS

Pull-in and stiction failure are often considered detrimental effects in the operation of NOEMS. Here we have demonstrated a method based on the atomic deposition of alumina that prevents the stiction failure after pull-in of mechanically-tunable photonic crystal membranes.

The operation of the device as a static and dynamic optical switch is demonstrated, with the possibility to reversibly modulate the wavelength of a PhC mode over ≈ 50 nm.

These results not only represent a crucial step towards real-world applications of this current NOEMS, but also open the way to new devices that exploit the intrinsic non-linearity of the pull-in to achieve digital optical switching and mechanical memories.

In addition, in the context of QPIC applications, the reliable control over the cavity mode in a c-QED experiment, without the risk of compromising the mechanical and optical properties of the structure during its operation, constitutes a clear step towards NOEMS-regulated single-photon sources stable against voltage fluctuations and environment perturbations.

7

WAVEGUIDE COUPLING

This chapter describes the integration of the tunable single-photon source presented in the previous chapters with a photonic circuit. Firstly, we describe the mode adapter employed to interconnect the double-membrane PhC cavity to a supported ridge waveguide. Then we examine the PhC design adopted to couple a cavity defect to a PhCWG. Then, we discuss the strategies adopted to electrically isolate the diodes in a waveguide-coupled geometry. Using these structures, we show that, by bringing a single dot line into resonance with a waveguide-coupled cavity mode, a Purcell-enhanced dot emission can be efficiently transferred to a ridge waveguide. Next, we present the realization of a beam splitter compatible with this material platform. An integrated anti-bunching experiment is realized with sources integrated with an on-chip splitter.

7.1 INTRODUCTION

All the experiments discussed so far have been carried out collecting the cavity and dot emission from a top objective or from a fibre located above the sample. Broadly speaking, in an optimized PhC cavity this coupling is generally inefficient, since the collected emission arises from the leaky modes of the cavity. In an optimized PhC cavity, the distribution of the k -vectors components of the resonant mode is mostly located outside the light cone. The residual k -vector distribution inside the light cone usually does not match the numerical aperture of the collecting objective, unless specific designs are adopted [345]. Differently from other micro-resonators, such as micro pillars, PhC structures are more suitable for side-coupling and specifically for being integrated with a planar photonic circuit. For this purpose, a narrow-band cavity can be coupled to a photonic crystal waveguide in order to inject the emission originated from a Purcell-enhanced dot into a broadband mode propagating in-plane. In principle, a complex photonic circuit comprising couplers, filters and modulators can be realized making use of PhC elements only. However, losses in PhC waveguides are very sensitive to fabrication disorder. On the other side, GaAs-based PhCs are realized on suspended membranes to provide sufficient confinement in the vertical direction. This makes these structures susceptible to buckling due to the accumulated stress, and sensitive to mechanical instabilities. In the case of a photonic architecture based on a double-layer material platform, this problem is even more pronounced due of the fact that the upper membrane is characterized by a relatively low stiffness and can be also affected by bending for device area larger than $\approx 20 \times 20 \mu\text{m}^2$. A solution consists in transferring the light generated by the mechanically-reconfigurable source to conventional ridge waveguides (RW), which are widely-employed for low-

loss transmission in photonic circuits [170]. One of the main advantages of coupling to standard ridge waveguides consists in the possibility to exploit pre-existing optical components, developed in classical photonic circuits, in the context of QPICs. RWs can be employed not only to transport single photons along the chip, but also to distribute the optical pump among many sources, in order to simultaneously trigger the single-photon emission from distant cavity-emitter nodes. Integrating tuneable sources with RWs represents the first step towards the full-integration with waveguide-coupled SSPDs. Before discussing the fabrication and the experimental results, the setup employed for the electro-optical characterization of the devices is presented in the next paragraph.

7.2 EXPERIMENTAL SETUP

The experimental setup employed for the LT characterization of the samples discussed in this chapter is shown in fig. 7.1. This setup was designed by dr. J.P. Sprengers (TU/e) and employs a customized cryostat from Janis Research. The main peculiarity of this apparatus consists in the presence of both fibres and probes inside the cryostat chamber. Two fibres are located on two independent XYZ piezo-stages (Attocube systems) and, depending on the specific application, they can be positioned in a transmission configuration (I/O 2 and I/O 3(B)) or from the same side of the chip (I/O 2 and 3(A)). The fibres employed in these experiments have a lensed shape with a nominal spot diameter of $(2.0 \pm 0.5) \mu\text{m}$ (from Oz-Optics). These are polarization maintaining fibres designed for 1300 nm. The main polarization axis is set horizontally - orthogonal to the growth direction - with an accuracy better than ± 10 degrees. Two probes, positioned on two additional XYZ stages, can supply up to four different voltage signals to the samples ¹. All the piezo stages are interfaced with electronic controllers (ANC300). The maximum tuning range of the piezo is 5 mm. For this reason, the sample holder is relatively small 5 mmx7 mm. Two typologies of electrical probes have been used: a microwave (50 Ω , 40 GHz) three-fingers probe, having a Ground-Signal-Ground configuration (from GGD Industries) and a custom designed four-fingers probe in the G-S-G-S configuration (Wentworthlabs). The spacing between the fingers is set to 100 μm , in accordance with the standard geometry of the contacts pads. The setup is equipped with a top optical arm, embodying a movable μ -PL setup. A white LED and a CCD camera allow for the illumination and visualization of the sample. The top arm can be employed in two different configurations (i) to collect μ -PL spectra from the objective (NA=0.4, Mitutoyo); in this case a dichroic beam splitter (DBS) is used to separate the 780-nm excitation laser from the PL-signal; (ii) to focus two different laser spots on the same sample, in order to excite multiple sources; in this case, the DBS is replaced by a standard beam splitter (BS). In general, the setup is characterized a triple I/O optical access: a top collection (I/O 1) and two side-collection paths (I/O 2, I/O 3). Two free-space

¹ Notice that, the ground of coaxial cables of the probes is in common with the ground of the cryostat; therefore, in the case of p-i-n-i-p configurations, the ground must be connected to the n-pad of device

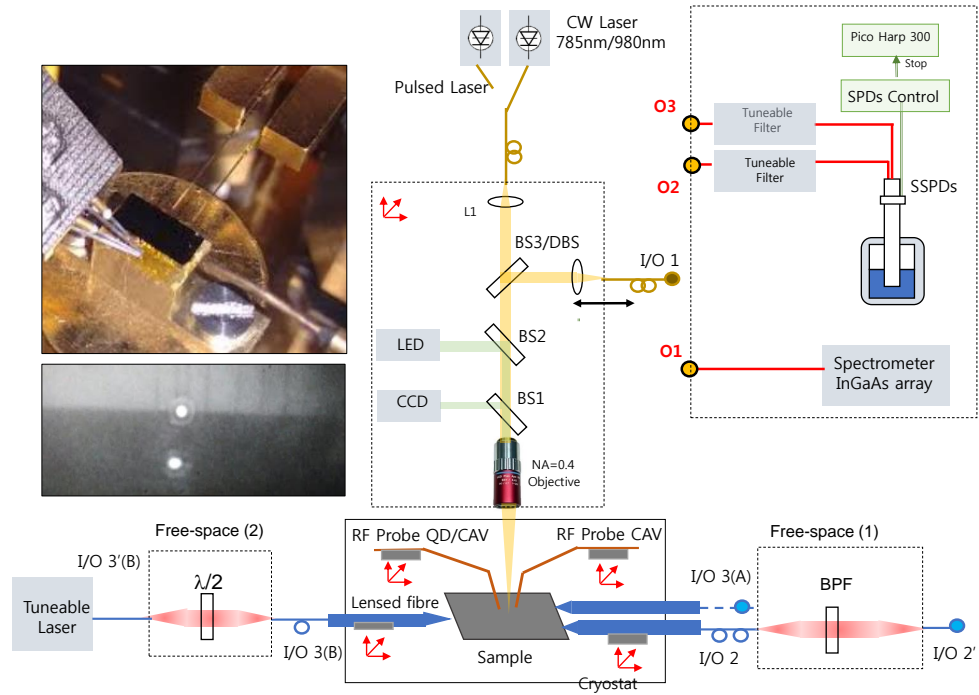


Figure 7.1: Experimental setup. Two probes and two fibres, mounted on XYZ nano-positioners, allow the electro-optical characterization of the devices. A movable top arm can be employed either for top PL experiments (I/O 1) or to focus multiple laser spots. The collection from fibres can be analysed using two free-space setups and re-directed either to a spectrometer (O₁) or to a correlation setup (O₂, O₃). Insets: (top left) photograph of the sample stage (bottom) CCD image during alignment of a fibre to a RW. BS: Beam Splitter, BPF: Band pass filter, DBS: dichroic beam splitter

setups, comprising two mirrors and fibre-couplers (not shown) are employed to modify the polarization state of the input laser or to insert optical filters. In the case of transmission experiments, a half-wave plate is employed to align the polarization of a tunable laser to the TE-polarization of the RW. For collection, long-pass and band-pass filters are used to suppress the laser scattering. The maximum coupling efficiency of these free-space filter setups is typically 40-50 % fibre-to-fibre. Their output can be connected to a spectrometer (O₁) or to single-photon detectors (O₂, O₃) via additional fibres. The typical alignment procedure consists in pumping the ridge waveguide in proximity of the edge of the sample, and maximizing the signal collected from the fibre using the spectrometer ².

² As a reference for the alignment process, typical values of maximum counts rate ranges from 2000 to 3000 cts/s for ensembles of low-density QDs at LT, with a laser power in the range of few mW. The values of laser power presented in this chapter are measured at the lens L₁ in top arm of the setup. The coupling efficiency from L₁ to the sample \approx 0.5%)

7.3 RIDGE WAVEGUIDE

In what follows we employ trapezoidal ridge waveguides, using a similar etching procedure developed for single-layer membranes [115]. The waveguides can be fabricated exploiting the anisotropic etching of AlGaAs in cold (1 °C) HCl solutions. In fact, the etching rate of this solution is different along the two orthogonal directions $011/01\bar{1}$ and the etching stops at a specific crystal plane of the AlGaAs [367]. Based on the crystallographic axis on which the ridge waveguide is aligned, two different waveguide profiles (type A and B) can be obtained (fig. 7.2), forming a waveguide supported by a pedestal made of AlGaAs. When the waveguide is aligned to the (011) crystallographic direction (type A), an inverted trapezoidal pedestal is created both underneath the bottom GaAs membrane and in between two membranes, as displayed in fig. 7.2 (left). This support has a base smaller than its top part. Vice versa, aligning the ridge to the $(00\bar{1})$ direction (type B) results in a pedestal with a small top apex (fig. 7.2 (right)). The angle of the trapezoidal supports strongly depends on the concentration of Aluminium, and it has been found experimentally to be $\approx 52^\circ$ for the Al concentration (70%) in our samples. In principle, both types of RWs can be adopted to transmit single-photons along the circuit. However, in the following, we focus on RW type B, which ensures a higher mechanical stability for waveguides having a small width.

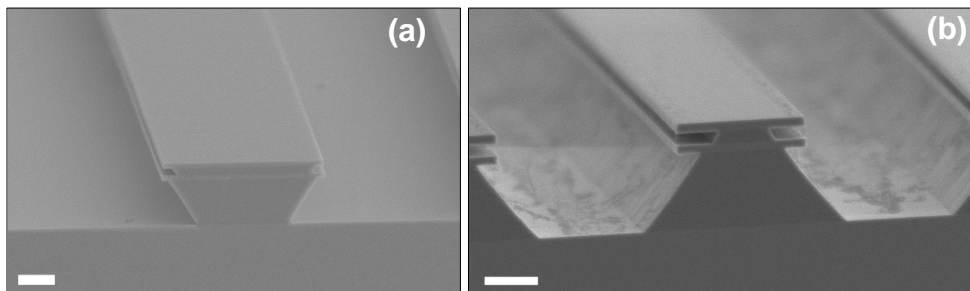


Figure 7.2: SEM images of the two types of ridge waveguides obtained for RWs patterned along (011) (left, type A) and $(01\bar{1})$ (right, type B) direction. The white bar corresponds to 1 μm

TRANSMISSION RIDGE WAVEGUIDE In order to estimate the absorption losses of the ridge waveguides and the coupling efficiencies from fibre to the RW, we carried out a series of transmission experiments on straight waveguides (width = $5\mu\text{m}$). To this end, a tunable laser diode is coupled from the end-facet of one of the RWs via a lensed fibre, and the transmitted light is collected via a second lensed fibre at the output waveguide. The polarization of the laser is set to excite only the TE mode of the RW. The scheme employed here is based on the Fabry–Pérot method (see e.g. [84]) and previously employed for single-membrane (SM) RWs [115]. Due to the partial reflections at the facets of the RW, a series of fringes is caused by the interference from multiple round-trips inside the RW (fig.7.3). Constructive interference takes place when the phase accumulated in one round-trip ($\Delta\phi$)

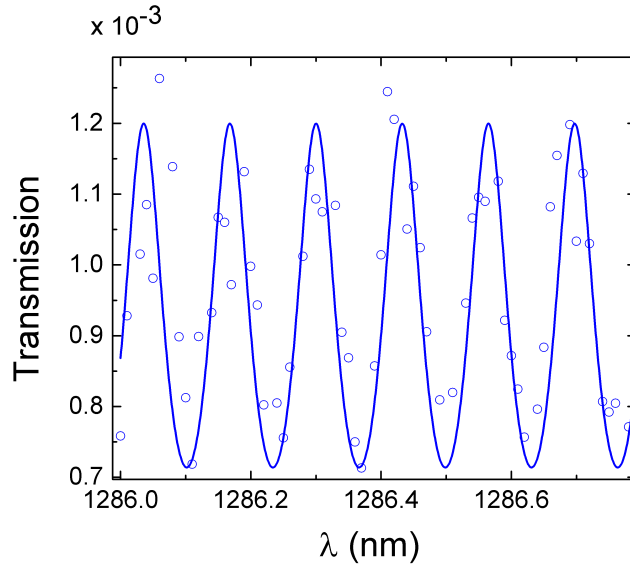


Figure 7.3: (dots) Experimental transmission through the ridge waveguide as a function of the excitation wavelength and (continuous line) fit from eq. 7.1

is an even multiple of π . Given n_g , the group velocity of the ridge waveguide³, this condition reads $\Delta\phi = 2n_g L\beta = 2m\pi$, where m is an integer number, and L and $\beta = 2\pi/\lambda$ are the measured length of the RW and the vacuum wave number for a certain excitation wavelength λ . The period of the fringes as a function of λ can be then calculated as $\Delta\lambda = \frac{\lambda^2}{2n_g L}$. Assuming the simulated value $n_{eff} = 3.193$ for the fundamental TE mode, and the measured $L = 0.167 \pm 0.002$ cm, the expected fringe period is $\Delta\lambda = 0.15$ nm which is close to the period observed in fig. 7.3 (~ 0.13 nm), the difference being attributed to the uncertainty in the index value. The transmission power is fitted with the Airy function (continuous line) [84]

$$T_{FP} = \eta_C^2 \frac{(1-R)^2 e^{-\alpha L}}{(1-\tilde{R})^2 + 4\tilde{R} \sin^2(\frac{\Delta\phi}{2})}. \quad (7.1)$$

In this equation, we assumed that the coupling efficiency for the input and output fibre is identical, $\eta_1 = \eta_2 = \eta_C$. Besides, we introduced the *loss-reflection* coefficient $\tilde{R} = R e^{-\alpha L}$, which depends both on the reflection coefficient R at the cleaved facet and on the propagation loss per unit length (α). From the 2-parameters fit, we can extract $\eta_C = 3.5\%$ and $\tilde{R} = 0.129$. In order to estimate α , R can be calculated from Fresnel equations

$$R = \left| \frac{n_{eff} - 1}{n_{eff} + 1} \right|^2 = 0.274 \quad (7.2)$$

obtaining

$$\alpha = \frac{1}{L} \log\left(\frac{R}{\tilde{R}}\right) \quad (7.3)$$

By repeating this procedure over three nominally identical RWs and calculating the average and the standard deviation, we obtained an estimation for

³ Here we approximate n_g with the simulated effective refractive index

$\bar{\eta}_C = (3.5 \pm 1.2) \times 10^{-2}$ and $\bar{\alpha} = 1.9 \pm 0.3 \text{ cm}^{-1}$. This absorption coefficient is slightly smaller compared to the value obtained for SM-RWs based on the same technology ([115], $4\text{-}5 \text{ cm}^{-1}$). We speculate that, since the mode of DM-RW is more confined in the bottom membrane (fig 7.5), the field at the surface is smaller, which reduces the scattering loss. On the other side, the low out-coupling efficiency of the end-fire configuration is one of the hindering factors to the collection of high count rates, in particular for free-space application and correlation experiments. A better out-coupling efficiency might be achieved making use of the evanescent coupling between a fibre and a suspended nanobeam [83, 210], or by the use of grating couplers. Further optimization is needed to adapt this geometry to the double-membrane platform.

7.4 COUPLING TO RIDGE WAVEGUIDES

The scheme adopted to transfer single-photons from the PhC cavity to RWs is sketched in fig. 7.4. Firstly, the cavity is coupled to a photonic crystal waveguide realized on both membranes. Then, the PhCWG is interconnected to a RW via a *mode adapter*. These two transitions are separately discussed in the next paragraphs.

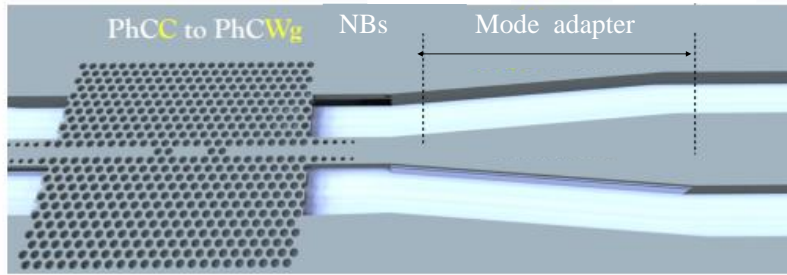


Figure 7.4: Artistic sketch of the transition from the suspended PhC region of the photonic crystal membranes to the ridge waveguide through a pair of suspended nanobeams (NBs). Only the top membrane is shown

7.4.1 Mode adapter

The output of the photonic crystal waveguide consists of two suspended nanobeams (NBs). The width of the nanobeam is $2a\sqrt{3}$, where a is the lattice constant of the crystal. This structure supports two TE modes, having a symmetric (S) and anti-symmetric (AS) field profile (fig. 7.5 (left)) and a simulated effective refractive index $n_{\text{NB},S} = 2.623$ and $n_{\text{NB},AS} = 2.564$, respectively. On the one hand, the fundamental TE mode of a $2.5 \mu\text{m}$ -wide ridge waveguide (fig. 7.5 (right)) has a simulated effective refractive index of $n_{\text{eff},RW} = 3.169$. An abrupt transition between these two regions would cause high losses arising from the high modal mismatch. A convenient solution to overcome this problem employs an adiabatic taper to convert the

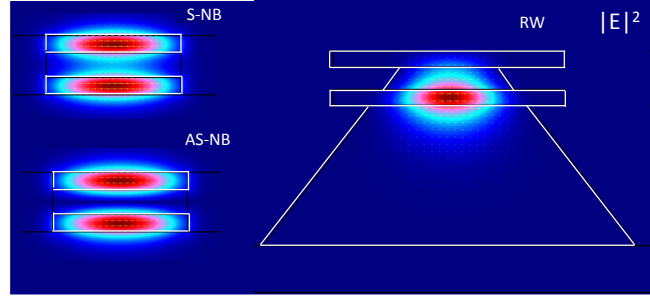


Figure 7.5: Simulated intensity profile of the TE modes (S and AS) of the suspended nanobeams (left) and the RW (right)

modes of the double nanobeams into the RW. The width of the nanobeams can be gradually increased along the propagation direction in order to create an AlGaAs spacer both in between the two membranes and underneath the bottom membrane. After a critical width of $w_{th} \approx 1.65 \mu\text{m}$, a supporting post is created, which sustains both membranes. The width of the basis of this AlGaAs trapezoidal pedestal increases accordingly to the width of the taper. The main advantage of using this mode adapter consists in its fabrication simplicity, since it does not require additional lithographic steps, avoiding offsets between the PhC region and the access waveguide. In fact, the supported waveguide can be created during the same patterning and etching steps employed for the PhC structure.

Specifically, we employed a linear taper characterized by a length of $L_{tap} = 8 \mu\text{m}$ and an angle of $\theta = 6.7^\circ$. The adiabatic theorem [184] ensures that if this transition is smooth enough, i.e. the tapering angle is sufficiently small, the initial mode can be fully converted into the fundamental mode of the output waveguide. In principle, the longer is the taper, the lower are the losses associated to this transition. However, in the case of the dual-layer architecture, the taper cannot be arbitrary long, due to the presence of buckling, as observed for structures longer than $10 \mu\text{m}$. In the future realizations, better performances might be obtained by transferring the S mode to the bottom waveguide by a longer, fully-suspended taper structure that employs lateral nano-tethers.

SIMULATIONS In order to give a quantitative estimation of the losses associated with the transition from suspended to supported regions, we simulated the evolution of the S and AS nanobeam modes through the mode adapter (Fig.7.6 (top)). The full 3D structure is built based on the dimensions measured from SEM pictures. However, the simulated taper has a reduced length ($6 \mu\text{m}$), due to computational limitations. We use a zx -symmetry plane passing across the structure, imposing an even symmetry for the E_y component (Perfect Electric Conductor, Comsol 5.2 [75]). A perfectly matched layer is located underneath the ridge to simulate the absorption from the GaAs substrate.

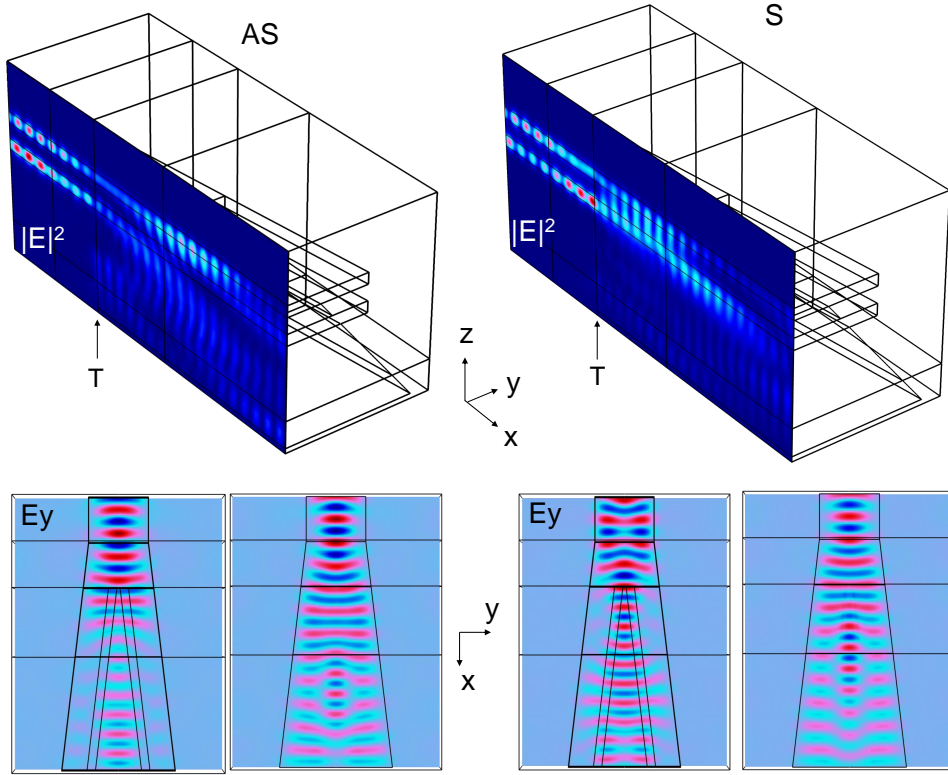


Figure 7.6: 3D simulation of the transmission for the AS (left) and S (right) TE modes of the nanobeams, propagating through the mode adapter. (top) Evolution of the modulus squared of the electric field for the two modes in the zx plane. (bottom) Y-component of the electric field in the bottom (left) and upper (right) membrane

First of all, two different ports are defined. The input port is located in the nanobeam section ($d\Omega_1$), while the output port is placed at the end of the RW ($d\Omega_2$). The 2D-eigenmodes are computed over these two boundaries, obtaining the fields $\vec{E}_1(y, z)$ and $\vec{E}_2(y, z)$. Then, Maxwell's equations are solved in the frequency domain, using \vec{E}_1 as a source term. The transmission and reflection coefficients (power ratios) of the structure can be calculated as $T = S_{12} \cdot S_{12}^*$ and $R = S_{11} \cdot S_{11}^*$, where the S-parameters, S_{ij} , are defined as[75]

$$S_{11} = \frac{\int_{d\Omega_1} (\vec{E} - \vec{E}_1) \cdot \vec{E}_1^*}{\int_{d\Omega_1} \vec{E}_1 \cdot \vec{E}_1^*} \quad S_{12} = \frac{\int_{d\Omega_2} \vec{E} \cdot \vec{E}_2^*}{\int_{d\Omega_2} \vec{E}_2 \cdot \vec{E}_2^*},$$

and $\vec{E}(x, y, z)$ represents the calculated propagating mode. Fig. 7.6(top) shows the intensity profile ($|\vec{E}|^2$) of the computed mode when the AS (left) or S (right) modes are excited in the double nanobeams.

At the transition point T, where the AlGaAs layers are created, scattering of light is manifested for both modes and part of incoming light is absorbed in the underlying substrate. This transition is more evident in the E_y component, shown for the upper and bottom membranes (bottom panels, fig.7.6).

The calculated transmission coefficient for the S and AS mode are $T_S = 40.5\%$ and $T_{AS} = 29.6\%$

7.4.2 Design PhC-PhCWG Coupling

In this section we focus on the coupling between a PhC cavity and a PhC waveguide realized on a double-membrane. Our starting point is represented by the optimized L₃ cavity illustrated in fig. 7.7. The radii and positions of 10 holes surrounding the cavity defect have been optimized by Ž. Zobenica in order to obtain PhC resonances with high quality factors and featuring a large ($\approx 20\text{nm}$) free spectral range. Given a and r the lattice

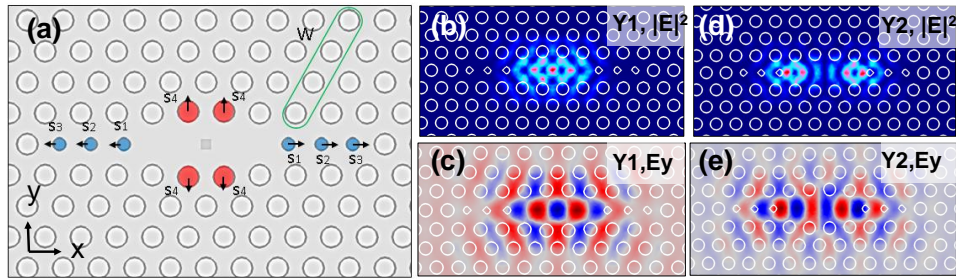


Figure 7.7: (a) Sketch of the modified L₃ Cavity. Electric field intensity of the fundamental (b) and first-order (d) modes of the unloaded cavity. (c) and (e) show respectively the E_y component of the Y1 and Y2 modes

constant of the unmodified cavity, the six holes located along the cavity axis (blue circles) have a reduced radius ($0.6r$) and are shifted away from the cavity centre by the displacements $\{s_1 = 0.3a, s_2 = 0.225a, s_3 = 0.1a\}$. In addition, four holes located above and below the cavity defect (red circles) are displaced along the y -direction by $s_4 = 0.05a$. This cavity, referred to as L_{3m}, supports several modes including the fundamental mode Y1 (fig.7.7 (b,c)) and the first-order mode, labelled Y2 (fig.7.7 (d,e)). Each of these modes splits into a S and an AS modes, due to the vertical coupling between the membranes. In following table, a summary of the quality factors and the wavelengths of the PhCC modes calculated by 3D FEM simulations is reported.

Mode	Vertical Symmetry	Q_0	λ (nm)
Y1	S	54920	1356
Y2	S	42600	1333
Y1	AS	37993	1319
Y2	AS	12854	1296

Here we study the evanescent coupling of this cavity to a photonic crystal waveguide, realized by removing a single row of holes from the hexagonal lattice of the photonic crystal (W1). To achieve high coupling efficiency, the PhCC modes must be matched spatially and in energy with a guided mode supported by the photonic crystal waveguide. Due to the similar symmetry, these modes are suited to be coupled with the fundamental Bloch mode of

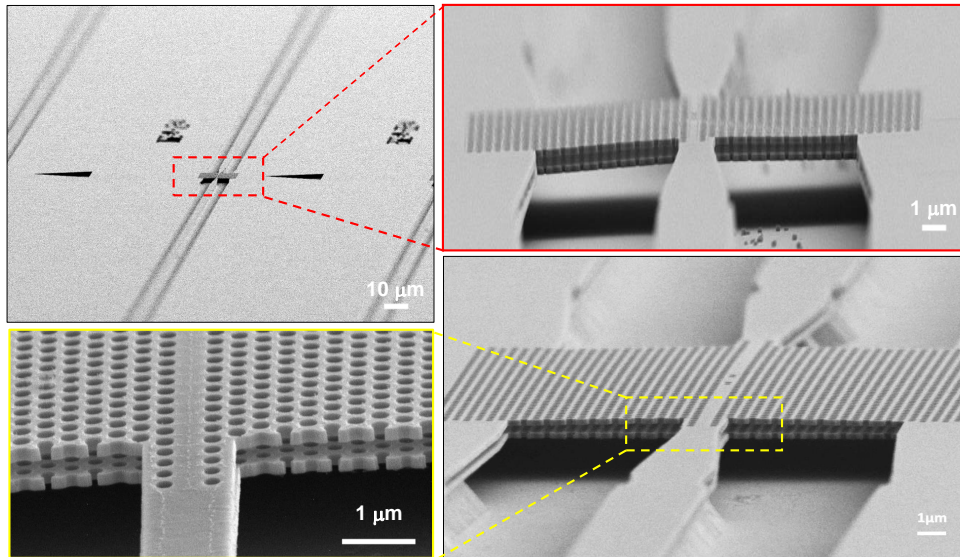


Figure 7.8: SEM pictures of a waveguide-coupled device from several perspectives. The cavity employed is a L3 inline coupled with two W1s, used in preliminary experiments

the W1. In order to experimentally investigate the coupling, we fabricated the devices shown in fig. 7.8, using the fabrication recipe described in chapter 2. The devices are characterized by membrane thicknesses of $t = 170$ nm, a gap of $d = 240$ nm and without AlGaAs barriers. In the next paragraph we discuss the optical properties of the PhCWG.

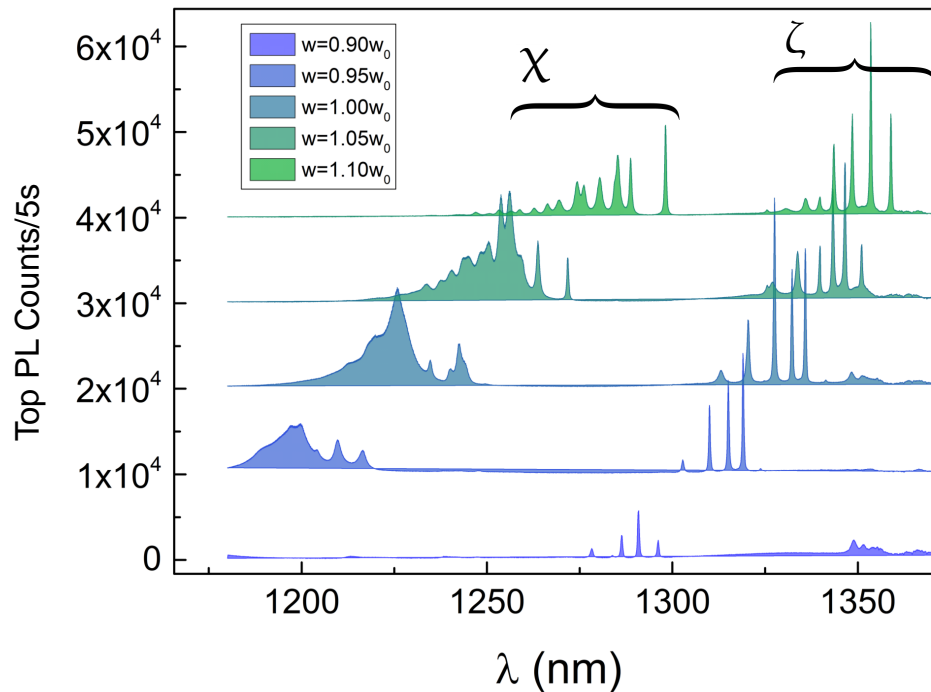


Figure 7.9: Top RT μ -PL spectra of the PhCWG, as a function of the width w

Photonic Crystal Waveguide Fig. 7.9 shows the top μ -PL spectra collected exciting the PhC waveguide region as a function of the width (w) of the PhC waveguide. Due to the asymmetry in the membrane thickness discussed in chapter 3, only vertical AS modes are visible in these spectra. Here w is lithographically varied from $0.9w_0$ to $1.1w_0$, where $w_0 = \sqrt{3}a$ is the original width of the photonic crystal waveguide. Two sets of modes appear in these experiments. We will refer to these modes as ζ (located at higher wavelengths) and χ , which have been associated, respectively, with the fundamental (even) mode and the first-order (odd) mode of the photonic crystal waveguide. As the width of the PhC is lithographically increased by steps of $0.05w_0$, the modes shift to the red by $\approx 15\text{nm}$ per step.

ζ is characterized by sharp resonances, shown in fig. 7.10 (a). These modes arise from the Fabry-Pérot modes located in the slow-light region of the dispersion curve, due to reflections at the air-semiconductor boundaries at the end of the patterned structure. Although these modes propagate in-plane - along the defect line - they can be collected from the top due to the scattering induced by disorder in the PhC region.

Since the length of the PhCWG is smaller than the photon localization length [457], the formation of Anderson-localized modes is not allowed in these structures. The spacing between these resonances decreases for higher wavelengths, as expected from the FPs located in slow-light region of the dispersion curve, close to the cut-off wavelength [18, 356]. Besides, as displayed in fig.7.10(a), the quality factors increase in proximity of the cut-off wavelength. This is due to the increased photon lifetime in the waveguide region associated with the reduced group velocity. It is worth mentioning that a saturation of the quality factor is observed for mode FP1 and FP2, while an exponential increase in the quality factor is expected for an ideal structure. This effect is attributed to the presence of fabrication disorder, which sets an upper bound to the maximum quality factor $Q_{fab} \approx 3000$, achieved in this fabrication run (see also discussion below). We can extract the group index, from the wavelength separation between two consecutive FP modes ($\Delta\lambda$), using the equation $n_g = \frac{\lambda^2}{2L\Delta\lambda}$, where $L = 6\mu\text{m}$ is the length of the PhCWG. Fig 7.10(c) shows the group index increases up to $n_g=40$, when the slow light is approached, in agreement with the single membrane experiments [18]. It is well known the slow-light is affected by high propagation losses [168]. Thus, it is convenient to couple the modes Y1 and Y2 to the linear part of the PhCWG. Tuning of the width of the PhCWG, as presented in fig. 7.10, provides a simple way to control the detuning between the dispersion edge of ζ and Y_i , without perturbing the field of the cavity [123].

PhCC-PhCWG coupling: simulations A spatial overlap between waveguide and cavity is needed in order to obtain high coupling into the waveguide [452]. A number of previous studies discussed the possible configurations to achieve high coupling efficiency between a localized PhCC mode and a PhCWG [32, 73, 111, 115, 198, 236, 251, 256, 267, 313, 385, 452]. In particular as proposed by Faraon *et al.* in [111] - and as can be observed from fig. 7.7 (c) - the spatial profile of the fundamental mode of an L3(m) cavity extends in a direction tilted to 30 degrees with respect to the axis (x) of the cavity. Besides, the first-order mode Y2 shows the same feature (fig.

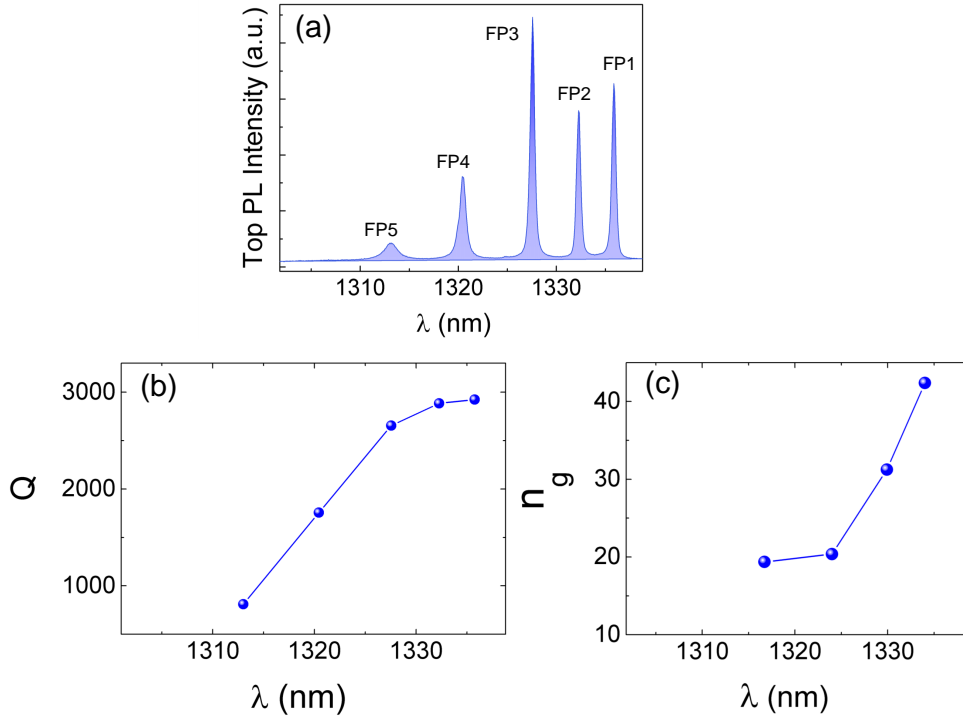


Figure 7.10: (a) Spectrum of the AS FPs modes located in the region of the fundamental ζ mode. (b) Quality factors and (c) group index extracted from the μ -PL spectrum, for $\omega = \omega_0$

7.7(e)). For this reason, Faraon *et al.* [111], proposed to align the waveguide at 60 degrees angle to the cavity axis (fig.7.7 (a), green line), in order to maximize the mode field overlap. This particular angle is imposed by the symmetry of the hexagonal crystal. The same considerations apply also for double membrane structures, for the S and AS modes de-localized over the two membranes. In what follows we focus on the analysis of the vertical AS modes, although we expect the same considerations to be valid also for the S modes. The eigenvalue problem is solved using 3D FEM simulations, obtaining the eigenfunction $\vec{E}(\vec{r}, t) = \text{Re}(\vec{E}e^{-i\omega t - \kappa t})$, where κ is the field loss rate. The obtained Q-factor ($Q_{\text{loaded}} = \omega/2\kappa$) for the waveguide-coupled cavities, is plotted in fig. 7.11(a) as a function of the number holes (nH) composing the barrier. The E_y component for the Y1 and Y2 mode is reported in 7.11(c,d). Q_{loaded} tends to the value of the unloaded Q-factor for nH=5 for both modes. While a monotonic increase is observed for Y1, a local minimum is observed for nH=4 for the mode Y2. A similar behaviour has been observed in literature ([111, 267]) and has been attributed to the overlap of one anti-node of the waveguide (cavity) mode with the node of the cavity (waveguide) mode. The presence of the waveguide introduces a decay channel in the unperturbed cavity mode, with a loss rate Q_{wg} . Given the simulated quality factor of the isolated cavity Q_0 , the quality factor in the presence of the waveguide (Q_{loaded}) can be computed by

$$\frac{1}{Q_{\text{loaded}}} = \frac{1}{Q_0} + \frac{1}{Q_{\text{wg}}} \quad (7.4)$$

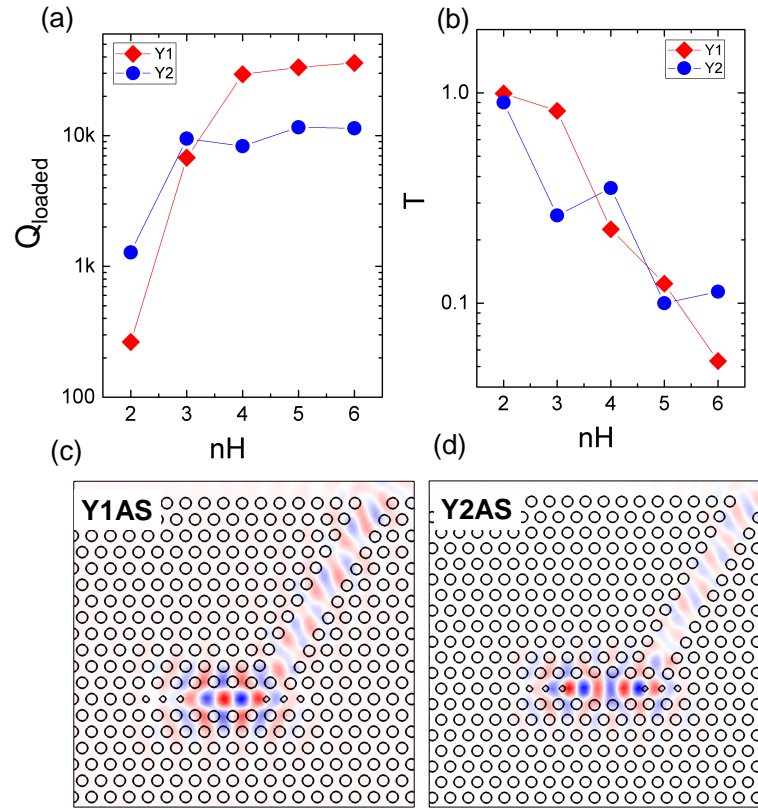


Figure 7.11: (a) Theoretical Q-factors and (b) transmission values for the L3m cavity. (T). E_y component for the (c) Y1 and (d) Y2 mode, coupled to a PhCWG ($w = 1.1w_0$) for $nH=2$

By engineering the dimensions of the barrier, Q_{wg} can be varied from 2.7×10^2 to 6.8×10^5 for the Y1 mode, and from 1.4×10^3 to 1.2×10^5 for the Y2 mode. The coupling efficiency T of the cavity-waveguide transition can be calculated from the ratio Q_{loaded}/Q_{wg} , as shown in fig. 7.11 (right panel). From these simulations it is clear that good transmission comes at the expenses of a lower quality factor. Depending on the specific application in the context of QPIC, single-photon efficiency can be preferred to the realization of non-linearities that require high-Q ($Q > 5K$) resonators. If the cavity is used as a (tunable) filter, quality factors above 10^3 must be employed in order to isolate single-dot lines.

PhCC-PhCWG coupling: Experiments In order to validate these predictions, we fabricated devices comprising $nH=2,3,4$ with a varying width w (Fig. 7.12) with $a = 380$ nm and $r/a=0.31$. Fig. 7.13 shows the experimental quality factors extracted from the μ -PL spectra as a function of the number of holes in the barrier (nH), the width (W) of the PhCWG, for the two AS mode $Y1_{AS}$ (red dots) and $Y2_{AS}$ (blue dots). The experimental values are sensitive to the disorder produced during fabrication. For this reason, the maximum value of the quality factors is reduced compared to simulations.

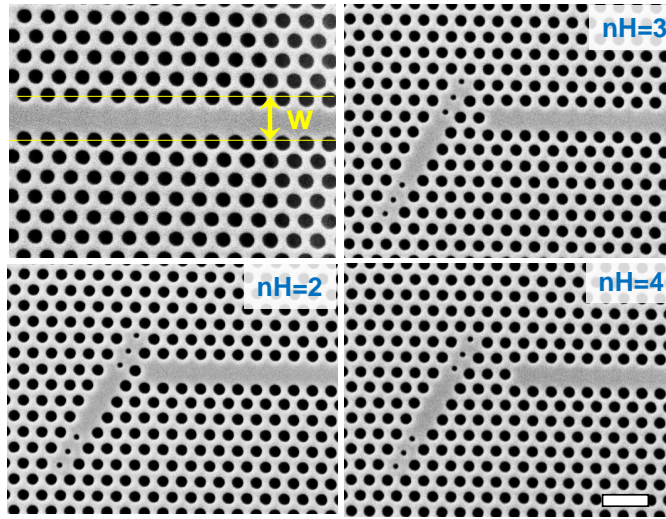


Figure 7.12: Fabricated cavity coupled to PhCW for different barrier length, $nH=2, 3, 4$)

The experimental quality factor of the uncoupled Y_{2AS} mode, measured over

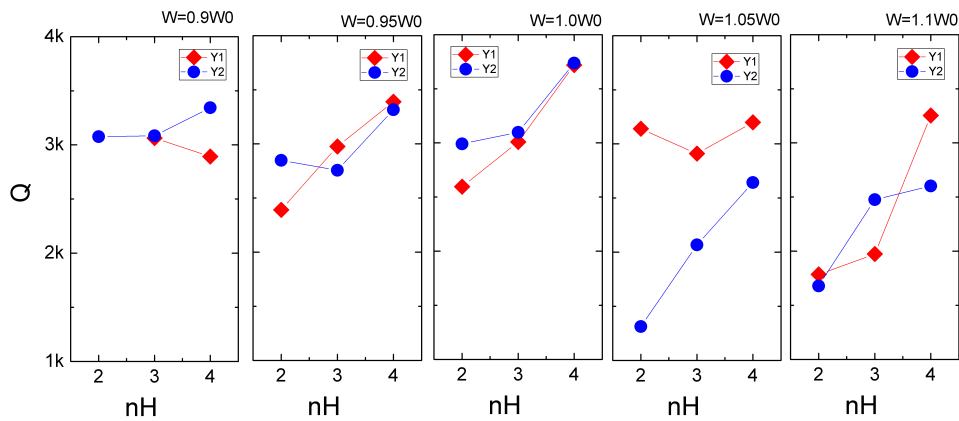


Figure 7.13: Experimental quality factors as a function of the number of holes (nH) and the width of the waveguide w

5 different devices, is $Q_{Y_{2AS}, nH=\infty} = 3300 \pm 300$. This value is identified with the loss channel associated with fabrication disorder. For $w \leq w_0$, the measured quality factor remains above 2.4×10^3 , indicating poor coupling efficiency. This is expected from the fact that, for these values of w s, the cut-off wavelength of the $W1$ is blue-shifted compared to the wavelength of $Y2$ (and $Y1$). For $w = 1.1w_0$, the behaviour of the experimental Q -factor resembles the calculated one: $Q(Y1, nH=4)$ is fabrication-limited as expected from the poor spatial coupling with the PhC waveguide, while a drastic decrease of Q is observed for a decreasing barrier length. For $w = 1.05w_0$, the quality factor of the fundamental mode is practically constant $Q(Y1) \approx Q_{dis}$ for different barrier lengths, while $Q(Y1)$ increase for increasing nH . This is related to the fact, contrary to $Y2$, for $w = 1.05w_0$, $Y1$ lies outside the fundamental mode of $W1$. A residual dependence on the barrier length is observed also for $w=0.95w_0$ and $w=1.0w_0$ and attributed to a small coupling

to the AS dielectric band of the W1. Following [111], we can estimate the coupling efficiency, by assuming $Q_0 = Q_{\text{dis}}$ in eq. 7.4. For $w = 1.1w_0$, the transmission coefficients are summarized in the following table

Mode	nH	T
Y1	2	0.48 ± 0.08
Y1	3	0.42 ± 0.04
Y1	4	0.04 ± 0.01
Y2	2	0.51 ± 0.1
Y2	3	0.27 ± 0.09
Y2	4	0.23 ± 0.06

From this analysis and for the current experimental value of Q_{dis} , we conclude that the design $nH = 2$ provides a relatively high transmission into the waveguide for both modes ($T \approx 0.5$) while preserving a sufficiently high quality factor $Q > 1600$. These features are essential for filtering a single dot line among the several excitonic transition produced via non-resonant excitation and to provide a significant enhancement via the Purcell effect. Besides, it is worth mentioning that controlling the barrier length allows the selective collection of one of the two modes under consideration, due to their different in-plane spatial confinement. This is in particular evident for a barrier length of $nH = 4$, that enables to collect only the mode Y2as, while the collection of Y1 is practically suppressed. This design is particularly appealing for applications that require a large free spectral range combined with a relatively high Q factor ($Q(\text{Y2}) \approx 2600$), such as integrated spectrometers and filters.

Side-collection The analysis based on the quality factor is a necessary but not a sufficient condition to achieve good collection from the RW facet. In particular, detrimental losses in the slow-light region can reduce the emitted side-PL and are not accounted in Q-factor analysis. In addition, scattering from defects located in the supporting AlGaAs can further decrease the PL signal collected from the fibre. For these reasons, we measured the PL emission from objective and from the cleaved facet of the ridge, on the devices presented in the previous paragraph. Fig. 7.14 (a-c) shows the RT side-PL acquired exciting either the cavity region (red curves) or the PhC waveguide (blue curves) (d) for devices having $w = 1.1w_0$ and a varying barrier length from 2 to 4 holes ⁴. In this way, the resonances can be assigned to the FPs originated in the Wg close to the band-edge, or to the cavity modes. The latter can be then associated with the theoretical modes presented in par 7.4.2 from their expected wavelength difference. Although a quantitative estimation of the transmitted power is difficult since the effective power emitted by the dot ensemble is generally unknown, we observed that the integrated intensity of the cavity modes collected from the side is comparable to the top collection (fig. 7.14(d)). In fig.7.14 (c) for a barrier with $n_H = 4$, the Y1 mode is barely visible as expected from the analysis on the quality factors. Besides we observed that symmetric modes are also scarcely evident. This is associated with the possible thickness asymmetry between the membranes,

⁴ The measured laser excitation power is 800 μW in all of these measurements

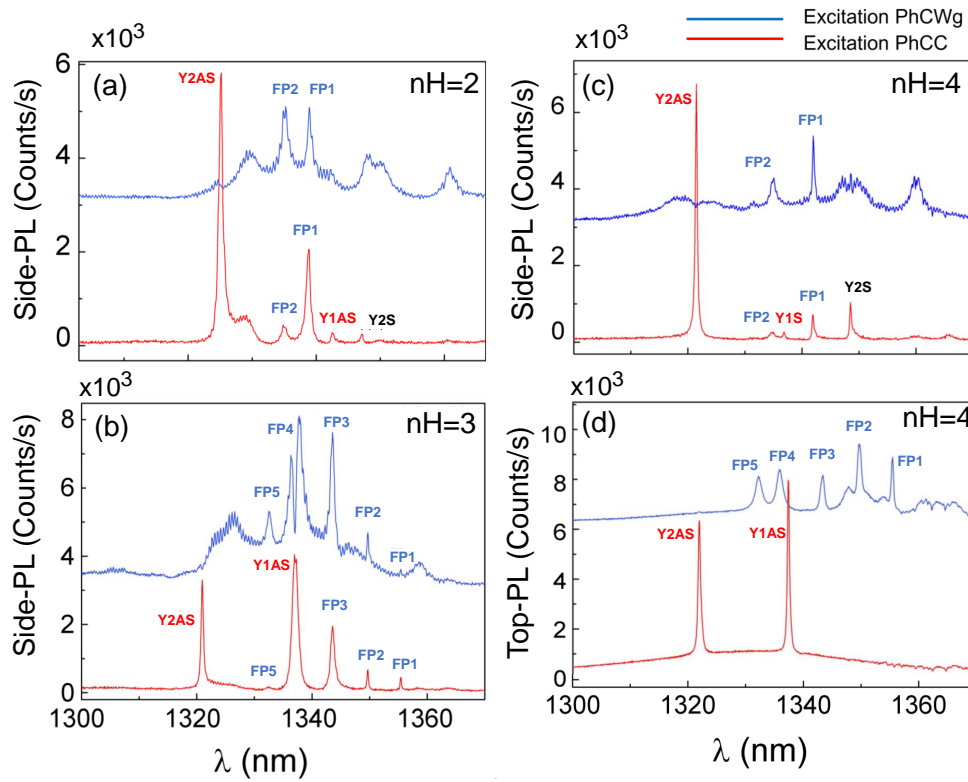


Figure 7.14: Micro-photoluminescence spectra acquired exciting either the PhCWG (blue lines) or the PhC cavity (red line) for several waveguide-coupled designs. (a-c) and (d) are acquired from the side facet of the RW and from the top, respectively. Designs employed (upper-right corner): L3m-nH with n indicating the number of holes composing the barrier. The width of the photonic crystal waveguide is $w = 1.1w_0$

that reduces the field overlap of the QD region with the S modes. A series of fringes are also visible in the side-PL spectra, due to the FP reflections at the RW-facet. Besides, a dip in the waveguide emission is evident as expected from the increased power transmitted in the cavity at the wavelength resonant with the coupled cavity mode. Compared with the transmission values estimated by the Q-factor analysis, the mode Y1as for $nH = 3$ shows a side-PL intensity higher than for $nH = 2$. We speculate that this originates from the fact that in the latter geometry this mode is off resonance with the FP modes of the waveguide 7.14 (a). Broadly speaking, the presence of the FPs in the spectral region of the mode Y1 complicates the Q-factor analysis discussed in the previous paragraphs, where a broadband waveguide mode is assumed. On the other hand, the mode Y2, is located in the linear dispersion part of the PhCWG and is not affected by the effects of the FP-coupling. For these reasons, it will be employed in the remaining part of this chapter. Importantly, one of main advantage of the side coupling with this optimized design is the fact the QD-emission can be easily transferred to a fibre, which is a clear benefit both for classical and quantum applications.

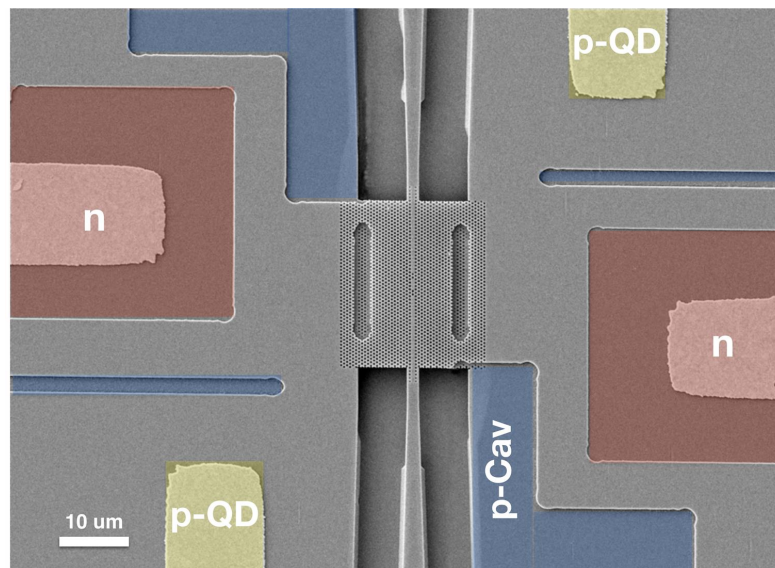


Figure 7.15: SEM picture of a Wg-coupled PHCC, equipped with a set of diodes for cavity actuation and quantum dot Stark-tuning. The cavity employed here is an L3 in-line coupled with two W1, which shows poor side-coupling efficiency

7.5 TUNING

ELECTRICAL INSULATION In this section we explored the possibility to apply the tuning techniques presented in chapter 3 to wg-coupled PhCCs. The presence of the waveguide imposes however some geometrical restrictions on the geometry of the contacts. The two series of contacts fabricated around the PhC region for QD and cavity actuation (widely employed in chapter 4 and 5), cannot be directly used due to the presence of the access waveguide. We designed the contact pads in a lateral configuration, with the waveguide running parallel to contact region, as shown in fig. 7.15. In the first fabrication runs, the devices exhibited bad IV characteristics with high reverse currents (hundreds of μA) and current flowing also below the expected threshold ($V_{\text{th}} \approx 1.3\text{V}$) of the diode (fig.7.16 (b)). This prevented the devices from tuning.

We attributed this effect to the current leakage between the two diodes to the rest of the chip. A similar behaviour has been reported by Shambat *et al.* [390] in the context of photonic crystal LEDs. We studied the possibility to isolate the device by etching a series of $\approx 3\text{-}\mu\text{m}$ wide trenches around the contact regions. These isolation trenches can be etched towards the bottom membrane (fig.7.17(c)) or through both membranes (fig.7.17(d)). IVs with small reverse currents (in the range of tens of nA), have been obtained adopting deeply etched trenches. We will make use of this electrical isolation scheme the remaining part of this chapter.

CAVITY TUNING Fig. 7.18 shows a typical LT (10K) cavity tuning experiment where the PL emission from the cavity is collected from the facet of the RW facet. The device employed here features an L3m cavity, diagonally con-

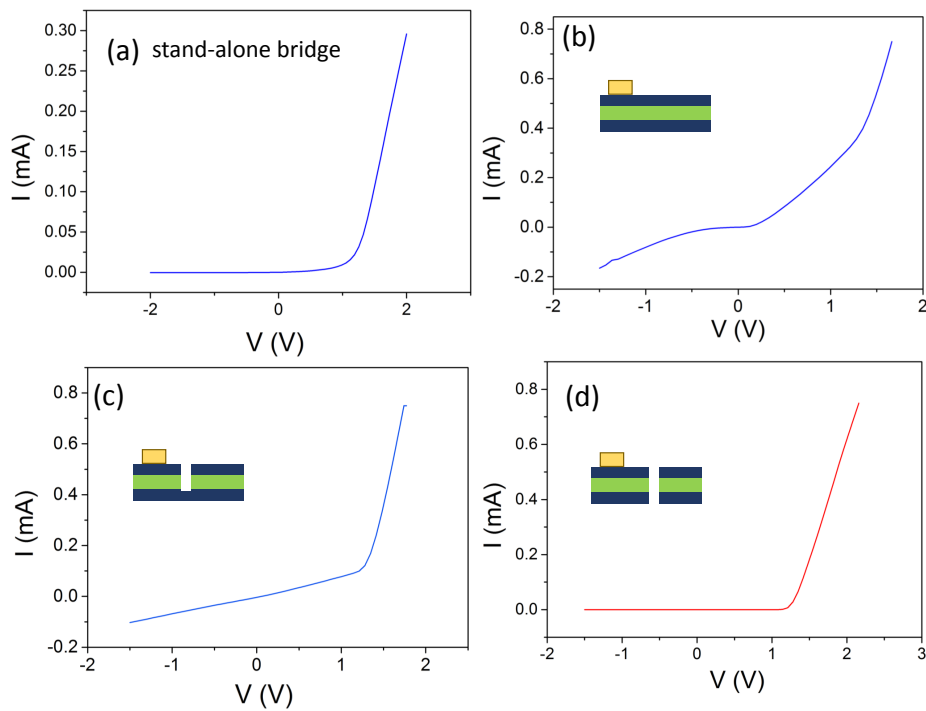


Figure 7.16: Comparison between the IV characteristic of the cavity diodes with different isolation trenches. IV-curve of the cavity diode of a device not coupled to waveguides (a), a wg-coupled device without isolation trenches (b), and with isolation-trenches etched until the AlGaAs spacer (c) or through both membranes (d)

nected to a photonic crystal waveguide with a barrier $nH = 4$, as discussed in paragraph 7.4.2. A maximum blue shift of 3.25 nm is obtained for this device, when the actuation voltage is varied from $V_{CAV} = 0V$ to $V_{CAV} = -3V$. The tuning rate increases as a function of the actuation voltage, as expected by the non-linear behaviour of the NOEMS. The cavity mode is identified with the $Y2_{AS}$. The maximum tuning range obtained experimentally for wg-coupled devices is ≈ 7 nm, smaller than the ones reported in stand-alone devices. We speculate that this reduced tuning range can be due to the residual strain associated with the presence nanobeam. The implementation of stress-releasing structures can increase this range, as demonstrated for standard stand-alone bridges. Nevertheless, this tuning range is sufficient to overcome the energy mismatch between different cavities fabricated on the same chip for QPIC applications. Importantly, the possibility to electrically shift the cavity wavelength in this waveguide-coupled geometry is crucial to implement an on-chip filter.

STARK TUNING In the next set of experiment we investigate the possibility to excite a tunable exciton line located in a PhCC and collect its emission 1 mm from the excitation area at the exit facet of the RW. Fig. 7.19 shows the LT side-PL intensity collected by exciting the cavity region of a second device ($nH = 4$) employing an above-bandgap excitation. As a reference, the top panel shows the PL spectrum of the cavity mode acquired with high

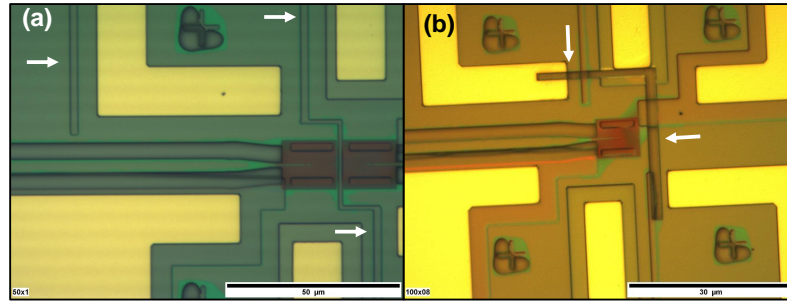


Figure 7.17: Optical microscope picture of devices realized with trenches (indicated by arrows) realized across the top membrane (left) and across both membranes (right)

excitation power ($700 \mu\text{W}$). This is characterized by a quality factor $Q \approx 1800$ and is identified with the mode Y_{2AS} described in the previous paragraphs. The bottom panel shows the single dot photoluminescence signal collected at lower power ($10 \mu\text{W}$) sweeping the QD voltage from 300 to 420 mV in forward bias. A clear enhancement of all the QD lines - and in particular of QD₁ indicated by an arrow - is evident when they cross the cavity mode central wavelength. The doublet denoted QD₂ is tentatively associated to the fine structure splitting of a neutral exciton. This wavelength splitting is increased from $0.09 \pm 0.02 \text{ nm}$ to 0.40 nm , due to the presence of the vertical Stark field [26]. In the next experiments, we focus on the line denoted as to QD₁.

LIFETIME MEASUREMENTS We carried out a series of time-resolved (TR) experiments to investigate the dynamics of the exciton line QD₁ for different values of the cavity-emitter detuning. When the dot is positioned on resonance with the cavity mode ($V_{\text{QD}} = 360 \text{ mV}$, $\lambda_1 = 1278.42 \text{ nm}$), a clear reduction of its decay time is visible compared to the case when it is blue-tuned (red dots, $V_{\text{QD}} = 420 \text{ mV}$, $\lambda_2 = 1277.42 \text{ nm}$) or red-tuned (black dots, $V_{\text{QD}} = 310 \text{ mV}$, $\lambda_3 = 1279.34 \text{ nm}$) with respect to the central wavelength of the cavity mode (λ_{CAV}). The emission from the bulk of the same sample (green dots) is reported for reference. Both the on-resonance and the off-resonance decays are well represented by a double exponential decay (continuous lines), where the slower decay ($>2 \text{ ns}$) is associated to the presence of the dark exciton transition. As extensively described in the previous chapters, the fast decay time of the dot in a PhC-diode is given by three contributions $\tau^{-1} = \tau_{\text{PhC}}^{-1} + \tau_{\text{Leaky}}^{-1} + \tau_{\text{tun}}^{-1}$, where τ_{PhC}^{-1} is associated with the decay rate into the cavity mode, τ_{tun}^{-1} is related to the tunnelling rate out of the dot, and τ_{Leaky}^{-1} is the (negligible) decay rate into the leaky modes. From the fit, we obtain $\tau_{\text{ON}} = (340 \pm 20) \text{ ps}$ ⁵ for the fast decay measured for the resonance condition, $\tau_{\text{OFF,blue}} = (710 \pm 30) \text{ ps}$ and $\tau_{\text{OFF,red}} = (650 \pm 30) \text{ ps}$ for the blue- and red-shifted configurations, respectively. Although the absolute detuning ($\Delta = |\lambda_{\text{CAV}} - \lambda_{\text{QD}}|$) from the cavity wavelength is larger for λ_1 , we observe that $\tau_{\text{OFF,red}} < \tau_{\text{OFF,blue}}$. This constitutes an indication

⁵ The error is estimated from the standard deviation of two TR-traces measured in the same experimental conditions

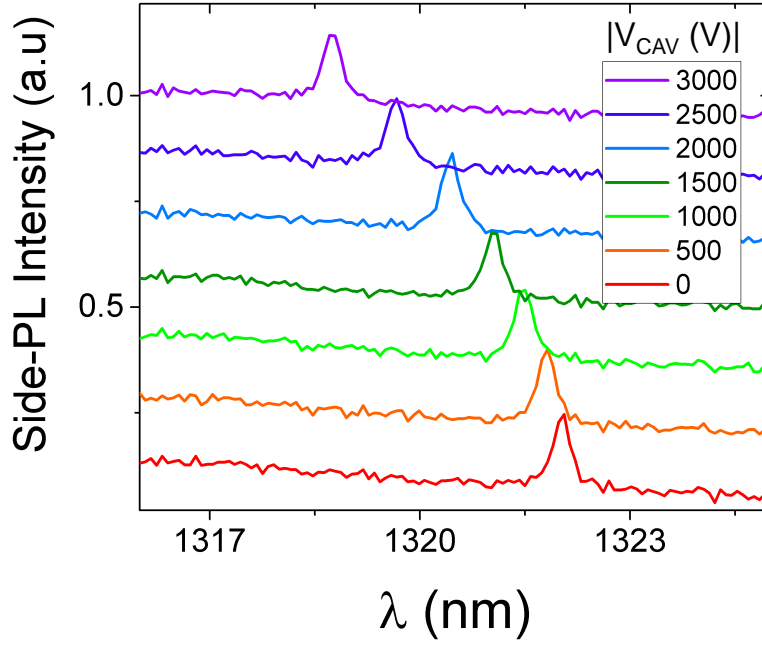


Figure 7.18: Cavity tuning experiment carried out on the fundamental Y_{2AS} of the wg-coupled L3m. The emission is collected from the side facet of the RW

that, differently from the sample with AlGaAs barriers, tunnelling effects are not negligible in this range of Stark-voltage values. We measured a linear dependence of the tunnelling rate on V_{QD} for dots embedded in a region located outside the PhC, for the narrow range of the Stark-voltage values investigated in these experiments. From a linear interpolation of τ_{tun}^{-1} and assuming that [107]

$$\tau_{\text{PhC}}(\lambda_i) = \frac{\tau_{\text{PhC}}(\lambda_{\text{CAV}})}{1 + 4Q^2 \left(\frac{\lambda_{\text{PhC}}}{\lambda_i} - 1 \right)^2} \quad (7.5)$$

we derived $\tau_{\text{PhC}} \approx 550$ ps. Using the extracted decay time in the cavity mode, we can then calculate a Purcell factor as $F_p = \frac{\tau_{\text{bulk}}}{\tau_{\text{PhC}}} \approx 2.6$.

The efficient transfer of Purcell-enhanced single photons generated in a PhCC to a ridge waveguide has been previously demonstrated, employing either a monolithic approach relying on a single material (GaAs)[115] or, more recently, adopting an hybrid GaAs/SiN photonic crystal nanobeam [81]. However, in the former demonstration, the QD-energy was controlled by changing the global temperature of the sample. As we discussed in chapter 1, this dramatically increases the dephasing rate, whereas it is not compatible with the use of on-chip SSPDs. On the other side, in the latter study [81] the deposition of nitrogen was employed to shift the cavity wavelength with respect to the exciton transition, while the control on the quantum dot wavelength, needed in multi-source experiments, was not addressed. As shown in these paragraphs, the implementation of electrical gates in a waveguide-coupled double-membrane device allows controlling the energy of emitters and cavity resonances funnelled into a waveguide channel, and therefore

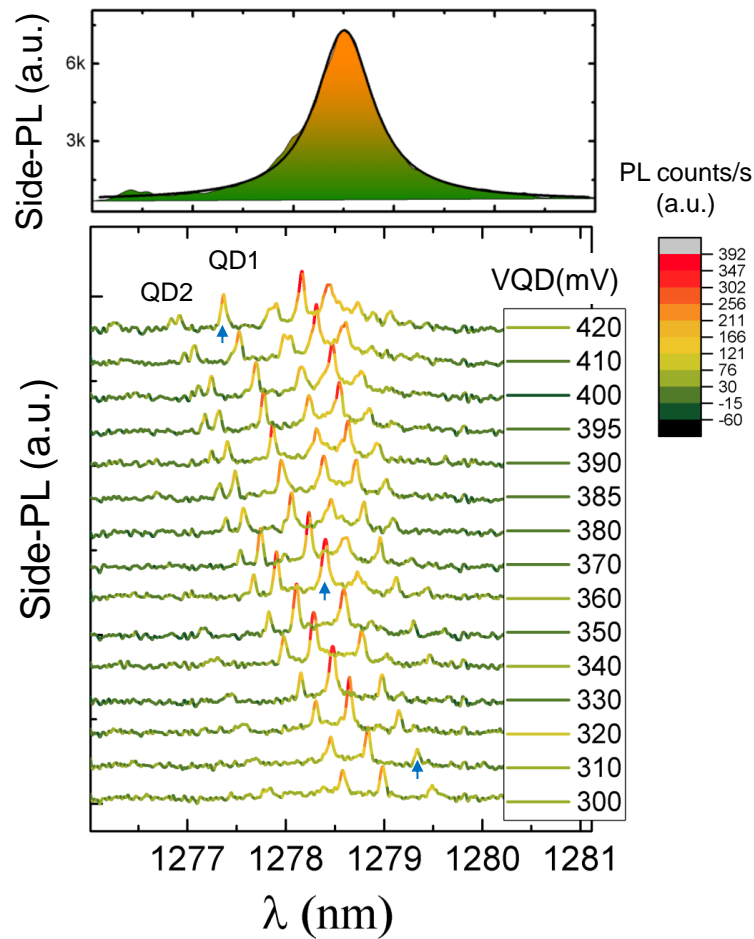


Figure 7.19: Electrical energy control of single dots located in a waveguide-coupled cavity mode. The top panel shows the side-PL intensity of the cavity mode, acquired with high excitation power. The bottom panel displays the single-exciton PL acquired while sweeping the QD-voltage

represents a clear advance towards electrically-regulated quantum circuits based on deterministic single-photon sources.

7.6 BEAM SPLITTER

Once the link between the photonic crystal and the ridge waveguide is realized, a number of optical components developed for classical photonic circuits, such as phase-shifters and couplers, can be realized to implement LOQC functionalities or boson sampling circuits. Beam splitters operated at the single-photon regime are at the core of many of these schemes. After the first demonstration of a probabilistic CNOT gate employing four beam splitters (BSs) on a silica-on-silicon platform[342], the number of BSs employed for integrated single-photon applications has gradually increased. Recently, up to 30 beam splitters interconnected in a complex network have been adopted in boson sampling protocols [53]. However, most of these

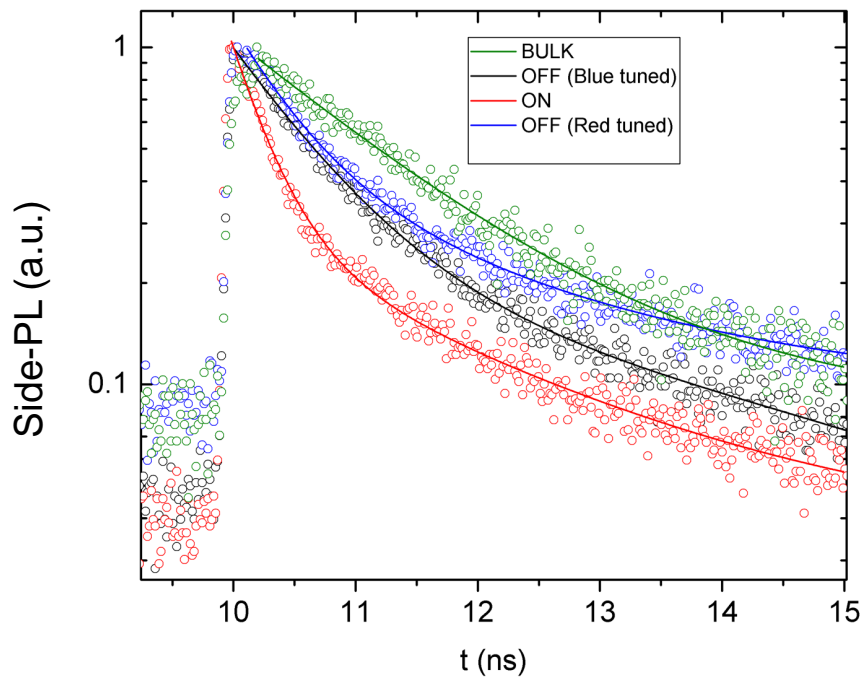


Figure 7.20: Decay curves of QD1 positioned at several energies with respect to the cavity mode, as indicated in fig 7.19. (red) On resonance, (black) blue-shifted (blue) red-shifted, (green) bulk decay traces). The continuous lines are obtained from a single (for the bulk) or double exponential fit

experiments still rely on external sources to inject single photons into the propagating mode of the waveguides, resulting in detrimental losses and stability issues. An appealing solution to overcome these problems consists in integrating quantum emitters within a passive photonic circuit. In this context, only a few works have shown the possibility to route and to split the emission from single excitons with an on-chip architecture. Specifically, QDs have directly integrated with ribs waveguides [186, 386, 408] and with suspended nanobeams [348] surrounded by an air-cladding, in order to carry out an integrated HBT experiment. The former approach relies on the excitation of emitters with relatively low beta-factors (estimated in the range of 7%) related to the large mode volume of ridge waveguides, which leads to low extraction efficiencies. On the other hand, higher extraction efficiencies can be obtained in photonic nanobeams. However, the length of these structures is limited by the occurrence of bending, buckling and - in general - mechanical instabilities. These drawbacks can be circumvented by taking the advantages of both approaches using an hybrid solution, where the photon extraction is carried out in a photonic crystal waveguide region which can provide near-unity beta factors [13], while the linear manipulation of the photonic state is obtained using standard ridge waveguides, illustrated in the previous paragraphs. Besides, if the a double-membrane platform is employed, the accurate control of the PhC node is possible as well.

In this section, we present the design a 50:50 beam splitter based on a multimode interferometer, and then we integrate this component in our GaAs

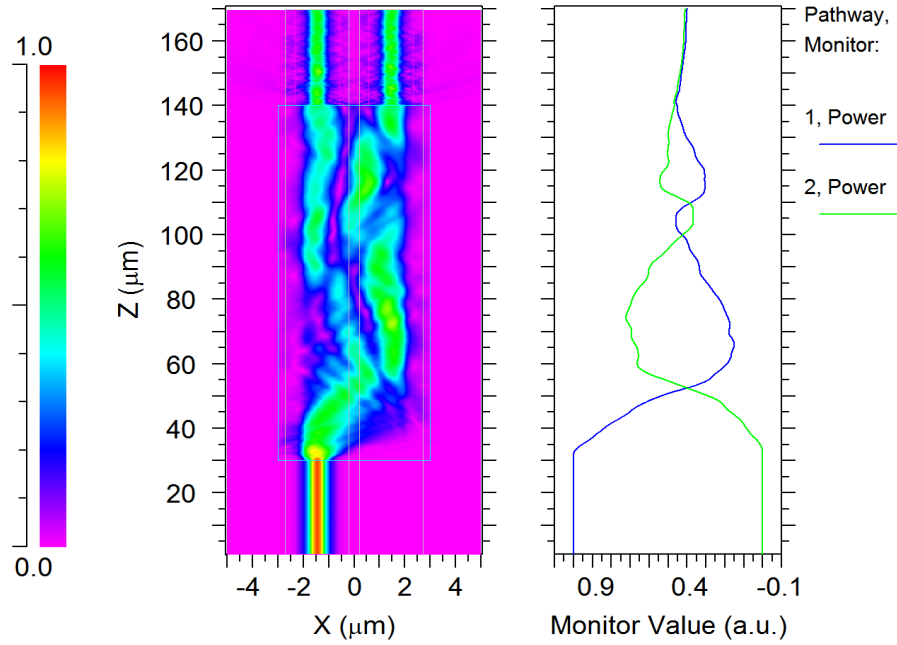


Figure 7.21: Simulated intensity profile -injected from the left input waveguide-through the MMI (left panel). The power at the two output waveguides is shown on the (right panel) as a function of the longitudinal coordinate Z

double-membrane platform. Using this strategy, a Hanbury-Brown-Twiss (HBT) prototype experiment is carried out on single photons generated from emitters integrated in a PhC waveguide. The light emitted from a PhC source is splitted on-chip and the correlation function is measured using off-chip detectors. In the following, we firstly present the design of a 2x2 splitter based on a trapezoidal double-membrane waveguide. Then, we discuss its optical characterization at classical and single-photon level.

DESIGN Multimode interference structures (MMIs) are integrated optical components able to split and redirect the power injected from N input waveguides into M output waveguides. These devices typically consist of a wide waveguide that supports a relatively large number of propagating modes. The device is based on the fact that a number of modes can be excited inside the MMI region, each of them propagating with a different phase velocity (β) [399]. After a certain length, these modes can interfere constructively. In order to describe this interference, the optical input can be expanded in the basis formed by m -countable eigenmodes

$$E(x, y, 0) = \sum_{\nu=0}^{m-1} c_{\nu} \psi_{\nu}(x, y) \quad (7.6)$$

After a certain propagation length, the field will evolve according to the equation

$$E(x, y, z) = \sum_{\nu=0}^{m-1} c_{\nu} \psi_{\nu}(x, y) \exp(i(\phi_{\nu} z)), \quad (7.7)$$

where ϕ_ν is the propagation constant of the mode ψ_ν . It can be shown that $\phi_\nu = \frac{\nu(\nu+2)}{3L_\pi}\pi$ in a step-index multimode waveguide [399], where $L_\pi = \frac{\pi}{\Delta\beta}$ is the beating length between the two lowest-order modes of the MMI and $\Delta\beta$ is the difference in their propagation constant. For $\bar{z} = \frac{p}{2}(3L_\pi)$, where p is an integer number, the field intensity is symmetric with respect to the longitudinal axis of the MMI, i.e. $|E(x, y, \bar{z})|^2 = |E(-x, y, \bar{z})|^2$ [399].

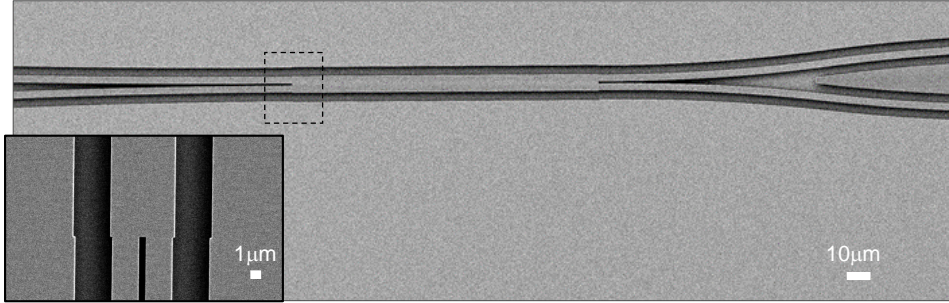


Figure 7.22: SEM images of the fabricated 2x2 multi-mode interferometer. (Inset) Zoom in on the input ports. The radius of the input and output S-bends is $1191 \mu\text{m}$ and $1740 \mu\text{m}$, respectively. The radius of the input S-bend is designed in order to employ the beam-splitter for experiments with closely spaced sources (see next chapter)

Therefore, given a certain MMI-width, and knowing $\Delta\beta$, a 50-50 splitting ratio can be designed with a length of \bar{z} . Beam propagation methods (BPM) have been employed to simulate the spatial evolution of the electric field intensity along the MMI. In particular, the splitting ratio of the MMI can be adjusted by optimizing the length of the MMI. Fig. 7.21 shows the 3D simulated evolution of the input mode as a function of the propagation distance. The fundamental eigenmode of the RW is launched at left input waveguide ($\lambda = 1.27 \mu\text{m}$) and the power is monitored at both output waveguides (green and blue curves, right panel). These simulations have been carried out by dr. F. Pagliano (TU/e). The separation between the inner edge of the access waveguides is set to $0.6 \mu\text{m}$, while the width of the MMI is $6 \mu\text{m}$. The simulated optimal value of the length of the MMI is $110 \mu\text{m}$, obtaining a theoretical splitting ratio of 0.5/0.5 and an insertion loss of -1.6 dB .

Following the recipe presented in chapter 2, we fabricated the beam-splitter shown in Fig. 7.22 with a varying length from $L = 104 \mu\text{m}$ to $116 \mu\text{m}$, on a DM structure with membrane thickness $t = 170 \text{ nm}$ and inter-membrane gap $d = 240 \text{ nm}$.

CHARACTERIZATION OF THE BEAM SPLITTER In order to validate the MMI design, we measured the power transmitted through the two output ports of the MMI, when one input is excited with a laser diode (wavelength = 1270 nm , laser power $600 \mu\text{W}$). These measurements have been carried out by dr. S. Birindelli (TU/e) and dr. F.M. Pagliano (TU/e). We define the transmission coefficients T_{ij} as the ratio between the power collected from the output j and the power injected in the input i . The experimental transmission coefficients are shown in Fig. 7.23 for the TE (left) and TM (right) mode. An optimum length of $L_{\text{MMI}} = 112 \mu\text{m}$ is found experimentally giving a split-

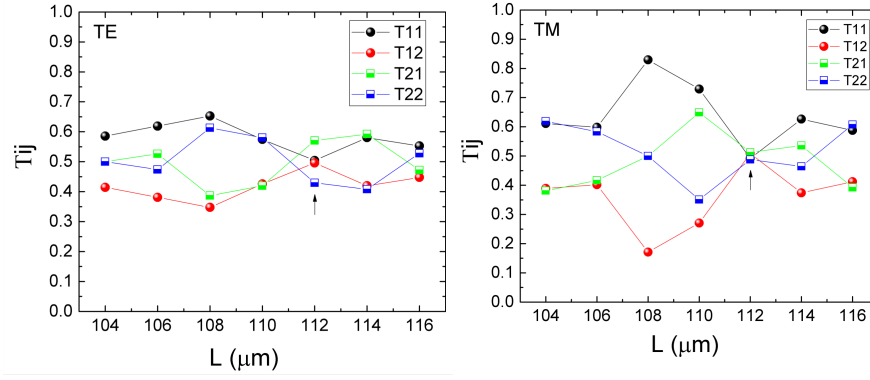


Figure 7.23: Transmission coefficients T_{ij} measured injecting light in the input i and collecting j , for two orthogonal polarization: left (TE), right (TM). The arrow indicated the experimental optimal value of the MMI length to obtain a 50:50 splitting ratio

ting ratio close to 50/50 for both polarizations. A small deviation from the designed value can be due to the discrepancy between the simulated AlGaAs profile and the experimental one. Notably, we obtain $L_{MMI,TE} = L_{MMI,TM}$. This can be explained by the fact that the simulated difference in the propagation constants between the fundamental and first-order modes of the MMI presents similar values for the TE ($\Delta\beta_{TE}$) and the TM ($\Delta\beta_{TM}$) modes. In fact, from the simulations we obtain $\Delta\beta_{TE} = 39.45 \text{ mm}^{-1}$ and $\Delta\beta_{TM} = 39.65 \text{ mm}^{-1}$, which results in a length ratio $\frac{z_{TE}}{z_{TM}} = 1.005$. An alternative way to characterize the beam splitter exploits the internal emitters as a broadband source. This technique consists in exciting several parts of the device with a fixed excitation power and a fixed collection at the end-facet of the RW. Fig.7.24 shows a typical LT side-PL spectrum of the ground state emission of the QDs, collected exciting four different points of the device. The blue and red curves have been collected exciting the two input waveguides (I_1, I_2), while the PL signal collected focusing the laser spot at the output of the MMI (I_3) and close to the end of ridge waveguide (I_4) are shown in green and black, respectively. Assuming that the dot-density is constant over the sample, we can estimate the splitting ratios ($\Xi_1 = I_1/(I_1 + I_2)$, $\Xi_2 = I_2/(I_1 + I_2)$)⁶ and the insertion loss of the beam splitter (η_{MMI}) and the s-bends (η_S), by integrating the dot-emission over the wavelength range of the ground state of the dot (Γ)

$$\eta_{MMI} = \frac{\int_{\Gamma} I_1(\lambda) d\lambda + \int_{\Gamma} I_2(\lambda) d\lambda}{\int_{\Gamma} I_3(\lambda) d\lambda} \quad \eta_S = \frac{\int_{\Gamma} I_3(\lambda) d\lambda}{\int_{\Gamma} I_4(\lambda) d\lambda} \quad (7.8)$$

By averaging over two nominally-identical devices we obtain $\Xi_1/\Xi_2 \approx 46/54$ and $\eta_{MMI} = 0.77 \pm 0.08$ and $\eta_S = 0.73 \pm 0.1$. The value of the insertion loss for the MMI is similar to the calculated one. A small asymmetry can be observed in the spectra of I_1 and I_2 presented in fig.7.24, which is not expected from simulations. We ascribe this discrepancy to the small fabrication deviations in the angle of the trapezoidal support, which can induce

⁶ Note that - in general- $\Xi_1 = \frac{T_{11}}{T_{11}+T_{12}}$, where T_{ij} are the transmission coefficients defined before

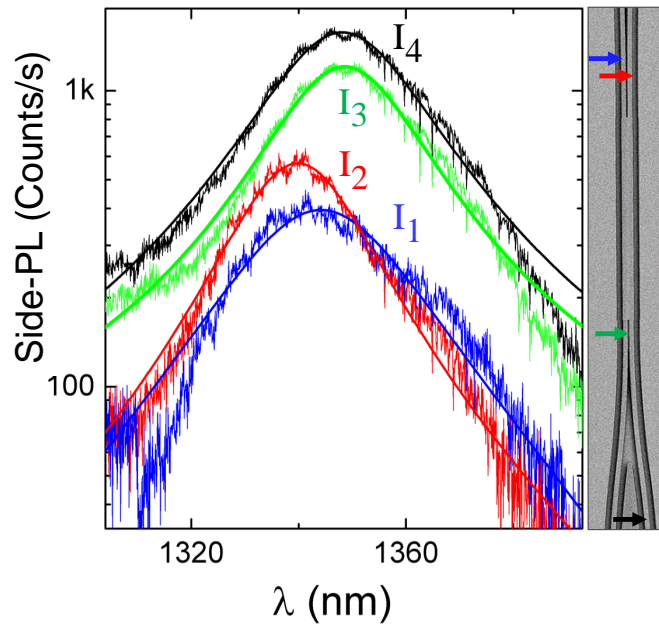


Figure 7.24: μ -PL signal acquired from the RW-facet exciting different spots (right panel) of the device, while keeping the excitation power and the excitation area constant

a wavelength-dependent imbalance between the outputs of the BS, as discussed in [37, 159]. It is worth mentioning that in these measurements the TM mode of the access ridge waveguide is not excited, since QDs emit predominantly in the plane. The S-bend transition can be further optimized introducing a suitable set of lateral offsets between the RWs and the beam splitter.

7.7 INTEGRATED HANBURY BROWN-TWISS EXPERIMENT

In the following set of experiments, we investigate the operation of the beam splitter in the single-photon level, by performing an Hanbury Brown and Twiss experiment on the light generated by an integrated quantum dot. To this end, a single-exciton transition located in the PhCWG region of the device is optically excited with an above-bandgap laser with a power of $P \approx 500$ nW and the generated light is splitted in two arms using the integrated MMI (fig.7.25, left panel). Then, the QD-emission is collected by two distinct fibres positioned at the cleaved facet of the RWs in a butt-coupled configuration and sequentially acquired by a spectrometer.

Fig. 7.25 (a) and Fig. 7.25 (b) show the side-PL spectra acquired at the two arms (A and B) of the beam splitter. Three different QD-lines, labelled QD3, QD4 and QD5 are visible in both spectra. Specifically, the excitonic transition QD4 located at ≈ 1298 nm shows a splitting ratio of $\approx 56/44$, in agreement with the splitting ratio calculated in the previous paragraph. No-

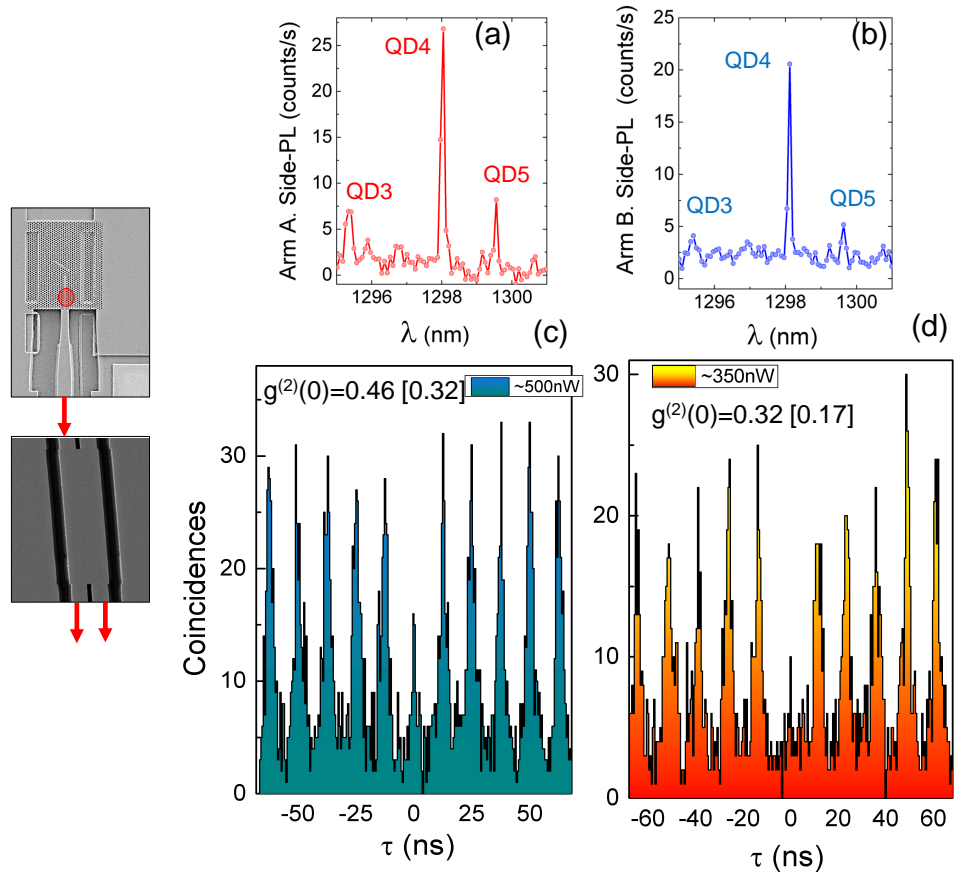


Figure 7.25: Integrated HBT experiments carried out exciting a dot in the photonic crystal waveguide (left panel). (a) and (b) side-PL spectra collected at the output of arm A and arm B of the beam splitter, respectively. (c) and (d) raw coincidence histogram collected with an excitation power of 500 nW and 300 nW, respectively

tably, the spectrometer count rates in these experiments are comparable with count rates obtained in top-collection experiments from similar dots coupled to PhCC (see for example Chapter 4), which indicates the efficient routing of the dot-emission across the chip. In order to validate the single-photon operation of the beam splitter, the dot line QD4 is isolated from the other lines using off-chip filters. In particular, a pair of long-pass filters (cut-off wavelength 1050 nm) and tunable-filters are inserted in the two off-chip optical paths of the setup (I/O 3(A) and I/O 2 in fig. 7.1). Next, each optical path is sent to an SSPD. The electrical signals generated by the detectors are acquired by a time-correlated SP counting module (PicoHarp 300) for correlation measurements. Fig. 7.25 (c) shows the raw coincidences histograms acquired when QD4 is excited with a pulsed laser diode ($P_1 \approx 500\text{nW}$) with a repetition rate of 80 MHz. The bin resolution is 512 ps. A suppression of the zero-delay peak is evident compared to the peaks at a multiple of the repetition period ($T_p = 12.5$ ns). This constitutes a strong evidence that the non-classical nature of these emitters is preserved after the beam splitter. For a perfect SP source and a balanced beam splitter, the central peak is zero, corresponding to the complete suppression of photon pair detection. We attributed the discrepancy from the ideal case to the relatively high

pumping level in this experiment, resulting in an increased probability of generating of multi-photon states [393]. To further investigate this effect, we repeated the same experiment but with a lower excitation power ($P_2=300$ nW). In this experimental setting, a reduced zero-delay peak is observed as shown in fig. 7.25 (d). It is worth mentioning that a constant background is evident in all the delay channels for these experiments and is attributed to the combination of the residual stray light in one of the free-space setups and the dark counts of the detectors (≈ 20 Hz). The background level (bkg) can be roughly estimated by the average of the coincidence events at a period $T_p/2 + m \cdot T_p$, with $m = \{\pm 1, \pm 2, \dots\}$. In this way, we derived $\text{bkg} = 4$ and $\text{bkg} = 3$ coincidences/channel for the two values of power employed. In order to quantitatively estimated the purity of this SP source,

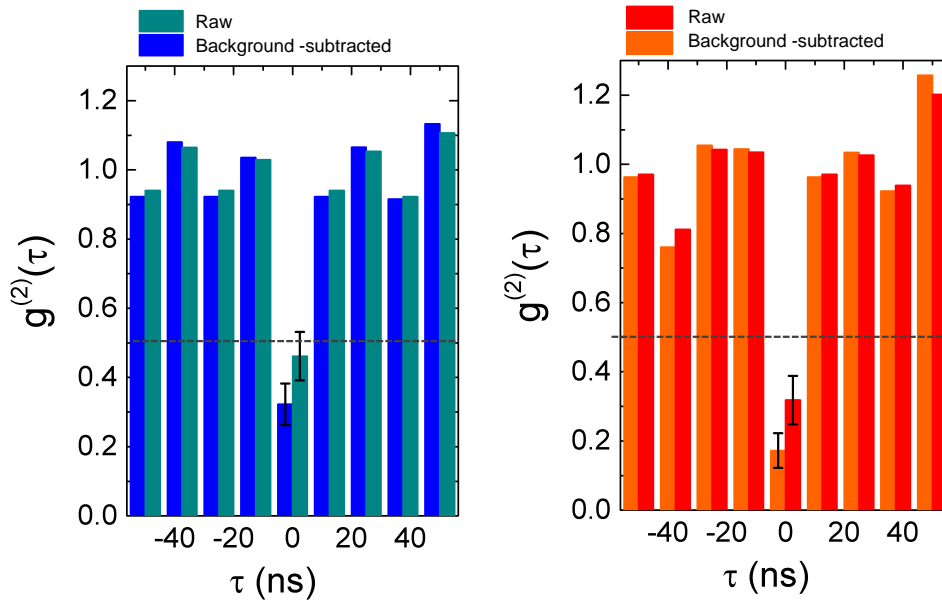


Figure 7.26: Normalized second-order autocorrelation function for the dot QD4 excited with 500 nW (left panel) and 300 nW (right panel). Both the raw values and the values corrected with the background subtraction are here reported

the normalized second-order autocorrelation function is calculated by dividing the area of the coincidence peaks with the average area of the peaks at $\tau \neq 0$ (A_m). Fig. 7.26 shows the histograms obtained for P_1 and P_2 , adopting an integration window of 4ns. The values of the raw second-order correlation function at zero-delay are $g^{(2)}(\tau = 0, P = P_1) = 0.46 \pm 0.07$ and $g^{(2)}(\tau = 0, P = P_2) = 0.32 \pm 0.07$ for the two power values employed. Here the error is calculated as $\sigma_{g^{(2)}(0)} = g^{(2)}(0) \cdot 2\sigma/A_m$, where σ is the standard deviation of the area of the first 10 coincidence peaks around $\tau \neq 0$. The values of the $g^{(2)}(\tau)$ corrected with the subtracted background are also reported in fig. 7.26, giving $\bar{g}^{(2)}(\tau = 0, P = P_1) = 0.32 \pm 0.05$ and $\bar{g}^{(2)}(\tau = 0, P = P_2) = 0.17 \pm 0.06$. From these results, we conclude that the single-photon nature of the QD-emission is maintained after the beam splitter, since $g^{(2)}(\tau = 0) < 0.5$.

7.8 CONCLUSIONS

The implementation of a tunable source integrated with a waveguide channel is an unquestionable key goal in quantum photonic integrated circuits. Here, we have demonstrated the efficient funnelling of the cavity emission from an optimized PhC cavity into a mechanically-stable ridge waveguide. By a careful experimental optimization of the PhC layout and of the contact geometry, cavity tuning is achieved for modes coupled to an in-plane waveguide. The possibility to electrically program the cavity wavelength of this device upon the application of electro-mechanical forces, combined with its relatively optical sharp resonances ($\text{FWHM} \approx 0.5 \text{ nm}$), represents an important improvement towards on-chip filtering of a single-exciton lines. Besides, in contrast to thermo-optic tuning, the generated thermal load is negligible since these devices are operated in reverse bias. In principle, this feature makes this architecture compatible with the use of on-chip SSPDs. The cavity tuning range (3.25 nm) is limited in these experiments by the residual stress induced in the fabrication process, which can be suppressed by implementing stress-releasing structures [178]. Importantly, we have shown that single exciton transitions located in the wg-coupled PhC cavity can be transferred to the end of the ridge waveguide and collected by a fibre. The ability to tune their energy into resonance with the central wavelength of the cavity mode via the quantum-confined Stark-effect allowed demonstrating a two-fold Purcell-enhancement of their emission. Moreover, the wavelength control over fibre-coupled single photons emitting in the telecom band, open new possibilities for metropolitan quantum cryptography based on wavelength division multiplexing. Furthermore, by using an array of fibres coupled to the output of the ridge waveguides, the generation of a parallel stream of single photons from a single chip is practically feasible, opening the way to applications that require multiple SP sources at the cost of a single cryogenic environment. Finally, the integration of this platform with a beam-splitter - essential to build on-chip non-deterministic quantum gates - is here examined. The design of this integrated component is validated using both external and internal sources. The generation and routing of single photons, extracted from a PhC node, is demonstrated along with an integrated anti-bunching experiment with source and splitter on the same chip. The current value of the single-photon purity is mainly limited by the background originated by the non-resonant excitation and can be further be improved by adopting resonant or quasi-resonant pumping strategies. Finally, the combination of the single-photon source, the beam-splitter and a phase shifter would open the way to on-chip switching of single-photons, particularly useful in future time-multiplexed single-photon experiments.

8

INTEGRATION OF MULTIPLE SINGLE-PHOTON SOURCES

In this chapter, we discuss our efforts towards the realization of a quantum photonic chip operating with several single photons. As a demonstration, we consider the case of integrated two-photon interference experiments from two remote quantum dots. The tunable architecture presented in the previous chapters has been adopted to control the relative energies of separate cavities and emitters. Besides, we discuss the coherence properties of these emitters in a nano-structured photonic environment, along with the preliminary results on a bunching experiment. These measurements have been carried out in collaboration with dr. S. Birindelli (TU/e).

8.1 INTRODUCTION

Apart from quantum key distribution, most of the schemes in quantum information processing require indistinguishable single photons. These include linear optical quantum computing [213], quantum teleportation [132], and the generation of NOON states for quantum sensing [141]. Indistinguishability demands that single photons must have identical properties, i.e polarization, energy, time and spatial profiles. The degree of indistinguishability of two single-photons is operationally quantified combining them on a balanced beam splitter [164]. The outcome of this experiment cannot be predicted by classical electromagnetism: the photons will always exit together from one output of the beam splitter. This comes from the counter-intuitive argument that the probability amplitudes of the trajectories that produce a single-photon at both outputs interfere destructively, producing a final state that can be written as $|\Psi\rangle = \frac{1}{\sqrt{2}}(|20\rangle + |02\rangle)$. After the pioneering experiment of Hong, Ou and Mandel using SPDC sources [164], this so-called quantum coalescence (or photon bunching) has been investigated employing a number of systems, namely trapped atoms [38], donor impurities in quantum wells [375], nitrogen vacancy centers in diamond [36], organic molecules [241], and semiconductor quantum dots. In particular, since the first demonstration in 2002 [377], two photon interference (TPI) from photons emitted by a single quantum dot has been explored in many studies [91, 133, 155, 210, 275, 302, 441, 444, 458]. In these realizations, the QD-emission is typically delayed by employing an imbalanced Michelson or a Mach-Zehnder interferometer and TPI takes place between consecutive single photons originated from the same source. A strategy to implement small QIP protocols and boson circuits [254, 454] is based on the time multiplexing of the emission generated by a single QD. This scheme involves splitting and redirecting a train of single-photon pulses generated by a bright QD transition into a number of different spatial channels. However, in the context of QPICs, implementing integrated delays to synchronize single-photon pulses

is particularly challenging. Besides, it is clear that the use of time multiplexing schemes drastically reduces the single-photon rate when the number of channels is increased. It is expected that advanced QIP schemes, such as the realization of quantum networks [206], will benefit from the generation of indistinguishable photons generated from distinct emitters. In this direction, TPI experiments have been realized employing distant QD sources, both in CW- [217, 327] and pulsed- excitation [86, 120, 132, 140, 142, 203, 358, 426]. In most of these demonstrations, the emitters were located in two samples placed inside two different cryostats. More recently, TPI has been also demonstrated from the far-field collection of the emission of dots located in the same sample [217], by exploiting pre-characterized dots integrated with microlenses [426] and PhC cavities [203]. In the context of quantum photonic integrated circuits, generating and interfering a pair of single photons on the same chip stands for an ambitious goal, since it represents a step forward in the realization of parallel arrays of indistinguishable single-photon sources interconnected via a linear circuit.

8.2 DESIGN

Fig 8.1 shows the fabricated chip for integrated HOM experiments. This comprises two sources equipped with four different diodes, for the simultaneous control of the energy of the cavity modes and quantum dots of each source. The fabrication employs the process described in chapter 2.

The two PhC sources are integrated with ridge waveguides, which are then connected to the inputs of a MMI via two S-bends (S_1, S_2) as shown in figure 8.1(top panel). We adopt the optimized designs of PhC cavity and the MMI presented in the previous chapter. The output of the MMI is integrated with two S-bends (S_3, S_4), which redirect the QD-light to the cleaved part of the wafer. The radius of curvature of S_1 and S_2 (S_3 and S_4) is $1191 \mu\text{m}$ ($1740 \mu\text{m}$). In the following experiments, two external lensed fibres are positioned at the end of the two RWs to collect the QD-emission from both facet of the RWs, as described in par.7.2. For the sake of clarity, we will refer to the pair of PhC structures as *device* and to the single PhC structures as *node A* and *node B*. The distance between the PhC nodes ($w = 22\mu\text{m}$) is designed to excite both nodes with a pair of laser spots focused by the same objective. A set of isolation trenches is deeply-etched around the device and in between the two PhC nodes for electrical isolation. This was found to be necessary in order to minimize the electrical cross-talk. For the cavity and QD diodes we employ two series of mesas in the $\{n\text{-p}_{\text{QD}}\text{-n-p}_{\text{CAV}}\text{-n}\}$ configuration, which is compatible with the use of both 3-finger (G-S-G) and 4-finger (G-S-G-S) probes.

8.3 CROSS-TALK CAVITY TUNING

First and foremost, we investigated the possibility to individually control the photonic crystal resonances of two adjacent cavities, with the aim of bringing two cavity modes into mutual resonance. Fig. 8.2 (left panels)

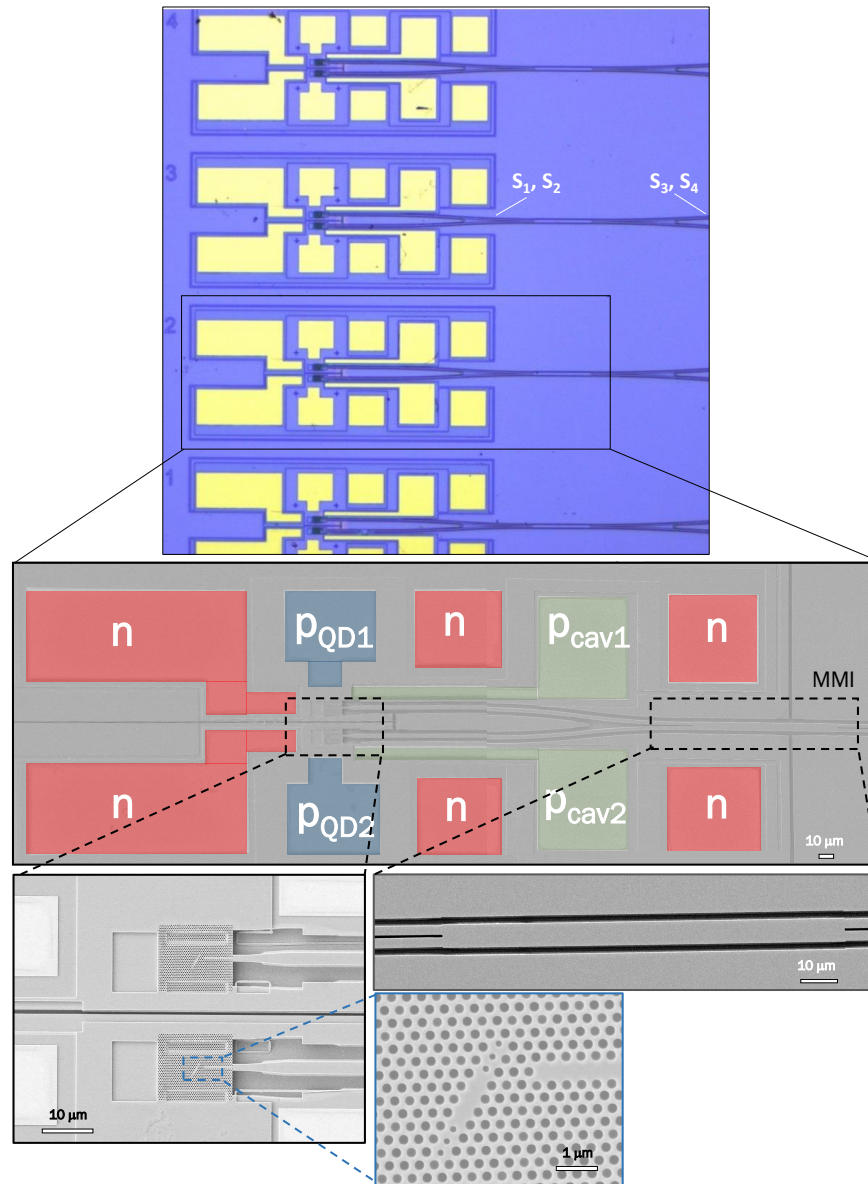


Figure 8.1: Optical (top) and SEM pictures (bottom) of the fabricated chip for two-photon interference experiments. Four sets of diodes are fabricated to tune the cavity and quantum dot energy of the two cavity-emitter systems. Only the top membrane of the double-membrane architecture is shown

shows the PL signal collected from one output of the beam splitter, by exciting the cavity region of a photonic crystal node (A). PL spectra are acquired while varying either the voltage of its cavity-diode (V_{CAV}^A , top panel) or the voltage of the adjacent node (V_{CAV}^B , bottom panel). In these LT-experiments, the power of the laser diode (780 nm) is sufficiently high ($1000 \mu\text{W}^1$) that the emission from the cavity mode is observed. A blueshift of the PhCC mode is observed in both configurations, indicating the presence of a non-negligible crosstalk. The direction of the shift upon the effect of electromechanical ac-

¹ In this chapter the power is measured at the input of the top arm in fig. 7.1. The power impinging on the sample is ≈ 200 times smaller

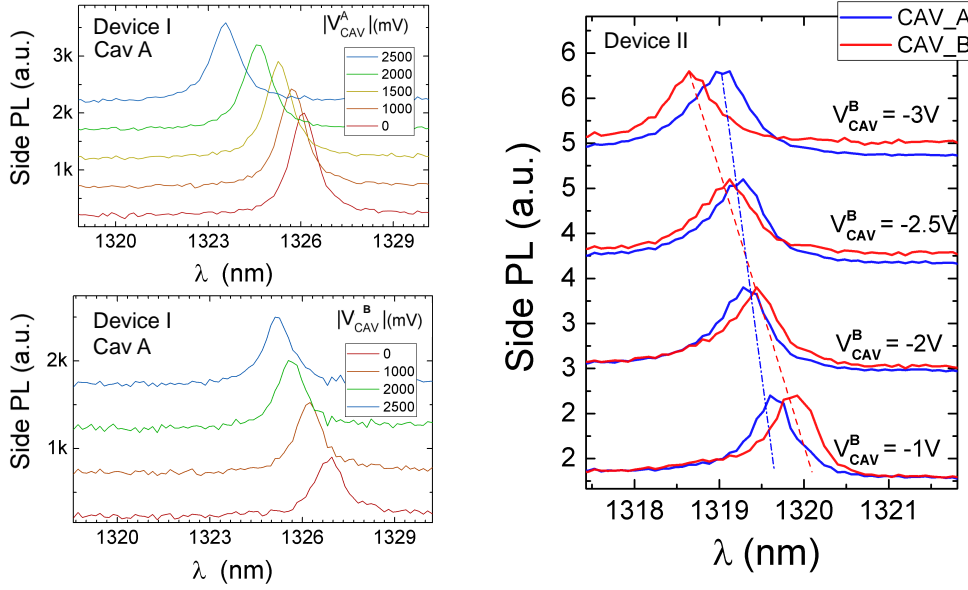


Figure 8.2: (left panels) Electromechanical actuation of a cavity mode obtained controlling the voltage applied to its cavity-diode (top). (bottom) Cavity cross-tuning obtained when the cavity-diode of the neighbouring device is controlled. (Right panel) Resonance condition obtained between the modes of a PhC pair, by controlling the electromechanical voltage of one node. The dashed lines serve as a guide for the eye

tuation indicates that this mode is anti-symmetric. The magnitude of the wavelength shift ($\Delta\lambda_{CAV}^A$) when V_{CAV}^A is varied is roughly a factor of two larger than the shift ($\Delta\lambda_{CAV}^B$) obtained controlling V_{CAV}^B . It is convenient to define the cavity cross tuning coefficient ξ_{CAV} as

$$\xi_{CAV} = \frac{\Delta\lambda_{CAV}^B}{\Delta\lambda_{CAV}^A}. \quad (8.1)$$

By repeating this procedure on four devices - having nominally identical mechanical and electrical properties - we obtain $\xi_{CAV} = 0.53 \pm 0.11$. We speculate that this cross-talk takes place at the MMI, which constitutes the only electrical path interconnecting the two nodes. In the future, the use of a directional coupler or better isolation schemes - such as proton implantation [418] or the removal of doped layers in the passive region- might reduce this effect. Despite the fact that electromechanical tuning does not provide an independent control over the cavity wavelengths in these fabricated chips, the resonance condition between a pair of PhCC nodes can be achieved, as displayed in fig.8.2 (right panel). Here, the PhCC region of node A (blue line) and node B (red line) are optically pumped, while the cavity voltage of the node B is swept from -1V to -3V. The fabrication disorder induces an initial wavelength mismatch between these resonances, $\Delta\lambda_{AB} = \lambda_A - \lambda_B = 0.30$ nm at $V_{CAV}^B = -1$ V. For $V_{CAV}^B = -3$ V, the detuning has a different sign, $\Delta\lambda_{AB} = -0.36$ nm, indicating the suppression cavity detuning at $V_{CAV}^B \approx -2.2$ V.

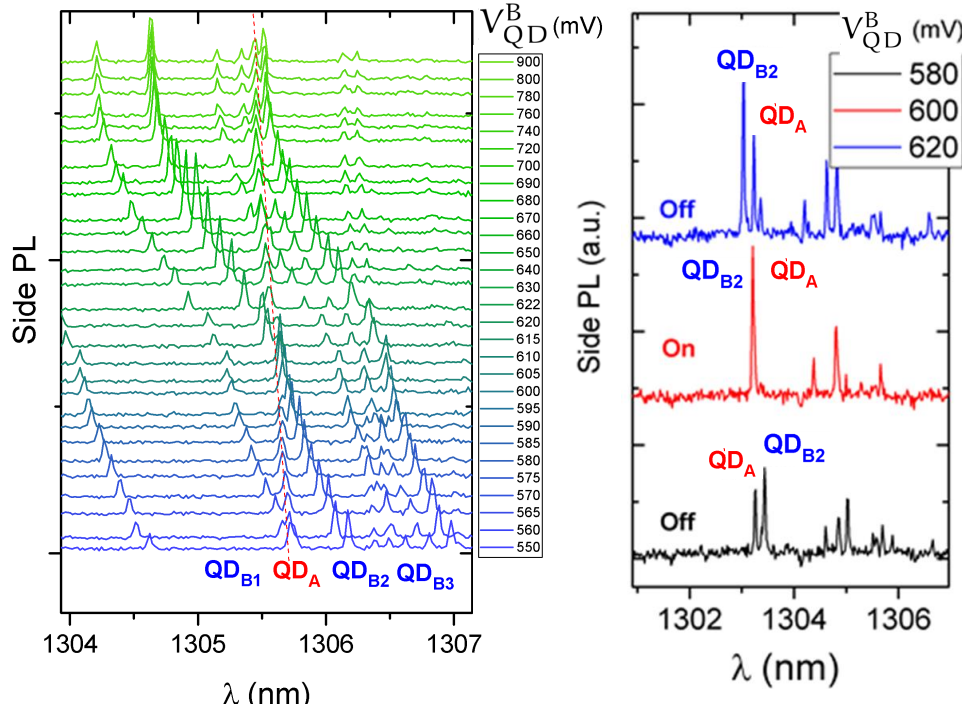


Figure 8.3: (left panel) Single dot PL collected at one output of the beam splitter by simultaneously exciting two PhCWGs labelled 'A' and 'B', and varying the Stark-voltage of one node (B). Several excitonic lines located in the node B (QD_{B1} , QD_{B2} , and QD_{B3}) are tuned into resonance with an exciton positioned in the node A (QD_A). (right panel) Energy-matching condition obtained for QD_A and QD_{B2}

8.4 BRINGING TWO DOTS ON RESONANCE

We experimentally found that locating two dots in adjacent PhCWGs with suitable characteristics for anti-bunching (and bunching) experiments is more probable than in a pair of PhCCs. Therefore, in the following experiments we examined exciton transitions that (1) are sufficiently isolated from other lines present in the same excitation area, so that can be filtered by off-chip tunable filters (bandwidth 0.4-0.8 nm); (2) show a negligible background, which is typically characterized by poissonian statistics and hence increases the value of the measured $g^{(2)}(0)$. Fig.8.3 shows a set of PL spectra collected from one output of the beam splitter, when the regions of two neighbouring PhCWGs are simultaneously excited by a low-power ($0.5\mu\text{W}$ after objective) 780-nm laser diode. We attributed the QD-lines to the nodes A or B, by comparing these spectra with the ones obtained exciting the two regions separately (not shown). The QD-signal is collected by varying the voltage applied to the QD-diode of one of the nodes (V_{QD}^B) from 550 to 900 mV (lines from blue to green). When V_{QD}^B is increased, a blue shift of the all the QD-lines as a function of the Stark-voltage is observed, as expected by the reduction of the built-in field of the diode in forward bias [333]. In particular, the excitonic transition QD_A is brought on resonance with several QD-lines generated in the node B (QD_{B1} , QD_{B2} , QD_{B3}). The energy-

matching condition is achieved with QD_{B1} at $V_{QD}^B = 550$ mV ($\lambda = 1305.73$ nm), with QD_{B2} at $V_{QD}^B = 600$ mV ($\lambda = 1305.66$ nm), and with a group of spectrally-closed lines labelled QD_{B3} for $V_{QD}^B > 650$ mV ($\lambda < 1305.51$ nm). High-resolution spectra - corresponding to the configurations when QD_A and QD_{B2} are brought on- and off- resonance - are presented in the left panel of fig.8.3. For the voltage values investigated in these experiments the tuning range of the QD-lines belonging to the node B is $\Delta\lambda_{QD}^B = 1.54$ nm, while QD_A shows a cross-tuning of $\Delta\lambda_{QD}^B = 0.29$ nm. The quantum dot cross tuning coefficient can be defined as

$$\xi_{QD} = \frac{\Delta\lambda_{QD}^A}{\Delta\lambda_{QD}^B} \approx 0.19. \quad (8.2)$$

This relatively small cross-talk greatly facilitates the energy-matching of remote QDs, which is one of the key challenges to generate indistinguishable single photons from multiple integrated emitters.

8.5 SPECTRAL DEPENDENCE ON THE EXCITATION POWER

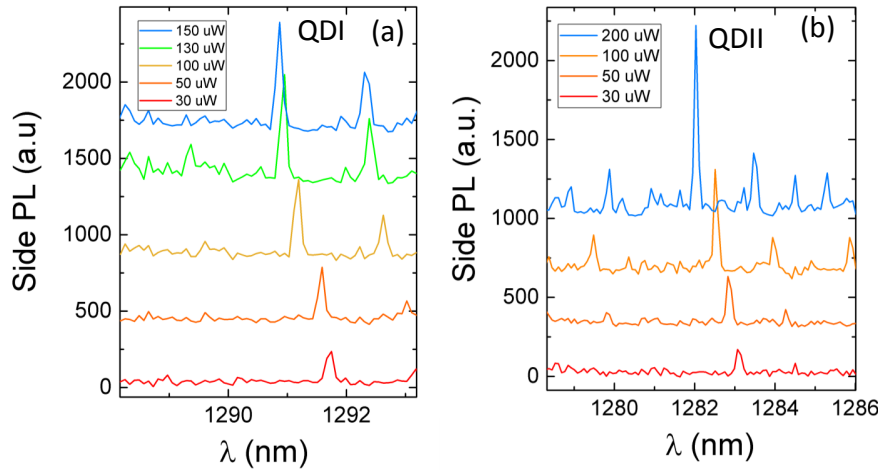


Figure 8.4: Optically-induced DC-Stark effect measured in two devices (a) and (b). A blue-shift is obtained when the excitation power is increased. The devices are in open circuit (no probe applied)

We observed that the QD lines shift as a function of the excitation power (fig.8.4 (a) and (b)). This behaviour has been previously reported by Englund *et al.* in a p-i-n PhC membrane and has been attributed to a DC-Stark effect mediated by the presence of photo-generated free-carriers [106]. In accordance with the results obtained in [106], when the excitation power is increased, the excitonic lines experience a blue-shift, associated with the reduction of the absolute value of the Stark-Field. The dot wavelengths measured at high power intensity (blue lines, QDI and QDII in fig.8.4) tend to the values measured in forward bias (i.e. when the Stark-field is zero), indicating that the photo-generated carriers screen the built-in voltage of the

QD-diode. The optically-induced DC-Stark (OIDCS) effect shows a maximum tuning range of 1 nm with a typical tuning rate of ≈ 0.5 nm/mW.

Although this effect can be in principle exploited to align two dots without the need of external probes and the fabrication of diodes, it constitutes a challenging problem to maintain the energy-matching condition between two dots over a long time. In fact, due to the unavoidable drift of the setup during long correlation measurements, the effective excitation power can fluctuate, inducing an energy shift of one or both lines. Since this drift is practically accompanied by a decrease in the (filtered) count rate, a practical strategy to mitigate this effect consists in maintaining the latter parameter constant over time by feedback-regulated displacement of the excitation stage. Furthermore, the implementation of either electrical or (quasi-) resonant excitation strategies in devices coupled to waveguides can alleviate the effects of OIDCS.

8.6 COHERENCE TIME

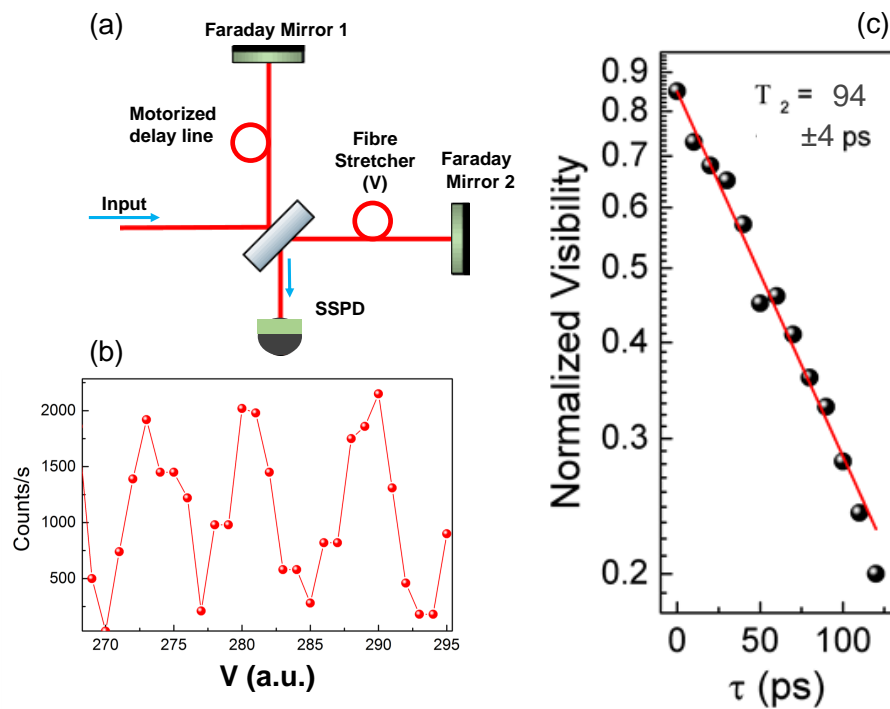


Figure 8.5: (a) Michelson interferometer employed to measure the first order coherence function of the QD-emission. Faraday mirrors are employed to compensate for the birefringence of the fibres. (b) Typical interferometric fringes at 10 ps delay. (c) Extracted visibility of the interferometric measurement, carried out on the dot line QD_{B1} displayed in fig.8.3 for $V_{QD}^B = 1000$ mV

As outlined in the introduction paragraph, indistinguishability is an imperative prerequisite for quantum interference between two single photon pulses. Generally speaking, the maximum indistinguishability of a single-

photon source is determined by its coherence properties. This can be qualitatively understood imagining that the occurrence of an elastic scattering event with a thermal reservoir leaves a trail in the temporal waveform of the single-photon, making it distinguishable from other single photons emitted by the same or different emitter. The degree of coherence is often quantified by the ratio $T_2/2T_1$, where T_1 is the lifetime of the emitter and T_2 is the total coherence time (i.e. the inverse of the linewidth). In a simple approximation, considering only dephasing events mediated by Markovian processes [49, 252], the emission of a two-level system is characterized by a Lorentzian spectrum with a linewidth $1/T_2$ given by

$$\frac{1}{T_2} = \frac{1}{2T_1} + \frac{1}{T_2^*}, \quad (8.3)$$

where $\gamma^*/2 = 1/T_2^*$ is the rate at which dephasing events occur. This relation does not take into account the slower spectral diffusion induced by charge fluctuations and spin noise, which occurs over μs - ms time-scales [223]. A number of previous works investigated the coherence properties of dots located in bulk [191, 226, 494] and embedded in photonic crystal structures [190, 231], under non-resonant excitation. Here, we measured the coherence properties of dot QD_{B2} shown in fig.8.3, upon the application of a positive Stark-voltage ($V_{\text{QD}}^{\text{B}} = 1000 \text{ mV}$). We employed the fibre-based Michelson interferometer depicted in fig. 8.5 (a). The QD-emission is collected from one output of the MMI and - after being filtered from the other QD-lines - it is coupled to the input of the interferometer. At this stage, it is splitted in two paths by a 50:50 beam splitter. Each arm of the interferometer contains a delay line and ends in a Faraday mirror operating at 1310 nm. A long delay (τ) is introduced by a motorized delay line in steps of 10 ps, while a fibre-stretcher provides a fine delay to resolve the interferometric fringes. The output of the setup is connected to a SSPD, characterized by a dark count rate of $\approx 10 \text{ Hz}$. Examples of interferometric fringes for $\tau = 10 \text{ ps}$ are shown in fig. 8.5 (b). The normalized visibility (V) is calculated as

$$V = \frac{C_{\text{max}} - C_{\text{min}}}{C_{\text{max}} + C_{\text{min}}}, \quad (8.4)$$

where C_{max} and C_{min} are the maximum and minimum count rates, respectively. Fig.8.5 (c) shows the normalized visibility as a function of the delay time. These data can be well fitted with a single exponential curve (red line), $V(\tau) = e^{-\tau/T_2}$, obtaining a total decoherence time $T_2 = (92 \pm 4) \text{ ps}^2$. This indicates that dephasing produces a homogeneous broadening, as expected by pure dephasing processes. Finally, the single-photon indistinguishability of this dot line can be calculated as $M_{\text{B}} = T_2/2T_1 \approx 0.03$, where $T_1 \approx 1.48 \text{ ns}$ is the measured decay time at this voltage level.

8.7 PRELIMINARY EXPERIMENTS

Before discussing the experimental data, it is convenient to examine the expected bunching dip in the case of single photons that are not Fourier-transformed limited (i.e. $\gamma^* \neq 0$). As outlined in the previous section, this

² the error is obtained by the standard deviation of the least-squares fit

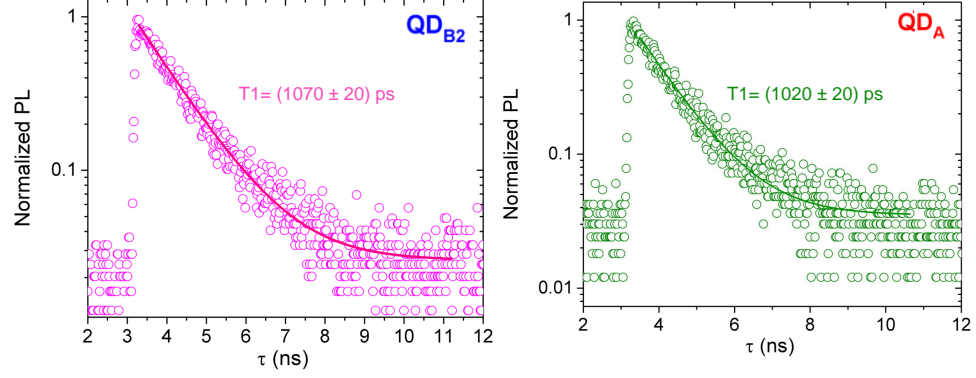


Figure 8.6: Time resolved traces of QD_{B2} (left) and QD_A (right) at $V_{QD}^B = 600\text{mV}$

is the case of single photons produced by non resonant-excitation of QDs coupled to the linear dispersion region of PhCWgs. Several studies investigated the TPI effect from a theoretical perspective [209, 237, 239, 326, 415]. Here we follow the description presented in Giesz *et al.*[140]. In this framework, blinking [187], time-jitter, and spectral diffusion [328] are neglected. Assuming two single-photon sources A and B with vanishing $g^{(2)}(0)$, the theoretical probability (P) to obtain photon coalescence at the outputs of the beam splitter is given by [140]

$$P = R^2 + T^2 - 2 \cdot R \cdot T \cdot M_{AB} \quad (8.5)$$

where R and T are the reflection and transmission coefficient of the beam splitter, and M_{AB} is the so-called *photon overlap*, given by

$$M_{AB} = \frac{\gamma_A \gamma_B}{\gamma_A + \gamma_B} \frac{\gamma_A + \gamma_B + \gamma_A^* + \gamma_A^*}{\Delta\omega/\hbar + [(\gamma_A + \gamma_B + \gamma_A^* + \gamma_A^*)/2]^2} \quad (8.6)$$

In this equation, γ_A (γ_B) is the decay time of the source A (B), $\delta\omega$ is the difference in angular frequency between the two sources, and $\gamma_A^*/2$ ($\gamma_B^*/2$) is the pure dephasing rate. The coalescence probability is experimentally accessed by dividing the area A_0 of the zero-delay peak of the autocorrelation function by the average area A_{mT} of the peak at a time mT , where T is the repetition rate of the excitation laser, and m is an integer. In general, this quantity deviates from P because of the non-purity of the single-photon sources, which can be accounted by the following equation [140]

$$\frac{A_0}{A_{mT}} = \frac{g_A^{(2)}(0)}{2} + \frac{g_B^{(2)}(0)}{2} + P. \quad (8.7)$$

From equation 8.6 we can estimate the expected photon overlap between the dots QD_{B2} and QD_A shown in fig.8.3, when their energy-mismatch is suppressed. In general, the decay time for Stark-tunable QDs depends on the applied voltage due to tunnelling, as discussed in the previous chapters. In particular, for the dot QD_{B2} we measured a decay time varying from $T_{B2} = (1480 \pm 30)$ ps at $V_{QD}^B = 1000$ mV, to $T_{B2} = (660 \pm 20)$ ps at $V_{QD}^B = 400$

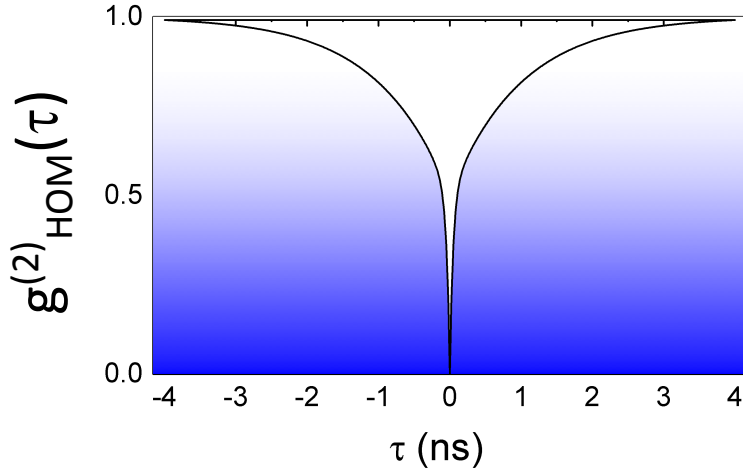


Figure 8.7: Theoretical cross correlation function of a HOM experiment, calculated assuming a balanced beam-splitter with equal losses ($c_1 = c_2$), a perfect single-photon purity $g^{(2)}(0) = 0$ for both sources, and zero mode mismatch ($\eta = 1$), assuming the measured decay and coherence time

mV. The decay times of the two dots at the resonant condition ($V_{\text{QD}}^{\text{B}} = 600$ mV) are $T_{\text{B}2} = (1070 \pm 10)$ ps and $T_{\text{A}1} = (1015 \pm 20)$ ps (Fig. 8.6). Taking into account the measured pure dephasing rate ($\gamma^* = \frac{2}{T_2} - \frac{1}{T_1} = 20$ GHz) and assuming $\gamma_{\text{B}}^* = \gamma_{\text{A}}^*$, we expect a small photon overlap ($M_{\text{AB}} = 4.5\%$) for these QD-lines. Therefore, the expected visibility of pulsed HOM experiments is dramatically reduced ($\mathcal{V}_{\text{pulsed}} = 0.09$), and would be hard to measure experimentally.

Alternatively, CW post-selected TPI experiments employing fast detectors may provide sufficient resolution to distinguish the temporal window where the two photons coalesce [32, 241, 326–328]. In this case, assuming a negligible uncorrelated background, the cross correlation function at the output of the 50:50 beam splitter can be written as [241]

$$g_{\text{HOM}}^{(2)}(\tau) = c_{\text{A}}^2 g_{\text{A}}^{(2)}(\tau) + c_{\text{B}}^2 g_{\text{B}}^{(2)}(\tau) + 2 \cdot c_{\text{A}} c_{\text{B}} [1 - \eta |g_{\text{A}}^{(1)}(\tau)| |g_{\text{B}}^{(1)}(\tau)| \cos(\Delta\omega\tau)] \quad (8.8)$$

with $c_i = \frac{I_i}{I_{\text{A}} + I_{\text{B}}}$, where I_i is the single-photon intensity of the source i . The first two terms represent a weighted sum of the second-order correlation function $g_i^{(2)}(\tau) = 1 - \exp(-|\tau|/T_i)$ of the individual sources, while the latter term arises from the quantum interference between the two sources. In particular $g_i^{(1)}(\tau)$ is the first order correlation function [255], which can be written as $g_i^{(1)}(\tau) = \exp(-i\omega\tau) \exp((\gamma_i + \gamma_i^*)|\tau|/2)$. η accounts for the mode mismatch at the beam splitter. Since perfect mode matching is expected for an integrated bunching experiment, it is reasonable to assume $\eta = 1$. Notably, for small but non-zero frequency mismatch ($\Delta\omega$) a beating is expected as reported in [238, 241, 326]. Fig.8.7 shows the theoretical bunching curve, obtained with the experimental parameters reported in this section, supposing pure single-photon sources and balanced intensities. For distinguishable

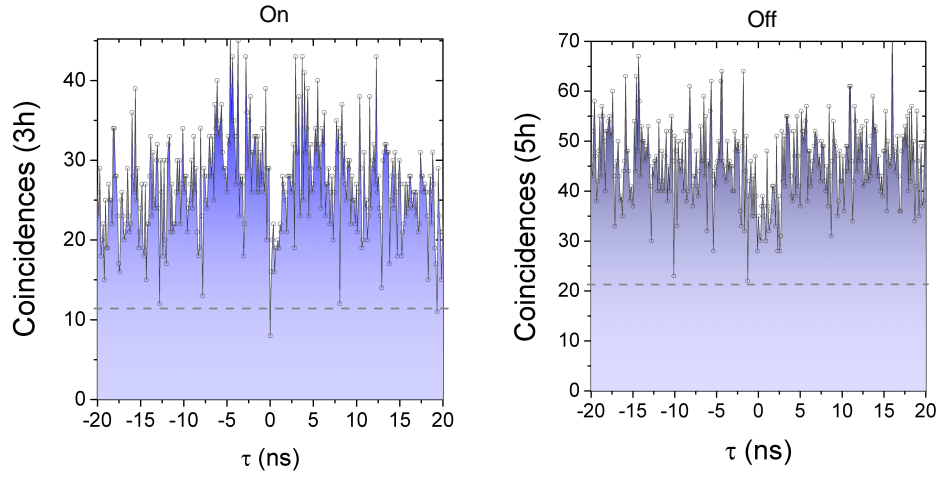


Figure 8.8: Preliminary correlation histogram obtained when two quantum dots (QD_{B_2} and QD_A) are on-resonance (left) or off-resonance (right). The time bin is 128 ps and the total count rate at the two detector is ≈ 12 KHz

single photons ³ the third term is 0.5, and $g_{\text{HOM}}^{(2)}(0) = 0.5$, as demanded from the single particle nature of the sources. As pointed out in Patel *et al.* [328], the figure of merit that quantifies the visibility in post-selected CW excitation, differs from the visibility in pulsed excitation calculated before. In fact, in this case the visibility can be expressed as the ratio $V_{\text{CW}} = 2\delta t/T_2$, where δt is the temporal resolution of the detectors. Therefore, provided a sufficiently high temporal resolution, the central dip shown in fig. 8.7 can be fully reconstructed. If the temporal resolution is comparable with the dot coherence time, a convolution with the response function of the detectors is needed [328]. In the case of our current SSPD system, the temporal resolution is in the order of 50 ps, slightly smaller than the width $\approx 2T_2$ of the expected bunching dip.

In free-space TPI experiments from SPs emitted by the same or different dots, the TPI visibility is calculated by making the two photons distinguishable by rotating the polarization of one photon with respect to the other. Alternatively, a delay in the arrival of a photon can be introduced before the beam splitter. These strategies are challenging to implement in the configuration presented in fig.8.1, where the beam splitter is integrated with the sources on the same chip. Nevertheless, the two single-photon sources can be made distinguishable by controlling their energy detuning. For sufficiently small detuning a quantum beating, manifested as fringes in the bunching dip, is expected [238, 241, 326], while for large detuning the two sources can be made distinguishable [241]. In this case, the visibility can be defined as

$$V = \frac{g_{\text{OFF}}^{(2)}(0) - g_{\text{ON}}^{(2)}(0)}{g_{\text{OFF}}^{(2)}(0)} \quad (8.9)$$

In the following, we experimentally investigate the possibility to observe two-photon interference from the dots shown in fig.8.3. The dot-emission

³ i.e. when $1/\Delta\omega < \delta t$ or $1/T_2 < \delta t$, where δt is the resolution of the detectors

is collected at the outputs of the on-chip beam splitter by two tapered fibres. Then, each optical path is filtered by a separate tunable filter and fed into a SSPD detector. The bandwidth of the filter allows the collection of both lines. The excitation power is calibrated in order to obtain a similar counts rate for the two QD-lines. Fig 8.8 shows a preliminary coincidence histogram rerecorded using a CW-excitation, when the dots QD_{B₂} and QD_A are on- ($V_{\text{QD}}^{\text{B}} = 600\text{mV}$) and off- ($V_{\text{QD}}^{\text{B}} = 620\text{mV}$) resonance. The dip in the

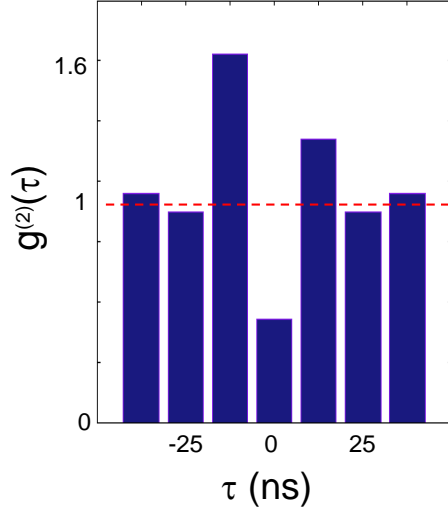


Figure 8.9: Pulsed anti-bunching experiment performed on QD_{B₂} for $V_{\text{QD}}^{\text{B}} = 620\text{mV}$

correlation histogram when the two photons are energetically indistinguishable is more pronounced with respect to the off-resonance configuration, which suggests a signature of the two-photon-interference. From the raw data we tentatively extract $g_{\text{OFF}}^{(2)}(0) = 0.60 \pm 0.15$ and $g_{\text{ON}}^{(2)}(0) = 0.35 \pm 0.20$. The error is calculated from the standard deviation of coincidences at long time delay. However, the signal-to-noise ratio must be improved to better substantiate this conclusion and to evaluate the visibility of the experiment. The value of $g_{\text{OFF}}^{(2)}(0)$ is higher than the expected value for perfect single-photon sources (0.5), due to the non-zero value of the original single-photon source [375]. A small bunching effect is also visible for finite time delays in the on-resonance configuration. This has also been observed in the single-photon statistics of QD_{B₂}, as can be observed in the HBT histogram shown in fig. 8.9, collected employing a pulsed excitation with a period of 12.5 ns. The observed behaviour is expected from an exciton coupled to a dark state [82]. The reason for which the bunching behaviour is not observed in the off-resonance histogram is currently unclear.

8.8 CONCLUSIONS

In this chapter we outlined some avenues to prove the scalability of the tunable sources presented in this thesis. We have demonstrated that a si-

multaneous control of multiple cavities and emitters located on the same device is possible, although the interdependency between the different tuning knobs must be reduced. In this context, the use of better isolation techniques might simplify the electrical alignment of two neighbouring cavity-emitter systems. A number of technological and fundamental improvements can be foreseen to improve on-chip interference experiments. Firstly, the off-chip coupling efficiency must be optimized, since the current count rates (tens of kHz) require hours-long integration time and make the experiment sensitive to dark counts and drifts of the setup. In particular, high signal-to-noise ratios are compulsory for post-selected CW experiments. Although CW-experiments can give a hint of two photon coalescence, in terms of applications, the demonstration of non-postselected pulsed TPI is important. In this case, it is crucial to probe the interference of two Purcell-enhanced dots, exploiting the full developed architecture, in particular if non-resonant excitation is employed. A better control over the dot density, or the use of site-controlled quantum dots will enhance the possibility to find two cavity-coupled excitons suitable for TPI experiments. Gaining control over the spatial alignment of cavity-emitter nodes will pave the way for circuits with an arbitrary number of indistinguishable single-photons sources. Finally, by exploiting resonant excitation strategies both the coherence properties and the brightness of the single-photon sources can be significantly improved [251].

9

CONCLUSIONS AND PERSPECTIVES

Quantum photonic integrated circuits hold great potential for sparking a novel class of technologies that exploit the evolution of quantum states of light in a chip to manipulate information. The ability to program the properties of single-photon sources based on integrated emitters will play a crucial role in the realization of large-scale quantum circuits able to simulate complex molecules, and to perform boson sampling experiments or advanced quantum key distributions protocols. In this regard, a key requirement for scaling the number of sources for intra- and inter-chip applications consists in simultaneously reconfiguring the status of multiple c-QED nodes by external triggers. This thesis addresses a number of aspects crucial to the construction of electrically-adaptable cavity-enhanced single-photon sources.

The main original results presented in this work are summarized as follows.

- An ultra-wide wavelength control of the photonic crystal resonances of a double-slab photonic crystal cavity is achieved via the local pressure induced by a SNOM tip. This actuation scheme is not limited by the pull-in instability and can be, in principle, extended in a wavelength range spanning over 100 nm. Besides, the high-resolution obtained through the read-out of the mechanical and optical properties of the system gives a direct access to the structural parameters of the device, necessary to accurately model its behaviour.
- An integrated cavity quantum electrodynamic node composed of an electrically-tuneable quantum dot coupled to an electrically-tuneable cavity mode is experimentally demonstrated. By controlling the Stark-voltage applied to the emitters and the mechanical positions of a pair of PhC slabs through capacitive forces, the tuning of the full cavity-emitter node is realized, achieving a Purcell enhancement at two different energies.
- The electrical excitation of a single quantum dot transition in a photonic crystal cavity is proved for the first time. Firstly, a tuneable PhC LED featuring a large tuning range (≈ 15 nm) is realized. Then, the devices are operated at the single-emitter level. The application of electromechanical forces in the PhC NOEMS makes it possible to bring an electrically-pumped excitonic transition into resonance with a cavity mode. In this way, a light emitting diode that shows a clear anti-bunching statistic is demonstrated.
- An anti-stiction coating is developed to make the PhC NOEMS reliable against the pull-in-induced stiction of the membranes. In fact, by coating the PhC NOEMS with a conformal alumina layer deposited via ALD methods, we demonstrated that the device can be actuated

from pull-in back to its release status, both in static and in dynamic experiments. This allows for the exploitation of the device as a switch between two mechanical configurations, corresponding to two optical states separated by ≈ 50 nm in wavelength.

- The QD-PhCC node is integrated with ridge waveguides, which provide low-loss channels to transfer the single-photon emission across the chip. The QD-light is firstly funnelled into a broadband photonic crystal waveguide, and then it is converted into the modes of supported waveguides via a tapered mode adapter. We theoretically and experimentally explored different designs over a wide parameter space in order to maximize the coupling efficiency from the PhC node into the photonic circuit. By equipping these devices with electrical gates for cavity actuation, the side-collection of a mechanically-tuneable and narrow ($Q = 2000$) waveguide-coupled photonic crystal mode is realized, which is essential to filter a single exciton line on a chip. The additional integration with Stark contacts enables the transfer of energy-programmable single photons into the passive circuit, while proving Purcell enhancement in this geometry as well.
- The wg-coupled architecture has been further integrated with a 50:50 beam splitter based on the double-membrane platform. This component has been characterized both classically and at the single-photon level. An integrated Hanbury-Brown and Twiss experiment, featuring a source and a splitter on the same chip, is carried out from the single-exciton emission generated in the PhC region. Additionally, multiple tuneable c-QED nodes have been integrated on a single chip. The tuning methods developed in this work have thus been employed to suppress the energy mismatch of dots and cavities from different devices, providing a way to produce indistinguishable single-photons from remote emitters.

Despite the progress made towards experiments featuring multiple deterministic SP sources in a photonic circuit, a number of open problems must be addressed in the short- and long-term before the advent of fully-integrated QPICs.

In the short term, the possibility to obtain cavity-enhanced single photons without the need of external lasers is particularly appealing towards experiments with SP sources and waveguide-coupled SP detectors co-integrated on the same chip. In order to close the gap between the integration of these two fundamental components it is indispensable to demonstrate a clear anti-bunching experiment without the need of external optical elements. The quality of the anti-bunching dip depends on the ability to suppress any light different from the one generated from a single-exciton transition. The single-photon LED developed in chapter 5, combined with the electromechanically-tuneable waveguide-coupled cavity presented chapter 7, meet this requirement. A first step in this direction consists in adapting the contact geometry for lateral current injection in wg-coupled devices.

Nevertheless, the QD-tuning range obtained in current-driven SP sources is typically limited to 1 – 1.5 nm and tangled with the pumping rate. The

implementation of a third tuning knob, such as strain tuning, can be considered to increase the QD tuning range for multi-source experiments. Besides, implementing electrical excitation in a pulsed operation will be beneficial for applications that require a train of single photons with a well-defined temporal profile.

A general open question concerns the optimization of the coherence properties of single-photons generated by the excitation of QD embedded in nanostructured photonic systems, such as photonic nanobeams and PhC waveguides [430]. An important point that should be addressed in this regard is the evaluation of the coherence time of cavity-coupled dots under electrical injection. Previous investigations have shown that a coherence time of 325 ps and a linewidth of $\approx 6\mu\text{eV}$ can be obtained in mesa structures [328] and unidimensional LED nanobeams [33], respectively. Coherence is essential for the implementation of two-photon interference experiments, for the entanglement swapping between remote cavity-emitters systems, and for superradiance phenomena. In this context, the QD community has shown that resonant excitation is an excellent solution to boost the coherence time, the indistinguishability, and the internal efficiency of semiconductor QDs. In fact, in the low resonant pumping excitation regime, the long coherence time of the laser is inherited by the QD transitions. However, implementing these strategies in integrated structures is practically difficult because the suppression of the resonant laser scattering is typically challenging. While resonant fluorescence has been achieved in nanobeams [266], PhCWGs [190] and PhCCs [251], these demonstrations still rely on the use of external polarizers to suppress the laser scattering, which are hardly compatible with on-chip detectors [194]. In this respect, a theoretical exploration is needed in order to find a nanocavity - integrated in a waveguide geometry - that is able to decouple the laser and the QD contributions while maintaining high Purcell enhancements.

From a technological perspective, the interdependency between the energy tuning of cavity modes and emitters within a single device and between different devices can be further improved with better electrical isolation schemes. The main limiting factor for the simultaneous fully-independent tuning in a single c-QED node is represented by the fact that the two p-i-n diodes share a common n-doped layer. Introducing two isolated n-layers in the epitaxial structure might subdue the electrical cross-talk between the diodes. On the other hand, the cross talk between different devices can be curtailed by increasing the distance between two neighbouring devices, currently limited by the field of view imposed by a top excitation strategy. In this connection, it is essential to implement not only the light collection from the QD, but also their optical excitations via ridge waveguides. Furthermore, if quasi- or strictly-resonant schemes are employed, the optical-induced DC-stark effect (detrimental to maintain the energy indistinguishability between remote dots over time long period) might be reduced.

In this thesis, the electromechanical control has been mainly employed for cavity actuation. Nevertheless, a number of devices for QPIC applications, such as reconfigurable phase-shifters and splitters or more advanced elements obtained by inverse designs algorithms, can be conceived based on the alteration of the effective refractive index of two or more optical wave-

uities. A further improvement in the performance of these devices consists of testing the anti-stiction coating at low temperatures.

For off-chip applications it is of pivotal importance to increase the coupling efficiency from a ridge waveguide to a collecting fibre, that is currently limited below 5 – 10%. To this aim, a practical systematic study on different waveguide geometries and different types of lensed fibres must be carried out. Alternatively, evanescent coupling can be implemented on suspended nanobeams to further increase the out-coupling efficiency. The internal coupling efficiency from the NOEMS to ridge waveguides can be increased as well by making use of long suspended tapers supported by lateral nanobeams, but at the expense of mechanical stability.

In a long-term vision, the deterministic control of the spatial location of the dot with respect to the cavity's anti-node is needed to achieve a unitary yield in obtaining QD-cavity coupling and to reach the strong coupling regime crucial to build single-photon non-linearities, which is possible with the best quality factors (≈ 15000) offered by the current fabrication process. While the site-control of QD has already been implemented by several groups [197, 279, 382, 396, 483], including its integration with photonic crystal cavities [180], the coherence time and the internal efficiency of these emitters is still not comparable with the figure of merits of dots grown via self-nucleation. The control of the spatial alignment of cavity-dot systems, along with the energy-tuning methods developed during this thesis project, will pave the way to cavity-emitter nodes with a deterministic maximal coupling.

In addition, the fabrication of phase shifters will be important to both implement non-deterministic linear optics gates, and to demultiplex a train of SPs emitted by a single source into many spatial channels [283]. The management of different electrical signals on the same chip, together with the packaging to an array of fibres in closed-looped cryostat [381], may represent an attractive solution to make tuneable SP sources available for free-space quantum photonic experiments.

Finally, the fabrication methods employed here are based on a single monolithic material platform consisting of GaAs membranes on top of Al-GaAs layers. The possible integration with silicon in a hybrid platform - via for example wafer bonding - can be particularly appealing. In fact, this would make it possible to combine the advantages of using deterministic SPs generated in a direct bandgap material with the low loss measured in SOI waveguides and compatibility with CMOS electronics.

ACRONYMS

AC	Alternating current
AFM	Atomic force microscope
ALD	Atomic layer deposition
AS	Antisymmetric
BS	Beam Splitter
CMOS	Complementary metal-oxide semiconductor
c-QED	Cavity-quantum electrodynamics
CW	Continuous wave
DBR	Distributed Bragg reflector
DC	Direct current
DM	Double-membrane
DOI	Diamond on insulator
EBL	Electron-beam lithography
EL	Electroluminescence
EO	Electro-optic
FC	Free carriers
FEM	Finite-element method
FP	Fabry-Pérot
FSS	Fine structure splitting
FWHM	full-width half maximum
HBT	Hanbury Brown-Twiss
ICP	Inductively-coupled plasma
IRF	Instrument response function
JC	Jaynes-Cummings
KLM	Knill, Laflamme, and Milburn
LBA	Linear buckling analysis
LC	Liquid Crystal
LDOS	Local density of states
LED	Light-emitting diode
LOQC	Linear optics quantum computation
LT	Low-temperature
MBE	Molecular beam epitaxy
MEMS	Micro-electromechanical systems
MMI	multimode interferometer
MOEMS	Micro-opto-electro-mechanical systems
NA	Numerical Aperture
NOEMS	Nano-opto-electro-mechanical system
OIDCS	Optically-induced DC-Stark effect
OL	Optical lithography
OSE	Optical Stark-effect
PEC	Proximity effect correction
PECVD	Plasma-enhanced chemical vapour deposition
PGB	Photonic band-gap

PhC Photonic crystal
PhCC Photonic crystal cavity
PhCWG Photonic crystal waveguide
PL Photoluminescence
PNR Photon number resolving
PR Photoresist
PS Phase-shifter
PSF Point spread function
Q Quality factor
QCSE Quantum-confined Stark effect
QD Quantum dot
QIP Quantum information processing
QKD Quantum Key distribution
QPIC Quantum photonic Integrated circuit
RIE Reactive ion etching
RW Ridge waveguide
S Symmetric
SAW Surface-acoustic waves
SEM Scanning electron microscope
SFWM Spontaneous four-wave mixing
SK Stranski-Krastanov
SM Single-membrane
SNOM Scanning-near field microscope
SOI Silicon on insulator
SP Single-photon
SPD Single-photon detectors
SPS Single-photon sources
SSPD Superconducting single-photon detectors
TE Transverse Electric
TIR Total internal reflection
TM Transverse Magnetic
TPI Two-photon interference
WG Waveguide

ACKNOWLEDGEMENTS

Although my name might be alone in the cover of this dissertation, I had the opportunity to interact with a number of people that contributed to this work.

Firstly, I would like to thank my first promotor Prof. Andrea Fiore for his guidance throughout the entire project, for his patience in the revisions of my drafts, for challenging my data with healthy criticism, and for sharing his creative vision.

I would like to thank the members of my defense committee: prof.dr. J. Gómez Rivas, prof.dr.ir. G.M.W. Kroesen, prof.dr. K.A. Williams, prof.dr. J. Finley, and prof.dr. A. Rastelli for providing valuable feedback to the manuscript.

I wish to express my gratitude to the scientific staff of the PSN-AND group: prof.dr. Paul Koenraad, prof.dr. Erik Bakkers, dr. Jos Haverkort, dr. Andrei Silov, and dr. González Curto. I am particularly thankful to dr. Rob van der Heijden for giving me access to his setup and being always open to prolific discussions on both theoretical and practical aspects.

I am deeply indebted to Francesco, who has been my source of inspiration for many ideas, for his passion and drive, for teaching me how to use my hands to transform a design into a device, and for the fundamental training sessions in the lab. I would like to thank: Simone, for being an outstanding teammate in low-temperature and overnight experiments, for his strong commitment to common goals, and for being a tireless companion; Giulia, for being a great science fellow, for working together in ambitious projects and for her contagious positivity. Michele, for introducing me to some secrets of the u-PL setup and for being a nice buddy. Sartoon, for giving me valuable hints on the fabrication of ridges waveguides and for his peculiar sense of humor. Daniele, for his help in the final experiments and for the time spent outside the working hours. Chaoyuan, for his help in the use of the single-photon detectors and fruitful discussions about science. Rosalinda, for her generosity and availability when I requested to borrow her equipment. Žarko, for being a great office/cleanroom/lab mate, for letting me hijack the purpose of his samples, and for beating me at squash with no mercy. Bruno, for the nice moments that we shared and for his sane curiosity.

I would like to wish my sincere gratitude to the remaining fellows of Andrea's past-future sub-group: Döndü, Zili, Tianran, Pierre, Federico, and Yongjin, for contributing and preserving the open spirit of the subgroup. I would like to take the chance to acknowledge the students that I supervised: Kaylee, Jette and Marteen. You taught me how to effectively transfer concepts from my mind to yours and vice versa. I would like to thank Sybren and Massimo Valerio for the many discussions during my first PhD year.

In this regard, I would like to thank Heijmar for the nice moments we shared while teaching optics and for the lasagna.

The fabrication process of the devices presented in this dissertation is challenging. I wish to express my gratitude to Tian and Leonardo for transferring their knowledge and experience with their original recipe, and highlighting some of the critical steps. Besides, I would like to thank Leonardo for his FEM libraries, which were particularly useful during the initial phase of this research, and for being always available to clarify dark points. Besides, I would like to thank the Nanolab@TU/e management and technicians for the numerous trainings and their assistance in the cleanroom: Huub Ambrosius, Erik Jan Geluk, Jeroen Bolk, Barry Smalbrugge, Tjibbe de Vries, Nando Harmsen and Robert van de Laar. Barry, Erik Jan and Tjibbe, thanks for your magic tips about etching, patterning and etching-depositing, respectively. You are a great source of knowledge. I wish to express my gratitude to some PhD students and post-docs working in the PhI group for valuable discussions on fabrication: Vadim, Domenico, Aura, Alonso, Giovanni.

Thanks to Martine, Henny and Gerald for providing help and support in the lab.

I am greatly indebted to dr. Lianhe Li and prof.dr Edmund Linfield from the University of Leeds and to Frank van Otten (TU/e) for the epitaxial growth of the wafers.

Along the way of my PhD journey, I visited in several occasions the group of prof. Massimo Gurioli at the European Laboratory for Non-Linear Spectroscopy (LENS) in Florence for exploring the interaction between a SNOM tip and the double-membrane system. This experience, besides being a demonstration that the membranes can survive a flight transportation, resulted in a strong exchange of ideas. I am grateful to Massimo, Francesca, Federico and Niccolò for their hospitality, for all the deep discussions and the experiments that we carried out. It has been a privilege to work with you. I would like to thank Dario and Nicoletta as well, for their recent efforts on ongoing and future experiments.

While carrying out my PhD, I had also the chance to spend few months working on silicon QPICs in Bristol. I would like to thank prof.dr. Mark Thompson for accepting me as a visitor student and for his openness and enthusiasm. I would like to thank Stefano, Antonio, Jianwei, and Raffaele for giving me the opportunity to join their project on Hamiltonian learning. Thanks Stefano for letting me put my hands in your original Mathematica script. It was definitely an experience outside my comfort zone. I would like to thank the entire group for providing a warm environment. Our friendship will continue for many years. My sincere thanks go to Döndü for her warm guidance and availability.

I would like to thank dr. Valerio Zardetto and Alfredo Mameli for spending some time on coating our system. It was a fruitful collaboration. I am also grateful to Sebastian for the challenging FIB experiments.

I would like to thank the past and present members of the PSN/AND group in a random order: Rianne, Luca, Simone A., Alessandro, Davide, Alain, Hans, Yangchao, Ang, Yizhen, Saša, Daniel, Ruben, Diana, Elham, Ghada, Milo, Bas, Claudiu, Roy, Alfonso, Thuy, Christian, Sebastian, Philipp, Matthijs and Mohammad. Thanks for the questions during our group lunch presentations. A special thanks goes to the secretaries of our groups,

Thérèse-Anne and Simone, for their kind availability when taking care of bureaucracy.

I would also like to thank the members of the PSN football for sharing the few victories on the field.

I wish to thank my family for their continuous support and for believing in me. I would like to also thank my second family for the same reason: Roberto, Semito, Luigi, Febo, Giovanni and Vito.

Finally, I would like to express my deep gratitude to Myriam, my partner, for her unremitting encouragement and for accompanying me along this and many future adventures.

LIST OF PUBLICATIONS

PEER-REVIEWED JOURNAL PUBLICATIONS

- M. Petruzzella, S. Birindelli, F.M. Pagliano, D. Pellegrino, Ž. Zobenica, S. Fattah Poor, F.W.M. van Otten, L.H. Li, E.H. Linfield and A. Fiore, "Tuneable Waveguide-Coupled cavity-dot node," in preparation (2017)
- M. Petruzzella, Ž. Zobenica, M. Cotrufo, V. Zardetto, A. Mameli, F.M. Pagliano, S. Koelling, F.W.M. van Otten, F. Roozeboom, W.M.M. Kessels, R.W. van der Heijden, and A. Fiore, "Anti-stiction coating for nano-membrane photonic crystal devices," under review (2017)
- M. Cotrufo, L. Midolo, M. Petruzzella, Ž. Zobenica, F.W.M. van Otten, A. Fiore, "Active control of the optical field in nanomechanical photonic crystal structures," under review (2017)
- M. Petruzzella, F.M. Pagliano, Ž. Zobenica, S. Birindelli, M. Cotrufo, F.W.M. van Otten, R.W. van der Heijden, and A. Fiore, "Electrically driven quantum light emission in electromechanically-tunable photonic crystal cavities," under review (2017)
- Ž. Zobenica, R.W. van der Heijden, M. Petruzzella, F.M. Pagliano, R. Leijssen, T. Xia, L. Midolo, M. Cotrufo, Y. Cho, F.W.M. van Otten, E. Verhagen and A. Fiore, "Integrated nano-opto-electro-mechanical sensor for spectrometry and nanometrology," accepted in Nat. Commun. (2017)
- J. Wang, S. Paesani, R. Santagati, S. Knauer, A. Gentile, N. Wiebe, M. Petruzzella, J. O'Brien, J.G. Rarity, J.L.A. Laing and M. G. Thompson, "Experimental quantum Hamiltonian learning", Nat. Physics, 13, 551-555 (2017)
- G. Digeronimo, M. Petruzzella, S. Birindelli, R. Gaudio, S. Fattah Poor, F.W.M. van Otten, and A. Fiore, "Integration of Single-Photon Sources and Detectors on GaAs," Photonics, vol. 3, no. 4, 55 (2016).
- M. Petruzzella, F. China, F. Intonti, N. Caselli, M. De Pas, F.W.M. van Otten, M. Gurioli, and A. Fiore, "Nanoscale mechanical actuation and near-field read-out of photonic crystal molecules," Phys. Rev. B, 94, no. 11, 115413 (2016).
- M. Petruzzella, T. Xia, F.M. Pagliano, S. Birindelli, L. Midolo, Ž. Zobenica, L.H. Li, E.H. Linfield, and A. Fiore, "Fully tuneable, Purcell-enhanced solid-state quantum emitters," Appl. Phys. Lett. 107, no. 14, 141109 (2015), Selected in Research Highlights of Nature Photonics 9, 780 (2015)

- F.P. Mezzapesa, M. Petruzzella, M. Dabbicco, H. E. Beere, D.A. Ritchie, M.S. Vitiello, and G. Scamarcio, "Continuous-wave reflection imaging using optical feedback interferometry in terahertz and mid-infrared quantum cascade lasers," *IEEE Transactions on Terahertz Science and Technology* 4, no. 5, 631-633 (2014).

CONFERENCE ORAL PRESENTATION

- M. Petruzzella, S. Birindelli, F.M. Pagliano, D. Pellegrino, Ž. Zobenica, M. Cotrufo, F.W.M. van Otten, R.W. van der Heijden, L.H. Li and E.H. Linfield, and A. Fiore, "Single photons from electrically-driven reconfigurable photonic crystal cavities," *SPIE Quantum Photonic Devices*, 6-10 August 2017, San Diego (California, United States) (Invited)
- M. Petruzzella, F.M. Pagliano, Ž. Zobenica, S. Birindelli, M. Cotrufo, F.W.M. van Otten, R.W. van der Heijden, and A. Fiore. "Tuneable Quantum Light from a Photonic Crystal LED," *European Conference on Lasers and Electro-Optics - European Quantum Electronics Conference, CLEO-EQEC*, 25-29 June 2017, Munich (Germany)
- M. Petruzzella, S. Birindelli, F.M. Pagliano, Ž. Zobenica, L. Midolo, L.H. Li, E. Linfield, and A. Fiore. "Tunable Cavity-Enhanced Quantum Light Sources for Integrated Quantum Photonics," *Frontiers in Optics*, pp. FTu5G-3. OSA, 17-21 October 2016, Rochester (New York, USA).
- M. Petruzzella, T. Xia, F.M. Pagliano, S. Birindelli, L. Midolo, Ž. Zobenica, L.H. Li, E.H. Linfield, and A. Fiore, "Waveguide-integrated electrically tunable quantum nodes," *39th Annual Meeting NNV AMO*, 13-14 October 2015, Lunteren (The Netherlands).
- M. Petruzzella, T. Xia, F.M. Pagliano, S. Birindelli, L. Midolo, Ž. Zobenica, L.H. Li, E. H. Linfield, and A. Fiore. "Waveguide-coupled electrically-tunable cavity-emitter system," *European Conference on Lasers and Electro-Optics - European Quantum Electronics Conference, CLEO-EQEC*, p. JSV25, 21-25 June 2015, München (Germany).
- M. Petruzzella, T. Xia, F.M. Pagliano, S. Birindelli., L. Midolo, Ž. Zobenica, L.H. Li, E.H. Linfield, and A. Fiore, "Tuning solid-state single-photon sources into resonance with each other," *Progress In Electromagnetics Research Symposium*, 6-9 July 2015, Prague (Czech Republic). (Invited)
- M. Petruzzella, T. Xia, F.M. Pagliano, S. Birindelli, L. Midolo, Ž. Zobenica, L.H. Li, E.H. Linfield, and A. Fiore, "Fully-tunable, Purcell-enhanced on-chip quantum emitters," *Conference on Lasers and Electro-Optics (CLEO/QELS 2015)*, 10-15 May 2015, San Jose (USA). (Invited)
- M. Petruzzella, T. Xia, F.M. Pagliano, S. Birindelli, L. Midolo, Ž. Zobenica, L.H. Li, E. H. Linfield, and A. Fiore, "Fully-tuneable Purcell-

enhanced on-chip quantum sources," PICQUE Integrated Quantum Photonics Workshop, 7-9 January 2015, Oxford (UK).

BIBLIOGRAPHY

- [1] Scott Aaronson and Alex Arkhipov. "The computational complexity of linear optics". In: *Proceedings of the forty-third annual ACM symposium on Theory of computing*. ACM. 2011, pp. 333–342.
- [2] BP Abbott et al. "Observation of gravitational waves from a binary black hole merger". In: *Phys. Rev. Lett.* 116.6 (2016), p. 061102.
- [3] Shahina MC Abdulla et al. "Mechano-optical wavelength tuning in a photonic crystal microcavity with sub-1 V drive voltage". In: *Optics Letters* 37.11 (2012), pp. 2010–2012.
- [4] Mark L Adams et al. "Microfluidic integration of porous photonic crystal nanolasers for chemical sensing". In: *IEEE Journal on Selected Areas in Communications* 23.7 (2005), pp. 1348–1354.
- [5] Thomas M Adams and Richard A Layton. *Introductory MEMS: fabrication and applications*. Vol. 70. Springer Science & Business Media, 2009.
- [6] Yoshihiro Akahane et al. "High-Q photonic nanocavity in a two-dimensional photonic crystal". In: *nature* 425.6961 (2003), pp. 944–947.
- [7] N Akopian et al. "Hybrid semiconductor-atomic interface: slowing down single photons from a quantum dot". In: *Nature Photonics* 5.4 (2011), pp. 230–233.
- [8] N Akopian et al. "Tuning single GaAs quantum dots in resonance with a rubidium vapor". In: *Applied Physics Letters* 97.8 (2010), p. 082103.
- [9] A. R. Alija et al. "Tuning of spontaneous emission of two-dimensional photonic crystal microcavities by accurate control of slab thickness". In: *Applied Physics Letters* 86.14 (2005), p. 141101. DOI: [10.1063/1.1896427](https://doi.org/10.1063/1.1896427). eprint: <http://dx.doi.org/10.1063/1.1896427>. URL: <http://dx.doi.org/10.1063/1.1896427>.
- [10] Alfonso R Alija et al. "Tuning of spontaneous emission of two-dimensional photonic crystal microcavities by accurate control of slab thickness". In: *Applied Physics Letters* 86.14 (2005), p. 141101.
- [11] Blandine Alloing et al. "Growth and characterization of single quantum dots emitting at 1300 nm". In: *Applied Physics Letters* 86.10 (2005), p. 101908.
- [12] B Alloing et al. "Structural and optical properties of low-density and In-rich In As/ Ga As quantum dots". In: *Journal of applied physics* 101.2 (2007), p. 024918.
- [13] Marta Arcari et al. "Near-unity coupling efficiency of a quantum emitter to a photonic crystal waveguide". In: *Physical review letters* 113.9 (2014), p. 093603.

- [14] T Asano et al. "Dynamic wavelength tuning of channel-drop device in two-dimensional photonic crystal slab". In: *Electronics Letters* 41.1 (2005), p. 1.
- [15] Markus Aspelmeyer, Tobias J Kippenberg, and Florian Marquardt. "Cavity optomechanics". In: *Reviews of Modern Physics* 86.4 (2014), p. 1391.
- [16] Markus Aspelmeyer, Tobias J. Kippenberg, and Florian Marquardt. "Cavity optomechanics". In: *Rev. Mod. Phys.* 86 (4 Dec. 2014), pp. 1391–1452. DOI: [10.1103/RevModPhys.86.1391](https://doi.org/10.1103/RevModPhys.86.1391). URL: <http://link.aps.org/doi/10.1103/RevModPhys.86.1391>.
- [17] Alan Aspuru-Guzik and Philip Walther. "Photonic quantum simulators". In: *Nat Phys* 8.20 (2012), pp. 285–291.
- [18] Thang Ba Hoang et al. "Enhanced spontaneous emission from quantum dots in short photonic crystal waveguides". In: *Applied Physics Letters* 100.6 (2012), p. 061122.
- [19] Albert G Baca and Carol IH Ashby. *Fabrication of GaAs devices*. 6. IET, 2005.
- [20] L Balet et al. "Enhanced spontaneous emission rate from single InAs quantum dots in a photonic crystal nanocavity at telecom wavelengths". In: *Applied Physics Letters* 91.12 (2007), p. 123115.
- [21] Russell J Barbour et al. "A tunable microcavity". In: *Journal of applied physics* 110.5 (2011), p. 053107.
- [22] Paul E Barclay, Kartik Srinivasan, and Oskar Painter. "Nonlinear response of silicon photonic crystal microresonators excited via an integrated waveguide and fiber taper". In: *Optics express* 13.3 (2005), pp. 801–820.
- [23] Klaus-Jürgen Bathe. *Finite element procedures*. Klaus-Jurgen Bathe, 2006.
- [24] J Beetz et al. "Anisotropic strain-tuning of quantum dots inside a photonic crystal cavity". In: *Semiconductor Science and Technology* 28.12 (2013), p. 122002.
- [25] J Beetz et al. "In-plane manipulation of quantum dots in high quality laterally contacted micropillar cavities". In: *Applied Physics Letters* 98.19 (2011), p. 191111.
- [26] AJ Bennett et al. "Electric-field-induced coherent coupling of the exciton states in a single quantum dot". In: *Nature Physics* 6.12 (2010), pp. 947–950.
- [27] AJ Bennett et al. "Microcavity single-photon-emitting diode". In: *Applied Physics Letters* 86.18 (2005), p. 181102.
- [28] AJ Bennett et al. "Single-photon-emitting diodes: a review". In: *physica status solidi (b)* 243.14 (2006), pp. 3730–3740.
- [29] Anthony J Bennett et al. "Giant Stark effect in the emission of single semiconductor quantum dots". In: *Appl. Phys. Lett.* 97.3 (2010), p. 031104.

- [30] Charles H Bennett and Gilles Brassard. "Quantum cryptography: Public key distribution and coin tossing". In: *Proceedings of IEEE International Conference on Computers, Systems and Signal Processing* 175 (1984), p. 8.
- [31] Oliver Benson et al. "Regulated and entangled photons from a single quantum dot". In: *Physical review letters* 84.11 (2000), p. 2513.
- [32] C Bentham et al. "On-chip electrically controlled routing of photons from a single quantum dot". In: *Applied Physics Letters* 106.22 (2015), p. 221101.
- [33] C Bentham et al. "Single-photon electroluminescence for on-chip quantum networks". In: *Applied Physics Letters* 109.16 (2016), p. 161101.
- [34] Marco Bentivegna et al. "Experimental scattershot boson sampling". In: *Science advances* 1.3 (2015), e1400255.
- [35] Felipe Bernal Arango et al. "Optofluidic tuning of photonic crystal band edge lasers". In: *Applied Physics Letters* 91.22 (2007), p. 223503.
- [36] Hannes Bernien et al. "Two-photon quantum interference from separate nitrogen vacancy centers in diamond". In: *Physical Review Letters* 108.4 (2012), p. 043604.
- [37] Pierre A Besse et al. "Optical bandwidth and fabrication tolerances of multimode interference couplers". In: *Journal of Lightwave Technology* 12.6 (1994), pp. 1004–1009.
- [38] Jérôme Beugnon et al. "Quantum interference between two single photons emitted by independently trapped atoms". In: *arXiv preprint quant-ph/0610149* (2006).
- [39] Alvaro Blanco et al. "Large-scale synthesis of a silicon photonic crystal with a complete three-dimensional bandgap near 1.5 micrometres". In: *Nature* 405.6785 (2000), pp. 437–440.
- [40] Uwe Bog et al. "High-Q microfluidic cavities in silicon-based two-dimensional photonic crystal structures". In: *Optics letters* 33.19 (2008), pp. 2206–2208.
- [41] Simeon Bogdanov et al. "Material platforms for integrated quantum photonics". In: *Optical Materials Express* 7.1 (2017), pp. 111–132.
- [42] Cristian Bonato et al. "Strain tuning of quantum dot optical transitions via laser-induced surface defects". In: *Physical Review B* 84.7 (2011), p. 075306.
- [43] Cristian Bonato et al. "Tuning micropillar cavity birefringence by laser induced surface defects". In: *Applied Physics Letters* 95.25 (2009), p. 251104.
- [44] Alberto Boretti et al. "Electrically Driven Quantum Light Sources". In: *Advanced Optical Materials* 3.8 (2015), pp. 1012–1033.
- [45] Ranojoy Bose et al. "All-optical coherent control of vacuum Rabi oscillations". In: *Nature Photonics* 8.11 (2014), pp. 858–864.
- [46] Ranojoy Bose et al. "All-optical tuning of a quantum dot in a coupled cavity system". In: *Appl. Phys. Lett.* 100.23 (2012), p. 231107.

- [47] R Bose et al. "Large optical Stark shifts in semiconductor quantum dots coupled to photonic crystal cavities". In: *Applied Physics Letters* 98.12 (2011), p. 121109.
- [48] Garnett W Bryant et al. "Effect of mechanical strain on the optical properties of quantum dots: controlling exciton shape, orientation, and phase with a mechanical strain". In: *Physical review letters* 105.6 (2010), p. 067404.
- [49] Sonia Buckley, Kelley Rivoire, and Jelena Vučković. "Engineered quantum dot single-photon sources". In: *Reports on Progress in Physics* 75.12 (2012), p. 126503.
- [50] Hans-Jürgen Butt, Brunero Cappella, and Michael Kappl. "Force measurements with the atomic force microscope: Technique, interpretation and applications". In: *Surface science reports* 59.1 (2005), pp. 1–152.
- [51] Tao Cai et al. "Controlled coupling of photonic crystal cavities using photochromic tuning". In: *Appl. Phys. Lett.* 102.14 (2013), p. 141118.
- [52] HJ Carmichael et al. "Subnatural linewidth averaging for coupled atomic and cavity-mode oscillators". In: *Physical Review A* 40.10 (1989), p. 5516.
- [53] Jacques Carolan et al. "Universal linear optics". In: *Science* 349.6249 (2015), pp. 711–716.
- [54] A Casas-Bedoya et al. "Slow-light dispersion engineering of photonic crystal waveguides using selective microfluidic infiltration". In: *Optics letters* 37.20 (2012), pp. 4215–4217.
- [55] Niccolò Caselli et al. "Ultra-subwavelength phase-sensitive Fano-imaging of localized photonic modes". In: *Light: Science & Applications* 4.9 (2015), e326.
- [56] N Caselli et al. "Antibonding ground state in photonic crystal molecules". In: *Physical Review B* 86.3 (2012), p. 035133.
- [57] N Caselli et al. "Post-fabrication control of evanescent tunnelling in photonic crystal molecules". In: *Applied Physics Letters* 101.21 (2012), p. 211108.
- [58] N Chauvin et al. "Controlling the charge environment of single quantum dots in a photonic-crystal cavity". In: *Physical Review B* 80.24 (2009), p. 241306.
- [59] Charlton J Chen et al. "Deterministic tuning of slow-light in photonic-crystal waveguides through the C and L bands by atomic layer deposition". In: *Applied Physics Letters* 96.8 (2010), p. 081107.
- [60] Charlton J Chen et al. "Selective tuning of high-Q silicon photonic crystal nanocavities via laser-assisted local oxidation". In: *Optics express* 19.13 (2011), pp. 12480–12489.
- [61] W-Y Chen et al. "Temperature stability of single-photon emission from InGaAs quantum dots in photonic crystal nanocavities". In: *Applied physics letters* 90.21 (2007), p. 211114.

- [62] Yan Chen et al. "Controlling the exciton energy of a nanowire quantum dot by strain fields". In: *Applied Physics Letters* 108.18 (2016), p. 182103. DOI: [10.1063/1.4948762](https://doi.org/10.1063/1.4948762). eprint: <http://dx.doi.org/10.1063/1.4948762>. URL: <http://dx.doi.org/10.1063/1.4948762>.
- [63] Yan Chen et al. "Wavelength-tunable entangled photons from silicon-integrated III-V quantum dots". In: *Nature communications* 7 (2016).
- [64] Xiongyeu Chew et al. "An in-plane nano-mechanics approach to achieve reversible resonance control of photonic crystal nanocavities". In: *Optics express* 18.21 (2010), pp. 22232–22244.
- [65] Xiongyeu Chew et al. "Dynamic tuning of an optical resonator through MEMS-driven coupled photonic crystal nanocavities". In: *Optics letters* 35.15 (2010), pp. 2517–2519.
- [66] Xiongyeu Chew et al. "Enhanced resonance tuning of photonic crystal nanocavities by integration of optimized near-field multipole nanoprobes". In: *Journal of Nanophotonics* 5.1 (2011), pp. 059503–059503.
- [67] Xiongyeu Chew et al. "Nanomechanically tunable photonic crystal resonators utilizing triple-beam coupled nanocavities". In: *IEEE Photonics Technology Letters* 23.18 (2011), pp. 1310–1312.
- [68] Jae-Hyuck Choi et al. "A high-resolution strain-gauge nanolaser". In: *Nature communications* 7 (2016).
- [69] Harold MH Chong and RM De La Rue. "Tuning of photonic crystal waveguide microcavity by thermo-optic effect". In: *IEEE Photonics Technology Letters* 16.6 (2004), pp. 1528–1530.
- [70] TH Chung et al. "Selective carrier injection into patterned arrays of pyramidal quantum dots for entangled photon light-emitting diodes". In: *Nature Photonics* (2016).
- [71] L Claudio Andreani, Giovanna Panzarini, and J-M Girard. "Strong-coupling regime for quantum boxes in pillar microcavities: Theory". In: *PHYSICAL REVIEW-SERIES B* 60 (1999), pp. 13–276.
- [72] Benoit Cluzell et al. "A near-field actuated optical nanocavity". In: *Opt. Express* 16.1 (2008), pp. 279–286.
- [73] RJ Coles et al. "Waveguide-coupled photonic crystal cavity for quantum dot spin readout". In: *Optics express* 22.3 (2014), pp. 2376–2385.
- [74] Pierre Colman et al. "Ultrafast coherent dynamics of a photonic crystal all-optical switch". In: *Physical Review Letters* 117.23 (2016), p. 233901.
- [75] "COMSOL Multiphysics® v. 5.2. www.comsol.com. COMSOL AB, Stockholm, Sweden." In: ().
- [76] M Cotrufo. "Light-matter interaction in nanophotonic structures, PhD thesis". In: (2017).
- [77] Andrea Crespi et al. "Integrated multimode interferometers with arbitrary designs for photonic boson sampling". In: *Nature Photonics* 7.7 (2013), pp. 545–549.

- [78] Georgios Ctistis et al. "Ultimate fast optical switching of a planar microcavity in the telecom wavelength range". In: *Applied Physics Letters* 98.16 (2011), p. 161114.
- [79] Dan Dalacu et al. "Deterministic emitter-cavity coupling using a single-site controlled quantum dot". In: *Physical Review B* 82.3 (2010), p. 033301.
- [80] Dan Dalacu et al. "Postfabrication fine-tuning of photonic crystal microcavities in In As/ In P quantum dot membranes". In: *Applied Physics Letters* 87.15 (2005), p. 151107.
- [81] Marcelo Davanco et al. "A heterogeneous III-V/silicon integration platform for on-chip quantum photonic circuits with single quantum dot devices". In: *arXiv preprint arXiv:1611.07654* (2016).
- [82] Marcelo Davanço et al. "Multiple time scale blinking in InAs quantum dot single-photon sources". In: *Physical Review B* 89.16 (2014), p. 161303.
- [83] Raphael S Daveau et al. "Efficient fiber-coupled single-photon source based on quantum dots in a photonic-crystal waveguide". In: *Optica* 4.2 (2017), pp. 178–184.
- [84] Alfredo De Rossi et al. "Measuring propagation loss in a multimode semiconductor waveguide". In: *Journal of applied physics* 97.7 (2005), p. 073105.
- [85] FW DelRio et al. "Atomic layer deposition of Al/sub 2/O/sub 3//ZnO nano-scale films for gold RF MEMS". In: *Microwave Symposium Digest, 2004 IEEE MTT-S International*. Vol. 3. IEEE. 2004, pp. 1923–1926.
- [86] Aymeric Delteil et al. "Generation of heralded entanglement between distant hole spins". In: *arXiv preprint arXiv:1507.00465* (2015).
- [87] David Deutsch and Richard Jozsa. "Rapid solution of problems by quantum computation". In: *Proceedings of the Royal Society of London A: Mathematical, Physical and Engineering Sciences*. Vol. 439. 1907. The Royal Society. 1992, pp. 553–558.
- [88] Christof P Dietrich et al. "GaAs integrated quantum photonics: Towards compact and multi-functional quantum photonic integrated circuits". In: *Laser & Photonics Reviews* (2016).
- [89] Giulia Enrica Digeronimo et al. "Integration of Single-Photon Sources and Detectors on GaAs". In: *Photonics*. Vol. 3. 4. Multidisciplinary Digital Publishing Institute. 2016, p. 55.
- [90] F Ding et al. "Tuning the exciton binding energies in single self-assembled InGaAs/GaAs quantum dots by piezoelectric-induced biaxial stress". In: *Physical review letters* 104.6 (2010), p. 067405.
- [91] Xing Ding et al. "On-demand single photons with high extraction efficiency and near-unity indistinguishability from a resonantly driven quantum dot in a micropillar". In: *Physical review letters* 116.2 (2016), p. 020401.

- [92] Gijs Dingemans and WMM Kessels. "Status and prospects of Al₂O₃-based surface passivation schemes for silicon solar cells". In: *Journal of Vacuum Science & Technology A: Vacuum, Surfaces, and Films* 30.4 (2012), p. 040802.
- [93] Aleksander Divochiy et al. "Superconducting nanowire photon-number-resolving detector at telecommunication wavelengths". In: *Nature Photonics* 2.5 (2008), pp. 302–306.
- [94] Han Du, Fook Siong Chau, and Guangya Zhou. "Mechanically-Tunable Photonic Devices with On-Chip Integrated MEMS/NEMS Actuators". In: *Micromachines* 7.4 (2016), p. 69.
- [95] Han Du et al. "Lateral shearing optical gradient force in coupled nanobeam photonic crystal cavities". In: *Applied Physics Letters* 108.17 (2016), p. 171102.
- [96] Han Du et al. "Precise control of coupling strength in photonic molecules over a wide range using nanoelectromechanical systems". In: *Scientific reports* 6 (2016).
- [97] S Dufferwiel et al. "Strong exciton-photon coupling in open semiconductor microcavities". In: *Applied Physics Letters* 104.19 (2014), p. 192107.
- [98] MA Dündar et al. "Birefringence-induced mode-dependent tuning of liquid crystal infiltrated InGaAsP photonic crystal nanocavities". In: *Applied Physics Letters* 95.18 (2009), p. 181111.
- [99] Mehmet A Dündar et al. "Optothermal tuning of liquid crystal infiltrated InGaAsP photonic crystal nanocavities". In: *JOSA B* 28.6 (2011), pp. 1514–1517.
- [100] B Dzurnak et al. "Quantum key distribution with an entangled light emitting diode". In: *Applied Physics Letters* 107.26 (2015), p. 261101.
- [101] M Ediger et al. "Peculiar many-body effects revealed in the spectroscopy of highly charged quantum dots". In: *Nature Physics* 3.11 (2007), pp. 774–779.
- [102] MD Eisaman et al. "Invited review article: Single-photon sources and detectors". In: *Review of scientific instruments* 82.7 (2011), p. 071101.
- [103] Bryan Ellis et al. "Ultralow-threshold electrically pumped quantum-dot photonic-crystal nanocavity laser". In: *Nature Photonics* 5.5 (2011), pp. 297–300.
- [104] David JP Ellis et al. "Cavity-enhanced radiative emission rate in a single-photon-emitting diode operating at 0.5 GHz". In: *New Journal of Physics* 10.4 (2008), p. 043035.
- [105] Alexandre Enderlin et al. "High guided mode–cavity mode coupling for an efficient extraction of spontaneous emission of a single quantum dot embedded in a photonic crystal nanobeam cavity". In: *Physical Review B* 86.7 (2012), p. 075314.
- [106] Dirk Englund et al. "An optical modulator based on a single strongly coupled quantum dot-cavity system in a pin junction". In: *Optics express* 17.21 (2009), pp. 18651–18658.

- [107] Dirk Englund et al. "Controlling the spontaneous emission rate of single quantum dots in a two-dimensional photonic crystal". In: *Phys. Rev. Lett.* 95.1 (2005), p. 013904.
- [108] David Erickson et al. "Nanofluidic tuning of photonic crystal circuits". In: *Optics Letters* 31.1 (2006), pp. 59–61.
- [109] Weileun Fang and JA Wickert. "Determining mean and gradient residual stresses in thin films using micromachined cantilevers". In: *Journal of Micromechanics and Microengineering* 6.3 (1996), p. 301.
- [110] Andrei Faraon and Jelena Vučković. "Local temperature control of photonic crystal devices via micron-scale electrical heaters". In: *Appl. Phys. Lett.* 95.4 (2009), p. 043102.
- [111] Andrei Faraon et al. "Efficient photonic crystal cavity-waveguide couplers". In: *Applied Physics Letters* 90.7 (2007), p. 073102.
- [112] Andrei Faraon et al. "Fast electrical control of a quantum dot strongly coupled to a photonic-crystal cavity". In: *Physical review letters* 104.4 (2010), p. 047402.
- [113] Andrei Faraon et al. "Local quantum dot tuning on photonic crystal chips". In: *Appl. Phys. Lett.* 90.21 (2007), p. 213110.
- [114] Andrei Faraon et al. "Local tuning of photonic crystal cavities using chalcogenide glasses". In: *Applied Physics Letters* 92.4 (2008), p. 043123.
- [115] S Fattah Poor et al. "Efficient coupling of single photons to ridge-waveguide photonic integrated circuits". In: *Applied Physics Letters* 102.13 (2013), p. 131105.
- [116] William S Fegadolli et al. "Compact and low power consumption tunable photonic crystal nanobeam cavity". In: *Optics express* 21.3 (2013), pp. 3861–3871.
- [117] Mark J Fernée, Halina Rubinsztein-Dunlop, and GJ Milburn. "Improving single-photon sources with Stark tuning". In: *Physical Review A* 75.4 (2007), p. 043815.
- [118] R Ferrini et al. "Planar photonic crystals infiltrated with liquid crystals: optical characterization of molecule orientation". In: *Optics letters* 31.9 (2006), pp. 1238–1240.
- [119] JJ Finley et al. "Quantum-confined Stark shifts of charged exciton complexes in quantum dots". In: *Physical Review B* 70.20 (2004), p. 201308.
- [120] Edward B Flagg et al. "Interference of single photons from two separate semiconductor quantum dots". In: *Physical Review Letters* 104.13 (2010), p. 137401.
- [121] M Francardi et al. "Enhanced spontaneous emission in a photonic-crystal light-emitting diode". In: *Applied Physics Letters* 93.14 (2008), p. 143102.
- [122] M Francardi et al. "Enhanced spontaneous emission in a photonic-crystal light-emitting diode". In: *Applied Physics Letters* 93.14 (2008), p. 143102.

- [123] Lars H Frandsen et al. "Photonic crystal waveguides with semi-slow light and tailored dispersion properties". In: *Optics Express* 14.20 (2006), pp. 9444–9450.
- [124] Ian W Frank et al. "Programmable photonic crystal nanobeam cavities". In: *Opt. Express* 18.8 (2010), pp. 8705–8712.
- [125] PW Fry et al. "Inverted electron-hole alignment in InAs-GaAs self-assembled quantum dots". In: *Physical review letters* 84.4 (2000), p. 733.
- [126] Daniel A Fuhrmann et al. "Dynamic modulation of photonic crystal nanocavities using gigahertz acoustic phonons". In: *Nature Photonics* 5.10 (2011), pp. 605–609.
- [127] Ilya Fushman et al. "Ultra Fast Nonlinear Optical Tuning of Photonic Crystal Cavities". In: *Conference on Lasers and Electro-Optics*. Optical Society of America. 2007, CFQ2.
- [128] Ilya Fushman et al. "Ultrafast nonlinear optical tuning of photonic crystal cavities". In: *Appl. Phys. Lett.* 90.9 (2007), p. 091118. DOI: <http://dx.doi.org/10.1063/1.2710080>. URL: <http://scitation.aip.org/content/aip/journal/apl/90/9/10.1063/1.2710080>.
- [129] A Gaggero et al. "Nanowire superconducting single-photon detectors on GaAs for integrated quantum photonic applications". In: *Applied Physics Letters* 97.15 (2010), p. 151108.
- [130] DP Gaillot et al. "Dispersion control in two-dimensional superlattice photonic crystal slab waveguides by atomic layer deposition". In: *Applied Physics Letters* 91.18 (2007), p. 181123.
- [131] Xuetao Gan et al. "Nanophotonic filters and integrated networks in flexible 2D polymer photonic crystals". In: *arXiv preprint arXiv:1307.5621* (2013).
- [132] WB Gao et al. "Quantum teleportation from a propagating photon to a solid-state spin qubit". In: *Nature communications* 4 (2013), p. 2744.
- [133] O Gazzano et al. "Bright solid-state sources of indistinguishable single photons". In: *Nature communications* 4 (2013), p. 1425.
- [134] JR Gell et al. "Modulation of single quantum dot energy levels by a surface-acoustic-wave". In: *Applied Physics Letters* 93.8 (2008), p. 081115.
- [135] JM Gérard et al. "Enhanced spontaneous emission by quantum boxes in a monolithic optical microcavity". In: *Physical review letters* 81.5 (1998), p. 1110.
- [136] BD Gerardot et al. "Manipulating exciton fine structure in quantum dots with a lateral electric field". In: *Applied Physics Letters* 90.4 (2007), p. 041101.
- [137] DG Gevaux et al. "Enhancement and suppression of spontaneous emission by temperature tuning InAs quantum dots to photonic crystal cavities". In: *Applied physics letters* 88.13 (2006), p. 131101.

- [138] Mohsen Ghali, Yuzo Ohno, and Hideo Ohno. "Vertical electric field induced suppression of fine structure splitting of excited state excitons in a single GaAs/AlGaAs island quantum dots". In: *Applied Physics Letters* 107.12 (2015), p. 123102.
- [139] Mohsen Ghali et al. "Generation and control of polarization-entangled photons from GaAs island quantum dots by an electric field". In: *Nature communications* 3 (2012), p. 661.
- [140] V Giesz et al. "Cavity-enhanced two-photon interference using remote quantum dot sources". In: *Physical Review B* 92.16 (2015), p. 161302.
- [141] Vittorio Giovannetti, Seth Lloyd, and Lorenzo Maccone. "Advances in quantum metrology". In: *Nature photonics* 5.4 (2011), pp. 222–229.
- [142] P Gold et al. "Two-photon interference from remote quantum dots with inhomogeneously broadened linewidths". In: *Physical Review B* 89.3 (2014), p. 035313.
- [143] GN Gol'Tsman et al. "Picosecond superconducting single-photon optical detector". In: *Applied Physics Letters* 79.6 (2001), pp. 705–707.
- [144] Elton Graugnard et al. "Photonic band tuning in two-dimensional photonic crystal slab waveguides by atomic layer deposition". In: *Applied physics letters* 89.18 (2006), p. 181108.
- [145] Staffan Greek and Nicolae Chitica. "Deflection of surface-micromachined devices due to internal, homogeneous or gradient stresses". In: *Sensors and Actuators A: Physical* 78.1 (1999), pp. 1–7.
- [146] Lukas Greuter et al. "Towards high-cooperativity strong coupling of a quantum dot in a tunable microcavity". In: *Physical Review B* 92.4 (2015), p. 045302.
- [147] Christian Grillet et al. "Nanowire coupling to photonic crystal nanocavities for single photon sources". In: *Optics express* 15.3 (2007), pp. 1267–1276.
- [148] Lov K Grover. "A fast quantum mechanical algorithm for database search". In: *Proceedings of the twenty-eighth annual ACM symposium on Theory of computing*. ACM. 1996, pp. 212–219.
- [149] Tingyi Gu et al. "Deterministic integrated tuning of multi-cavity resonances and phase for slow-light in coupled photonic crystal cavities". In: *arXiv preprint arXiv:1012.5805* (2010).
- [150] Tingyi Gu et al. "Deterministic integrated tuning of multicavity resonances and phase for slow-light in coupled photonic crystal cavities". In: *Applied Physics Letters* 98.12 (2011), p. 121103.
- [151] Jan Gudat et al. "Permanent tuning of quantum dot transitions to degenerate microcavity resonances". In: *Applied Physics Letters* 98.12 (2011), p. 121111.
- [152] Sangyoon Han et al. "Large-scale silicon photonic switches with movable directional couplers". In: *Optica* 2.4 (2015), pp. 370–375.

- [153] Nicholas C Harris et al. "Bosonic transport simulations in a large-scale programmable nanophotonic processor". In: *arXiv preprint arXiv:1507.03406* (2015).
- [154] HA Haus et al. "Coupled-mode theory of optical waveguides". In: *Lightwave Technology, Journal Of* 5.1 (1987), pp. 16–23.
- [155] Yu-Ming He et al. "On-demand semiconductor single-photon source with near-unity indistinguishability". In: *Nature nanotechnology* 8.3 (2013), pp. 213–217.
- [156] Tobias Heindel et al. "Quantum key distribution using quantum dot single-photon emitting diodes in the red and near infrared spectral range". In: *New Journal of Physics* 14.8 (2012), p. 083001.
- [157] K Hennessy et al. "Tuning photonic crystal nanocavity modes by wet chemical digital etching". In: *Applied Physics Letters* 87.2 (2005), p. 021108.
- [158] K Hennessy et al. "Tuning photonic nanocavities by atomic force microscope nano-oxidation". In: *Applied Physics Letters* 89.4 (2006), p. 041118.
- [159] Martin T Hill et al. "Optimizing imbalance and loss in 2/spl times/2 3-dB multimode interference couplers via access waveguide width". In: *Journal of lightwave technology* 21.10 (2003), pp. 2305–2313.
- [160] Thang B Hoang et al. "Widely tunable, efficient on-chip single photon sources at telecommunication wavelengths". In: *Opt. Express* 20.19 (2012), pp. 21758–21765.
- [161] B Höfer et al. "Independent tuning of excitonic emission energy and decay time in single semiconductor quantum dots". In: *Applied Physics Letters* 110.15 (2017), p. 151102.
- [162] Ulrich Hohenester et al. "Phonon-assisted transitions from quantum dot excitons to cavity photons". In: *Physical Review B* 80.20 (2009), p. 201311.
- [163] Nils D Hoivik et al. "Atomic layer deposited protective coatings for micro-electromechanical systems". In: *Sensors and Actuators A: Physical* 103.1 (2003), pp. 100–108.
- [164] CK Hong, Zhe-Yu Ou, and Leonard Mandel. "Measurement of sub-picosecond time intervals between two photons by interference". In: *Physical review letters* 59.18 (1987), p. 2044.
- [165] WCL Hopman et al. "Nano-mechanical tuning and imaging of a photonic crystal micro-cavity resonance". In: *Optics express* 14.19 (2006), pp. 8745–8752.
- [166] Xiaoyong Hu et al. "All-optical switching of defect mode in two-dimensional nonlinear organic photonic crystals". In: *Applied Physics Letters* 87.23 (2005), p. 231111.
- [167] Michael CY Huang, Ye Zhou, and Connie J Chang-Hasnain. "A nanoelectromechanical tunable laser". In: *Nature Photonics* 2.3 (2008), pp. 180–184.

- [168] Stephen Hughes et al. "Extrinsic optical scattering loss in photonic crystal waveguides: role of fabrication disorder and photon group velocity". In: *Physical review letters* 94.3 (2005), p. 033903.
- [169] Chad Husko et al. "Ultrafast all-optical modulation in GaAs photonic crystal cavities". In: *Applied Physics Letters* 94.2 (2009), p. 021111.
- [170] Hiroaki Inoue et al. "Low loss GaAs optical waveguides". In: *IEEE Transactions on Electron Devices* 32.12 (1985), pp. 2662–2668.
- [171] Francesca Intonti et al. "Mode tuning of photonic crystal nanocavities by photoinduced non-thermal oxidation". In: *Applied Physics Letters* 100.3 (2012), p. 033116.
- [172] Francesca Intonti et al. "Rewritable photonic circuits". In: *Applied physics letters* 89.21 (2006), p. 211117.
- [173] Francesca Intonti et al. "Spectral tuning and near-field imaging of photonic crystal microcavities". In: *Phys. Rev. B* 78.4 (2008), p. 041401.
- [174] Francesca Intonti et al. "Tuning of photonic crystal cavities by controlled removal of locally infiltrated water". In: *Applied Physics Letters* 95.17 (2009), p. 173112.
- [175] Francesca Intonti et al. "Young's type interference for probing the mode symmetry in photonic structures". In: *Physical review letters* 106.14 (2011), p. 143901.
- [176] Norihiro Ishikura et al. "Photonic crystal tunable slow light device integrated with multi-heaters". In: *Applied Physics Letters* 100.22 (2012), p. 221110.
- [177] Satoshi Iwamoto et al. "Observation of micromechanically controlled tuning of photonic crystal line-defect waveguide". In: *Applied physics letters* 88.1 (2006), p. 011104.
- [178] Eiji Iwase et al. "Control of buckling in large micromembranes using engineered support structures". In: *Journal of Micromechanics and Microengineering* 22.6 (2012), p. 065028.
- [179] Saeedeh Jahanmirinejad et al. "Photon-number resolving detector based on a series array of superconducting nanowires". In: *Applied Physics Letters* 101.7 (2012), p. 072602.
- [180] C Jarlov et al. "Exciton dynamics in a site-controlled quantum dot coupled to a photonic crystal cavity". In: *Applied Physics Letters* 107.19 (2015), p. 191101.
- [181] Chao-Yuan Jin et al. "Ultrafast non-local control of spontaneous emission". In: *Nat. Nanotechnol.* 9 (2014), pp. 886–890.
- [182] John D Joannopoulos et al. *Photonic crystals: molding the flow of light*. Princeton university press, 2011.
- [183] Sajeed John. "Strong localization of photons in certain disordered dielectric superlattices". In: *Physical review letters* 58.23 (1987), p. 2486.
- [184] Steven G Johnson et al. "Adiabatic theorem and continuous coupled-mode theory for efficient taper transitions in photonic crystals". In: *Physical review E* 66.6 (2002), p. 066608.

- [185] KD Jöns et al. "Dependence of the Redshifted and Blueshifted Photoluminescence Spectra of Single In_xGa_{1-x}As/GaAs Quantum Dots on the Applied Uniaxial Stress". In: *Physical review letters* 107.21 (2011), p. 217402.
- [186] Klaus D Jöns et al. "Monolithic on-chip integration of semiconductor waveguides, beamsplitters and single-photon sources". In: *Journal of Physics D: Applied Physics* 48.8 (2015), p. 085101.
- [187] Klaus D Jöns et al. "Two-photon interference from two blinking quantum emitters". In: *arXiv preprint arXiv:1702.03278* (2017).
- [188] Pascale El-Kallassi et al. "Local infiltration of planar photonic crystals with UV-curable polymers". In: *JOSA B* 25.10 (2008), pp. 1562–1567.
- [189] Pascale El-Kallassi et al. "Optical tuning of planar photonic crystals infiltrated with organic molecules". In: *JOSA B* 24.9 (2007), pp. 2165–2171.
- [190] Sokratis Kalliakos et al. "In-plane emission of indistinguishable photons generated by an integrated quantum emitter". In: *Applied Physics Letters* 104.22 (2014), p. 221109.
- [191] C Kammerer et al. "Interferometric correlation spectroscopy in single quantum dots". In: *Applied Physics Letters* 81.15 (2002), pp. 2737–2739.
- [192] Yoshiaki Kanamori, Takashi Kitani, and Kazuhiro Hane. "Control of guided resonance in a photonic crystal slab using microelectromechanical actuators". In: *Applied physics letters* 90.3 (2007), p. 031911.
- [193] Yoshiaki Kanamori, Kazunori Takahashi, and Kazuhiro Hane. "An ultrasmall wavelength-selective channel drop switch using a nanomechanical photonic crystal nanocavity". In: *Applied Physics Letters* 95.17 (2009), p. 171911.
- [194] Michael Kaniber et al. "Integrated superconducting detectors on semiconductors for quantum optics applications". In: *Applied Physics B* 122.5 (2016), p. 115.
- [195] M Kaniber et al. "Electrical control of the exciton–biexciton splitting in self-assembled InGaAs quantum dots". In: *Nanotechnology* 22.32 (2011), p. 325202.
- [196] Stephan Kapfinger et al. "Dynamic acousto-optic control of a strongly coupled photonic molecule". In: *Nature communications* 6 (2015).
- [197] E Kapon et al. "Site-and energy-controlled pyramidal quantum dot heterostructures". In: *Physica E: Low-dimensional Systems and Nanostructures* 25.2 (2004), pp. 288–297.
- [198] Guk-Hyun Kim et al. "Coupling of small, low-loss hexapole mode with photonic crystal slab waveguide mode". In: *Optics express* 12.26 (2004), pp. 6624–6631.
- [199] Se-Heon Kim et al. "Optofluidic integration of a photonic crystal nanolaser". In: *Optics express* 16.9 (2008), pp. 6515–6527.
- [200] Hyochul Kim et al. "Independent tuning of quantum dots in a photonic crystal cavity". In: *Applied Physics Letters* 95.24 (2009), p. 243107.

- [201] Hyochul Kim et al. "Magnetic field tuning of a quantum dot strongly coupled to a photonic crystal cavity". In: *Appl. Phys. Lett.* 98.9 (2011), p. 091102.
- [202] Hyochul Kim et al. "Strong coupling between two quantum dots and a photonic crystal cavity using magnetic field tuning". In: *Optics express* 19.3 (2011), pp. 2589–2598.
- [203] Je-Hyung Kim et al. "Two-photon interference from the far-field emission of chip-integrated cavity-coupled emitters". In: *Nano Letters* 16.11 (2016), pp. 7061–7066.
- [204] Myung-Ki Kim et al. "All-optical bistable switching in curved microfiber-coupled photonic crystal resonators". In: *Applied physics letters* 90.16 (2007), p. 161118.
- [205] Myung-Ki Kim et al. "Reconfigurable microfiber-coupled photonic crystal resonator". In: *Optics express* 15.25 (2007), pp. 17241–17247.
- [206] H.J. Kimble. "The quantum internet". In: *Nature* 453.7198 (2008), pp. 1023–1030.
- [207] Laura Kinnischtzke et al. "Graphene mediated Stark shifting of quantum dot energy levels". In: *Applied Physics Letters* 108.21 (2016), p. 211905.
- [208] S Kiravittaya et al. "Tuning optical modes in slab photonic crystal by atomic layer deposition and laser-assisted oxidation". In: *Journal of Applied Physics* 109.5 (2011), p. 053115.
- [209] Atature Kiraz, M Atatüre, and A Imamoğlu. "Quantum-dot single-photon sources: Prospects for applications in linear optics quantum-information processing". In: *Physical Review A* 69.3 (2004), p. 032305.
- [210] Gabija Kiršanskė et al. "Indistinguishable and efficient single photons from a quantum dot in a planar nanobeam waveguide". In: *arXiv preprint arXiv:1701.08131* (2017).
- [211] C Kistner et al. "Demonstration of strong coupling via electro-optical tuning in high-quality QD-micropillar systems". In: *Optics Express* 16.19 (2008), pp. 15006–15012.
- [212] NAJM Kleemans et al. "Many-body exciton states in self-assembled quantum dots coupled to a Fermi sea". In: *Nature Physics* 6.7 (2010), pp. 534–538.
- [213] Emanuel Knill, Raymond Laflamme, and Gerald J Milburn. "A scheme for efficient quantum computation with linear optics". In: *nature* 409.6816 (2001), pp. 46–52.
- [214] A Femius Koenderink et al. "Controlling the resonance of a photonic crystal microcavity by a near-field probe". In: *Phys. Rev. Lett.* 95.15 (2005), p. 153904.
- [215] T Kojima et al. "Accurate alignment of a photonic crystal nanocavity with an embedded quantum dot based on optical microscopic photoluminescence imaging". In: *Applied Physics Letters* 102.1 (2013), p. 011110.

- [216] Pieter Kok et al. "Linear optical quantum computing with photonic qubits". In: *Reviews of Modern Physics* 79.1 (2007), p. 135.
- [217] K Konthasinghe et al. "Field-field and photon-photon correlations of light scattered by two remote two-level InAs quantum dots on the same substrate". In: *Physical review letters* 109.26 (2012), p. 267402.
- [218] A Koray Erdamar et al. "Tuning of a cavity in a silicon photonic crystal by thermal expansion of an elastomeric infill". In: *Applied Physics Letters* 99.11 (2011), p. 111113.
- [219] K Kowalik et al. "Influence of an in-plane electric field on exciton fine structure in InAs-GaAs self-assembled quantum dots". In: *Applied Physics Letters* 86.4 (2005), p. 041907.
- [220] Alexander G Krause et al. "A high-resolution microchip optomechanical accelerometer". In: *Nature Photonics* 6.11 (2012), pp. 768–772.
- [221] PE Kremer et al. "Strain-tunable quantum dot embedded in a nanowire antenna". In: *Physical Review B* 90.20 (2014), p. 201408.
- [222] Hari Krovi. "Models of optical quantum computing". In: *Nanophotonics* 6.3 (2017), pp. 531–541.
- [223] Andreas V Kuhlmann et al. "Charge noise and spin noise in a semiconductor quantum device". In: *arXiv preprint arXiv:1301.6381* (2013).
- [224] Christopher E Kuklewicz et al. "Electro-elastic tuning of single particles in individual self-assembled quantum dots". In: *Nano letters* 12.7 (2012), pp. 3761–3765.
- [225] S Kumar et al. "Strain-induced tuning of the emission wavelength of high quality GaAs/AlGaAs quantum dots in the spectral range of the 87Rb D2 lines". In: *Applied Physics Letters* 99.16 (2011), p. 161118.
- [226] T Kuroda et al. "Single-photon interferography in In As/ In P quantum dots emitting at 1300 nm wavelength". In: *Applied Physics Letters* 91.22 (2007), p. 223113.
- [227] DA Lapshin et al. "Direct measurement of the absolute value of the interaction force between the fiber probe and the sample in a scanning near-field optical microscope". In: *Applied physics letters* 81.8 (2002), pp. 1503–1505.
- [228] Ludovico Latmiral, Nicolò Spagnolo, and Fabio Sciarrino. "Towards quantum supremacy with lossy scattershot boson sampling". In: *New Journal of Physics* 18.11 (2016), p. 113008.
- [229] A Laucht et al. "Electrical control of spontaneous emission and strong coupling for a single quantum dot". In: *New J. Phys.* 11.2 (2009), p. 023034.
- [230] JM Laucht A; Villas-Bôas et al. "Mutual coupling of two semiconductor quantum dots via an optical nanocavity". In: *Physical Review B* 82.7 (2010), p. 075305.
- [231] S Laurent et al. "Indistinguishable single photons from a single-quantum dot in a two-dimensional photonic crystal cavity". In: *Applied Physics Letters* 87.16 (2005), p. 163107.

- [232] G Le Gac et al. "Tuning of an active photonic crystal cavity by an hybrid silica/silicon near-field probe". In: *Optics express* 17.24 (2009), pp. 21672–21679.
- [233] HS Lee et al. "Local tuning of photonic crystal nanocavity modes by laser-assisted oxidation". In: *Applied Physics Letters* 95.19 (2009), p. 191109.
- [234] JP Lee et al. "Electrically driven and electrically tunable quantum light sources". In: *Applied Physics Letters* 110.7 (2017), p. 071102.
- [235] Michael W Lee et al. "Photowritten high-Q cavities in two-dimensional chalcogenide glass photonic crystals". In: *Optics letters* 34.23 (2009), pp. 3671–3673.
- [236] Po-Tsung Lee et al. "Photonic crystal circular-shaped microcavity and its uniform cavity-waveguide coupling property due to presence of whispering gallery mode". In: *Optics express* 15.15 (2007), pp. 9450–9457.
- [237] Thomas Legero et al. "Characterization of single photons using two-photon interference". In: *Advances In Atomic, Molecular, and Optical Physics* 53 (2006), pp. 253–289.
- [238] Thomas Legero et al. "Quantum beat of two single photons". In: *Physical review letters* 93.7 (2004), p. 070503.
- [239] Thomas Legero et al. "Time-resolved two-photon quantum interference". In: *Applied Physics B: Lasers and Optics* 77.8 (2003), pp. 797–802.
- [240] leica-microsystems. "Leica, EM CPD 300 Manual". In: ().
- [241] R Lettow et al. "Quantum interference of tunably indistinguishable photons from remote organic molecules". In: *Physical review letters* 104.12 (2010), p. 123605.
- [242] Hsuan Lin et al. "Stress tuning of strong and weak couplings between quantum dots and cavity modes in microdisk microcavities". In: *Physical Review B* 84.20 (2011), p. 201301.
- [243] Shawn-yu Lin et al. "A three-dimensional photonic crystal operating at infrared wavelengths". In: *Nature* 394.6690 (1998), p. 251.
- [244] Tong Lin et al. "Design of mechanically-tunable photonic crystal split-beam nanocavity". In: *Optics letters* 40.15 (2015), pp. 3504–3507.
- [245] Tong Lin et al. "Dynamic control of the asymmetric Fano resonance in side-coupled Fabry–Pérot and photonic crystal nanobeam cavities". In: *Applied Physics Letters* 107.22 (2015), p. 223105. DOI: [10.1063/1.4936657](https://doi.org/10.1063/1.4936657). eprint: <http://dx.doi.org/10.1063/1.4936657>. URL: <http://dx.doi.org/10.1063/1.4936657>.
- [246] Tong Lin et al. "Dynamic control of the asymmetric Fano resonance in side-coupled Fabry–Pérot and photonic crystal nanobeam cavities". In: *Applied Physics Letters* 107.22 (2015), p. 223105.
- [247] Tong Lin et al. "In-plane rotation of the doubly coupled photonic crystal nanobeam cavities". In: *Journal of Optics* 18.5 (2016), 05LT02.

- [248] Tong Lin et al. "Out-of-plane nano-electro-mechanical tuning of the Fano resonance in photonic crystal split-beam nanocavity". In: *Applied Physics Letters* 107.15 (2015), p. 153107. DOI: [10.1063/1.4934187](https://doi.org/10.1063/1.4934187). eprint: <http://dx.doi.org/10.1063/1.4934187>. URL: <http://dx.doi.org/10.1063/1.4934187>.
- [249] Tong Lin et al. "Out-of-plane nano-electro-mechanical tuning of the Fano resonance in photonic crystal split-beam nanocavity". In: *Applied Physics Letters* 107.15 (2015), p. 153107.
- [250] Fenfei Liu et al. "Sub-pg mass sensing and measurement with an optomechanical oscillator". In: *Optics express* 21.17 (2013), pp. 19555–19567.
- [251] F Liu et al. "High Purcell factor generation of coherent on-chip single photons". In: *arXiv preprint arXiv:1706.04422* (2017).
- [252] Peter Lodahl, Sahand Mahmoodian, and Søren Stobbe. "Interfacing single photons and single quantum dots with photonic nanostructures". In: *Rev. Mod. Phys.* 87.2 (2015), pp. 347–400.
- [253] Peter Lodahl et al. "Chiral quantum optics". In: *Nature* 541.7638 (2017), pp. 473–480.
- [254] JC Loredó et al. "Boson sampling with single-photon Fock states from a bright solid-state source". In: *Physical Review Letters* 118.13 (2017), p. 130503.
- [255] Rodney Loudon. *The quantum theory of light*. OUP Oxford, 2000.
- [256] Ling Lu, Adam Mock, and John O'Brien. "Efficient coupling between a photonic crystal nanocavity and a waveguide with directional end-facet emission". In: *Journal of Optics* 14.5 (2012), p. 055502.
- [257] Tsan-Wen Lu and Po-Tsung Lee. "Ultra-high sensitivity optical stress sensor based on double-layered photonic crystal microcavity". In: *Optics express* 17.3 (2009), pp. 1518–1526.
- [258] Tsan-Wen Lu et al. "One-dimensional photonic crystal nanobeam lasers on a flexible substrate". In: *Applied Physics Letters* 99.7 (2011), p. 071101.
- [259] Jun-Wei Luo et al. "Influence of the atomic-scale structure on the exciton fine-structure splitting in InGaAs and GaAs quantum dots in a vertical electric field". In: *Physical Review B* 86.16 (2012), p. 161302.
- [260] IJ Luxmoore et al. "Interfacing spins in an InGaAs quantum dot to a semiconductor waveguide circuit using emitted photons". In: *Physical review letters* 110.3 (2013), p. 037402.
- [261] IJ Luxmoore et al. "Optical control of the emission direction of a quantum dot". In: *Applied Physics Letters* 103.24 (2013), p. 241102.
- [262] IJ Luxmoore et al. "Restoring mode degeneracy in H₁ photonic crystal cavities by uniaxial strain tuning". In: *Applied Physics Letters* 100.12 (2012), p. 121116.

- [263] Roya Maboudian, W Robert Ashurst, and Carlo Carraro. "Self-assembled monolayers as anti-stiction coatings for MEMS: characteristics and recent developments". In: *Sensors and Actuators A: Physical* 82.1 (2000), pp. 219–223.
- [264] Marc J Madou. *Fundamentals of microfabrication: the science of miniaturization*. CRC press, 2002.
- [265] Kristian Høeg Madsen and Peter Lodahl. "Quantitative analysis of quantum dot dynamics and emission spectra in cavity quantum electrodynamics". In: *New Journal of Physics* 15.2 (2013), p. 025013.
- [266] Maxim N Makhonin et al. "Waveguide coupled resonance fluorescence from on-chip quantum emitter". In: *Nano letters* 14.12 (2014), pp. 6997–7002.
- [267] T Malhotra et al. "Quasinormal mode theory and design of on-chip single photon emitters in photonic crystal coupled-cavity waveguides". In: *Optics express* 24.12 (2016), pp. 13574–13583.
- [268] Stefano Mancini et al. "Entangling macroscopic oscillators exploiting radiation pressure". In: *Physical review letters* 88.12 (2002), p. 120401.
- [269] JD Mar et al. "Bias-controlled single-electron charging of a self-assembled quantum dot in a two-dimensional-electron-gas-based n-i-Schottky diode". In: *Physical Review B* 83.7 (2011), p. 075306.
- [270] JD Mar et al. "Electrical control of fine-structure splitting in self-assembled quantum dots for entangled photon pair creation". In: *Applied Physics Letters* 97.22 (2010), p. 221108.
- [271] S Marcet, K Ohtani, and H Ohno. "Vertical electric field tuning of the exciton fine structure splitting and photon correlation measurements of GaAs quantum dot". In: *Applied Physics Letters* 96.10 (2010), p. 101117.
- [272] Iwan Märki, Martin Salt, and Hans Peter Herzig. "Tuning the resonance of a photonic crystal microcavity with an AFM probe". In: *Optics Express* 14.7 (2006), pp. 2969–2978.
- [273] Iwan Märki et al. "Optically tunable microcavity in a planar photonic crystal silicon waveguide buried in oxide". In: *Optics letters* 31.4 (2006), pp. 513–515.
- [274] J Martz et al. "Liquid crystal infiltration of InP-based planar photonic crystals". In: *Journal of applied physics* 99.10 (2006), p. 103105.
- [275] Clemens Matthiesen, Anthony Nickolas Vamivakas, and Mete Atatüre. "Subnatural linewidth single photons from a quantum dot". In: *Physical Review Letters* 108.9 (2012), p. 093602.
- [276] Brett Maune et al. "Liquid-crystal electric tuning of a photonic crystal laser". In: *Applied Physics Letters* 85.3 (2004), pp. 360–362.
- [277] Brett Maune et al. "Optically triggered Q-switched photonic crystal laser". In: *Optics express* 13.12 (2005), pp. 4699–4707.
- [278] Dennis McPhail, Martin Straub, and Min Gu. "Electrical tuning of three-dimensional photonic crystals using polymer dispersed liquid crystals". In: *Applied Physics Letters* 86.5 (2005), p. 051103.

- [279] LO Mereni et al. "A site-controlled quantum dot system offering both high uniformity and spectral purity". In: *Applied Physics Letters* 94.22 (2009), p. 223121.
- [280] Michael Metcalfe et al. "Resolved sideband emission of InAs/GaAs quantum dots strained by surface acoustic waves". In: *Physical review letters* 105.3 (2010), p. 037401.
- [281] L Midolo. "Electromechanical tuning of photonic crystal cavities". PhD thesis. Ph. D. dissertation, Eindhoven University of Technology, 2013.
- [282] Leonardo Midolo and Andrea Fiore. "Design and Optical Properties of Electromechanical Double-Membrane Photonic Crystal Cavities". In: *Quantum Electronics, IEEE Journal of* 50.6 (2014), pp. 404–414.
- [283] Leonardo Midolo et al. "Electro-optic routing of photons from single quantum dots in photonic integrated circuits". In: *arXiv preprint arXiv:1707.06522* (2017).
- [284] Leondardo Midolo et al. "Electromechanical wavelength tuning of double-membrane photonic crystal cavities". In: *Appl. Phys. Lett.* 98.21 (2011), p. 211120.
- [285] L Midolo et al. "Electromechanical tuning of vertically-coupled photonic crystal nanobeams". In: *Optics express* 20.17 (2012), pp. 19255–19263.
- [286] L Midolo et al. "Spontaneous emission control of single quantum dots by electromechanical tuning of a photonic crystal cavity". In: *Appl. Phys. Lett.* 101.9 (2012), p. 091106.
- [287] Alan L Migdall, D Branning, and Stefania Castelletto. "Tailoring single-photon and multiphoton probabilities of a single-photon on-demand source". In: *Physical Review A* 66.5 (2002), p. 053805.
- [288] Javier Miguel-Sánchez et al. "Cavity quantum electrodynamics with charge-controlled quantum dots coupled to a fiber Fabry–Perot cavity". In: *New Journal of Physics* 15.4 (2013), p. 045002.
- [289] Sergei F Mingaleev et al. "Tunable photonic crystal circuits: concepts and designs based on single-pore infiltration". In: *Optics letters* 29.24 (2004), pp. 2858–2860.
- [290] Momchil Minkov and Vincenzo Savona. "Automated optimization of photonic crystal slab cavities". In: *Scientific reports* 4 (2014), p. 5124.
- [291] Toshiyuki Miyazawa et al. "Development of electrically driven single-quantum-dot device at optical fiber bands". In: *Japanese journal of applied physics* 45.4S (2006), p. 3621.
- [292] Toshiyuki Miyazawa et al. "Electric field modulation of exciton recombination in InAs/GaAs quantum dots emitting at $1.3 \mu\text{m}$ ". In: *Journal of Applied Physics* 104.1 (2008), p. 013504.
- [293] Toshiyuki Miyazawa et al. "Exciton dynamics in current-injected single quantum dot at $1.55 \mu\text{m}$ ". In: *Applied Physics Letters* 92.16 (2008), p. 161104.

- [294] Iwan Mírki, Martin Salt, and Hans Peter Herzig. "Tuning the resonance of a photonic crystal microcavity with an AFM probe". In: *Optics express* 14.7 (2006), pp. 2969–2978.
- [295] Gregory Moille, Sylvain Combrié, and Alfredo De Rossi. "Modeling of the carrier dynamics in nonlinear semiconductor nanoscale resonators". In: *Physical Review A* 94.2 (2016), p. 023814.
- [296] Jessica P Mondia et al. "Ultrafast tuning of two-dimensional planar photonic-crystal waveguides via free-carrier injection and the optical Kerr effect". In: *JOSA B* 22.11 (2005), pp. 2480–2486.
- [297] Galan Moody et al. "Electronic enhancement of the exciton coherence time in charged quantum dots". In: *Physical review letters* 116.3 (2016), p. 037402.
- [298] E Moreau et al. "Single-mode solid-state single photon source based on isolated quantum dots in pillar microcavities". In: *Applied Physics Letters* 79.18 (2001), pp. 2865–2867.
- [299] S Mosor et al. "Scanning a photonic crystal slab nanocavity by condensation of xenon". In: *Appl. Phys. Lett.* 87.14 (2005), p. 141105.
- [300] Sushil Mujumdar et al. "Near-field imaging and frequency tuning of a high-Q photonic crystal membrane microcavity". In: *Optics express* 15.25 (2007), pp. 17214–17220.
- [301] Andreas Muller et al. "Creating polarization-entangled photon pairs from a semiconductor quantum dot using the optical stark effect". In: *Physical review letters* 103.21 (2009), p. 217402.
- [302] Markus Müller et al. "On-demand generation of indistinguishable polarization-entangled photon pairs". In: *Nature Photonics* 8.3 (2014), pp. 224–228.
- [303] Pierce Munnelly et al. "A pulsed nonclassical light source driven by an integrated electrically triggered quantum dot microlaser". In: *IEEE Journal of Selected Topics in Quantum Electronics* 21.6 (2015), pp. 681–689.
- [304] Pierce Munnelly et al. "An electrically tunable single-photon source triggered by a monolithically integrated quantum dot microlaser". In: *ACS Photonics* (2017).
- [305] Tatsuya Nakamura et al. "Controlling the emission of quantum dots embedded in photonic crystal nanocavity by manipulating Q-factor and detuning". In: *Physical Review B* 84.24 (2011), p. 245309.
- [306] T Nakaoka et al. "Competing influence of an in-plane electric field on the Stark shifts in a semiconductor quantum dot". In: *Applied Physics Letters* 99.18 (2011), p. 181109.
- [307] Alex Neville et al. "No imminent quantum supremacy by boson sampling". In: *arXiv preprint arXiv:1705.00686* (2017).
- [308] J Nilsson et al. "Quantum teleportation using a light-emitting diode". In: *Nature Photonics* 7.4 (2013), pp. 311–315.

- [309] Susumu Noda et al. "Full three-dimensional photonic bandgap crystals at near-infrared wavelengths". In: *Science* 289.5479 (2000), pp. 604–606.
- [310] Masaya Notomi et al. "Optomechanical wavelength and energy conversion in high-Q double-layer cavities of photonic crystal slabs". In: *Phys. Rev. Lett.* 97.2 (2006), p. 023903.
- [311] Masaya Notomi et al. "Toward fJ/bit optical communication in a chip". In: *Optics Communications* 314 (2014), pp. 3–17.
- [312] AK Nowak et al. "Deterministic and electrically tunable bright single-photon source". In: *Nature communications* 5 (2014).
- [313] Kengo Nozaki, Hideki Watanabe, and Toshihiko Baba. "Photonic crystal nanolaser monolithically integrated with passive waveguide for effective light extraction". In: *Applied Physics Letters* 92.2 (2008), p. 021108.
- [314] Kengo Nozaki et al. "Sub-femtojoule all-optical switching using a photonic-crystal nanocavity". In: *Nature Photonics* 4.7 (2010), pp. 477–483.
- [315] Ryuichi Ohta et al. "Electro-mechanical Q factor control of photonic crystal nanobeam cavity". In: *Japanese Journal of Applied Physics* 52.4S (2013), 04CG01.
- [316] Ryuichi Ohta et al. "Strong coupling between a photonic crystal nanobeam cavity and a single quantum dot". In: *Applied Physics Letters* 98.17 (2011), p. 173104.
- [317] Adeline Orioux and Eleni Diamanti. "Recent advances on integrated quantum communications". In: *Journal of Optics* 18.8 (2016), p. 083002.
- [318] Yasutomo Ota et al. "Vacuum Rabi spectra of a single quantum emitter". In: *Physical review letters* 114.14 (2015), p. 143603.
- [319] R Oulton et al. "Manipulation of the homogeneous linewidth of an individual In (Ga) As quantum dot". In: *Physical Review B* 66.4 (2002), p. 045313.
- [320] FM Pagliano. "Dynamic control of the spontaneous emission of single quantum dots in photonic crystal cavities, PhD thesis". In: (2014).
- [321] Francesco Pagliano et al. "Dynamically controlling the emission of single excitons in photonic crystal cavities". In: *Nat. Commun.* 5 (2014), p. 5786.
- [322] Oskar Painter et al. "Lithographic tuning of a two-dimensional photonic crystal laser array". In: *IEEE Photonics Technology Letters* 12.9 (2000), pp. 1126–1128.
- [323] Jun Pan et al. "Aligning microcavity resonances in silicon photonic-crystal slabs using laser-pumped thermal tuning". In: *Applied Physics Letters* 92.10 (2008), p. 103114.
- [324] Taofiq K Paraiso et al. "Position-squared coupling in a tunable photonic crystal optomechanical cavity". In: *Physical Review X* 5.4 (2015), p. 041024.

- [325] Hong-Gyu Park et al. "Electrically driven single-cell photonic crystal laser". In: *Science* 305.5689 (2004), pp. 1444–1447.
- [326] Raj B Patel et al. "Quantum interference of electrically generated single photons from a quantum dot". In: *Nanotechnology* 21.27 (2010), p. 274011.
- [327] Raj B Patel et al. "Two-photon interference of the emission from electrically tunable remote quantum dots". In: *Nature photonics* 4.9 (2010), pp. 632–635.
- [328] RB Patel et al. "Postselective two-photon interference from a continuous nonclassical stream of photons emitted by a quantum dot". In: *Physical review letters* 100.20 (2008), p. 207405.
- [329] Lorenzo Pavesi and David J Lockwood. *Silicon photonics*. Vol. 1. Springer Science & Business Media, 2004.
- [330] Raviv Perahia et al. "Electrostatically tunable optomechanical "zipper" cavity laser". In: *Applied Physics Letters* 97.19 (2010), p. 191112.
- [331] R. Perahia et al. "Electrostatically tunable optomechanical "zipper" cavity laser". In: *Appl. Phys. Lett.* 97.19, 191112 (2010). DOI: <http://dx.doi.org/10.1063/1.3515296>. URL: <http://scitation.aip.org/content/aip/journal/apl/97/19/10.1063/1.3515296>.
- [332] Wolfram HP Pernice et al. "High-speed and high-efficiency travelling wave single-photon detectors embedded in nanophotonic circuits". In: *Nature communications* 3 (2012), p. 1325.
- [333] M Petruzzella et al. "Fully tuneable, Purcell-enhanced solid-state quantum emitters". In: *Appl. Phys. Lett.* 107.14 (2015), p. 141109.
- [334] M Petruzzella et al. "Nanoscale mechanical actuation and near-field read-out of photonic crystal molecules". In: *Physical Review B* 94.11 (2016), p. 115413.
- [335] Alexander Y Piggott et al. "Photo-oxidative tuning of individual and coupled GaAs photonic crystal cavities". In: *Opt. Express* 22.12 (2014), pp. 15017–15023.
- [336] D Pinotsi et al. "Charge controlled self-assembled quantum dots coupled to photonic crystal nanocavities". In: *Photonics and Nanostructures-Fundamentals and Applications* 10.3 (2012), pp. 256–262.
- [337] Alessandro Pitanti et al. "Strong opto-electro-mechanical coupling in a silicon photonic crystal cavity". In: *Optics express* 23.3 (2015), pp. 3196–3208.
- [338] Taras Plakhotnik et al. "Single molecule spectroscopy: maximum emission rate and saturation intensity". In: *Optics communications* 114.1-2 (1995), pp. 83–88.
- [339] JD Plumhof et al. "Strain-induced anticrossing of bright exciton levels in single self-assembled GaAs/Al_xGa_{1-x}As and In_xGa_{1-x}As/GaAs quantum dots". In: *Physical Review B* 83.12 (2011), p. 121302.
- [340] Johannes D Plumhof et al. "Experimental methods of post-growth tuning of the excitonic fine structure splitting in semiconductor quantum dots". In: *Nanoscale research letters* 7.1 (2012), p. 336.

- [341] Alberto Politi et al. "Integrated quantum photonics". In: *IEEE Journal of Selected Topics in Quantum Electronics* 15.6 (2009), pp. 1673–1684.
- [342] Alberto Politi et al. "Silica-on-silicon waveguide quantum circuits". In: *Science* 320.5876 (2008), pp. 646–649.
- [343] MA Pooley et al. "Energy-tunable quantum dot with minimal fine structure created by using simultaneous electric and magnetic fields". In: *Physical Review Applied* 1.2 (2014), p. 024002.
- [344] MA Pooley et al. "Engineering quantum dots for electrical control of the fine structure splitting". In: *Applied Physics Letters* 103.3 (2013), p. 031105.
- [345] Simone L Portalupi et al. "Planar photonic crystal cavities with far-field optimization for high coupling efficiency and quality factor". In: *Optics express* 18.15 (2010), pp. 16064–16073.
- [346] John Preskill. "Quantum computing and the entanglement frontier". In: *arXiv preprint arXiv:1203.5813* (2012).
- [347] Stefan Prorok et al. "Configurable silicon photonic crystal waveguides". In: *Applied Physics Letters* 103.26 (2013), p. 261112.
- [348] N Prtljaga et al. "Monolithic integration of a quantum emitter with a compact on-chip beam-splitter". In: *Applied Physics Letters* 104.23 (2014), p. 231107.
- [349] Demetri Psaltis, Stephen R Quake, and Changhuei Yang. "Developing optofluidic technology through the fusion of microfluidics and optics". In: *Nature* 442.7101 (2006), pp. 381–386.
- [350] E. Purcell. "Proceedings of the American Physical Society". In: *Phys. Rev.* 69 (11-12 June 1946), pp. 674–674. DOI: [10.1103/PhysRev.69.674](https://doi.org/10.1103/PhysRev.69.674). URL: <http://link.aps.org/doi/10.1103/PhysRev.69.674.2>.
- [351] Jens Pustiowski et al. "Independent dynamic acousto-mechanical and electrostatic control of individual quantum dots in a LiNbO₃-GaAs hybrid". In: *Applied Physics Letters* 106.1 (2015), p. 013107. DOI: [10.1063/1.4905477](https://doi.org/10.1063/1.4905477). eprint: <http://dx.doi.org/10.1063/1.4905477>. URL: <http://dx.doi.org/10.1063/1.4905477>.
- [352] Marina Radulaski, Kevin Fischer, and Jelena Vuckovic. "Nonclassical Light Generation from III-V and Group-IV Solid-State Cavity Quantum Systems". In: *arXiv preprint arXiv:1701.03039* (2017).
- [353] F Raineri et al. "Tuning a two-dimensional photonic crystal resonance via optical carrier injection". In: *Optics letters* 30.1 (2005), pp. 64–66.
- [354] MT Rakher et al. "Externally mode-matched cavity quantum electrodynamics with charge-tunable quantum dots". In: *Physical review letters* 102.9 (2009), p. 097403.
- [355] DV Regelman et al. "Semiconductor quantum dot: A quantum light source of multicolor photons with tunable statistics". In: *Physical review letters* 87.25 (2001), p. 257401.
- [356] Thorsten Reichert et al. "Highly directed emission from self-assembled quantum dots into guided modes in disordered photonic-crystal waveguides". In: *Physical Review B* 90.11 (2014), p. 115310.

- [357] Michael E Reimer et al. "Electric field induced removal of the biexciton binding energy in a single quantum dot". In: *Nano letters* 11.2 (2011), pp. 645–650.
- [358] Marcus Reindl et al. "Phonon-assisted two-photon interference from remote quantum emitters". In: *Nano Letters* (2017).
- [359] Andreas Reinhard et al. "Strongly correlated photons on a chip". In: *Nature Photonics* 6.2 (2012), pp. 93–96.
- [360] Günther Reithmaier et al. "On-chip generation, routing, and detection of resonance fluorescence". In: *Nano letters* 15.8 (2015), pp. 5208–5213.
- [361] Günther Reithmaier et al. "On-chip time resolved detection of quantum dot emission using integrated superconducting single photon detectors". In: *arXiv preprint arXiv:1302.3807* (2013).
- [362] Johann Peter Reithmaier. "Strong exciton–photon coupling in semiconductor quantum dot systems". In: *Semiconductor Science and Technology* 23.12 (2008), p. 123001.
- [363] S Reitzenstein and A Forchel. "Quantum dot micropillars". In: *Journal of Physics D: Applied Physics* 43.3 (2010), p. 033001.
- [364] S Reitzenstein et al. "Control of the strong light-matter interaction between an elongated In_{0.3}Ga_{0.7}As quantum dot and a micropillar cavity using external magnetic fields". In: *Physical review letters* 103.12 (2009), p. 127401.
- [365] Qijun Ren et al. "Spin-resolved Purcell effect in a quantum dot microcavity system". In: *Nano letters* 12.7 (2012), pp. 3455–3459.
- [366] JJ Renema et al. "Experimental test of theories of the detection mechanism in a nanowire superconducting single photon detector". In: *Physical review letters* 112.11 (2014), p. 117604.
- [367] RP Ribas et al. "Bulk micromachining characterization of 0.2 μm HEMT MMIC technology for GaAs MEMS design". In: *Materials Science and Engineering: B* 51.1 (1998), pp. 267–273.
- [368] Jacob T Robinson et al. "Ultrasmall mode volumes in dielectric optical microcavities". In: *Physical review letters* 95.14 (2005), p. 143901.
- [369] Peter P Rohde, Timothy C Ralph, and Michael A Nielsen. "Optimal photons for quantum-information processing". In: *Physical Review A* 72.5 (2005), p. 052332.
- [370] Peter P Rohde et al. "Will boson-sampling ever disprove the Extended Church-Turing thesis?" In: *arXiv preprint arXiv:1401.2199* (2014).
- [371] Döndü Sahin et al. "Integrated autocorrelator based on superconducting nanowires". In: *Optics express* 21.9 (2013), pp. 11162–11170.
- [372] D Sahin et al. "Waveguide photon-number-resolving detectors for quantum photonic integrated circuits". In: *Applied Physics Letters* 103.11 (2013), p. 111116.

- [373] Toshio Saito, Toshihiro Nakaoka, and Yasuhiko Arakawa. "Effect of lateral electric field on the transition energies of neutral and charged excitons in In_{0.5}Ga_{0.5}As/GaAs quantum dots". In: *Physical Review B* 91.11 (2015), p. 115306.
- [374] CL Salter et al. "An entangled-light-emitting diode". In: *Nature* 465.7298 (2010), pp. 594–597.
- [375] Kaoru Sanaka et al. "Indistinguishable photons from independent semiconductor nanostructures". In: *Physical review letters* 103.5 (2009), p. 053601.
- [376] R Santagati et al. "Quantum simulation of Hamiltonian spectra on a silicon chip". In: *arXiv preprint arXiv:1611.03511* (2016).
- [377] Charles Santori et al. "Indistinguishable photons from a single-photon device". In: *nature* 419.6907 (2002), p. 594.
- [378] C Santori et al. "Nanophotonics for quantum optics using nitrogen-vacancy centers in diamond". In: *Nanotechnology* 21.27 (2010), p. 274008.
- [379] Yoshiya Sato et al. "Strong coupling between distant photonic nanocavities and its dynamic control". In: *Nature Photonics* 6.1 (2012), pp. 56–61.
- [380] S Schartner et al. "Post-fabrication fine-tuning of photonic crystal quantum well infrared photodetectors". In: *Applied Physics Letters* 94.23 (2009), p. 231117.
- [381] Alexander Schlehahn et al. "A stand-alone fiber-coupled single-photon source". In: *arXiv preprint arXiv:1703.10536* (2017).
- [382] C Schneider et al. "Single site-controlled In (Ga) As/GaAs quantum dots: growth, properties and device integration". In: *Nanotechnology* 20.43 (2009), p. 434012.
- [383] Florian JR Schülein et al. "Acoustically regulated carrier injection into a single optically active quantum dot". In: *Physical Review B* 88.8 (2013), p. 085307.
- [384] Ch Schuller et al. "Tunable photonic crystals fabricated in III-V semiconductor slab waveguides using infiltrated liquid crystals". In: *Applied Physics Letters* 82.17 (2003), pp. 2767–2769.
- [385] Andre Schwagmann et al. "In-plane single-photon emission from a L₃ cavity coupled to a photonic crystal waveguide". In: *Optics express* 20.27 (2012), pp. 28614–28624.
- [386] Mario Schwartz et al. "Generation, guiding and splitting of triggered single photons from a resonantly excited quantum dot in a photonic circuit". In: *Optics express* 24.3 (2016), pp. 3089–3094.
- [387] Stefan Seidl et al. "Effect of uniaxial stress on excitons in a self-assembled quantum dot". In: *Applied Physics Letters* 88.20 (2006), p. 203113.
- [388] Stephen D Senturia. *Microsystem design*. Springer Science & Business Media, 2007.

- [389] Min-Kyo Seo et al. "Controlled sub-nanometer tuning of photonic crystal resonator by carbonaceous nano-dots". In: *Opt. Express* 16.13 (2008), pp. 9829–9837.
- [390] Gary Shambat et al. "Electrically driven photonic crystal nanocavity devices". In: *IEEE Journal of Selected Topics in Quantum Electronics* 18.6 (2012), pp. 1700–1710.
- [391] Gary Shambat et al. "Ultrafast direct modulation of a single-mode photonic crystal nanocavity light-emitting diode". In: *Nature communications* 2 (2011), p. 539.
- [392] Peng Shi et al. "Tuning the quality factor of split nanobeam cavity by nanoelectromechanical systems". In: *Optics express* 23.15 (2015), pp. 19338–19347.
- [393] AJ Shields et al. *Generation of single photons using semiconductor quantum dots*. Elsevier, 2002.
- [394] Peter W Shor. "Algorithms for quantum computation: Discrete logarithms and factoring". In: *Foundations of Computer Science, 1994 Proceedings., 35th Annual Symposium on*. IEEE. 1994, pp. 124–134.
- [395] Joshua W Silverstone et al. "Silicon quantum photonics". In: *IEEE Journal of Selected Topics in Quantum Electronics* 22.6 (2016), pp. 390–402.
- [396] Joanna Skiba-Szymanska et al. "Narrow emission linewidths of positioned InAs quantum dots grown on pre-patterned GaAs (100) substrates". In: *Nanotechnology* 22.6 (2011), p. 065302.
- [397] Cameron LC Smith et al. "Microfluidic photonic crystal double heterostructures". In: *Applied Physics Letters* 91.12 (2007), p. 121103.
- [398] Cameron L Smith et al. "Reconfigurable microfluidic photonic crystal slab cavities". In: *Optics express* 16.20 (2008), pp. 15887–15896.
- [399] Lucas B Soldano and Erik CM Pennings. "Optical multi-mode interference devices based on self-imaging: principles and applications". In: *Journal of lightwave technology* 13.4 (1995), pp. 615–627.
- [400] Immo Söllner et al. "Deterministic photon-emitter coupling in chiral photonic circuits". In: *Nature nanotechnology* 10.9 (2015), pp. 775–778.
- [401] Nicolò Spagnolo et al. "Experimental validation of photonic boson sampling". In: *Nature Photonics* 8.8 (2014), pp. 615–620.
- [402] Noud WL Speijcken et al. "In situ optofluidic control of reconfigurable photonic crystal cavities". In: *Applied Physics Letters* 100.26 (2012), p. 261107.
- [403] JP Sprengers et al. "Waveguide superconducting single-photon detectors for integrated quantum photonic circuits". In: *Applied Physics Letters* 99.18 (2011), p. 181110.
- [404] Justin B Spring et al. "Boson sampling on a photonic chip". In: *Science* (2012), p. 1231692.
- [405] Deepak Sridharan et al. "A reversibly tunable photonic crystal nanocavity laser using photochromic thin film". In: *Optics express* 19.6 (2011), pp. 5551–5558.

- [406] Deepak Sridharan et al. "Reversible tuning of photonic crystal cavities using photochromic thin films". In: *Applied Physics Letters* 96.15 (2010), p. 153303.
- [407] V Stavarache et al. "Control of quantum dot excitons by lateral electric fields". In: *Applied physics letters* 89.12 (2006), p. 123105.
- [408] Petr Stepanov et al. "Quantum dot spontaneous emission control in a ridge waveguide". In: *Applied Physics Letters* 106.4 (2015), p. 041112.
- [409] R Mark Stevenson et al. "A semiconductor source of triggered entangled photon pairs". In: *Nature* 439.7073 (2006), pp. 179–182.
- [410] RM Stevenson et al. "Quantum teleportation of laser-generated photons with an entangled-light-emitting diode". In: *Nature communications* 4 (2013).
- [411] Magdalena Stobińska, Gernot Alber, and Gerd Leuchs. "Perfect excitation of a matter qubit by a single photon in free space". In: *EPL (Europhysics Letters)* 86.1 (2009), p. 14007.
- [412] Raoul Stöckle et al. "High-quality near-field optical probes by tube etching". In: *Appl. Phys. Lett.* 75.2 (1999), pp. 160–162.
- [413] Stefan Strauf et al. "Frequency control of photonic crystal membrane resonators by monolayer deposition". In: *Applied Physics Letters* 88.4 (2006), p. 043116.
- [414] Wonjoo Suh et al. "Displacement-sensitive photonic crystal structures based on guided resonance in photonic crystal slabs". In: *Applied physics letters* 82.13 (2003), pp. 1999–2001.
- [415] FW Sun, CW Wong, et al. "Indistinguishability of independent single photons". In: *Physical Review A* 79.1 (2009), p. 013824.
- [416] Shuo Sun et al. "Strain tuning of a quantum dot strongly coupled to a photonic crystal cavity". In: *Applied Physics Letters* 103.15 (2013), p. 151102.
- [417] Tobias Süß, Philipp Braeuninger-Weimer, and Christofer Hierold. "Stress reduction in ultra-small thin film Al₂O₃ diaphragms by atomic layer deposition". In: *Sensors and Actuators A: Physical* 212 (2014), pp. 159–164.
- [418] A Szerling et al. "Proton implantation for the isolation of AlGaAs/-GaAs quantum cascade lasers". In: *Semiconductor Science and Technology* 31.7 (2016), p. 075010.
- [419] Motoki Takahashi et al. "Local control of emission energy of semiconductor quantum dots using volume expansion of a phase-change material". In: *Applied Physics Letters* 102.9 (2013), p. 093120.
- [420] Takasumi Tanabe et al. "All-optical switches on a silicon chip realized using photonic crystal nanocavities". In: *Applied Physics Letters* 87.15 (2005), p. 151112.
- [421] Takasumi Tanabe et al. "Dynamic release of trapped light from an ultrahigh-Q nanocavity via adiabatic frequency tuning". In: *Physical review letters* 102.4 (2009), p. 043907.

- [422] Takasumi Tanabe et al. "Electro-optic adiabatic wavelength shifting and Q switching demonstrated using a pin integrated photonic crystal nanocavity". In: *Optics letters* 35.23 (2010), pp. 3895–3897.
- [423] Takasumi Tanabe et al. "Low power and fast electro-optic silicon modulator with lateral pin embedded photonic crystal nanocavity". In: *Optics express* 17.25 (2009), pp. 22505–22513.
- [424] Yoshinori Tanaka et al. "Dynamic control of the Q factor in a photonic crystal nanocavity". In: *Nature materials* 6.11 (2007), pp. 862–865.
- [425] Jing Tang et al. "Charge state control in single InAs/GaAs quantum dots by external electric and magnetic fields". In: *Applied Physics Letters* 105.4 (2014), p. 041109.
- [426] Alexander Thoma et al. "Two-photon interference from remote deterministic quantum dot microlenses". In: *Applied Physics Letters* 110.1 (2017), p. 011104.
- [427] Susanna M Thon et al. "Independent electrical tuning of separated quantum dots in coupled photonic crystal cavities". In: *Applied Physics Letters* 99.16 (2011), p. 161102.
- [428] Susanna M Thon et al. "Strong coupling through optical positioning of a quantum dot in a photonic crystal cavity". In: *Applied Physics Letters* 94.11 (2009), p. 111115.
- [429] Feng Tian et al. "Tuning of split-ladder cavity by its intrinsic nano-deformation". In: *Optics express* 20.25 (2012), pp. 27697–27707.
- [430] Petru Tighineanu et al. "Phonon Decoherence of Quantum Dots in Photonic Structures: Broadening of the Zero-Phonon Line and the Role of Dimensionality". In: *arXiv preprint arXiv:1702.04812* (2017).
- [431] Max Tillmann et al. "Experimental boson sampling". In: *Nature Photonics* 7.7 (2013), pp. 540–544.
- [432] Rinaldo Trotta and Armando Rastelli. "Engineering of quantum dot photon sources via electro-elastic fields". In: *Engineering the Atom-Photon Interaction*. Springer, 2015, pp. 277–302.
- [433] Rinaldo Trotta et al. "Highly entangled photons from hybrid piezoelectric-semiconductor quantum dot devices". In: *Nano letters* 14.6 (2014), pp. 3439–3444.
- [434] Rinaldo Trotta et al. "Independent control of exciton and biexciton energies in single quantum dots via electroelastic fields". In: *Physical Review B* 88.15 (2013), p. 155312.
- [435] Rinaldo Trotta et al. "Wavelength-tunable sources of entangled photons interfaced with atomic vapours". In: *Nature communications* 7 (2016).
- [436] R Trotta et al. "Nanomembrane Quantum-Light-Emitting Diodes Integrated onto Piezoelectric Actuators". In: *Advanced materials* 24.20 (2012), pp. 2668–2672.
- [437] R Trotta et al. "Universal recovery of the energy-level degeneracy of bright excitons in InGaAs quantum dots without a structure symmetry". In: *Physical review letters* 109.14 (2012), p. 147401.

- [438] Ansel C Ugural and Saul K Fenster. *Advanced strength and applied elasticity*. Pearson Education, 2003.
- [439] Ken-ichi Umemori, Yoshiaki Kanamori, and Kazuhiro Hane. “Photonic crystal waveguide switch with a microelectromechanical actuator”. In: *Applied physics letters* 89.2 (2006), p. 021102.
- [440] Thomas Unold et al. “Optical Stark effect in a quantum dot: Ultrafast control of single exciton polarizations”. In: *Physical review letters* 92.15 (2004), p. 157401.
- [441] Sebastian Unsleber et al. “Two-photon interference from a quantum dot microcavity: Persistent pure dephasing and suppression of time jitter”. In: *Physical Review B* 91.7 (2015), p. 075413.
- [442] Lieven MK Vandersypen et al. “Experimental realization of Shor’s quantum factoring algorithm using nuclear magnetic resonance”. In: *Nature* 414.6866 (2001), pp. 883–887.
- [443] Christiana Varnava et al. “An entangled-LED-driven quantum relay over 1 km”. In: *npj Quantum Information* 2 (2016), p. 16006.
- [444] S Varoutsis et al. “Restoration of photon indistinguishability in the emission of a semiconductor quantum dot”. In: *Physical Review B* 72.4 (2005), p. 041303.
- [445] Silvia Vignolini et al. “Mode hybridization in photonic crystal molecules”. In: *Applied Physics Letters* 97.6 (2010), p. 063101.
- [446] Silvia Vignolini et al. “Nanofluidic control of coupled photonic crystal resonators”. In: *Applied Physics Letters* 96.14 (2010), p. 141114.
- [447] Silvia Vignolini et al. “Nonlinear optical tuning of photonic crystal microcavities by near-field probe”. In: *Applied Physics Letters* 93.2 (2008), p. 023124.
- [448] MM Vogel et al. “Influence of lateral electric fields on multiexcitonic transitions and fine structure of single quantum dots”. In: *Applied Physics Letters* 91.5 (2007), p. 051904.
- [449] Stefan Völck et al. “Surface acoustic wave mediated carrier injection into individual quantum post nano emitters”. In: *Nanotechnology* 23.28 (2012), p. 285201.
- [450] S Volk et al. “H., Petroff, PM, Wixforth, A. & Krenner, HJ Enhanced sequential carrier capture into individual quantum dots and quantum posts controlled by surface acoustic waves”. In: *Nano Lett* 10 (2010), pp. 3399–3407.
- [451] Michael Wahl. “Time-Correlated Single Photon Counting”. In: *Technical Note, PicoQuant* (). URL: https://www.picoquant.com/images/uploads/page/files/7253/technote_tcspc.pdf.
- [452] Edo Waks and Jelena Vuckovic. “Coupled mode theory for photonic crystal cavity-waveguide interaction”. In: *Optics Express* 13.13 (2005), pp. 5064–5073.
- [453] Bowen Wang et al. “Controlling mode degeneracy in a photonic crystal nanocavity with infiltrated liquid crystal”. In: *Optics letters* 35.15 (2010), pp. 2603–2605.

- [454] Hui Wang et al. "Multi-photon boson-sampling machines beating early classical computers". In: *arXiv preprint arXiv:1612.06956* (2016).
- [455] Jianwei Wang et al. "Gallium arsenide (GaAs) quantum photonic waveguide circuits". In: *Optics Communications* 327 (2014), pp. 49–55.
- [456] Richard J Warburton et al. "Optical emission from a charge-tunable quantum ring". In: *Nature* 405.6789 (2000), pp. 926–929.
- [457] N. A. Wasley et al. "Disorder-limited photon propagation and Anderson-localization in photonic crystal waveguides". In: *Applied Physics Letters* 101.5 (2012), p. 051116. DOI: [10.1063/1.4742743](https://doi.org/10.1063/1.4742743). eprint: <http://dx.doi.org/10.1063/1.4742743>. URL: <http://dx.doi.org/10.1063/1.4742743>.
- [458] Yu-Jia Wei et al. "Deterministic and robust generation of single photons from a single quantum dot with 99.5% indistinguishability using adiabatic rapid passage". In: *Nano letters* 14.11 (2014), pp. 6515–6519.
- [459] Matthias Weiß et al. "Surface acoustic wave regulated single photon emission from a coupled quantum dot-nanocavity system". In: *arXiv preprint arXiv:1605.04956* (2016).
- [460] Barbara Wild et al. "Temperature tuning of the optical properties of planar photonic crystal microcavities". In: *Appl. Phys. Lett.* 84.6 (2004), pp. 846–848.
- [461] Martin Winger et al. "A chip-scale integrated cavity-electro-optomechanics platform". In: *Opt. Express* 19.25 (2011), pp. 24905–24921.
- [462] Martin Winger et al. "Explanation of photon correlations in the far-off-resonance optical emission from a quantum-dot-cavity system". In: *Physical review letters* 103.20 (2009), p. 207403.
- [463] Martin Winger et al. "Quantum dot spectroscopy using cavity quantum electrodynamics". In: *Physical review letters* 101.22 (2008), p. 226808.
- [464] XF Wu et al. "In situ tuning biexciton antibinding-binding transition and fine-structure splitting through hydrostatic pressure in single InGaAs quantum dots". In: *EPL (Europhysics Letters)* 107.2 (2014), p. 27008.
- [465] Xuefei Wu et al. "In situ tuning the single photon emission from single quantum dots through hydrostatic pressure". In: *Applied Physics Letters* 103.25 (2013), p. 252108. DOI: [10.1063/1.4856755](https://doi.org/10.1063/1.4856755). eprint: <http://dx.doi.org/10.1063/1.4856755>. URL: <http://dx.doi.org/10.1063/1.4856755>.
- [466] Xuefei Wu et al. "In situ tuning the single photon emission from single quantum dots through hydrostatic pressure". In: *Applied Physics Letters* 103.25 (2013), p. 252108.
- [467] Jan Hendrik Wülbern et al. "Electro-optic modulation in slotted resonant photonic crystal heterostructures". In: *Applied Physics Letters* 94.24 (2009), p. 241107.

- [468] Tian Xia. "Controlled coupling of semiconductor quantum dots to optical micro-cavities". PhD thesis. Technische Universiteit Eindhoven, 2015.
- [469] H Xu et al. "Observation of optomechanical buckling transitions". In: *Nature Communications* 8 (2017), p. 14481.
- [470] Xiaochuan Xu et al. "Flexible single-crystal silicon nanomembrane photonic crystal cavity". In: *ACS nano* 8.12 (2014), pp. 12265–12271.
- [471] Eli Yablonovitch. "Inhibited spontaneous emission in solid-state physics and electronics". In: *Physical review letters* 58.20 (1987), p. 2059.
- [472] Eli Yablonovitch, TJ Gmitter, and KM Leung. "Photonic band structure: The face-centered-cubic case employing nonspherical atoms". In: *Physical review letters* 67.17 (1991), p. 2295.
- [473] Lily Yang et al. "Optical spectroscopy of site-controlled quantum dots in a Schottky diode". In: *Applied Physics Letters* 108.23 (2016), p. 233102.
- [474] Xiaodong Yang et al. "Digital resonance tuning of high-Q/V m silicon photonic crystal nanocavities by atomic layer deposition". In: *Applied Physics Letters* 91.16 (2007), p. 161114.
- [475] Xiaodong Yang et al. "Digital resonance tuning of high-Q Vm silicon photonic crystal nanocavities by atomic layer deposition". In: *Applied Physics Letters* 91.16, 161114 (2007). DOI: <http://dx.doi.org/10.1063/1.2800312>. URL: <http://scitation.aip.org/content/aip/journal/apl/91/16/10.1063/1.2800312>.
- [476] Inah Yeo et al. "Strain-mediated coupling in a quantum dot-mechanical oscillator hybrid system". In: *Nature nanotechnology* 9.2 (2014), pp. 106–110.
- [477] Atsushi Yokoo et al. "Ultrahigh-Q nanocavities written with a nanoprobe". In: *Nano letters* 11.9 (2011), pp. 3634–3642.
- [478] Tomoyuki Yoshie et al. "Vacuum Rabi splitting with a single quantum dot in a photonic crystal nanocavity". In: *Nature* 432.7014 (2004), pp. 200–203.
- [479] Andrew B Young et al. "Polarization engineering in photonic crystal waveguides for spin-photon entanglers". In: *Physical review letters* 115.15 (2015), p. 153901.
- [480] Chun L Yu et al. "Stretchable photonic crystal cavity with wide frequency tunability". In: *Nano letters* 13.1 (2012), pp. 248–252.
- [481] Yi Yu et al. "Nonlinear switching dynamics in a photonic-crystal nanocavity". In: *Applied Physics Letters* 105.7 (2014), p. 071112.
- [482] Yi Yu et al. "Switching characteristics of an InP photonic crystal nanocavity: Experiment and theory". In: *Optics express* 21.25 (2013), pp. 31047–31061.
- [483] Jiayue Yuan et al. "Controlling polarization anisotropy of site-controlled InAs/InP (100) quantum dots". In: *Applied Physics Letters* 98.20 (2011), p. 201904.

- [484] Zhiliang Yuan et al. "Electrically driven single-photon source". In: *Science* 295.5552 (2002), pp. 102–105.
- [485] Emre Yüce et al. "Competition between electronic Kerr and free-carrier effects in an ultimate-fast optically switched semiconductor microcavity". In: *JOSA B* 29.9 (2012), pp. 2630–2642.
- [486] Tim Zander et al. "Epitaxial quantum dots in stretchable optical microcavities". In: *Optics express* 17.25 (2009), pp. 22452–22461.
- [487] Jiaxiang Zhang et al. "A Nanomembrane-Based Wavelength-Tunable High-Speed Single-Photon-Emitting Diode". In: *Nano Lett.* 13.12 (2013), pp. 5808–5813.
- [488] Jiaxiang Zhang et al. "High yield and ultrafast sources of electrically triggered entangled-photon pairs based on strain-tunable quantum dots". In: *Nature communications* 6 (2015).
- [489] Wen-Ming Zhang et al. "Electrostatic pull-in instability in MEMS/NEMS: A review". In: *Sensors and Actuators A: Physical* 214 (2014), pp. 187–218.
- [490] Yang Zhang et al. "Monolithically Integrated Microelectromechanical Systems for On-Chip Strain Engineering of Quantum Dots". In: *Nano Letters* 16.9 (2016), pp. 5785–5791.
- [491] Yuguang Zhang and Yaocheng Shi. "Post-trimming of photonic crystal nanobeam cavities by controlled electron beam exposure". In: *Optics express* 24.12 (2016), pp. 12542–12548.
- [492] Zili Zhou et al. "Superconducting series nanowire detector counting up to twelve photons". In: *Optics express* 22.3 (2014), pp. 3475–3489.
- [493] C Zinoni et al. "Time-resolved and antibunching experiments on single quantum dots at 1300 nm". In: *Applied Physics Letters* 88.13 (2006), p. 131102.
- [494] V Zwiller, T Aichele, and O Benson. "Single-photon Fourier spectroscopy of excitons and biexcitons in single quantum dots". In: *Physical Review B* 69.16 (2004), p. 165307.

Curriculum Vitae



Maurangelo Petruzzella was born on 21-09-1989 in Terlizzi, Italy.

After finishing high school in 2008 at *Istituto Tecnico Tecnologico G. Ferraris* in Molfetta (Italy) he studied Physics at the University of Bari (Italy), where he obtained a BSc with full marks and graduated with honors in 2011, with a thesis on quantum circuit models of computation. He carried out his Master's studies in Condensed Matter Physics at the same University, where he graduated *summa cum laude* in 2013, with a thesis on self-mixing interferometry employing terahertz quantum cascade lasers. In the same year, he was awarded a top student prize. In October 2013, he started a PhD project at the Eindhoven University of Technology (The Netherlands), the results of which are presented in

this dissertation.